Sequential Adaptation through Prediction of Structured Climate Risk

James Doss-Gollin

Submitted in partial fulfillment of the
requirements for the degree of
Doctor of Philosophy
under the Executive Committee
of the Graduate School of Arts and Sciences

COLUMBIA UNIVERSITY

2020

Abstract

Sequential Adaptation through Prediction of Structured Climate Risk

James Doss-Gollin

Infrastructure systems around the world face immediate crises and smoldering long-term challenges. Consequently, system owners and managers must balance the need to repair and replace the aging and deteriorating systems already in place against the need for transformative investments in deep decarbonization, climate adaptation, and transportation that will enable long-term competitiveness. Complicating these decisions are deep uncertainties, finite resources, and competing objectives.

These challenges motivate the integration of "hard" investments in physical infrastructure with "soft" instruments like insurance, land use policy, and ecosystem restoration that can improve service, shrink costs, scale up or down as future needs require, and reduce vulnerability to population loss and economic contraction. A critical advantage of soft instruments is that they enable planners to adjust, expand, or reduce them at regular intervals, unlike hard instruments which are difficult to modify once in place. As a result, soft instruments can be precisely tailored to meet near-term needs and conditions, including projections of the quasi-oscillatory, regime-like climate processes that dominate seasonal to decadal hydroclimate variability, thereby reducing the need to guess the needs and hazards of the distant future. *The objective of this dissertation is to demonstrate how potentially predictable modes of structured climate variability can inform the design of soft instruments and the formulation of adaptive infrastructure system plans.*

Using climate information for sequential adaptation requires developing credible projec-

tions of climate variables at relevant time scales. Part I considers the drivers of river floods in large river basins, which is used throughout this dissertation as an example of a high-impact hydroclimate extreme. First, chapter 2 opens by exploring the strengths and limitations of existing methodologies, and by developing a statistical-dynamical causal chain framework within which to consider flood risk on interannual to secular time scales. Next, chapter 3 describes the physical mechanisms responsible for heavy rainfall (90th percentile exceedance) and flooding in the Lower Paraguay River Basin (LPRB), focusing on a November-February (NDJF) 2015-16 flood event that displaced over 170 000 people. This chapter shows that

1. persistent large-scale conditions over the South American continent during NDJF 2015-16 strengthened the South American Low-Level Jet (SALLJ), bringing warm air and moisture to South East South America (SESA), and steered the jet towards the LPRB, leading to repeated heavy rainfall events and large-scale flooding;
2. while the observed El Niño event contributed to a stronger SALLJ, the Madden-Julien Oscillation (MJO) and Atlantic ocean steered the jet over the LPRB; and
3. while numerical sub-seasonal to seasonal (S2S) and seasonal models projected an elevated risk of flooding consistent with the observed El Niño event, they had limited skill at lead times greater than two weeks, suggesting that improved representation of MJO and Atlantic teleconnections could improve regional forecast skill.

Finally, chapter 4 shows how mechanistic understanding of the physical causal chain that leads to a particular hazard of interest – in this case heavy rainfall over a large area in the Ohio River Basin (ORB) – can inform future risks. Taking the GFDL coupled model, version 3 (CM3) as a representative general circulation model (GCM), this chapter shows that

1. the GCM simulates too many regional extreme precipitation (REP) events but under-simulates the occurrence of back to back REP days;
2. REP days show consistent large-scale climate anomalies leading up to the event;
3. indices describing these large-scale anomalies are well simulated by the GCM; and
4. a statistical model describing this causal chain and exploiting simulated large-scale indices from the GCM can be used to inform the future occurrence of REP days.

Even the best climate projections must confront epistemic uncertainties. Part II of this dissertation explores how intrinsically flawed projections should inform sequential adaptation. First, chapter 5 reviews approaches for planning under uncertainty, considering the role of classical decision theory, optimization, probability, and nonprobabilistic approaches. Next, chapter 6 considers how different physical mechanisms impart predictability at different time scales and the implications of secular, low-frequency cyclical, and high-frequency cyclical variability for selection between instruments with long and short planning periods. In particular, this chapter builds from three assertions regarding the nature of climate risk:

1. different climate risk mitigation instruments have different project lifespans;
2. climate risk varies on many scales; and
3. the processes which dominate this risk over the planning period depend on the planning period itself.

Defining M as the nominal design life of a structural or financial instrument and N as the length of the observational record (a proxy for total informational uncertainty), chapter 7 presents a series of stylized computational experiments to probe the implications of these premises. Key findings are that:

1. quasi-periodic and secular climate signals, with different identifiability and predictability, control future uncertainty and risk;
2. adaptation strategies need to consider how uncertainties in risk projections influence the success of decision pathways; and
3. stylized experiments reveal how bias and variance of climate risk projections influence risk mitigation over a finite planning period.

Chapter 7 elaborates these findings through a didactic case study of levee heightening in the Netherlands. Integrating a conceptual model of low-frequency variability with credible projections of sea level rise, chapter 7 uses dynamic programming to co-optimize hard (levee increase) and soft (insurance) instruments. Key findings are that

1. large but distant and uncertain changes (e.g., sea level rise) do not necessarily motivate immediate investment in structural risk protection;

2. soft adaptation strategies are robust to different model structures and assumptions while hard instruments perform poorly under conditions for which they were not designed; and
3. increasing the hypothetical predictability of near-term climate extremes significantly lowers long-term adaptation costs.

Finally, part III seeks to unpack the conceptual experiments of parts I and II to inform policy and future research. Chapter 8 describes how constructive narratives about climate change can discourage climate fatalism. Instead, chapter 8 emphasizes that while climate change is and will be a critical stressor of infrastructure systems, individuals, communities, and regions have agency and can mitigate its consequences. Finally, chapter 9 concludes by discussing the key findings of this dissertation and exploring how future work on decision under uncertainty, technology, and earth systems science can aid the design and management of effective infrastructure services.

Table of Contents

List of Tables

List of Figures

List of Acronyms

AA arctic amplification

ACC anthropogenic climate change

AMO Atlantic Meridional Oscillation

AMOC Atlantic Meridional Overturning Circulation

AR atmospheric river

BDT Bayesian decision theory

CBA cost-benefit analysis

CC Clausius-Clapeyron

CCA canonical correlation analysis

CM3 GFDL coupled model, version 3

CMIP climate model intercomparison project

CPC Center for Climate Prediction

DAPP dynamic adaptive policy pathways

DJF December-February

DOD Department of Defense

DP dynamic programming

DP16 Deconto and Pollard, 2016

DPS dynamic policy search

ECMWF European Centre for Medium-Range Weather Forecasts

ENSO the El Niño-Southern Oscillation

EOF empirical orthogonal function

EPA United States Environmental Protection Agency

EPG equator to pole temperature gradient

ESM Earth system model

ETC extratropical cyclone

FEMA the Federal Emergency Management Agency

GCM general circulation model

GEV generalized extreme value

GFDL Geophysical Fluid Dynamics Laboratory

GRFP Graduate Research Fellowship Program

HMM hidden Markov model

HXLR heteroscedastic extended logistic regression

IID independent and identically distributed

IPO Interdecadal Pacific Oscillation

IRI International Research Institute for Climate and Society

JJA June-August

K14 Kopp *et. al*, 2014

LBDA Living Blended Drought Analysis

LFV low-frequency variability

LPRB Lower Paraguay River Basin

LSL local sea level

MAM March-May

MDP Markov decision process

MJO Madden-Julien Oscillation

MORDM multiobjective robust decision-making

MOS model output statistics

NAO North Atlantic Oscillation

NCAR National Center for Atmospheric Research

NCEP National Center for Environmental Prediction

NDJF November-February

NHMM nonhomogeneous hidden Markov model

NPV net present value

NSF National Science Foundation

OLR outgoing longwave radiation

ORB Ohio River Basin

PCR principal components regression

PDF probability density function

PDO Pacific Decadal Oscillation

QBO Quasi-Biennial oscillation

RCP representative concentration pathway

RDM robust decision making

REP regional extreme precipitation

RL reinforcement learning

ROA real options analysis

S2D seasonal to decadal

S2S sub-seasonal to seasonal

SACZ South Atlantic Convergence Zone

SALLJ South American Low-Level Jet

SCAD South Central Atlantic Dipole

SDP stochastic dynamic programming

SERDP Strategic Environmental Research and Development Program

SESA South East South America

SST sea surface temperature

TC tropical cyclone

TME tropical moisture export

US United States

USACE United States Army Corps of Engineers

USGS United States Geological Survey

WT weather type

XLR homoscedastic extended logistic regression

Acknowledgements

This work would not have been possible had I not benefited from privileged access to resources for study and research, including incredible mentors and collaborators. Therefore as I recognize a need for systemic reforms that promote a more equitable access to these resources, I would also like to express my profound gratitude to everyone who helped and guided me along my journey.

First, it has been my great pleasure and honor to work for the past five years with Dr. Upmanu Lall. Manu treated me like a colleague from the day I arrived on campus, challenging me dive headfirst into new ideas and expand my understanding of what is possible. I am grateful not only for his guidance and patience, but also for the inspiring example of academic research driven by curiosity and empathy. I am also deeply grateful to the other members of my dissertation committee, Pierre Gentine, Casey Brown, Andrew Robertson, and Ngai Yin Yip, for their valuable insight, guidance, and mentorship.

I would next like to thank the many collaborators who pushed my thinking forward and contributed to my work. First, I want to thank the coauthors of the research presented in this dissertation: David J. Farnham, Michelle Ho, Upmanu Lall, Jonathan Lamontagne, Simon J. Mason, Ángel Muñoz, Max Pastén, and Scott Steinschneider. More generally, I would like to thank the brilliant, compassionate, and mission-oriented researchers at the Columbia Water Center and in the Department of Earth and Environmental Engineering, the members of Jonathan Lamontagne's research group at Tufts, and the broader water resources community for enriching my work, exposing me to new ideas, and helping me to maintain some semblance of sanity.

I would next like to thank the countless teachers and advisers who, over many years, helped me uncover my interests. In particular, I would like to thank the teachers at Wilbur Cross for their dedication to education. As an undergraduate I benefited from the opportunity to work in the research groups of Jan Schroers, Jaehong Kim, and Francisco de Assis de Souza Filho, and from the mentorship of Dave Sacco, Emily Byrne, James Saiers, Osny Enéas da Silva, and Patricia Melton. I would also like to thank my funders, colleagues, and community partners in Paraguay, Brazil, and Cameroon.

I am also grateful for other forms of support. My research benefited from the support of the Department of Defense (DOD) Strategic Environmental Research and Development Program (SERDP) and the National Science Foundation (NSF) Graduate Research Fellowship Program (GRFP) Climate and Large-Scale Atmospheric Dynamics program. I would also like to thank the Columbia Presidential Fellowship and the Nickolas and Liliana Themelis Fellowship for their financial support. I will strive to repay these investments by developing open tools and knowledge to address the deep societal problems that motivate my work, and by combating the systemic inequalities from which I have benefited. I would also like to thank the administrative staff who helped to support my research, and in particular Margo Weiss, Lisa Mucciacito, Thresine Nichols, and Elizabeth Allende. Further, I would like to extend my sincere thanks to the volunteer developers and maintainers of the software packages I used to organize data, build models, and compile this document.

In light of the frightening world conditions from which I write, I want to thank the healers, first responders, truth tellers, food workers, justice seekers, cleaners, organizers, and countless others who are guiding the world through the outbreaks of COVID-19, racism, and repression. You are heroes who inspire us all. At the same time, the inevitable stress of thesis writing has been greatly diminished (and the enjoyable aspects compounded!) by knowing what will come next. I am grateful to Klaus Keller and his research group at the Pennsylvania State University and to the Rice University Department of Civil and Environmental Engineering for their confidence. Great adventures lie ahead!

I would finally like to thank my friends and family for their support during this long process. Mari: you are the love of my life. You have made every frustration more bearable

and every triumph sweeter. Your resilience, determination, and compassion inspire me every day. Simon, Mom, and Dad: thank you for being my foundation and my guides. Your love, advice, support, and friendship have guided me every day of my life. To the rest of my friends and family: I consider surrounding myself with courageous, resilient, ambitious, and loving people to be my greatest accomplishment; I am fortunate beyond measure to have you in my life.

It was like facing an angry dark ocean. The wind was fierce enough that that day it tore away roofs, smashed windows, and blew down the smokestack - 130 feet high and 54 inches in diameter – at the giant A. G. Wineman & Sons lumber mill, destroyed half of the 110-foot-high smokestack of the Chicago Mill and Lumber Company, and drove great chocolate waves against the levee, where the surf broke, splashing waist-high against the men, knocking them off-balance before rolling down to the street. Out on the river, detritus swept past – whole trees, a roof, fence posts, upturned boats, the body of a mule.

John M. Barry, Rising Tide

1 Introduction

Many of the most powerful, terrifying, and mysterious deities encountered by human civilization, from Jupiter and Shango to Tupã and Thor, are associated with extreme weather, climate, and hydrology. Despite profound changes to nearly every aspect of society's relationship with nature since these stories developed, extreme hydroclimate events continue to wreak havoc upon life and property. Between 2010 and 2018, river floods in places such as Paraguay (*Doss-Gollin et al.*, 2018, and chapter 3), the Balkans (*Stadtherr et al.*, 2016), Central Europe (*Bissolli et al.*, 2011; *Grams et al.*, 2014), the Ohio River Basin (*Schubert et al.*, 2016; *Kornhuber et al.*, 2016; *Farnham et al.*, 2018, and chapter 4), and Pakistan (*Trenberth and Fasullo*, 2012; *Petoukhov et al.*, 2013; *Kornhuber et al.*, 2016) caused over 50 thousand deaths and displaced at least 55 million people (*Brakenridge*, 2018). Over the same period, persistent drought challenged the viability of cities such as Cape Town (*Muller*, 2018), Los Angeles (*Seager et al.*, 2014), and São Paulo (*Escobar*, 2015; *Seth et al.*, 2015), stunted global agricul-

tural production, and disrupted livelihoods and economies. Further contributions to death and destruction have manifested in the form of tropical cyclones (*Gale and Saunders*, 2013), tornadoes (*Lu et al.*, 2015), hailstorms (*Rädler et al.*, 2019), and landslides (*Cheng et al.*, 2018).

Physical infrastructure will play a pivotal role in managing hydroclimate risks over the next century, both because damage to built infrastructure and disruption to those who rely upon it is a critical impact of hydroclimate extremes, and because civil infrastructure is an expression of local and regional planning, which dramatically influences societal exposure and vulnerability (section 5.1.2). Of course, protection from hydroclimate hazards is just one of the many demands that society will make of its infrastructure systems over the 21st century. Deep decarbonization and mitigation of anthropogenic climate change (ACC) will require new infrastructure for energy generation, transmission, and storage at a massive scale (*MacDonald et al.*, 2016; *Jacobson et al.*, 2017; *Davis et al.*, 2018). Achieving universal access to water, electricity, telecommunications, and transportation services will require engineering designs and business models accessible to the world's poorest (*Sadoff et al.*, 2020). And remediating widespread environmental contamination, restoring degraded ecosystems, connecting the world through telecommunications, monitoring diseases, and facilitating sustainable urban growth through public transit and mobility will further demand changes of civil infrastructure systems.

In light of these many needs, infrastructure system designers and managers need to sequence and prioritize different types of investment. Three key factors complicate this task. First, existing infrastructure in the developed and developing world is aging and deteriorating (*Ho et al.*, 2017; *Brown and Willis*, 2006; *Harsha*, 2019) and was designed to meet now-inadequate societal and environmental requirements (*Lopez-Cantu and Samaras*, 2018; *Chester et al.*, 2020). This implies that planners need to evaluate new investments against the need to repair, replace, or abandon the infrastructure already in place. Second, while infrastructure has traditionally been designed to meet narrowly specified criteria, "deep uncertainty" as to future climate, technology, economics, and demographics means that these criteria are unlikely to meet the future needs of the infrastructure system as a whole or society more broadly (chapter 5). Finally, over-investment in large and static infrastructure projects can make com-

munities and utilities – the intended beneficiaries of infrastructure – more fragile (*Taleb*, 2012) by imposing debt payments (*Ansar et al.*, 2016, 2014; *Papakonstantinou et al.*, 2016) and maintenance obligations (*Marohn*, 2019). This leaves systems vulnerable to future scenarios in which funding becomes scarce or demand for services dissipates, leading to infrastructure decay. Examples of infrastructure decay such as lead poisoning in Flint and Newark or inadequate transit and housing in superstar cities highlight that the consequences of financial stress on infrastructure systems are felt most strongly by disadvantaged communities and people.

These challenges and opportunities underscore the need for better projections of future risks, better tools for planning under uncertainty, and better decision levers. These are broad challenges; this dissertation focuses in particular on integrating scientific understanding of potentially predictable and spatiotemporally structured modes of climate variability into proactive risk management strategies. A central premise is that planning is both sequential and path-dependent (*Wise et al.*, 2014), and so decisions made today necessarily affect the options available in the future. The remainder of this chapter elaborates upon the conceptual framework that motivates an emphasis on structured climate variability.

1.1 Conceptual Framework

This dissertation is divided into three parts. Part I explores the physical causal chains for significant river floods in large mid-latitude basins as an example of a high-impact hydroclimate extreme. Floods merit study given the high costs in life and property that they generate (*Munich Re*, 2017; *Swiss Re Institute*, 2017; *Brakenridge*, 2018). Part I builds on the premise that (i) hydroclimate extremes are driven by an interaction of boundary forcing, weather regimes, and synoptic weather patterns that organize and modulate large-scale moisture transport (section 2.1), and (ii) there is strong *potential* predictability of local climate risk at seasonal to decadal (S2D) timescales but deep uncertainty on multidecadal to century timescales. More specific hypotheses are articulated in section 1.1.1 and chapter 2, and novel research is presented in chapters 3 and 4.

Next, part II examines the implications of structured climate risk for infrastructure plan-

ning and management. This starting points for this discussion are that (i) uncertain future technology, costs, demographics, climate, local environmental conditions, and societal preferences imply that the design specifications of today are unlikely to meet the needs of the future; (ii) a mix of structural and flexible (e.g., financial and operational) policies may more effectively meet evolving future needs than a single static policy; and (iii) the role of science and decision theory in planning complex problems is to transparently and reproducibly map assumptions and preferences to outcomes. More specific hypotheses are outlined in section 1.1.2 and chapter 5 and novel research is presented in chapters 6 and 7.

Finally, Part III discusses the essential findings and implications of this work. Chapter 8 explores broadly applicable policy implications while chapter 9 considers future work that may better support adaptive, reliable, and cost-effective infrastructure services.

1.1.1 Causal Drivers of River Risks

In order to assess which predictive models may best inform sequential adaptation, it is critical to understand the causal dynamics that govern hydroclimate systems and, in particular, their extremes. Section 2.1 provides evidence for four hypotheses:

1. heavy rainfall over large river basins requires both large-scale moisture convergence and rainfall-generating mechanisms, which occur jointly in only a finite, and potentially identifiable, set of synoptic circulation patterns ("weather types;" section 2.1.1);
2. hemispheric-scale background circulations modulate these synoptic circulations, shifting the probability of basin-scale floods and droughts on sub-seasonal to seasonal (S2S) timescales ("weather regimes"; section 2.1.2);
3. low-frequency variability and anthropogenic climate change modulate the spatial and temporal expression of weather regimes on interannual and longer time scales, leading to nonstationarity of risk (section 2.1.3); and
4. low-order nonlinear dynamical systems provide an interpretable and informative framework for understanding the chaotic dynamics of hydroclimate extremes (section 2.1.4).

While there is intrinsic scientific value in understanding climate dynamics, the motivation for engineers and decision-makers to understand these phenomena is that better understand-

ing can lead to better decisions and outcomes. A range of engineering designs and policy decisions (see *Ayyub*, 2018, for examples from engineering practice) rely upon projections of relevant hydroclimate variables. Section 2.2 outlines two broad classes of widely used methodologies for estimating future risk:

1. data-driven methods that use predictive modeling to extrapolate future risk from one or more time series (section 2.2.1); and
2. dynamical models based on the numerical approximations to the laws of physics (section 2.2.2).

Though presented separately, there are deep theoretical links and shared challenges because these numerical models are also statistical models whose parameters must be calibrated or estimated, even if their functional forms derive from well-understood theories.

Section 2.3 considers how the full causal chain of relevant hydroclimate extremes may respond to ACC and how this understanding may be represented through models that integrate statistical and dynamical approaches. Key findings are that

1. the thermodynamic changes of weather extremes are moderately well understood, but dynamic changes remain deeply uncertain (section 2.3.1);
2. changes in the spatial expression, seasonality, persistence, and frequency of weather regimes are anticipated but often governed by conflicting and uncertain dynamics (section 2.3.2); and
3. hybrid statistical-dynamical models can bridge physical reasoning and statistical modeling to credibly quantify uncertainties, though they are dependent on the representation of underlying dynamics and exogenous conditions like the extent of ACC (section 2.3.3).

1.1.2 Sequential Adaptation and Transformation for Infrastructure Systems

Decisions about climate adaptation, systems planning, and infrastructure operation draw upon theoretical frameworks for decision science developed in other fields, including economics, policy, and business. These theories emphasize that

1. the axioms of rationality and Bayesian decision theory provide a calculus for value and choice, conditional upon subjective assessments of preference and belief (section 5.1.1);
2. many uncertainties that govern real-world planning problems cannot be described through a single, objective probability distribution (section 5.1.2);
3. the design and management of infrastructure is intrinsically "wicked" because objectives cannot be clearly defined and conflict is intrinsic (section 5.1.3); and thus
4. the role of decision theory, and science more broadly, for wicked problems should be to transparently link assumptions, preferences, and outcomes (section 5.1.4).

Various decision frameworks have been proposed for problems in wicked systems under deep (or "true") uncertainty. Despite significant differences, these frameworks generally agree in their

1. use of system models to explore the response to a wide range of plausible scenarios (section 5.2.1);
2. formulation of adaptive and sequential plans to exploit new information as it emerges over time (section 5.2.2); and
3. explicit quantification of competing tradeoffs (section 5.2.3).

In conjunction with developing more transparent and useful tools for decision under uncertainty, science can be used to develop new instruments so that better options are available to decision-makers. Improving the quality and reducing the cost of the options available to decision-makers can lead to better outcomes regardless of the formal decision framework used. In particular,

1. flexibility and optionality allow systems to manage changing conditions and generally increase robustness (section 5.3.1);
2. limiting exposure to hazards dramatically reduces losses (section 5.3.2); and
3. financial instruments, in coordination with other policy tools, can support proactive risk management strategies (section 5.3.3)

Part I

Understanding and Predicting Structured Climate Variability

First a subterranean sob rocked the cotton fields, curling them like waves of foam. Geologists had set up their seismographs weeks before and knew that the mountain had awakened again. For some time they had predicted that the heat of the eruption could detach the eternal ice from the slopes of the volcano, but no one heeded their warnings; they sounded like the tales of frightened old women. The towns in the valley went about their daily life, deaf to the moaning of the earth, until that fateful Wednesday night in November when a prolonged roar announced the end of the world, and walls of snow broke loose, rolling in an avalanche of clay, stones, and water that descended on the villages and buried them beneath unfathomable meters of telluric vomit.

Isabel Allende, De Barro Estamos Hechos
translated by Margaret Sayers Peden

2

Review of Methods for Projecting Future Flood Hazard

Although some uncertainties, particularly those depending upon human actions (including climate in the distant future) are deep (as defined in chapter 5), credible and accurate projections of hydroclimate variables can inform sequential adaptation decisions on shorter time scales (see *Nissan et al.*, 2019).

As in chapter 1, the specific methods and examples discussed in this chapter focus on projecting flood hazard over large river basins in the mid-latitudes, but the theoretical framework and broad methodological approaches are applicable to a range of hazards. The premise of this chapter is that quantifying future risks requires understanding the mechanisms that govern them. Section 2.1 begins by examining the drivers of persistent, heavy rainfall that can lead to floods over large river basins. Then, section 2.2 considers data-driven and model-driven

approaches for predicting future risk and their strengths and weaknesses. Finally, some opportunities for combining conceptual insight and imperfect models to constrain future risks are discussed in section 2.3.

2.1 Physical Drivers of Large River Floods

In order to assess which predictive models may best inform sequential adaptation, it is critical to understand the causal dynamics that govern hydroclimate systems and, in particular, their extremes. This section provides evidence for four hypotheses, shown schematically in fig. 2.1:

1. heavy rainfall over large river basins requires both large-scale moisture convergence and rainfall-generating mechanisms, which occur jointly in only a finite, and potentially identifiable, set of synoptic circulation patterns ("weather types;" section 2.1.1);
2. hemispheric-scale background circulations modulate these synoptic circulations, shifting the probability of basin-scale floods and droughts on sub-seasonal to seasonal (S2S) timescales ("weather regimes"; section 2.1.2);
3. low-frequency variability and anthropogenic climate change modulate the spatial and temporal expression of weather regimes over time, leading to temporal nonstationarity of risk (section 2.1.3); and
4. low-order nonlinear dynamical systems provide an interpretable and informative framework for understanding the chaotic dynamics of hydroclimate extremes (section 2.1.4) which motivate the use of specific methods for quantifying future risk (section 2.3).

2.1.1 Basin-Scale Drivers of Heavy Rainfall

The observational record provides substantial evidence that heavy rainfall over large river basins (the recurrence of which drives basin-scale flooding as discussed in section 2.1.2) requires organized transport and convergence of moisture.

Figure 2.1: Conceptual physical causal chain for riverine flooding in the mid-latitudes.

For example, atmospheric rivers (ARs) have been widely studied and linked to heavy rainfall and floods in many regions of the world (see *Gimeno et al.*, 2014; *Dacre et al.*, 2015; *Ralph and Dettinger*, 2011; *Payne et al.*, 2020, for a review). While a universal definition eludes the field of ARs, all definitions describe coherent filaments of moisture transported over long distances in the atmosphere, typically along the boundaries between large areas of divergent surface airflow. Often this large-scale moisture transport occurs in the warm conveyor belt of extratropical cyclones (ETCs) (*Bao et al.*, 2006). However, organized large-scale moisture transport can also occur along fronts (*Catto and Pfahl*, 2013) and in some cases what appears to be large-scale moisture transport is local convergence along the track (*Payne et al.*, 2020). In general, these distinctions are sensitive to place and definition used for ARs.

Cutting across different definitions are observational links between ARs, rainfall, and floods, particularly in the mid-latitudes. For example, statistical analyses have linked ARs to winter flooding in Britain (*Lavers et al.*, 2011), across Europe more generally (*Lavers and Villarini*, 2013a), and in the Midwestern United States (US) (*Lavers and Villarini*, 2013b; *Dirmeyer and Kinter*, 2011, 2010). Case studies of particular storms have demonstrated the relevance of ARs to meteorologically distinct regions including France (*Lu et al.*, 2013), Iran (*Dezfuli*, 2019), and Norway (*Stohl et al.*, 2008; *Sodemann and Stohl*, 2013). ARs are best known for their influence on rainfall and flooding in Western North America, particularly California where a large fraction of total annual rainfall is typically concentrated within a few AR events. This means that while ARs can cause floods, a lack of ARs can also cause drought (*Dettinger et al.*, 2011).

A complementary perspective to that of ARs, which often focus on their impact, is to study the hemispheric or global moisture cycle using a Lagrangian frame. For example, particle tracking studies have shown that a few small "source regions," typically oceanic, supply most of the moisture for continental rainfall (*Gimeno et al.*, 2010). These studies have also shown that large-scale sea surface temperature (SST) patterns including the El Niño-Southern Oscillation (ENSO) modulate this moisture budget (*van der Ent and Savenije*, 2013; *Castillo et al.*, 2014). Since the source regions that feed the mid-latitude hydrological cycle are typically tropical, this large-scale transport of water vapor is often called tropical moisture

export (TME) (*Knippertz and Wernli*, 2010; *Knippertz et al.*, 2013).

Although links between heavy rainfall, organized large-scale moisture transport, and rainfall generating mechanisms are most apparent in mid-latitude basins without adjacent moisture sources, there is also evidence that a finite set of potentially identifiable circulations is responsible for large-scale rainfall in other regions. For example, while Houston sits on the Gulf of Mexico (a dominant moisture source for the entire Great Plains; *Gimeno et al.*, 2010; *Dirmeyer and Kinter*, 2010), the severe "tax day floods" of 15 April 2016 were driven by a large-scale Ω block over the continental US which caused heavy precipitation, much of it as snowfall, across the entire Great Plains (*Fritz*, 2016). This emphasizes the importance of large-scale organization even when there are nearby moisture sources. Similarly, much of South East South America (SESA), a subtropical region (a subset of which is the subject of chapter 3), relies upon the South American Low-Level Jet (SALLJ) to inject warm, moist air from the Amazon, providing both moisture and a rainfall-generating mechanism (*Saulo et al.*, 2007; *Salio et al.*, 2002). Though anecdotal, this evidence suggests the relevance of this conceptual framework to adaptation and planning beyond the US and Western Europe.

2.1.2 Weather Regimes and S2S Variability

While individual large-scale rainfall events depend on organized moisture transport and a rainfall-generating mechanism, requiring specific synoptic circulation patterns, this does not fully explain floods and droughts over large basins on S2S time scales.

Several case studies illustrate this claim. For example, severe 2015-16 floods in the Lower Paraguay River Basin (LPRB) were the result of repeated heavy rainfall, rather than being driven by a single storm (see chapter 3). Similarly, *Trenberth and Fasullo* (2012) show that during the austral summer 2010, convection in the tropical Atlantic drove a wavetrain into Europe, creating anomalous cyclonic conditions over the Mediterranean. These interacted with an anomalously strong monsoon circulation, helping to support a persistent atmospheric anticyclonic regime over Russia and flooding in Pakistan (*Lau and Kim*, 2012). Similarly, *Nakamura et al.* (2013) showed that significant springtime floods in the Ohio River Basin (ORB) require several storms and positive anomalies of moisture transport over several weeks.

Najibi et al. (2019) find that in the adjacent Missouri River basin, a persistent block drives flood risk regardless of the presence of atmospheric and local moisture.

These persistent flow regimes shift hemispheric moisture cycles, and thus global flood and drought risk. For example, *Rothlisberger et al.* (2016) use indices of jet stream sinuosity to conclude that more meanders lead to more extremes. Similarly, *Screen and Simmonds* (2014) show that at monthly time scales, high amplitudes of particular planetary waves influence temperature and precipitation extremes. *Lehmann and Coumou* (2015) assess statistical relationships between the storm tracks (i.e., area of high baroclinicity through which ETCs tend to propagate) and hydroclimate extremes, finding that (i) summer heat extremes are associated with low storm track activity over large parts of mid-latitude continental regions, (ii) winter cold spells are related to low storm track activity over parts of eastern North America, Europe, and central- to eastern Asia, (iii) pronounced storm track activity favors monthly rainfall extremes throughout the year, and (iv) dry spells are associated with a lack thereof. And *Teng and Branstator* (2016) and *Seager et al.* (2014) show that a continuum of $k = 5$ circumglobal teleconnection patterns, originating in adiabatic processes in the midlatitudes independent of ENSO, cause many droughts in California.

These findings motivate further theoretical development. *Reinhold and Pierrehumbert* (1982) define interactions between quasi-stationary large-scale behavior and organized synoptic behavior as "weather regimes". The mechanisms that give rise to this behavior are described through a set of related yet distinct theoretical frameworks. For example, *Kaspi and Schneider* (2013) analyze the storm tracks through mean-eddy interaction theory. Alternatively, *Tyrlis and Hoskins* (2008) summarize the known literature on blocking, a special class of weather regimes whose intrinsic dynamics remain imperfectly understood. *Branstator* (2002) develops a "circumglobal global teleconnection" with meridional wavenumber $k \approx 5$. And *Woollings et al.* (2018, 2014a) explore large-scale variability of the jet, noting multi-modality of jet latitude and speed that vary on daily to decadal scales. The presence of regime behavior and multimodality motivates the use of low-order nonlinear dynamical systems as a conceptual framework for understanding these dynamics (see *Hannachi et al.*, 2017, and section 2.1.4).

Mechanistic understanding can help interpret past events and inform future possibilities. *Petoukhov et al.* (2013) derive a quasi-resonant summer mode, when waveguides for quasi-stationary Rossby waves with $6 \leq k \leq 8$ can form. Although quasi-resonance itself relies upon linear dynamics, the formation of these waveguides may depend upon more complex nonlinear phenomena such as Rossby wave breaking (*Palmer*, 2013; *Kornhuber et al.*, 2016). Quasi-resonance can also drive midlatitude synchronization of extreme heat and rainfall events on monthly (*Coumou et al.*, 2014) and other subseasonal (*Kornhuber et al.*, 2019a; *Coumou et al.*, 2014) timescales, and to specific flood events (e.g., *Stadtherr et al.*, 2016). This literature demonstrates the importance of understanding regimes and their effect on spatiotemporally clustered hydroclimate risk.

Although this section argues that large-scale transport of moisture drives hydroclimate extremes, this does not imply that all water falling as rainfall in a particular basin originates in a distant source region. For example, *Dirmeyer and Kinter* (2010) use Lagrangian moisture tracking to show that relatively little moisture supplying summer floods in the US Midwest comes directly from distant oceanic sources. However, they also show that the large-scale transport of moisture is linked to regional water recycling (see *Trenberth*, 1999, for a discussion of water recycling) and therefore that the variability of the large-scale transport drives interannual flood variability. This also is consistent with *Steinschneider and Lall* (2016), who find strong spatiotemporal co-variability between leading empirical orthogonal functions (EOFs) of TMEs and floods in the northeastern US. At the other end of the hydrological spectrum, *Roy et al.* (2018) compare a drought in Texas (2011) and the Upper Midwest (2012), finding that reduced advection from the tropical and midlatitude Atlantic drove the the drought in Texas while an absence of precipitation-generating mechanisms (which *Hoerling et al.*, 2014, link to reduced cyclone and frontal activity) caused the upper Midwest drought. Thus, while land-atmosphere feedbacks and other local dynamics likely contribute to regime behavior, it is important to understand local hydroclimate extremes within the context of the regional and hemispheric water cycles.

2.1.3 Interannual to Secular Modulation of Weather Regimes

Time series analyses of paleoclimate and historical records consistently show evidence of high-amplitude, quasi-periodic interannual to multidecadal modes of variability.

For example, *Cook et al.* (2010) use tree ring reconstructions to demonstrate that both the western US and the Mississippi River Valley have experienced multi-decade "megadroughts" several times in the past millennium. Similarly, *Swierczynski et al.* (2012) use sediment core analysis to produce a 1600 year record of flooding from the Austrian alps; this also shows strong multidecadal clustering of flood events. To generalize this insight *Hodgkins et al.* (2017) analyze an observational dataset from the US and Europe, finding that "changes over time in the occurrence of major floods were dominated by multidecadal variability rather than by long-term trend." Low-frequency variability (LFV) has been observed in a wide range of local, regional, and global processes including Antarctic sea ice extent (which interacts nonlinearly with mean SSTs; *Jenkins et al.*, 2018), North Atlantic jet latitude (*Woollings et al.*, 2014b; *Hannachi et al.*, 2011), and lightning activity in western Venezuela (*Muñoz et al.*, 2016a).

The mechanisms governing some modes of LFV are increasingly well understood; the most studied mode is the El Niño-Southern Oscillation (ENSO) (see *Sarachik and Cane*, 2009, for a comprehensive reference). ENSO is the leading mode of global hydroclimate variability and modulates of flood hazard and other hydroclimate hazards around the world (*Ward et al.*, 2014; *Ropelewski and Halpert*, 1987; *Cai et al.*, 2020; *Anderson et al.*, 2018; *Grimm*, 2003). While several dynamical frameworks have been proposed for understanding and predicting ENSO (e.g., *Zebiak and Cane*, 1987; *Timmermann et al.*, 2018), all note a variety of relevant frequencies whose frequencies are locked by specific nonlinear resonances within the Earth's annual cycle (*Jin et al.*, 1994). Such LFV may contribute to the strong potential predictability identified using numerical models (*Gonzalez and Goddard*, 2015) and convolutional neural networks (*Ham et al.*, 2019), though most dynamical models report lower predictability and struggle to capture the "diversity" of different ENSO events that lead to different impacts (*Capotondi et al.*, 2015; *Williams and Patricola*, 2018). *Zhang et al.* (2018) suggest that a key challenge for ENSO predictability is that it interacts with other low-frequency modes of Pacific variability (e.g., the Pacific Decadal Oscillation (PDO) and Interdecadal Pacific Oscillation (IPO)) and that

insufficient data is available to characterize these cross-timescale relationships. The modulation of ENSO predictability by these lower-frequency modes may explain why studies using different time periods for validation report different degrees of ENSO predictability.

The Hurst phenomenon, ENSO, and some examples of time series with high-amplitude LFV are discussed at length in chapter 6.

2.1.4 Synthesis: Cross-Timescale Chaotic Dynamics

The observational and modeling studies detailed above describe that hydroclimate hazards, including river floods in large basins, vary on a range of time scales.

A helpful framework through which to consider these dynamics is chaos theory (introduced and popularized by *Lorenz*, 1963, 1984). As suggested in sections 2.1.2 and 2.1.3, low-order dynamical representations of the climate consistently exhibit multiple modes and regime behavior as predicted by these simple models (*Hannachi et al.*, 2017; *Ghil*, 2020; *Ghil et al.*, 2011). While the climate is a high-dimensional nonlinear system, this suggests that low-dimensional nonlinear systems provide a valuable complement to linear wave theory for understanding persistent extremes.

For example, the response of the *Lorenz* (1963) model to boundary forcing is (up to a threshold) to shift the probability associated with the system being in each of the two regimes, rather than to shift the properties of either regime (*Palmer*, 1993, 1999; *Corti et al.*, 1999). A significant obstacle to the real-world application of these theories is that defining the phase space of a system is an arbitrary and open-ended decision (*Kimoto and Ghil*, 1993). Despite limitations as predictive tools, these theories provide a helpful framework for understanding more detailed theories for how specific climate mechanisms (e.g., changing seasonality and Hadley expansion; see section 2.3) may change under anthropogenic warming.

While this section has emphasized mid-latitude dynamics (e.g., the jet, storm tracks, and blocking), other mechanisms (e.g., the Madden-Julien Oscillation (MJO) and ENSO) drive hydroclimate variability in the tropics on S2S timescales. Like mid-latitude dynamics, these phenomena are also modulated by lower-frequency modes of variability as discussed in section 2.1.3 (defined in *Muñoz et al.*, 2015, 2016b, as "cross-timescale interactions"). It is there-

fore reasonable to argue that this section's key conclusions – that quantification of future hydroclimate risk must explicitly take into account regime behavior and LFV – apply to hydroclimate risks beyond river floods in large mid-latitude basins, though the specific causal chains will depend on the hazard and location of interest.

2.2 Methods for Constraining Hydroclimate Risks

While there is intrinsic scientific value in understanding climate dynamics, the motivation for engineers and decision-makers to understand these phenomena is that better understanding can lead to better decisions and better outcomes. A broad range of engineering designs and policy decisions (see *Ayyub*, 2018, for examples from engineering practice) rely upon projections of relevant hydroclimate variables. This section outlines two broad classes of widely used methodologies for estimating future risk:

1. data-driven methods that use predictive modeling to extrapolate future risk from one or more time series (section 2.2.1); and
2. dynamical models based on the laws of physics, that simulate numerical representations of key processes (section 2.2.2).

Though presented separately, there are deep theoretical links and shared challenges because these numerical models are also statistical models whose parameters must be calibrated or estimated, even if their functional forms derive from well-understood theories. Hybrid methods that combine statistical parameterization and physical understanding are considered in section 2.3.3.

2.2.1 Curve-Fitting Methods

An intuitive way to constrain future risk is to use historical records of the quantity of interest, where available. Given N observations of this variable $\mathbf{y} = y_1, y_2, \ldots, y_N$, the parameters $\boldsymbol{\theta}$ of a particular distribution $\mathcal{D}$ can be estimated. Future observations $\hat{y}$ are then assumed to follow this distribution: $\hat{y} \sim \mathcal{D}(\boldsymbol{\theta})$ (the statistical notation used throughout approximately follows the convention of *Gelman et al.*, 2014).

The past, however, is unlikely to be a perfect proxy for the future. First, short records of fat-tailed distributions offer limited information about the tails of the distribution (*Lall*, 1986). When large floods do eventually arrive, they incur a high degree of surprise (*Smith et al.*, 2018), emphasizing the difficulty and intrinsic uncertainty of modeling tail probabilities. Second, "nonstationarity" (*Milly et al.*, 2008) due to global climate change, local environmental change, and water management practices (*Merz et al.*, 2014) implies that risks are changing in time. To address nonstationarity, one or more predictors $X = \mathbf{x}_1, \mathbf{x}_2, \ldots, \mathbf{x}_N$ (the most common of which is time) can be added so that the full model to estimate is

$$y_i|\mathbf{x}_i \sim \mathcal{D}(\boldsymbol{\theta}_i(\mathbf{x}_i)), \tag{2.1}$$

implying that y_i continues to follow $y_i \sim \mathcal{D}(\boldsymbol{\theta}_i)$ but that $\boldsymbol{\theta}_i$ depends on $\mathbf{x}_i$. These are referred to as "nonstationary" models and, in the special case where $\mathbf{x}$ is just time, as trend models. The future distribution of y, ($\hat{y}$), can be estimated analytically or numerically by plugging estimates for $\boldsymbol{\theta}$ into a model for future values of $\mathbf{x}$.

To build a predictive model for $\hat{y}$, the analyst must choose the distribution $\mathcal{D}$, the predictors $\mathbf{x}$ (if any), the "nonstationary" parameterization $\boldsymbol{\theta}(\mathbf{x})$, and an estimator. Even in the stationary case, the choice of distribution $\mathcal{D}$ and estimator for $\boldsymbol{\theta}$ have occupied substantial attention; see *Matalas and Fiering* (1977) and *Loucks* (2017) for an overview or *Stedinger* (1997) for a discussion of which questions different formulations are best suited to answer. In the case of trend distributions, the most common formulation for $\boldsymbol{\theta}(\mathbf{x})$ involves imposing a linear dependence for one or more of the parameters $\boldsymbol{\theta}$ on time (e.g., *Obeysekera et al.*, 2014; *Obeysekera and Salas*, 2016; *Salas et al.*, 2014; *Read and Vogel*, 2016a) though other formulations are also used (see *Salas et al.*, 2018, for a comprehensive review). In general these trend models lack theoretical foundation and may extrapolate poorly (*Montanari and Koutsoyiannis*, 2014; *Serinaldi and Kilsby*, 2015; *Matalas*, 2012).

One key assumption that these models make is that observations of y are independent and identically distributed (IID). In practice, hydroclimate time series exhibit strong spatiotemporal dependence, which renders this assumption doubtful. For example, *Cohn and Lins* (2005) uses simple simulation models to show that the statistical significance of standard models

is inaccurate in the presence of LFV. This matters, as many methods use trend detection for formal selection (e.g., *El Adlouni et al.*, 2008; *Salas et al.*, 2018); further simulations illustrating this pitfall are presented in chapter 7. In a similar spirit, *Pizarro* (2006) shows that in the presence of LFV, IID assumptions lead to biased estimates of flood risk and under-representation of true variability. However, *Pizarro* (2006) also finds that if LFV is explicitly modeled and accounted for (i.e., by adding sufficient information to eq. (2.1) to model $y|\mathbf{x}$ as conditionally IID), credible risk projections can be developed. This point is revisited in section 2.3 and chapter 4.

A second limitation of this approach is that, when many combinations of model formulation are considered and their cumulative uncertainties considered jointly, uncertainties become very large, particularly as the analyst extrapolates farther into the future (or, more generally, out of sample). For example, *Wong et al.* (2018) combine four models, each with linear relationships between the North Atlantic Oscillation (NAO) and parameters of a generalized extreme value (GEV) distribution, using Bayesian model averaging and find that the total uncertainty is larger that of any individual model. Many methods for model selection in the hydrological literature look for the model that performs the best, by some metric, over the historical time series or use hypothesis testing (e.g., a trend test) to determine whether to expand a model (*El Adlouni et al.*, 2008; *Read and Vogel*, 2016a,b). However, the literature on Bayesian model selection emphasizes that selecting a single best model without a strong theoretical rationale is a form of over-fitting that can lead to poor out of sample prediction and, by neglecting model structure uncertainty, artificially inflate the certainty of projections produced (*Heinze et al.*, 2018; *Greenland*, 2008; *Heinze and Dunkler*, 2017; *Van der Weele*, 2019; *Gelman and Loken*, 2013; *Yao et al.*, 2018; *McShane et al.*, 2017; *MacGillivray*, 2019).

2.2.2 Numerical Climate Prediction

The increasing skill and ubiquity of general circulation models (GCMs) and other Earth system models (ESMs) (the term GCM is used henceforth) suggest that they should play an important role quantifying local hydroclimate hazards.

A motivating advantage of GCMs relative to purely statistical models (stationary or oth-

erwise) is that their physical basis constrains quantities estimated under extrapolation, such as hydroclimate hazard in a warmer world. Originally developed as sandboxes within which to conduct numerical experiments, GCMs are now widely used for numerical weather prediction, S2S and seasonal to decadal (S2D) prediction (*Cassou et al.*, 2018; *Meehl et al.*, 2014; *Merryfield et al.*, 2020; *Kushnir et al.*, 2019), and to study response to boundary conditions (e.g., anthropogenic climate change (ACC)).

Despite advantages, GCMs are also intrinsically limited for informing long-term planning. One challenge is their representation of rainfall, which *Stephens et al.* (2010) describe as "dreary" because GCM precipitation fields tend to "smear" rainfall in space and time, leading to artificially high counts of rainy days and biased representation of extremes (*Dai*, 2006; *Kendon et al.*, 2012). These biases typically decrease as data are aggregated in space in time, and as model resolution increases (*Kendon et al.*, 2012). However, outputs from GCMs are commonly used as inputs for other models (e.g., crop yield and hydrological models), which also contain biases and errors, and as these model "chains" (*Merz et al.*, 2014) grow more complex, these biases and errors can propagate in counterintuitive ways (e.g., as described in *Dittes et al.*, 2018).

In light of these deficiencies, "bias correction" or model output statistics (MOS) approaches are commonly used to transform model outputs, thereby improving their performance (by some metrics) over the observational record. A simple and widely used form is quantile-quantile mapping, in which the quantile of the model output at each grid cell is mapped to the corresponding quantile of the observational record (e.g., *Block et al.*, 2009), but more sophisticated models are also used. For example, some models explicitly modify the model's temporal structure, e.g. by forcing a lagged autocorrelation to match that of observations at one or more time scales (*Johnson and Sharma*, 2012; *Rocheta et al.*, 2017). A fundamental assumption that these models make is that the relationship between model output and the true quantity of interest is stationary. This may be a reasonable assumption for weather prediction and even S2S forecasting, explaining some successes with these methods (*Piani et al.*, 2010; *Glahn and Lowry*, 1972; *Rajczak et al.*, 2016, and chapter 3). However, this stationary assumption is not in general valid, particularly under ACC, and can lead to poor extrapola-

tion even when bias correction schemes show good performance on observed data (*Lanzante et al.*, 2018; *Ehret et al.*, 2012). Not only do first principles (i.e., section 2.1) suggest that climate change may violate this relationship (for example, if the models do not accurately represent poleward shifts of the storm tracks) but studies have also shown that the presence of strong LFV can violate this relationship and lead to poor extrapolation (*Bock et al.*, 2018; *Maraun and Widmann*, 2018). Bias correction models also suffer from the model selection challenges outlined in section 2.2.1.

More fundamentally, GCM projections of hydroclimate variability on S2S and longer time scales seem to exhibit dynamical shortcomings that bias correction cannot, in general, remedy. Specifically, climate model intercomparison project (CMIP) models under-represent a wide range of LFV modes that, as discussed in section 2.1.3, drive global hydroclimate hazards such as monsoons, teleconnections, drought, and blocking (*Trenberth and Fasullo*, 2012; *Moon et al.*, 2018). For example, *Espinoza et al.* (2018) show that in general models underestimate AR frequency and moisture transport, albeit with substantial inter-model spread. CMIP models also underestimate the amplitude of many modes of LFV, such as the Atlantic Meridional Overturning Circulation (AMOC) (*Yan et al.*, 2018). *Kim et al.* (2020) show that just half of the CMIP climate models simulate the Quasi-Biennial oscillation (QBO), a dominant mode of interannual variability in the stratosphere, and that none of them capture the observed relationship between the QBO and the MJO, a dominant mode of subseasonal tropical variability. *Kravtsov et al.* (2018) find a discrepancy between simulated and observed multidecadal variability, even suggesting that there may be a missing mode of variability. *Greene and Robertson* (2017) find that just eight of 31 ensemble members studied reasonably reproduce the two leading modes of the seasonal rainfall cycle in the Upper Indus Basin. And *Feng et al.* (2019) show that most CMIP models drastically under-represent the true diversity of ENSO variability, possibly because of large differences in intrinsic ENSO dynamics of these models (*Wengel et al.*, 2018). This poor representation of LFV likely results from a combination of factors, including poor simulation of clouds and deep convection (*Muller et al.*, 2011) and artificial damping of variability to reduce the propagation of numerical errors and better fit the historical record (hypothesized in *Palmer*, 1999).

While one workaround is to select only the models or ensemble members that have performed the best over the historical record, there is no guarantee that these models will perform well in a warming world with different background dynamics. These findings emphasize the need for careful interpretation of the output of any model, including both GCMs and bias correction schemes, and for analysts to communicate uncertainties and limitations clearly (*Saltelli*, 2019; *Stainforth et al.*, 2007). Although model improvements are likely to reduce some of these specific limitations, the fundamental limitations of using models to extrapolate far into the future remain.

Some specific models MOS models for S2S prediction are discussed in more detail in chapter 3, and some additional perspectives on bias correction are explored in chapter 4.

2.3 Integrating Conceptual Understanding through Imperfect Models

While sections 2.2.1 and 2.2.2 argue that "plug and play" models that credibly project hydroclimate variables far into the future at an arbitrary location do not exist, it may be possible to create credible projections for specific variables and locations by integrating mechanistic understanding of the physical causal chain with careful statistical modeling. This section considers how synoptic weather, including ETCs and tropical cyclones (TCs), responds to ACC, then how weather regimes and LFV may respond, and finally how this understanding may be represented through models that integrate statistical and dynamical approaches. In particular, this chapter argues that:

1. thermodynamic changes of weather extremes are relatively well understood, but dynamic changes remain deeply uncertain (section 2.3.1);
2. changes in the spatial expression, seasonality, persistence, and frequency of weather regimes are anticipated but often governed by conflicting and uncertain dynamics (section 2.3.2); and
3. hybrid statistical-dynamical models can bridge physical reasoning and statistical modeling to credibly quantify uncertainties, though they are dependent on the representa-

tion of underlying dynamics (section 2.3.3).

Taken together, these findings imply that strong potential predictability of hydroclimate hazard in a particular location on S2D timescales but deep uncertainty on multidecadal to century timescales.

2.3.1 Response of Extreme Weather Patterns to ACC

The response of extreme-generating synoptic weather patterns, including ETCs and TCs, to warming has been the subject of extensive study.

In general, thermodynamic responses are better understood than dynamical ones. This literature builds on the well-known Clausius-Clapeyron (CC) equation, which relates the moisture holding capacity of air to temperature. CC theory predicts a water vapor increase of approximately 7.5% for every 1 K increase in moisture vapor, and indeed observations indicate that total column water scales approximately with the CC relation (*Held and Soden*, 2006). While large-scale moisture transport is likely to scale with total column water (and, hence, CC scaling), rainfall does not obey such simple relationships (*Pall et al.*, 2007). Instead, theory and simulation suggest that characteristics of rainfall, such as storm size and intensity, are more likely to respond to warming than bulk averages (*Trenberth et al.*, 2003). These dynamical changes are highly dependent upon specific mechanisms. For example, *Rädler et al.* (2019) build a regression model for thunderstorms and instability, finding that rising humidity near the earth's surface will likely increase instability, and thus thunderstorm-related hazard, over Europe. This is consistent with *Pendergrass and Knutti* (2018), who argue that the skewness of rainfall distributions is likely to increase under ACC, and with *Berg et al.* (2013), who combine radar measurements and rain gauge data over Germany to show that convective precipitation responds much more sensitively to temperature increases than stratiform precipitation. A general interpretation is that in many locations, and for many mechanisms, storms are anticipated to get smaller but more intense (*Chang et al.*, 2016). Other extensions of the CC scaling improve the fidelity of simulated rainfall, e.g. by adding a term for upward velocity ω (*O'Gorman and Schneider*, 2009; *O'Gorman*, 2015; *Nie et al.*, 2020; *Pfahl et al.*, 2017) or large-scale moisture transport (*Byrne and O'Gorman*, 2015). However, this approach induces

a dependence on the dynamical terms, which are themselves uncertain, emphasizing the role of dynamics for understanding future rainfall (*Palmer*, 2013).

One relatively well understood mechanism is TC intensity. The thermodynamics of Carnot processes gives a theoretical upper bound on the intensity of TCs (*Emanuel*, 1988), providing a sound basis to anticipate an intensification of TCs, at least for the most intense events, under climate change, *Knutson et al.* (2010). However, the response of more complex behaviors linked to high-impact storms in recent years, including rapid intensification and stalling, remains much less certain (*Emanuel*, 2017a). These uncertainties matter: simulation of a wide range of plausible, or "grey swan" TCs indicates that small changes in assumed dynamics can have a very large effect on the return periods of high-impact storms (*Lin and Emanuel*, 2016).

2.3.2 Response of Weather Regimes and LFV to Warming

While less well understood than the response of long-term averages over large areas or within-storm behavior, the response of weather regimes and LFV modes are likely to dominate changes in many types of hydroclimate risk, including river floods in large basins.

One motivation for understanding the role of these dynamics comes from the "time of emergence" literature, which uses GCMs to estimate the point at which the signal of ACC exceeds that of internal climate variability. *Hawkins and Sutton* (2012) shows that this time of emergence can be from 30 to 60 years, that estimates differ between representative concentration pathway (RCP) scenarios by a decade or more, and that time of emergence depends heavily on location (e.g., arriving sooner in the Arctic). Of course, some variables integrate past changes; the time of emergence for sea level is very different from that of extreme rainfall (*Lyu et al.*, 2014). Similarly, *Santer et al.* (2018) show that a classification model can distinguish between historical and current weather patterns at the global scale, signifying that even if the time of emergence for specific local hazards in a particular place is distant that global weather already shows measurable ACC impacts. While this literature often treats internal climate variability as a source of noise that complicates the estimation of ACC signals, these findings also highlight the importance of S2S and S2D modes of variability to adaptation policy.

There are some dynamical changes for which simple theories and model simulations agree, providing relative confidence. An example is the response of the Hadley circulation to warming, which simple theories (see *Vallis*, 2006, chapter 11), notably including (i) that angular momentum conservation sets the extent of the tropics (*Held and Hou*, 1980) and (ii) that the tropics extend to the latitude at which the tropical jet is baroclinically unstable (*Lu et al.*, 2007) project to expand with ACC. Idealized GCMs also have this effect (*Tandon et al.*, 2012), more realistic models estimate it at 2° by 2100 (*Seidel et al.*, 2007), and reanalysis also shows it (after adjusting for lack of mass conservation; see *Davis and Davis*, 2018). Even if the exact magnitude and timing are uncertain, the high confidence in Hadley expansion should inform long-term planning, not only in the subtropical regions directly affected, but also in regions exposed to phenomena including TCs (*Ng and Vecchi*, 2020; *Sharmila and Walsh*, 2018) that respond to changing background conditions.

The response of other phenomena, such as the storm tracks, mid-latitude jet, and blocking (see section 2.1.2) to warming remains more uncertain. Typically, the problem is not a lack of understanding but rather competition between opposing mechanisms. For example, *Shaw et al.* (2016) describe that as mean temperatures increase, short-wave radiative changes increase the equator to pole temperature gradient (EPG) while long-wave changes act to reduce it. Changes to the EPG have also been studied through the lens of arctic amplification (AA): while the lower tropopause has warmed (and is anticipated to continue to warm) faster in the Arctic than elsewhere, its impact on the jet stream remains uncertain. Although *Francis and Vavrus* (2012) found a statistical relationship between the lower troposphere EPG and the phase speed of ETCs, consistent with simple scaling relationships suggesting lower EPG would lead to slower wave speeds and more quasi-stationary behavior, these results proved sensitive to definitions and methods (*Barnes and Screen*, 2015). For example, while the EPG in the lower troposphere has weakened, it has strengthened at higher altitudes, which could instead strengthen the extratropical jet (*Cohen et al.*, 2014). This would agree with experiments from a dry idealized GCM that show a robust decline in blocked area and meridional wave amplitude as lower tropospheric EPG declines, despite the decrease in zonal winds and zonal Z_{500} gradient (*Hassanzadeh et al.*, 2014), part of a weak consensus that blocking may actually

decline with warming (*Hoskins and Woollings*, 2015). Other studies have found important second-order effects. For example, a slowing AMOC in response to ACC (*Rahmstorf et al.*, 2015) can cause cold SSTs over the northern Atlantic and favor blocking over Western Europe (*Duchez et al.*, 2016; *Coumou et al.*, 2018), which portends an increase in quasi-stationary behavior for some regions and seasons. Interaction between global mean temperatures and hemispheric or regional dynamic processes would be consistent with paleo records, e.g. for drought risk in Europe (*Markonis et al.*, 2018) or floods in the American Southwest (*Hoffman and Gelman*, 2011), though spatial patterns of future warming will differ from historical patterns and so these proxies are imperfect. Other anticipated changes include changing seasonality of floods (*Mallakpour and Villarini*, 2015), longer summers (*Pfleiderer et al.*, 2019), and increased quasi-resonant (as defined in section 2.1.2) wavetrains (though with large intermodel spread; *Huntingford et al.*, 2019; *Mann et al.*, 2018).

2.3.3 Hybrid Statistical-Dynamical Methods

A general challenge that complicates estimation of the response of regime behavior to warming is that GCMs and ESMs struggle to capture these dynamics, as discussed in section 2.2.2. This suggests a role for physically informed models that use statistical and machine learning tools to represent processes that GCMs do not adequately capture.

While naive statistical modeling of dynamical systems can be misleading, particularly for the characterization of extremes (*Faranda et al.*, 2013; *Lucarini et al.*, 2014), integrated statistical-dynamical models can shed light on a wide range of phenomena (see *Ghil et al.*, 2011; *Ghil*, 2020, for discussion and examples). For example, weather typing using clustering (*Lee and Sheridan*, 2018; *Muñoz et al.*, 2015; *Doss-Gollin et al.*, 2018; *Michelangeli et al.*, 1995), self-organizing maps (*Agel et al.*, 2018), and archetypes (*Steinschneider and Lall*, 2015a; *Hannachi and Trendafilov*, 2017) can diagnose the circulations and regimes that drive phenomena of interest. Complex networks and event synchronization tools can inform, for example, how extreme rainfall propagates through a given domain (*Boers et al.*, 2014; *Conticello et al.*, 2017; *Boers et al.*, 2013; *Conticello et al.*, 2020). Alternatively, metrics of persistence and complexity derived from dynamical systems theory can inform the potential predictability of different

flow regimes at low computational cost (*Faranda et al.*, 2017; *Messori et al.*, 2017).

Statistical-dynamical approaches can also quantify aspects of future hydroclimate of particular interest. For example, hidden Markov models (HMMs) (*Rabiner and Juang*, 1986) and nonhomogeneous hidden Markov models (NHMMs) can provide a quantitative framework for weather typing analyses, downscale rainfall from a GCM (*Robertson et al.*, 2004; *Holsclaw et al.*, 2015), reconstruct streamflow at multiple sites (*Bracken et al.*, 2016; *Steinschneider and Brown*, 2013), or feed a stochastic weather generator (*Steinschneider et al.*, 2019). *Farnham et al.* (2017) use EOFs of the Atlantic and Pacific jet to model winter rainfall over the US, conditional on large-scale climate indices. Hierarchical spatial models can be used to inform rainfall or flood hazard (*Lima and Lall*, 2010; *Lima et al.*, 2016), possibly conditioned on large-scale fields such as TMEs (*Steinschneider and Lall*, 2015b). *Delgado et al.* (2014) build a statistical-dynamical model of flood risk based on a mechanistic link between the Western Pacific monsoon and flood risk in the lower Mekong river (*Delgado et al.*, 2012). More purely data-driven approaches can also be valid, e.g. using analog prediction with deep learning for short-term weather prediction (*Kalchbrenner and Sønderby*, 2020; *Chattopadhyay et al.*, 2020) or a nonhomogeneous Markov renewal process for hurricane tracks (*Nakamura et al.*, 2015). Though extrapolation, i.e. out of sample performance, presents a challenge to models that make an assumption of stationarity between inputs and outputs, when carefully designed they can credibly inform a wide range of risks.

Chapter 3 illustrates how weather types can be used to help identify sequences of synoptic circulations that lead to significant risk of heavy rainfall and flooding in the LPRB, and chapter 4 exploits a credible mechanistic link for statistical prediction of rainfall hazard in the ORB.

Pero toda esa estampa borró la lluvia del verano. La crecida del río llegó con su canto de penas y angustias. Mi casita su puerta perdió, la invadieron las aguas. En canoa de pena subí, emigré hacia la altura pero un día a mi hogar volveré; erguiré sus paredes aliado al trabajo, al sol, a la fe.

But the summer rains washed it all away. The river rose with its song of sorrows and anguish and the invading waters carried away my door. So I climbed into a flimsy canoe and departed for higher ground, but one day I will return home to rebuild these walls with my sweat, the sun, and faith.

Maneco Galeano, Soy De La Chacarita

3

Heavy Rainfall in Paraguay During the 2015-2016 Austral Summer: Causes and Sub-Seasonal-to-Seasonal Predictive Skill

This chapter describes the physical mechanisms which are responsible for heavy rainfall and flooding in the Lower Paraguay River Basin (LPRB), focusing in particular on a November-February (NDJF) 2015-16 flood event that displaced over 170 000 people. This work addresses three specific questions; summarized conclusions are shown for each.

1. What physical mechanisms caused the NDJF 2015-16 flooding?
    - Persistent and recurrent heavy rainfall events, which were collectively but not individually exceptional, caused severe flooding due to the flat topography of the LPRB.

- Frequent and intense South American Low-Level Jet (SALLJ) events brought moisture and latent energy to South East South America (SESA).
- A persistent low-level anticyclonic circulation over central Brazil favored "No-Chaco" jet events, create vertical shear and favor mesoscale convection over the LPRB.

2. What climate modes were responsible for the persistence and recurrence of heavy rainfall in the LPRB during NDJF 2015-16?
    - The strong El Niño event observed favored SALLJ activity but does not itself explain why No-Chaco jet events were favored.
    - Interactions between the Madden-Julien Oscillation (MJO) and the El Niño-Southern Oscillation (ENSO) better explain observed sequences of weather patterns than ENSO alone.
    - During El Niño events, a persistent sea surface temperature (SST) dipole anomaly in the subtropical Atlantic can block extratropical wave activity from the Pacific, favoring No-Chaco jet events.
3. Did sub-seasonal to seasonal (S2S) climate models accurately predict flood risk during this event?
    - At lead times greater than two weeks, the ensemble-mean forecast did not show high probability of the heavy rainfall that was observed.
    - At weather timescales (less than one week), the ensemble-mean successfully predicts the timing and amplitude of area-averaged rainfall.
    - Model output statistics (MOS) approaches that explicitly model spatial modes substantially enhance the accuracy of heavy rainfall forecasts.

This chapter has been published as

Doss-Gollin, J., Á. G. Muñoz, S. J. Mason, and M. Pastén (2018), Heavy rainfall in Paraguay during the 2015-2016 austral summer: Causes and sub-seasonal-to-seasonal predictive skill, *Journal of Climate*, *31*(17), 6669–6685, doi: 10.1175/JCLI-D-17-0805.1

and is reproduced with permission of all authors.

3.1 Introduction

During the austral summer of 2015-16, repeated heavy rainfall events led to severe flooding in the LPRB (figs. 3.1 and 3.3), displacing approximately 170 000 people (*Brakenridge*, 2018) and causing tremendous damage to property and infrastructure (*MOPC*, 2016). Because population in South America tends to concentrate along coasts and rivers (fig. 3.2), flooding in the LPRB directly affects not only much of the population of Paraguay, but also of populations in Argentina and Uruguay who lie along the Paraná and la Plata rivers, into which the Paraguay River drains. Heavy rainfall and flooding in the LPRB also has important implications for hydropower generation, for agriculture, and for regional water resource management. The aim of this paper is to diagnose the drivers of the NDJF 2015-16 rainfall and flooding events, and to assess the skill of the associated S2S predictions.

The climatology of the LPRB varies strongly by season, with extratropical characteristics in the winter and monsoonal characteristics in the summer. The most notable circulation features during NDJF, which is the focus of this study, are the upper-tropospheric Bolivian High, the lower-level subtropical highs, the Chaco Low over northern Argentina, the South Atlantic Convergence Zone (SACZ), and the SALLJ (*Grimm and Zilli*, 2009; *Marengo et al.*, 2012). Rainfall peaks around $5\,\mathrm{mm\,d^{-1}}$ during the warm months (October-May) and reaches a minimum near $2\,\mathrm{mm\,d^{-1}}$ in July and August. However, the flat topography limits the river's ability to carry the summer runoff, causing seasonal inundation of the Pantanal and distributing the river discharge in time (*Bravo et al.*, 2012; *Barros et al.*, 2004). Thus, upstream of the Pantanal the streamflow maxima typically occurs in phase with precipitation, while downstream of the Pantanal - an area which we define in fig. 3.1 as the Lower Paraguay River Basin - the annual peak typically occurs between April and July.

During the warm season, a large fraction of rainfall, and nearly all heavy rainfall, in the LPRB is associated with mesoscale convection (*Velasco and Fritsch*, 1987). Previous studies of organized convection and precipitation across subtropical continental South America have found close correspondence with the exit region of the low-level jets (*Velasco and Fritsch*, 1987;

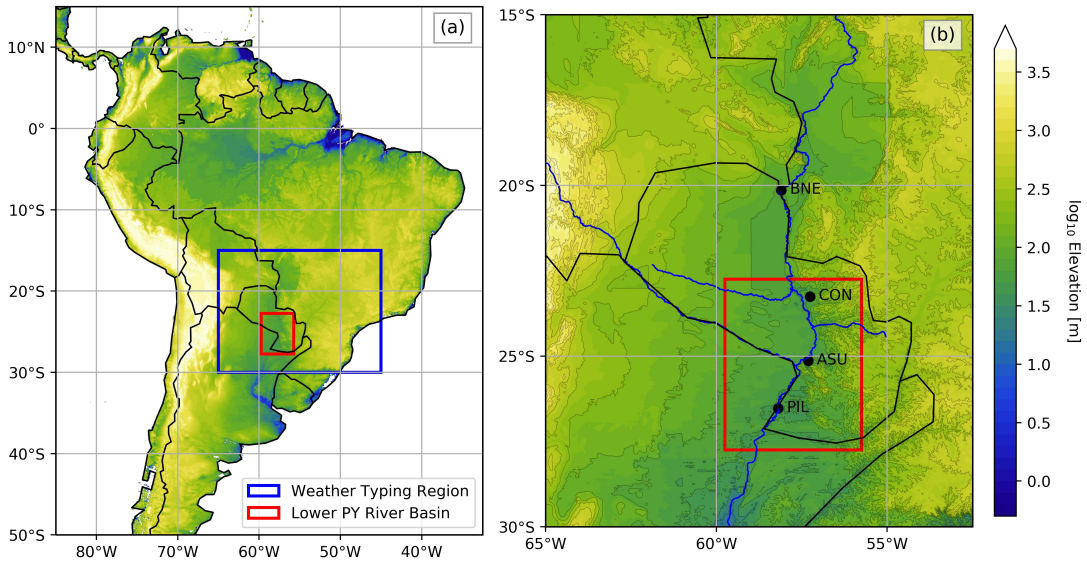

Figure 3.1: Topographical map of the study area. Colors indicate $\log_{10}$ of elevation, in m, from the Global Land One-Km Base Elevation project available at `http://iridl.ldeo.columbia.edu/SOURCES/.NOAA/.NGDC/.GLOBE/.topo/`. (a): all of South America. The domains of the Lower Paraguay River Basin and the domain used for weather typing are indicated in red and blue, respectively. (b): The Lower Paraguay River Basin (LPRB). As for (a), the LPRB is marked with a red box. Streamflow time series shown in fig. 3.5 were taken from the fours stations indicated. The Paraguay River and its tributaries, from the Natural Earth database (`www.naturalearthdata.com`), are also shown. Full station names are: Bahía Negra (Bne); Concepción (Conc); Asunción (Asu); Pilar (Pil).

Figure 3.2: Gridded estimate of population density (color; in units of persons per square kilometer) (image from *Center for International Earth Science Information Network*, 2016).

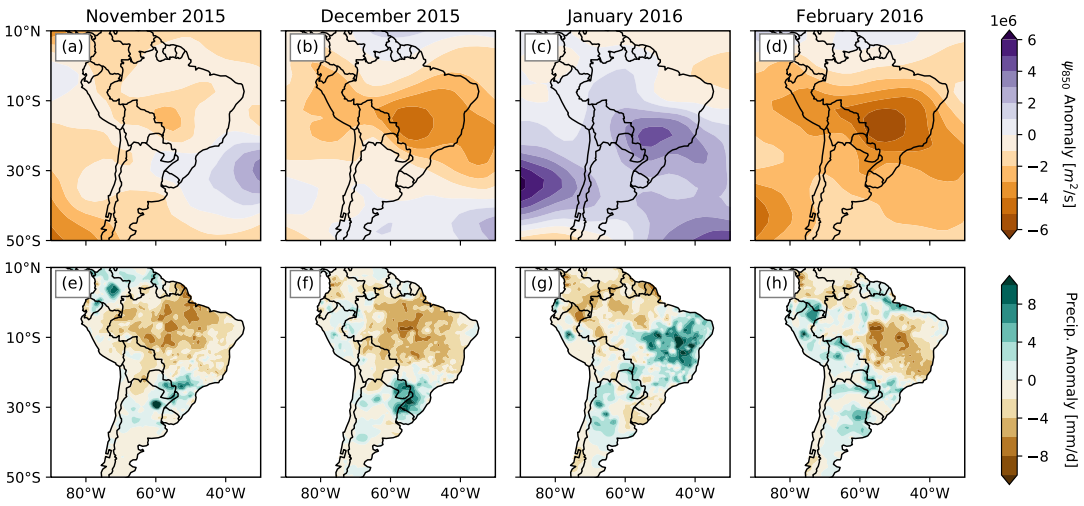

Figure 3.3: Monthly composite anomalies observed during NDJF 2015-16. Top row (a-d) shows streamfunction anomalies at 850 hPa, in units of $m^2\ s^{-1}$. Bottom row (e-h) shows rainfall anomalies, in units of $mm\ d^{-1}$.

Marengo et al., 2004; *Saulo et al.*, 2007; *Salio et al.*, 2007), which is influenced in both summer and winter by mid-latitude baroclinic wave trains that interact with the Andes topography to generate orographically bound cyclones and northerly low-level flow (*Campetella and Vera*, 2002; *Seluchi et al.*, 2006; *Boers et al.*, 2013, 2014). The strength and direction of this moisture transport varies substantially between events, and SALLJ exit regions range from central Argentina ("Chaco Jet Events"; *Salio et al.*, 2002) to Paraguay and southeastern Brazil ("No-Chaco Jet Events"; *Vera et al.*, 2006).

At sub-seasonal timescales, heavy rainfall and convection in the LPRB is modulated by a variety of drivers, notably including the SACZ and the MJO. During SACZ conditions, strong low-level convergence is observed over the Amazon basin with low-level divergence over southwestern Brazil, northern Argentina and Paraguay (*Herdies et al.*, 2002; *Carvalho et al.*, 2010a); the opposite is true for so-called No-SACZ conditions. SACZ occurrence is related to westerly wind regimes over South East South America, as well as "active" and "break" periods of the South American Monsoon System (*Marengo et al.*, 2004). The MJO has been associated with the South American "seesaw" pattern (*Nogués-Paegle and Mo*, 1997; *Paegle et al.*, 2000; *Liebmann et al.*, 2004), and has been identified as a source of rainfall predictability for the region (e.g. *Muñoz et al.*, 2015).

At seasonal timescales, ENSO is the dominant driver of convection variability in the LPRB. During El Niño years, a low-level anticyclonic anomaly over central Brazil enhances occurrence of the low-level jet, favoring the development of mesoscale convective systems (*Velasco and Fritsch*, 1987). The intensity and extent of this anomaly is relevant for the precise impact of ENSO events. The region also exhibits substantial variability between seasons of rainfall during El Niño years, including a reversal of rainfall anomalies between November of that year and January of the following one, influenced by land-surface interactions (*Grimm*, 2003; *Grimm and Zilli*, 2009). Even beyond El Niño years, regional land-surface feedbacks can cause regions that exhibit wet anomalies in the spring to experience more summer precipitation on average (*Grimm et al.*, 2007). Similarly, mid-latitude dynamics influence low-level wind anomalies on many time scales, though this relationship is complicated due to coupled tropical-extratropical interactions (*Jones and Carvalho*, 2002; *Carvalho et al.*, 2004). To address

these potential interactions, a cross-timescale approach based on synoptic circulation types is employed here to diagnose the causes of the rainfall events. This method has been used in previous work for southeastern South America (*Muñoz et al.*, 2015, 2016b) and other regions (*Moron et al.*, 2015).

The paper proceeds as follows. We first describe our data sources in section 3.2 and our methods in section 3.3. In section 3.4 we start our diagnosis highlighting the observed flooding and contextualizing it within a long river stage time series; we then use composites and a weather typing analysis to diagnose the circulation patterns associated with the heavy rainfall during NDJF 201516. We turn in section 3.5 to the question of whether the observed rainfall was successfully predicted by available models. To carry out this analysis we study both forecasts targeting the entire series for a limited area, and also forecasts targeting a large spatial area for only the first week of December, when the most important flooding events began. We also explore the impact on forecasts of several bias-correction schemes.

3.2 Data

The analysis presented makes use of both observations and model forecasts.

3.2.1 Observations

The period analyzed for diagnostic purposes is from 1 Nov 1979 through 28 Feb 2016. Figure 3.1 shows the study area and defines several spatial domains which are discussed throughout the paper.

Rainfall data are taken from the CPC Unified Gauge-based Analysis of Global Daily Precipitation dataset (*Chen et al.*, 2008). Spatial resolution is 0.500° and temporal resolution is daily. We define "heavy" rainfall events to be exceedances of the 90th percentile; while the value is different for each grid cell, the 90th percentile of area-averaged rainfall over the LPRB is approximately 15 mm d^{-1}.

Atmospheric circulations are diagnosed using daily data from the NCAR-NCEP Reanalysis II dataset (*Kanamitsu et al.*, 2002). Spatial resolution is 2.50°. Because the end-of-day time for the rainfall data is 12:00 GMT over most of South America (*Chen et al.*, 2008), we use six-

hour reanalysis data, and shift by twelve hours before re-sampling to the daily time step. This ensures that the time steps in the reanalysis and rainfall data sets are the same, but means that a day is defined as beginning at 12:00 GMT. Since most summer rainfall in this region occurs overnight (*Vera et al.*, 2006; *Salio et al.*, 2007), this end-of-day time (which translates to approximately 8:00 AM locally depending on the exact time zone) tends to separate distinct events. The primary atmospheric variable used was the 850 hPa streamfunction, calculated directly from the wind field as described in section 3.3. The streamfunction is preferable to, for example, the geopotential height Φ because Φ has weak gradients near the equator, making it difficult to visualize circulations that span from the tropics to the extratropics. The 850 hPa height level was used because it is representative of SALLJ activity and moisture transport in this region (*Marengo et al.*, 2004; *Salio et al.*, 2007).

Oceanic SST patterns are explored at the monthly time step using the 1° NOAA OI.v2 dataset (*Reynolds et al.*, 2002).

Streamflow data was collected by the Paraguayan Navy and National Administration of Navigation and Ports of Paraguay and was processed and distributed by the Paraguayan Directorate of Meteorology and Hydrology. Locations of streamflow gauges are shown in fig. 3.1. Because no stage-discharge curves are available, we present only the river stage values; while this is relevant from the perspective of flood damage, flow rates cannot be estimated without these curves (which are difficult to reconstruct as river geometry changes over time).

This study also makes use of some climate indices. Data on ENSO, specifically the NINO3.4 index, came from a statistical-dynamical interpolation (*Kaplan et al.*, 1998), which is constrained by relatively high-quality observations during the study period. Data on the MJO came from the Australian Bureau of Meteorology (*Wheeler and Hendon*, 2004).

3.2.2 Model Forecasts

This study analyzes probabilistic seasonal and sub-seasonal forecasts of heavy rainfall events, which we define as exceedance of the 90th percentile of NDJF daily precipitation across all ensemble members and initializations.

The seasonal predictions used are known as "flexible format" forecasts, provided by the International Research Institute for Climate and Society (IRI). These forecasts use a multi-model ensemble approach, with bias-corrected retrospective probabilistic forecasts produced using a total of 144 members forced by evolving SSTs and 68 members forced by persisted sea-surface temperatures; for details see *Barnston et al.* (2010). Flexible format means that the user of these forecasts can arbitrarily choose particular thresholds (percentiles) to compute the probability of exceedance (or non-exceedance) from the complete probability density function (PDF) of the climatological distribution, rather than using the more common tercile categories. The DJF 2015-2016 forecasts analyzed were produced in November 2015. Due to the short sample of flexible format forecasts available (only for 2012-2016 at the time of writing this paper), no verification was performed for these seasonal predictions. These forecasts are provided at a horizontal resolution of 2.50°. The DJF 2015-2016 forecasts analyzed were produced in November 2015.

The sub-seasonal forecasts used were issued by the European Centre for Medium-Range Weather Forecasts (ECMWF) using the IFS cycle 41R1 coupled model. These forecasts are available via the S2S Prediction Project Database (*Vitart et al.*, 2016) at 1.50° resolution. Forecasts consider the period starting in Dec 2015 until Mar 2016, and hindcasts to assess the real-time predictive skill consider the period Dec 1-7, 1995-2014. There is a total of 51 ensemble members for each forecast, and 11 ensemble members for each of the 20 hindcasts (Dec 1-7, 1995-2014).

Hindcasts were used to define the significant event threshold, and for probabilistic forecast verification; forecasts were used to analyze modeled rainfall during the entire NDJF 2015-16 season and in particular the week of Dec 1-7, 2015. For probabilistic analysis of the rainfall during the week 1-7 December 2015, rainfall forecasts and hindcasts considered were initialized on November 12th and 16th, 2015.

Anomalies were calculated relative to the seasonal mean from November 1979 to February 2016, and the anomalies thus contain information on intra-seasonal variability.

3.3 Methods

Several types of analyses are used to diagnose the causes of the heavy rainfall events, and to bias-correct and verify the forecasts. Computation was performed in the python environment using stable open source packages (*Hunter*, 2007; *McKinney*, 2010; *van der Walt et al.*, 2011; *Hoyer and Hamman*, 2017). All codes to reproduce or modify this analysis are available at the permanent link `https://doi.org/10.5281/zenodo.1243104`.

Given the behavior of the Paraguay River discussed above, we define the Lower Paraguay River Basin as the region bounded by $-59.8\,^{\circ}$W to $-55.8\,^{\circ}$W and $26.8\,^{\circ}$S to $22.8\,^{\circ}$S, as shown in fig. 3.1. In this region, given topography and previous studies (*Barros et al.*, 2004; *Bravo et al.*, 2012), one might hypothesize rainfall inputs to most closely correspond to river levels at the stream gauges in fig. 3.1.

3.3.1 Weather Typing

A cluster algorithm is used on daily data to diagnose mechanisms associated with the rainfall events of interest in this research.

The clustering was performed on the daily NDJF 850 hPa streamfunction field (ψ), calculated by integrating the meridional and zonal wind fields using spherical harmonics, as implemented in the `windspharm` package (*Dawson*, 2016), over the domain spanning $15\,^{\circ}$S to $30\,^{\circ}$S and $65\,^{\circ}$W to $45\,^{\circ}$W (fig. 3.1).

To facilitate clustering (which tends to perform poorly in high-dimensional spaces), the NDJF anomaly field of ψ_{850} was projected onto its four leading empirical orthogonal functions (EOFs), accounting for $> 95\%$ of the total observed variance. No meridional weighting was applied as the selected domain is relatively small and does not extend into high latitudes. Once the EOFs were calculated, the principal component time series were computed for each day and scaled to unit variance. This rescaling is not a necessary step; its effect is to treat all retained principal components as equally important, which provides relatively greater weight to EOFs 2, 3, and 4 than carrying out the clustering without re-scaling. Though our approach of first selecting the number of EOFs to use and then choosing to scale them equally involves more subjective decisions than an approach without rescaling, in this case the resulting phys-

ical patterns described by the EOFs more closely represent patterns identified in the literature; this is further discussed in section 3.4.

Next, the K-means algorithm was used to assign a single cluster value to each day on record using the 4-dimension principal component time series. The K-means technique is a partitioning method that classifies all days in the study into a predefined number of clusters. The algorithm proceeds as follows:

1. Randomly choose K cluster centers $\mu_1^{(0)}, \ldots, \mu_K^{(0)}$ (where 0 refers to the 0th iteration)
2. Iterate until convergence, indexing each iteration with j:
   (a) Assign each observation (day) x_i to the nearest cluster center; we define this using the Euclidean distance but other measures, such as the Mahalanobis distance, could also be used:

$$m_i^{(j+1)} := \arg \min_{k \in 1,\ldots,K} \left|\left| x_i - \mu_k^{(j)} \right|\right| \tag{3.1}$$

   (b) Recompute the cluster centers as the mean of all points assigned to that cluster

$$\mu_k^{(j+1)} := \frac{1}{\left|\left\{ i \middle| m_i^{(j+1)} = k \right\}\right|} \sum_{i|m_i^{(j+1)}=k} x_i \tag{3.2}$$

   where $|\cdot|$ denotes vector length.
   (c) Stop iteration if the change in centroids $\mu^{(j+1)} - \mu^{(j)}$ is less than a small but non-zero tolerance parameter τ.

The cluster centroids μ_k produced by the K-means algorithm can then be interpreted as a Voronoi decomposition of the phase space into K regions, and specifically as the Voronoi diagram which minimizes within-cluster variance.

The K-means algorithm is guaranteed to converge to a local minimum of inter-cluster variance; to select the best partition, 500 simulations were created using the implementation in Python's `scikit-learn` package (*Pedregosa et al.*, 2011). Next, the classifiability index of *Michelangeli et al.* (1995) was computed between each partition and the 499 others. The partition whose classifiability index, averaged for all 499 pairwise comparisons, was the highest

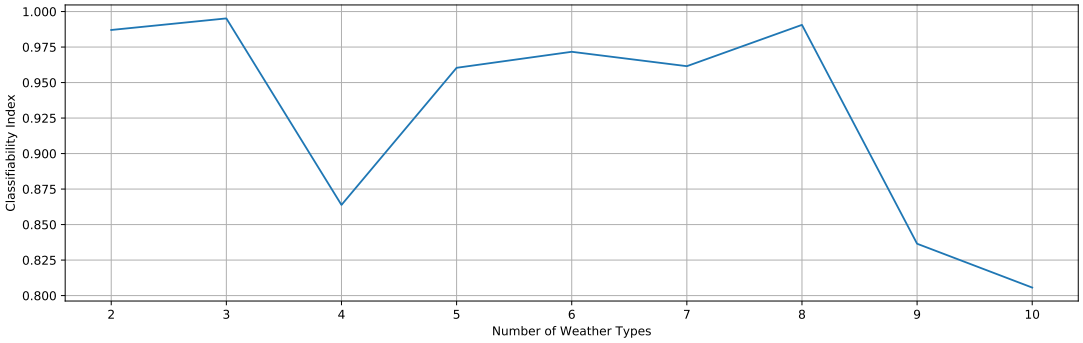

Figure 3.4: Classifiability index as a function of K (the number of weather types created).

was selected. Calculation of the classifiability index for several values of K (fig. 3.4) suggests that states with $K = 5, 6, \ldots, 8$ are all reasonable. We chose the solution $K = 6$ because the clusters identified are qualitatively similar to those determined over southeastern South America (*Muñoz et al.*, 2015, 2016b) and have an intuitive physical meaning, which we discuss further in the following sections. We refer to the resulting clusters as weather types (WTs). From a physical point of view, the K-means algorithm helps identify typical atmospheric circulation patterns in the EOF-filtered field via clustering of days with similar streamfunction configurations. These clusters can also be understood as proxies of the available states of the system, or the most frequently visited trajectories in the phase space of the physical system (*Muñoz et al.*, 2015, 2016b, 2017).

3.3.2 Forecasts and Model Output Statistics

A wide variety of methods, generically known as MOS (*Glahn and Lowry*, 1972), have been proposed to correct for different types of bias in model outputs. In this work, we analyze how well the rainfall events could have been predicted, both using the raw sub-seasonal forecasts and MOS-adjusted sub-seasonal forecasts. We use four types of MOS techniques: the homoscedastic extended logistic regression homoscedastic extended logistic regression (XLR); the heteroscedastic extended logistic regression (HXLR); principal components regression (PCR); and canonical correlation analysis (CCA).

Logistic regression models the probability of binary events, conditional on one or more predictors, and has been widely used in MOS. Nonetheless, when using logistic regression to

address multiple thresholds via independent fits, the predicted probabilities are, in general, not mutually consistent (*Messner et al.*, 2014). The XLR was designed to address this shortcoming via the consideration of a transformation of the thresholds of interest as an additional predictor variable (*Wilks*, 2009). The HXLR, a generalization of the XLR, was proposed to appropriately use the ensemble spread as predictor for the dispersion of the predictive distribution (*Messner et al.*, 2014).

CCA is a common statistical method frequently used to forecast rainfall using a purely empirical approach (*Mason and Baddour*, 2008; *Barnston et al.*, 2012; *Jolliffe and Stephenson*, 2012; *Barnston and Ropelewski*, 1992; *Wilks*, 2006). CCA identifies modes of co-variability, called canonical variates or canonical modes, by maximizing the correlation between linear combinations of the predictor and predictand's EOFs. The method forecasts spatial patterns of variability spanning across the region of interest rather than making forecasts for individual locations. In PCR, a special case of CCA, each grid cell in the predictand field is estimated by regression using a linear combination of the predictor's EOFs (*Mason and Baddour*, 2008; *Wilks*, 2006) rather than by identifying canonical modes. Unlike the XLR and HXLR models, which perform bias correction independently for each grid cell, the CCA and PCR models can address biases in both the magnitude and the spatial distribution of the modeled precipitation patterns.

For the purposes of MOS corrections, the predictand (variable to forecast) is the observed rainfall for the target period of interest, and the predictor (variable to be corrected) is the uncorrected S2S model forecast rainfall for the same period. Exceedance of the 90th percentile during the 1995-2014 period is used to define the heavy event cases. We use the same spatial domain [39 °S to 17 °S; 66 °W to 49 °W] for both the predictor and the predictand, except for the PCR and CCA cases, in which a larger domain [0 °S to 60 °S; 80 °W to 30 °W] was used to better capture the spatial patterns in the uncorrected S2S model forecast field. A variety of domains and ways to combine initialization times were explored; the best results were selected in terms of the corresponding Kendall's τ rank correlation coefficient between observations and hindcasts. A summary of the final candidate predictors found to be most skillful for each MOS model is presented in table 3.1.

Table 3.1: MOS methods used to correct the ECMWF sub-seasonal forecasts. Spatial domain for predictand is always the same (39 °S to 17 °S; 66 °W to 49 °W). Two initializations are used: Nov 12th and 16th, 2015.

Model	Region (Predictor)	Final predictor(s) selected
Raw	39 °S to 17 °S; 66 °W to 49 °W	Ensemble mean, computed using members from the two initializations. No correction performed.
XLR	39 °S to 17 °S; 66 °W to 49 °W	Ensemble mean, computed using members from the two initializations.
HLXR	39 °S to 17 °S; 66 °W to 49 °W	Ensemble mean and spread, computed using members from the two initializations.
PCR	60 °S to 0 °S; 80 °W to 30 °W	Linear combination of model's EOFs computed using both initializations as independent predictors (10 EOFs).
CCA	60 °S to 0 °S; 80 °W to 30 °W	Canonical modes computed using both initializations as independent predictors. (10 predictor EOFs, 4 predictand EOFs, 4 canonical modes)

To evaluate model skill, we use a cross-validation approach with a 5-year window. In this framework, five continuous years are left out of the record, the regression coefficients are computed with the remaining of the time series, and the resulting model is validated comparing the prediction for the third year left out (middle of the window) against observations. The 5-year-long window is redefined a year at a time, moving from the beginning of the record to its end.

To visualize the probability of heavy rainfall at each grid cell, we present all predictions in terms of odds relative to the climatological odds:

$$\text{odds}_r \equiv \frac{p}{(1-p)} \frac{(1-p_c)}{p_c} \tag{3.3}$$

where p and p_c represent the forecast probability for the exceedance of the 90th percentile, and the related climatological probability, respectively.

As indicated earlier, the IRI's seasonal forecasts are already provided with spatial MOS corrections of systematic errors of the individual models in the ensemble via CCA (*Barnston et al.*, 2012), and thus we did not perform any further MOS on the seasonal rainfall fields.

3.3.3 Probabilistic Forecast Verification

In addition to visually comparing predictions and observations to verify how well the heavy rainfall events could have been predicted, we use the Ignorance Score,

$$\mathrm{IGN} \equiv -\log_2 p(Y), \tag{3.4}$$

where Y is the observed outcome and $p(Y)$ is the density function of the forecast distribution (*Good*, 1952; *Roulston and Smith*, 2002; *Bröcker and Smith*, 2007). The Ignorance Score was introduced as an information theory-based verification measure, decomposable into easily interpretable components: reliability, resolution and uncertainty (*Weijs et al.*, 2010). Due to its close relationship to Shannon's information entropy, it is used to measure forecast utility, or the amount of information gain expected from a forecast (*Roulston and Smith*, 2002).

We also compute the Generalized Relative Operating Characteristics score, also known as the 2AFC score (*Mason and Weigel*, 2009), to evaluate skill of probabilistic rainfall forecasts. This score measures the "proportion of all available pairs of observations of differing category whose probability forecasts are discriminated in the correct direction" (*Mason and Weigel*, 2009). It has an intuitive interpretation as an indication of how often the forecasts are correct.

These two metrics, measuring reliability, resolution, uncertainty and discrimination, are deemed here to be sufficient to characterize the forecast skill for our events of interest. To conduct the verification in a consistent manner, we use the Climate Predictability Tool, developed and maintained by the IRI (*Mason and Tippett*, 2017).

3.4 Diagnostics

3.4.1 Observed Flooding

Figure 3.5 shows the streamflow time series at several gauges on the Paraguay River during NDJF 2015-16 in the context of their seasonality and decadal variability. During November and December 2015, the river rose rapidly at Concepción, Asunción, and Pilar, though not at Bahía Negra. As discussed in *Barros et al.* (2004); *Bravo et al.* (2012), the location of the Bahía Negra gauge (see fig. 3.1) in the Pantanal region means that it responds very slowly to

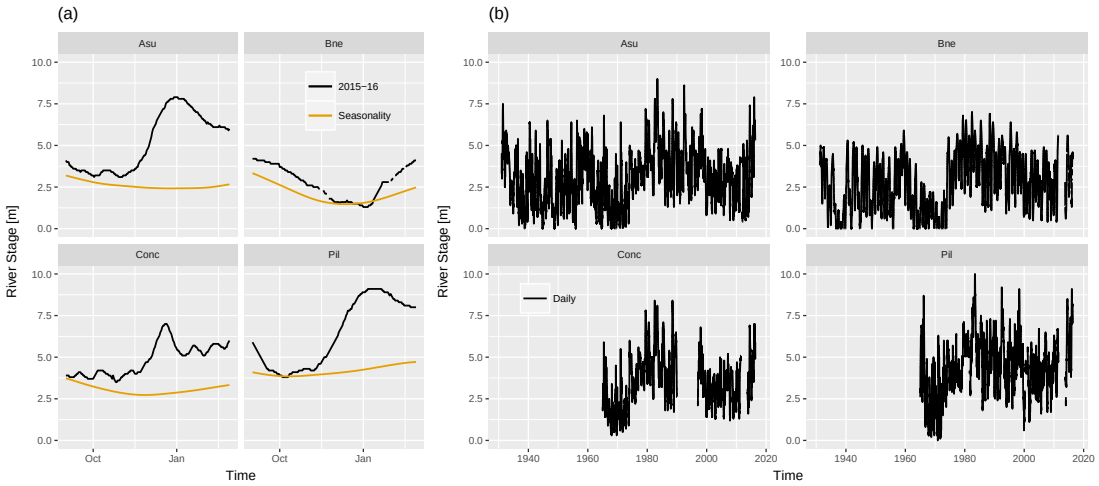

Figure 3.5: River stage (height; in m) for the Paraguay River at four gauges along the Paraguay River. The station names are shortened versions of those shown in fig. 3.1. (a): Seasonality (orange) and time series of 2015-16 observations (black) at each stream gauge. Seasonality was fit using local polynomial regression as implemented in the `locfit` package in the **R** statistical programming environment (*Loader*, 1999). (b): Time series of daily stage measurements from 1929 to 2016 at each station.

rainfall input. The three downstream gauges, because they are located in the LPRB, respond to the rainfall forcing with a slow but steady rise. Despite several very heavy storms, the streamflow record at Asunción and Pilar (which are downstream of Concepción) indicates relatively little response to individual storms. Because the region is so flat (see topographic data in fig. 3.1), river levels at a particular point may be affected not only by rain in the catchment corresponding to that point, but also by elevated river levels downstream which reduce the pressure gradient available to drive flow.

Examination of fig. 3.5b suggests multidecadal oscillation in the streamflow record. This is in agreement with previous studies (*Collischonn et al.*, 2001; *Carvalho et al.*, 2010b) which find a changepoint in the 1970s, possibly associated with low-frequency Pacific variability. Because only river stage data (and not discharge) are available, it is not possible to discern whether the observed changes in river stage are driven by sediment loading and local measurement characteristics or by large-scale climate fluctuations. Further treatment of this question is beyond the scope of this paper.

3.4.2 Heavy Rainfall: Climatological Drivers

To understand how circulation anomalies observed during NDJF 2015-2016 led to the observed floods it is helpful to first explore the atmospheric circulations which are typically associated with heavy rainfall in the lower Paraguay River during the full observed record.

Figure 3.6 shows time-lagged anomalies up to and after heavy rainfall dates (when area-averaged daily rainfall in the LPRB exceeds its NDJF 90th percentile) and is consistent with previous analysis of heavy rainfall and intense convection in this region (*Liebmann et al.*, 2004; *Marengo et al.*, 2004; *Salio et al.*, 2007; *Marwan and Kurths*, 2015). At $t = -2$ d a mid-latitude baroclinic system approaches the South American continent, intensifying and moving to the East from -1 d to 1 d. This system interacts with the sub-tropical low and the Andes Mountains to produce an anticyclonic anomaly over Brazil. Along the cold front associated with this system, a low-level northerly jet advects heat and moisture to the region. As the system progresses, the jet below 20 °S transitions from predominantly meridional flow ("Chaco Jet"; $t = -1$ d) to predominantly zonal flow ("No-Chaco Jet"; $t = 0$ d). The pattern resembles composites identified using one standard deviation exceedances of rainfall at 60 °W, 30 °S (*Liebmann et al.*, 2004) and analysis for the 95th or 99th percentiles of daily rainfall (not shown) yield similar results, implying that the synoptic mechanism for the most heavy events is not fundamentally distinct from the mechanism for moderate-intensity events. This mean field, like all composites, masks between-event variation but exploration of individual events (not shown) indicates that the core features identified are generally present.

3.4.3 Weather Type Analysis: Daily Circulation Patterns

We next use the weather typing algorithm outlined in section 3.33.3.1 to understand particular circulations and sequences of circulations associated with heavy rainfall in the LPRB.

The first step of the weather typing algorithm is to identify leading EOFs of the 850 hPa streamfunction ψ. The EOF loadings are shown in fig. 3.7. Of these, EOF 1 explains a substantial amount of variance ($\approx 72\%$) while EOFs 2, 3, and 4 collectively explain approximately 27% of total variance. The resulting WTs, shown in fig. 3.8, reveal patterns associated with synoptic- and regional-scale circulation regimes. This is consistent with the hypothesis that

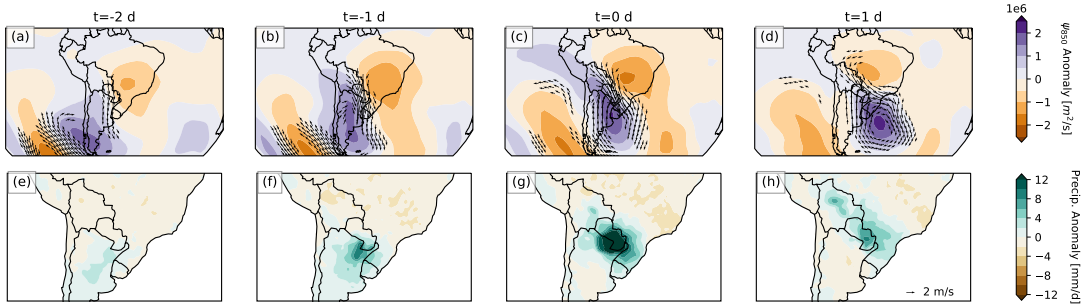

Figure 3.6: Composite anomalies associated with heavy rainfall (90th percentile exceedance of area-averaged rainfall in the Lower Paraguay River Basin). Lagged composites are shown, by column, for $t = -2$ d, -1 d, 0 d and 1 d relative to the date of heavy rainfall. Top row (a-d) shows composite streamfunction and wind anomalies at 850 hPa. Strongest 5% of wind anomaly vectors between 60 °S and 10 °N (all longitudes) are also shown. Bottom row (e-h) shows composite rainfall anomalies, in units of mm d^{-1}.

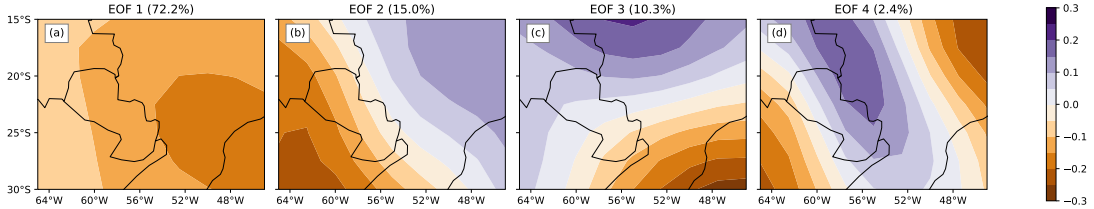

Figure 3.7: Loadings of the four leading EOFs of daily NDJF 850 hPa streamfunction over the weather typing region shown in fig. 3.1. Parentheses in sub-plot titles indicate the percentage of total variance explained by each EOF.

the EOFs over the study area are associated with large-scale patterns.

WT 1 describes a SALLJ event in which the strongest wind penetrates southward of 25 °S, leading to heavy rainfall over NE Argentina and Uruguay; this has been called a "Chaco Jet" event (*Salio et al.*, 2002). WT 4 also shows SALLJ activity, but the wind turns to the East northward of 25 °S, leading to heavy rainfall over Eastern Paraguay and SW Brazil; this has been called a "No-Chaco" Jet event (*Vera et al.*, 2006). Table 3.2 shows the centroids of each cluster, in the 4-dimensional phase space of the leading EOFs of 850 hPa streamfunction.

WTs 5 and 3 look loosely inverses of WTs 1 and 4, respectively, and are associated with dry anomalies over the LPRB. The fact that they are not exact inverses suggest important nonlinearities in the system. Weather types 1 and 5 resemble the two phases of the South American "seesaw" dipole, which is related to the SACZ (*Nogués-Paegle and Mo*, 1997). Finally, WTs 2 and 6 are related to a high-pressure configuration bringing below-average rainfall over

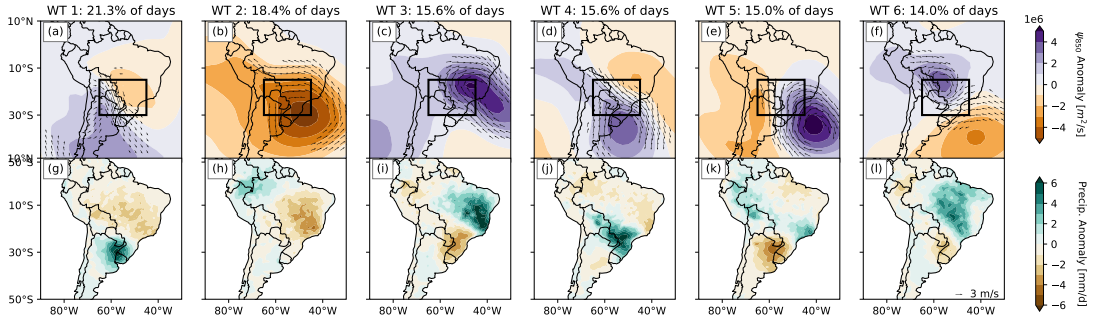

Figure 3.8: Composite anomalies associated with each weather type. Top row (a-f) shows streamfunction anomalies at 850 hPa. Strongest 20% of wind anomaly vectors over the plot area are also shown. Bottom row (g-l) shows rainfall anomalies, in units of mm d^{-1}. The relative frequency of occurrence of each weather type (in days) is presented on the top of each column.

WT	EOF 1	EOF 2	EOF 3	EOF 4
1	-0.325	1.035	-1.015	0.124
2	-0.887	0.519	0.647	-0.812
3	1.312	0.325	0.208	0.075
4	0.190	-0.807	-0.120	-0.844
5	-0.307	-0.849	-0.741	0.826
6	-0.334	0.057	1.093	1.033

Table 3.2: Centroids of each weather type in 4-dimensional phase space, where each dimension is an EOF of 850 hPa streamfunction over the weather typing region. These centroids are chosen by choosing the K-means partition which maximizes the Classifiability Index; see section 3.3. The weather type for each day is computed by projecting the 850 hPa onto its leading four EOFs, re-scaling the EOFs as discussed in Methods, and identifying the nearest (Euclidean distance) centroid.

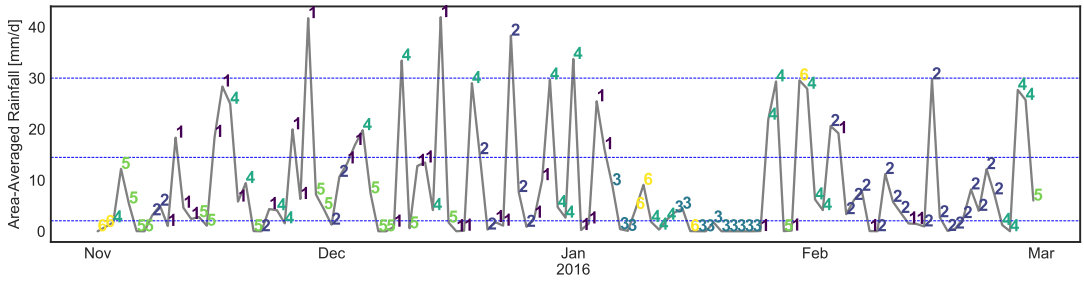

Figure 3.9: Time series of area-averaged rainfall in the Lower Paraguay River Basin (fig. 3.1) for each day of NDJF 2015-16. Lines indicate the rainfall value, in units of mm d^{-1}. The weather type corresponding to each day is indicated in an adjacent text label. Dashed blue lines indicate (from bottom to top) the climatological 50th, 90th, and 99th percentiles of NDJF area-averaged rain over the Lower Paraguay River Basin.

most of Brazil, and a dipole pattern conducive to above-average rainfall over central Brazil, respectively (fig. 3.8).

3.4.4 NDJF 2015-16: Circulation Sequences

We next use monthly-mean circulation anomalies (spatial patterns) and weather type sequences (temporal patterns) to understand the specific events of NDJF 2015-16.

While weather typing requires simplifying the dynamics of daily circulation patterns, its advantage is that it greatly facilitates the analysis of sequences of precipitation. Figure 3.9 shows a time series of area-averaged rainfall over the LPRB for NDJF 2015-16 and the corresponding weather types. This plot shows that heavy rainfall concentrated over a period spanning from mid-November 2015 through early January 2016, with shorter peaks in late January and mid-February.

As indicated in fig. 3.9, the most heavy rainfall occurred during WTs 1 and 4. During NDJF 2015-16, WTs 1 and 4 (Chaco and No-Chaco jet extensions, respectively), occurred more frequently than their climatology (table 3.3); WT 2 also occurred more frequently than its climatology, largely due to a long sequence in February 2016. In mid-January 2016, during a sequence of persistent low rainfall, WT 3 featured persistently, leading to heavy rainfall over central Brazil (not shown) and negative rainfall anomalies over the LPRB. Thus, while the intensity and persistence of heavy rainfall was atypical, the causal mechanism of the heavy rainfall observed during this season was consistent with climatology.

WT	NDJF 2015-16	Climatology
1	0.273	0.213
2	0.231	0.185
3	0.107	0.156
4	0.207	0.156
5	0.132	0.150
6	0.050	0.140

Table 3.3: Weather type occurrence fraction during NDJF 2015-16

Inspection of fig. 3.9 also suggests that at time scales of days to weeks, particular sequences of weather types tend to recur, and are associated with repeated rainfall storms. From mid November to late December 2015, nearly all days were weather types 1, 4, and 5, consistent with the anticyclonic anomaly observed over central Brazil during that time (fig. 3.3). Nearly all of the heavy rainfall occurred during WTs 1 and 4. During mid to late January 2016, repeated WT 3 days led to persistent low rainfall, and in mid February 2016 frequent occurrence of WT 2 led to frequent, though generally not intense, rainfall.

Transitioning from exploring the time evolution of the reduced-dimension system represented by the weather types, monthly-scale circulation anomalies (fig. 3.3) show a weak anticyclonic circulation that set up over central Brazil during November 2015 and strengthened into the following month. In January 2016 it weakened before returning in February 2016. The observed rainfall and circulation anomalies are consistent with the aggregation of the observed weather types shown in fig. 3.9 and discussed above.

3.5 Forecasts

In this section we analyze the extent to which forecasts were able to predict the persistent rainfall during summer of 2015-16. There are advantages in simultaneously considering useful climate information at multiple timescales, rather than just focusing on one of them (*Hellmuth et al.*, 2011; *Goddard et al.*, 2014). In this study we analyze probabilistic seasonal (DJF 2015-2016) and sub-seasonal (Dec 1-7, 2015) forecasts.

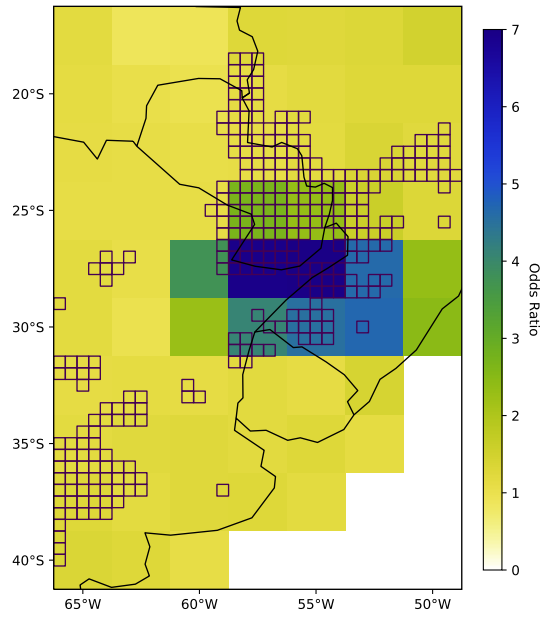

Figure 3.10: Seasonal model forecast for probability of exceedance of 90th percentile of DJF rainfall, as issued in November 2015. Color indicates the forecast probability of exceeding the 90th percentile of climatological rainfall during DJF 2015-16 – this is presented as the odds ratio as defined in eq. (3.3). A value greater than 1 indicates that the model forecast greater-than-average odds of rainfall exceeding the 90th percentile. Grid cells which observed an exceedance of the 90th percentile of DJF rainfall are outlined in black.

3.5.1 Seasonal Forecast

Heavy rainfall over the region was forecast for the DJF 2015-2016 season since at least November 2015 (see fig. 3.10). Relative odds as high as 9:1 are visible over southern Paraguay and Brazil, and northern Uruguay and Argentina, broadly in agreement with observations. The model predicted only very weakly increased odds of heavy rainfall in the Pantanal region (directly north of the LPRB) and in northern Argentina at $\approx$ 65 °W, and missed the heavy precipitation along most of the northeastern border of Paraguay. However, the regionally elevated forecast of heavy rainfall could have been used for disaster preparedness at least one month in advance.

3.5.2 Sub-Seasonal Forecasts

Sub-seasonal predictions are still too new to be used as operational tools, and their skill is normally not high enough to be useful for most decision-making (*Vigaud et al.*, 2017). Nonethe-

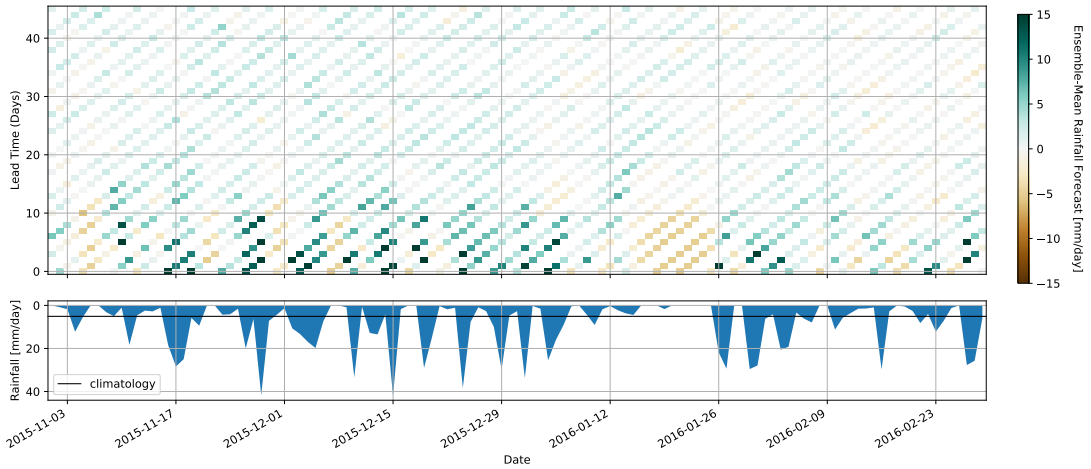

Figure 3.11: Chiclet diagram (see *Carbin et al.*, 2016) of ensemble-mean precipitation anomaly forecasts over the Lower Paraguay River Basin (see fig. 3.1) from uncorrected ECMWF S2S model forecast data, as a function of the forecast target date (horizontal axis) and lead time (vertical axis). Time series of CPC daily mean precipitation over the same area is plotted with y-axis inverted; horizontal black line denotes NDJF climatology.

less, the international S2S Prediction Project (*Vitart et al.*, 2016) provides free access to almost-real-time sub-seasonal forecasts from multiple models, an opportunity to explore how well the heavy rainfall events of the first week of December 2015 could have been predicted.

Figure 3.11 uses a Chiclet diagram (*Carbin et al.*, 2016) to visualize, as a function of lead time, the time evolution of the uncorrected, ensemble-mean rainfall anomaly forecast, spatially averaged over the LPRB. At times greater than about two weeks, the ensemble-mean forecast is for slightly positive rainfall anomalies at nearly all initialization dates and lead times. At weather timescales (less than one week), the ensemble-mean successfully predicts the timing and amplitude of the area-averaged rainfall. At timescales of one to three weeks, the ensemble average successfully forecast the strongest breaks and pauses in the rainfall, such as the heavy rainfall during December 2015 and the dry period during mid-January 2016.

To examine these forecasts more closely, we turn to the 14-19 day forecast of the December 1-7 2015 period. As seen in fig. 3.12, the raw (uncorrected) sub-seasonal forecast of the ECMWF model for Dec 1-7 2015 indicated very high relative odds for occurrence of heavy rainfall but with important biases in the actual location and spatial pattern; for Paraguay, it confidently suggests occurrence of heavy rainfall to the south-southeast of the country, which

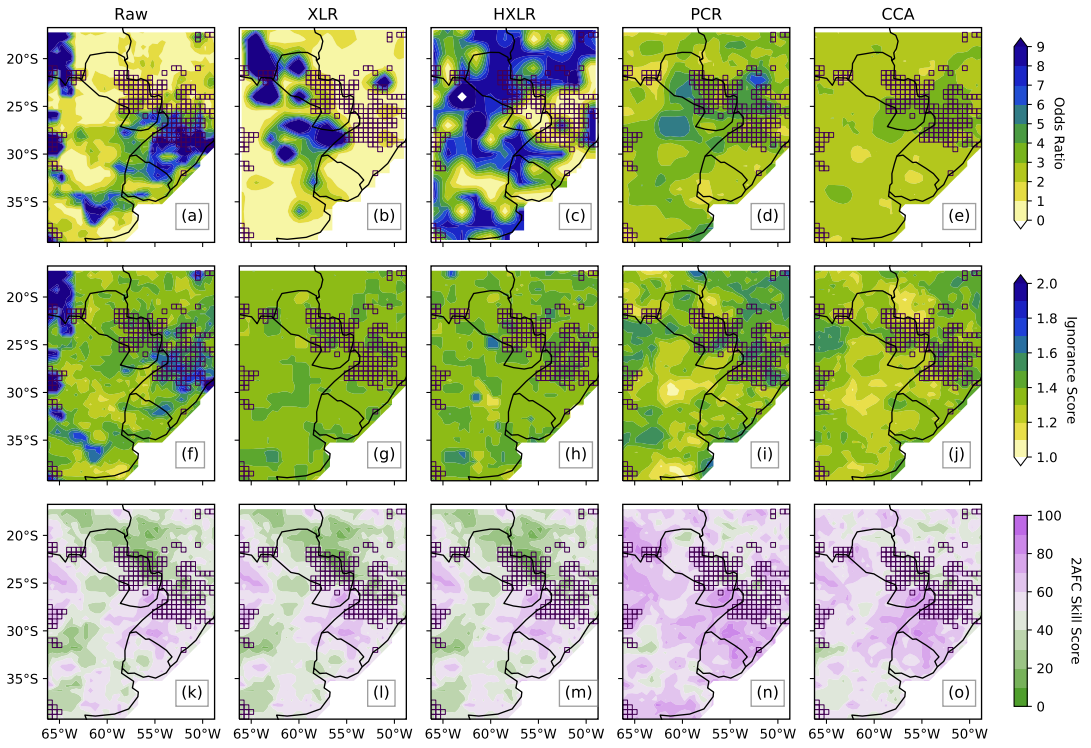

Figure 3.12: Raw and MOS-adjusted S2S model forecasts and skill scores for the methods indicated in table 3.1. Top row (a-e) shows the heavy rainfall forecast for 1-7 December 2015 as the odds ratio defined in eq. (3.3) over the target domain. A value greater than 1 indicates that the model forecast greater-than-average odds of rainfall exceeding the 90th percentile. Second row (f-j) shows the Ignorance Score defined in eq. (3.4), with zero indicating a perfect forecast. Bottom row (k-o) shows the 2AFC skill score for each grid cell; a value greater than 50 indicates that the model outperforms climatology. Columns separate different MOS models except for "Raw" (a,f,k), which indicates the uncorrected S2S model output. For all rows the grid cells which observed a 90th percentile exceedance for 1-7 December 2015 are outlined in black.

was mostly not observed. Overall, the 20-year skill of probabilistic forecasts for the first week of December is highest over southern Brazil, parts of Argentina and the western border of the domain under study (see fig. 3.12 f,k), but not over Paraguay. These skill scores indicate that the model is capturing a signal and suggest the use of MOS methods to explore the extent to which corrections in the magnitudes and spatial patterns may improve the forecast.

In general, the use of extended logistic regression models does not improve the forecast for the week. For example, with respect to the raw prediction, XLR tends to amplify the relative odds, and to cluster and shift the forecast location of the heavy rainfall events (fig. 3.12 a,b); the forecast tends to be better for Uruguay, but suggests heavy rainfall in the Paraguayan Chaco,

which was not present in the raw prediction. On the other hand, the use of the ensemble spread in the HXLR model does not help; this forecast tends to be over-confident on the events occurring in almost all the region of interest (fig. 3.12 c).

Comparison of long-term skill between the uncorrected S2S model forecast output and both extended logistic regression models shows similar results. Reliability, resolution and uncertainty, as measured by the Ignorance Score (fig. 3.12f-h), suggests slight skill improvement in southern Brazil, deterioration in Argentina and Uruguay, and basically the same as the uncorrected S2S model forecast for Paraguay and southeastern Bolivia. Changes in forecast discrimination exhibited by the extended logistic models, as measured via the 2AFC score (fig. 3.12k-m), are null. The extended logistic models operate on a grid-by-grid basis to recalibrate the probabilities, and so this recalibration happens monotonically. Since the 2AFC score is insensitive to monotonic transformations of forecasts, the forecast discrimination is unchanged.

Better forecasts are obtained when both magnitude and spatial corrections are performed, although with relative odds considerably less confident than the ones in the raw forecast. The PCR model correctly shows high relative odds in most of the places where heavy rainfall was observed (fig. 3.12 d), although it also indicates heightened risk in areas where heavy rainfall did not occur, like zones of western Paraguay and northeastern Argentina. The main problem with the CCA model is its lack of discrimination between occurrence or non-occurrence of heavy rainfall in the region: the spatial distribution of odds is too homogeneous (fig. 3.12 e).

The 20-year based skill maps of probabilistic forecasts computed with these two EOF-based models are very similar to each other, both in terms of the reliability, resolution and uncertainty measured by the Ignorance Score, and discrimination measured by the 2AFC score (fig. 3.12 i,j,n,o). In terms of long-term skill for the regions of interest over Paraguay, outputs from the PCR- and CCA-based MOS tend to outperform the raw forecasts and the extended logistic regression models, especially regarding discrimination (fig. 3.12 k-o). The enhanced skill is achieved through the spatial corrections via the EOF-based regressions, which - in contrast with the extended logistic models - use information from multiple grid-boxes, and thus the original forecasts are not in general calibrated monotonically.

Despite the particular errors in the Dec 1-7 2015 forecasts, on the long term both PCR and CCA verify considerably better than the raw, XLR, and HXLR predictions. Yet despite the generally high skill score for these forecasts, there are still zones along the eastern part of Paraguay with lower discrimination skill than that of climatology.

3.6 Discussion

Co-occurrence of WTs 1 and 4, particularly in late November through late December 2015, favored advection of moisture and moist static energy into the LPRBs, and low-level wind shear favored mesoscale convective activity, consistent with previous analyses in this region (*Velasco and Fritsch*, 1987; *Marengo et al.*, 2004; *Saulo et al.*, 2007; *Salio et al.*, 2007). Although many of the individual rainfall events of NDJF 2015-16 were intense, they were nonetheless driven by the climatological mechanism for heavy rainfall and intense convection shown in fig. 3.6 rather than by some other extreme mechanism. Consequently, the most striking hydrometeorological feature of this season, likely a key driver of the observed flooding, was the persistence of the heavy rainfall and the manner in which it switched "on" and "off" over the study region (fig. 3.9). In fact, this apparent "on" and "off" switching was manifest principally as a spatial shift in the rainfall occurrence (fig. 3.3) consistent with the increased occurrence of WT 3 during mid-late January 2016 (figs. 3.8 and 3.9); this pattern has been previously described as the South American "seesaw" pattern (*Nogués-Paegle and Mo*, 1997).

Although many news reports blamed the flooding on El Niño (*British Broadcasting Corporation*, 2015), NDJF 2015-16 featured more intense rainfall than previous major El Niño events, and this intense rainfall persisted for a longer time. While the link between El Niño and flooding in the LPRB is consistent with previous studies of ENSO and summertime rainfall in this region (*Velasco and Fritsch*, 1987; *Grimm et al.*, 2000; *Salio et al.*, 2002; *Grimm*, 2003; *Carvalho et al.*, 2004; *Grimm and Tedeschi*, 2009; *Bravo et al.*, 2012), both the "on"-"off" switching and the differences from previous major El Niño events suggest that other physical mechanisms, and their cross-timescale interactions, are relevant for understanding and predicting future events.

Figure 3.13 shows that WT 1 occurs more frequently during El Niño years for most MJO

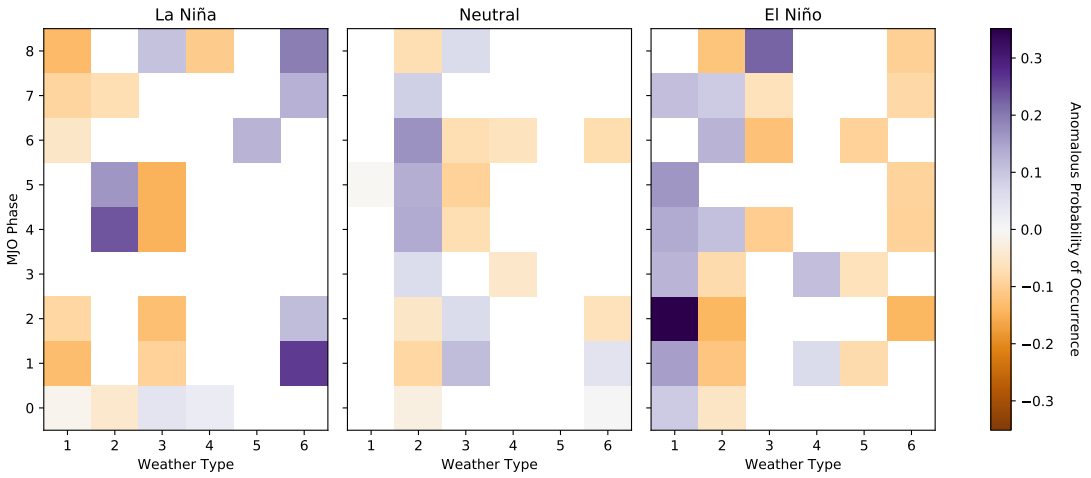

Figure 3.13: Anomalous probability of occurrence of each weather type concurrent with observance of each MJO phase. When MJO amplitude is less than 1, it is defined as neutral phase (0). Plots are shown separately for El Niño (NINO 3.4 > 1), La Niña (NINO 3.4 < -1), and Neutral ENSO phases. Only values which are significant at $\alpha = 0.10$, calculated with a bootstrap of 5000 samples, are shown.

phases, particularly during phase 2. During El Niño years, WT 3 - associated with dryness over the LPRB - occurs less frequently during MJO phases 4, 6, and 7, and more often during MJO phase 8; this is consistent with the lack of WT 3 during December 2015 and the frequent WT 3 occurrence in mid-January 2016 (fig. 3.9). Detailed consideration of the role of MJO-ENSO interaction with circulation patterns over the study region is beyond the scope of this paper, but these two patterns provided background conditions favorable for the weather type sequences observed during NDJF 2015-16.

By analyzing how the joint behavior physical mechanisms modulate the probability of occurrence of certain weather types, it may be possible to better understand the drivers of this and future extreme event(s). As a starting point, we consider the joint role of ENSO, discussed above, and the MJO. During NDJF 2015-16 the NINO 3.4 index was strongly positive, representing a strong El Niño state (figs. 3.14 and 3.15). The MJO began in November 2015 in a strong phase 3 and transitioned to phase 4 before losing amplitude around 21 November (fig. 3.16). It stayed neutral until early December where it strengthened from a weak phase 4 to a strong phase 4 ten days later. Maintaining a high amplitude, it transitioned through phases 4-8 and reached phase 1 in mid January 2016. The MJO then weakened slightly before emerging as a mid-strength phase 4 event in late January 2016 and moving through phases

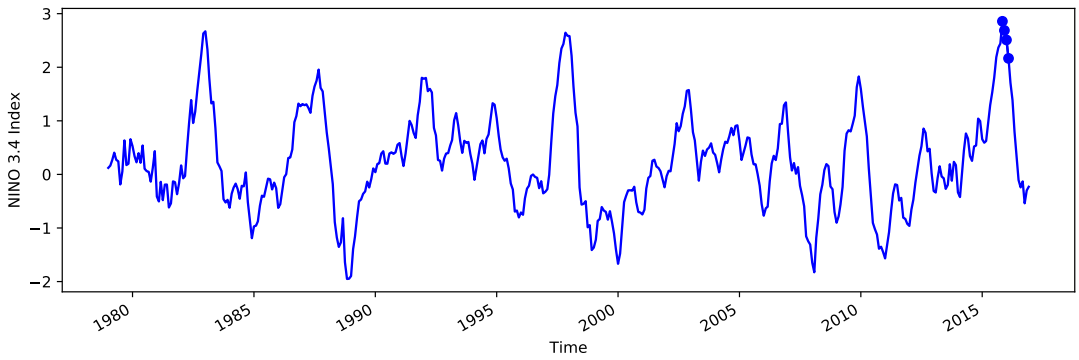

Figure 3.14: Monthly NINO 3.4 time series during the study period. Each month from November 2015 through February 2016 is specifically marked with a blue dot. Data from *Kaplan et al.* (1998).

5-7.

Of course, since a large fraction of the signal in fig. 3.13 seems to come from the ENSO signal, a logical question is why NDJF 2015-16 featured more persistent and intense rainfall in the LPRB than during other major El Niño events (fig. 3.15). Previous studies of the SALLJ (e.g., *Vera et al.*, 2006) and the modulation of rainfall in southeastern South America by extratropical transient wave trains during El Niño years emphasize the importance of Pacific-Atlantic interaction for forecasting climate events in this (and other) region(s) (*Barreiro*, 2017).

In particular, a persistent dipolar SST anomaly in the central southern Atlantic Ocean may favor the occurrence of WT 4 by blocking transient extratropical wave activity from the Pacific, facilitating transitions from "Chaco" jet events (WT 1) to "No-Chaco" jet events (WT 4) via enhanced low-level wind circulation from southern Brazil towards the Atlantic, and back to north-east Brazil and the Amazon (see fig. 3.17) due to land-sea temperature contrasts. We illustrate a schematic of this mechanism in fig. 3.17 and note that it is consistent with the mechanism found to produce heavy rainfall in the LPRB (fig. 3.6) and with previous studies (e.g., *Salio et al.*, 2002; *Liebmann et al.*, 2004; *Vera et al.*, 2006). We refer to his mechanism as the South Central Atlantic Dipole (SCAD) and measure it as the mean meridional SST gradient over the box shown in fig. 3.17. Examination of the SST anomalies observed during NDJF 2015-16 (fig. 3.15) indicates that the mechanism illustrated in fig. 3.17 was active - particularly in December 2015 when the most intense rainfall occurred. This suggests that not only did ENSO-MJO conditions favor SALLJ activity, but Atlantic-Pacific interactions specifically fa-

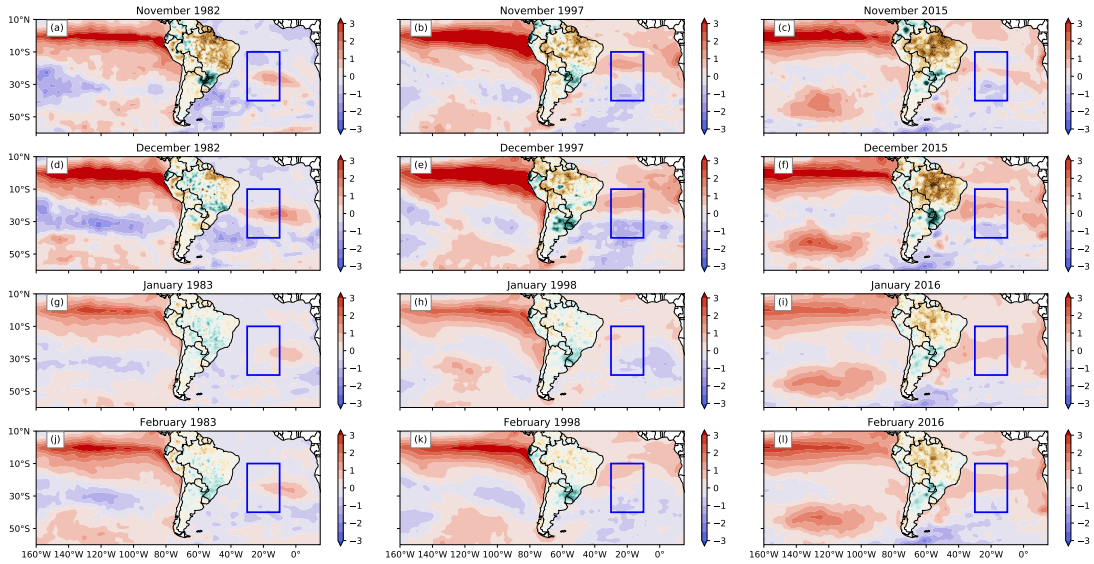

Figure 3.15: Monthly SST anomalies during December of three major El Niño events. Months shown are NDJF of (a,d,g,j): 1982-83, (b,e,h,k): 1997-98, and (c,f,i,l): 2015-16. Units are in °C. SST data from *Reynolds et al.* (2002). Also shown are rainfall anomalies over South America, from *Chen et al.* (2008). Rainfall contour intervals are 1 mm d^{-1}.

vored WT 4 occurrence, helping to explain why the most intense rainfall anomalies occurred specifically in the LPRB.

This Atlantic-Pacific interaction may also help to explain spatial uncertainty in model-based estimates of heavy rainfall in the region. In order to adequately forecast rainfall in certain parts of southeastern South America during El Niño years, models need to reproduce stationary wave trains originating in the Pacific and the Atlantic and their interactions (*Barreiro*, 2017). Other mechanisms that have been known to modulate rainfall signals in this region include the SACZ (*Carvalho et al.*, 2004; *Muñoz et al.*, 2015, 2016b) and land-biosphere-atmosphere interactions (*Grimm et al.*, 2000, 2007) which also tend to be poorly represented in models (*Koster et al.*, 2004; *Green et al.*, 2017). The stationary wavetrain interactions, land-atmosphere interactions, and topography may explain why simulating heavy rainfall in this region is so difficult (figs. 3.11 and 3.12). Improving understanding of these phenomena is important opportunity for S2S prediction, and is left for future work.

Finally, it is of interest to consider the link between the observed rainfall events and the observed flooding. Although we motivated this work by describing the impacts of severe flooding in the LPRB, the analysis presented has focused on climate drivers of rainfall. As

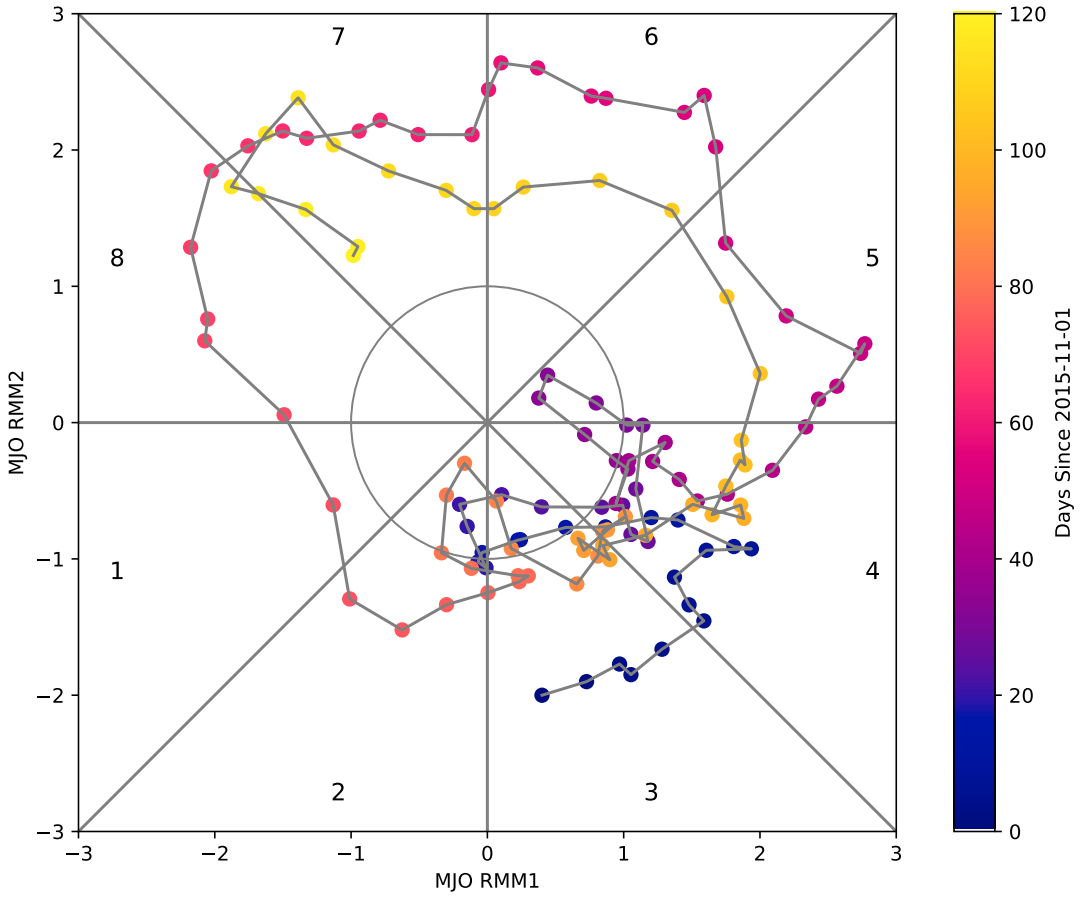

Figure 3.16: Evolution of the MJO during NDJF 2015-16. Points are plotted on RMM1 (x-axis) and RMM2 (y-axis), derived from leading EOFs of OLR fields (*Wheeler and Hendon*, 2004). Gray lines divide the plot into the eight phases used in the text. Colors show the time evolution of the system from 01 November 2015 (blue) to 29 February 2016 (yellow). Gray circle indicates the area of neutral MJO activity with amplitude < 0.

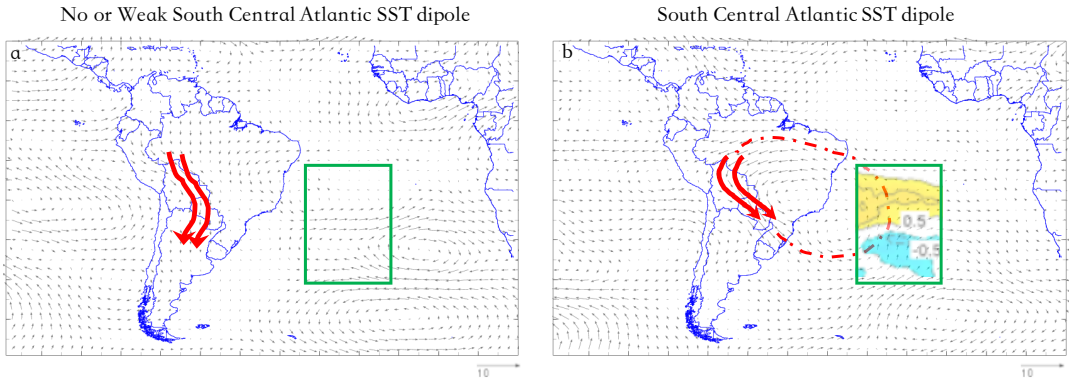

Figure 3.17: Schematics of low-level jet events (red arrows) during austral summer and El Niño years. Most jet events are of the "Chaco" type, particularly when SST anomalies in the central southern Atlantic Ocean (a, see green box) are weak. When a dipole SST anomaly occurs in the central southern Atlantic with the warmer pole equatorward, the meridional temperature gradient and sea-land temperature contrasts establish an anticyclonic circulation (dot-dashed line) conducive to increased occurrence of No-Chaco jet events (b). Other SST anomaly configurations tend to be present outside the green box (not shown). Winds in panels are typical for each case (at 850 hPa). Reference wind vector in $\mathrm{m\,s^{-1}}$. Green box shows location of SCAD.

explained in section 3.43.4.1, in this region the flat topography (fig. 3.1) means that the Lower Paraguay River reacts slowly to rainfall (*Bravo et al.*, 2012; *Barros et al.*, 2004), explaining the slow but steady rise in river levels from mid November 2015 to early January 2016, as shown in fig. 3.5. The observed flood peaks during 2015-16 also seem to occur in the context of an active phase of a multi-decadal oscillation, possibly associated with low-frequency Pacific activity (*Collischonn et al.*, 2001; *Huang et al.*, 2005). Parsing the relative impacts of deforestation and land use changes in the river basin, installation of hydroelectric generation at the Itaipu and Yacyreta sites, river channel modification, antecedent conditions, and climate variability on flood levels will require gathering improved hydrological data and building a comprehensive system model, which is beyond the scope of this paper.

From a policy perspective, reducing flood risk exposure in this region is key to reducing flood losses. Flood events not only in 2015-16 but also in 2014, 2017, and 2018 have caused substantial damage, and highlight the need for flood risk management strategies. Doing so will require compiling information on the properties, businesses, and infrastructure that are vulnerable to flooding. This study also suggests that proposed dredging of the upper Paraguay River Basin to facilitate navigation could lead to increased summertime streamflow from the

Upper Paraguay River Basin (Pantanal), effectively coupling the phases of streamflow from the Upper and Lower Paraguay River Basins which currently have a time-delay (*Bravo et al.*, 2012).

3.7 Summary

In this study we examined the regional climate drivers of the persistent and heavy NDJF 2015-16 rainfall over the Lower Paraguay River Basin which was associated with severe flood events.

Both enhanced moisture inflow from the low-level jet and convergence associated with baroclinic systems drove the observed heavy rainfall. Repeated SALLJ events, particularly No-Chaco jet events, led to favorable conditions for mesoscale convective activity in this region. Large-scale climate patterns at both seasonal and sub-seasonal scales favored the synoptic weather patterns observed. Notably, a strong El Niño and an active MJO in phases 4-5 favored SALLJ occurrence. The presence of a dipolar SST anomaly in the central southern Atlantic Ocean also favored the occurrence of No-Chaco jet events.

Numerical forecasts skillfully predicted enhanced risk of heavy rainfall at the seasonal scale, consistent with the observed ENSO signal, but biases in the spatial patterns of forecast rainfall suggest that models imperfectly capture the physical interactions between the Pacific and the Atlantic basins. At sub-seasonal time scales, uncorrected model forecasts of rainfall had limited skill beyond 15 days, though use of model output statistics – particularly the PCR and CCA methods that correct both spatial patterns and magnitudes – substantially improved forecast skill.

It all began on March 23, 1913, with a series of nearly a dozen tornadoes. Bodies fell from the sky, but the real terror was to come. The heavens opened with freezing rains and the flooding began. Some people drowned in their homes, others on the roads when they tried to flee. All the while, fires raged despite the torrent.

Geoffrey Williams, Washed Away: How the Great Flood of 1913, America's Most Widespread Natural Disaster, Terrorized a Nation and Changed It Forever

4

Regional Extreme Precipitation Events: Robust Inference from Credibly Simulated GCM Variables

General circulation models (GCMs) are widely used to estimate future precipitation, with application to a variety of engineering, planning, and financial use cases. Yet while theory predicts substantial sensitivity of the hydrologic cycle to anthropogenic climate change (ACC), there is generally low confidence in future projections of extreme precipitation frequency at the river basin scale. As described in chapter 2, some of these uncertainties stem from fundamental uncertainties as to the response of large-scale climate patterns (e.g., the storm tracks) to ACC while others stem from intrinsically flawed parameterization of local rainfall in GCMs. In this paper we focus on the latter limitation and build a statistical-dynamical

model using large-scale climate features from a GCM plus a statistical model for local rainfall extremes, conditional upon these large-scale features. We take the Ohio River Basin (ORB) as a case study because prior work has illuminated the drivers of large-scale river floods in this basin, reducing the need for diagnostic exploration. This chapter addresses four particular questions, with summarized conclusions shown below for each.

1. For the ORB, are the extreme springtime precipitation events that cause floods well simulated by the GCM?
    - Regional extreme precipitation (REP) events (defined in section 4.1) increase the probability of subsequent streamflow extremes in the ORB, particularly in the December-February (DJF) and March-May (MAM) seasons.
    - The GCM studied simulates too many REP days but under-simulates the occurrence of back-to-back REP days.
    - North-South movement of storms in the GCM is under-simulated, causing precipitation (particularly along cold fronts) to exit the study region too quickly.
2. Can atmospheric indices that are associated with the onset of REP events be identified from re-analysis?
    - Most REP days during the MAM season are associated with an extratropical cyclone (ETC) to the West of the basin and ridging in the West Atlantic.
    - Moisture from the Gulf of Mexico and Caribbean is steered by this zonal dipole.
    - An anomalous ridge in the northwestern Pacific Ocean, likely part of a low-frequency hemispheric pattern, is a precursor to REP days in the ORB.
3. Are suitably derived atmospheric indices associated with REP events in atmospheric re-analysis credibly simulated by the GCM?
    - The GCM credibly represents a set of five indices (in marginal distribution, autocorrelation, and tail persistence) that describe the above identified synoptic pattern.
4. If GCMs represent the large-scale atmospheric indices more credibly than they do the REP events, can we use the GCM derived atmospheric indices to directly simulate ex-

treme precipitation events in the current and future climate?

- A regression model for REP occurrence conditional on credibly simulated atmospheric indices mitigates the bias in GCM simulation of REP events.
- An increasing trend in REP day frequency is projected using the regression model, but the magnitude of this trend is smaller than that identified using only GCM simulations.

This chapter has been published as

> Farnham, D. J., J. Doss-Gollin, and U. Lall (2018), Regional extreme precipitation events: Robust inference from credibly simulated GCM variables, *Water Resources Research*, *54*(6), doi: 10.1002/2017wr021318

and is included with permission of all authors.

4.1 Introduction

Floods are responsible for significant loss of life and economic damages both within the United States (US) and worldwide. Flood impacts in the US are estimated at $USD 8 billion (in 2014 dollars) and 82 fatalities per year from 1984 to 2013, while worldwide flood losses were estimated to be about $USD 85 billion (in 2012 US dollars) in 1993 alone (*Kundzewicz et al.*, 2013). Furthermore, trends in population and urbanization are expected to increase exposure to hydroclimate extremes (including floods) into the future (*Jongman et al.*, 2012). Given that projections of extreme precipitation changes remain highly uncertain (*IPCC*, 2012), particularly in the mid-latitudes, improved estimation of future hydroclimate extremes is a key ingredient for the mitigation of future flood impacts.

The poor representation of precipitation fields (particularly extreme precipitation) in GCM simulations (*Dai*, 2006; *Stephens et al.*, 2010; *Kendon et al.*, 2012) complicate the projections of future hydroclimate extremes. Simulated precipitation fields are often used as inputs to hydrologic models (e.g. *Kundzewicz et al.*, 2010; *Hirabayashi et al.*, 2013; *Lehner et al.*, 2006; *Winsemius et al.*, 2016) after some form of bias correction (e.g. quantile-quantile mapping; *Gudmundsson et al.*, 2012)) or downscaling is applied. However, it is often difficult to justify

a bias correction approach, especially for extrapolation into the future, since there is no accompanying insight as to the underlying cause for the bias, or whether the bias correction used would be applicable in the future. In this paper we explore whether some atmospheric variables that are closely related to the occurrence of glsrep are well simulated by GCMs, such that their use for conditional prediction of REPs under seasonal forecasts or for climate change projections can be an effective strategy.

4.1.1 Research Questions

An important question is whether a GCM reproduces REP events well in the historical record. Since GCMs represent the coupled dynamics of the ocean-atmosphere-land systems, answering such a question is highly dependent on the physical parameterizations of each individual GCM. One possibility is that the GCMs credibly simulate large-scale climate circulations but that grid-scale (and sub grid-scale) precipitation mechanisms are not well represented. In this case it may be possible to use credibly simulated state variables from GCM simulations to derive or simulate credible sequences of REP events associated with major floods. We explore this possibility by focusing on a single GCM and a set of atmospheric circulation indices relevant to floods in the ORB. The following set of questions provide the framework for our overall goal of identifying the causal structure associated with REP events and developing an empirical model that allows the causal structure to be tested and used in a predictive context.

Q1 For the Ohio River basin, are the extreme springtime precipitation events that cause floods well simulated by the GCM?

Q2 Can atmospheric indices that are associated with the onset of REP events be identified from re-analysis?

Q3 Are suitably derived atmospheric indices associated with REP events in atmospheric re-analysis credibly simulated by the GCM?

Q4 If GCMs represent the large-scale atmospheric indices more credibly than they do the REP events, can we use the GCM derived atmospheric indices to directly simulate extreme precipitation events in the current and future climate?

4.1.2 Flooding, Extreme Precipitation, and Atmospheric Circulations in the ORB

We use the ORB, which has a long history of regional flooding, to examine the questions presented in section 4.1.1. Major events in 1933, 1937, 1945, 1997, and 2011 are among the numerous floods that have had high financial and human life costs. The springtime flood of 1913 caused over 450 deaths (*Perry*, 2000), while the springtime flood of 2011 is estimated to have cost over $3 billion in damages (*Smith et al.*, 2016). Although floods are influenced by water management strategies, land use, and soil characteristics, the floods in the ORB are generally associated with heavy and/or persistent precipitation events and/or snowmelt (*Nakamura et al.*, 2013). The dominance of the precipitation signal is also supported by *Mallakpour and Villarini* (2015), who primarily attribute changes in flood frequency in the central US to changes in heavy rainfall frequency and temperatures while noting that land surface changes play a secondary role.

In the study region, and in the mid-latitudes more generally, intense rainfall over a large area typically requires large-scale advection of moisture from the tropics (*Knippertz and Wernli*, 2010; *Lu et al.*, 2013; *Steinschneider and Lall*, 2016). Tropical moisture export-related precipitation over the central and eastern United States is dominated by the Great Plains activity center, which sources moisture primarily from the Gulf of Mexico and Caribbean Sea (*Gimeno et al.*, 2010; *Lavers and Villarini*, 2013b; *Steinschneider and Lall*, 2016). *Dirmeyer and Kinter* (2010) showed that large-scale flooding across the US Midwest is often associated with moisture sources extending through Texas, Eastern Mexico, the western Gulf of Mexico, and the Caribbean Sea (termed the "Maya Express"). *Nakamura et al.* (2013) showed that springtime extreme streamflow in the ORB is driven by a unique, recurrent, persistent and strong atmospheric anticyclonic circulation anomaly located to the east of the US Atlantic coast (i.e. the Bermuda High), which forces anomalous northward moisture transport from the Gulf of Mexico and tropical Atlantic.

The remainder of the paper is organized as follows: In section 4.2 we describe our methods and data sources. In section 4.3 we introduce the regional extreme precipitation index and evaluate its relationship to flood flows in the region. In section 4.4 we compare ob-

served precipitation records to historical GCM runs and discuss the origin of the GCM bias. In section 4.5 and section 4.6 we present the results of a diagnostic composite analysis, define atmospheric circulation and moisture indices associated with the regional extreme precipitation onset, and compare the indices as derived from reanalysis data vs. the historical GCM runs. In section 4.7 we present the results of the conditional simulation of the precipitation events given the GCM fields for the historical (1950-2005) and future (2006-2100) periods. In section 4.8 we summarize our results and discuss the broader implications of our findings.

4.2 Methods and Data

4.2.1 Methodological Overview

We build on the diagnostic literature discussed in section 4.1.2 in this paper and focus directly on predicting whether or not a REP process is likely to occur on a given day based on atmospheric conditions as summarized by a set of indices. The REP event is defined here as a day when at least 4 of the 15 sub-regions in the region of interest experiences a daily rainfall that exceeds the 99th percentile of daily rainfall at that location. Sub-regions are defined by the blue grid in fig. 4.1 and are based on the GCM's spatial grid. Thus, a spatiotemporal extreme precipitation process is implicitly considered conditional on variables that are derived from a climate model. Notably, we do not explicitly address issues related to the ability of GCMs to simulate extreme precipitation as a function of spatial resolution (such as in *Wehner et al.*, 2010).

We focus on flood-relevant extreme precipitation events and fit and simulate from a Bayesian model that propagates the parameter estimation uncertainties to the future simulations. This latter point is vital for decision making since understanding the range of possible future outcomes, via various prediction intervals, is helpful for determining our level of confidence in the projections and thus whether the projections represent actionable information or not.

Our approach is conceptually similar to a nonhomogeneous hidden Markov model (NHMM) (*Hughes et al.*, 1999; *Kwon et al.*, 2009; *Holsclaw et al.*, 2015; *Cioffi et al.*, 2016, 2017) for precipitation downscaling. In the NHMM approach, a stochastic model is considered for the daily

rainfall process, where rainfall occurrence is modeled conditionally on a latent (unobserved) state, and the probability of being in a particular hidden state is informed by a set of appropriate atmospheric circulation variables. This approach is useful in the context of flood modeling, since it preserves the sequence of rainfall occurrence and hence of antecedent conditions and event rainfall, both of which are important for determining flood potential. A challenge with this approach is that rainfall extremes may or may not be well represented, since often they are not explicitly conditioned on changing climate state. The end result of simulating a credible precipitation index time-series from dynamical model outputs is common to both our proposed method and many bias correction and statistical downscaling techniques (e.g. *Wilby et al.*, 2002; *Maraun et al.*, 2010; *Gutmann et al.*, 2014). Our method, however, places a central focus on identifying and representing the underlying dynamics of the process. We discuss bias-correction and downscaling approaches common to the literature in section 4.8.2.

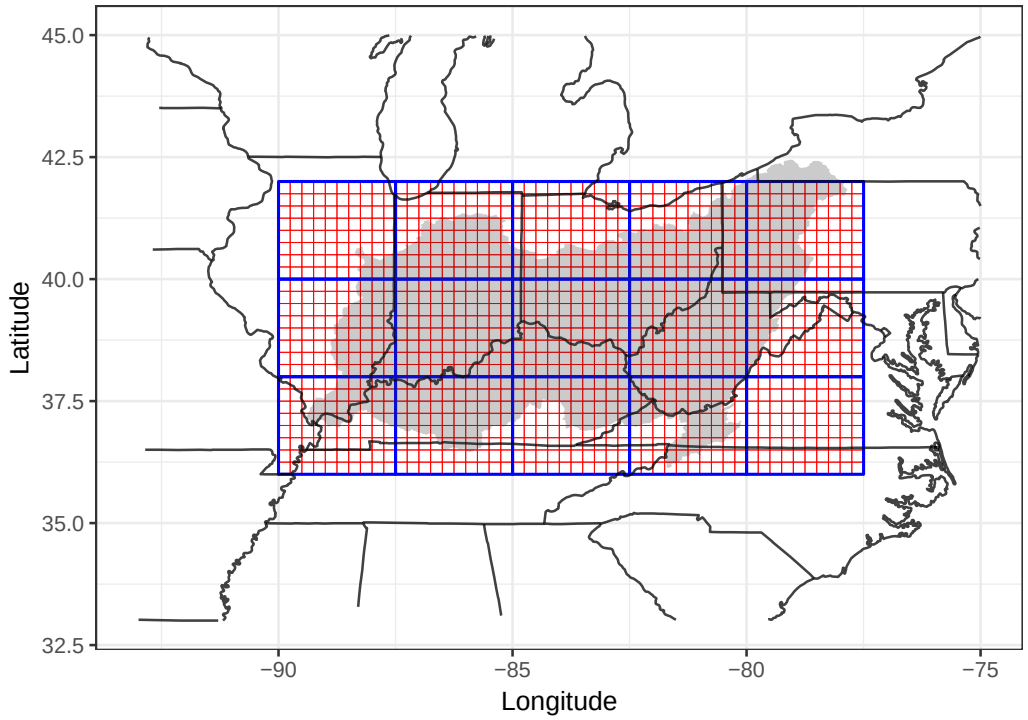

Figure 4.1: Map of study area. Blue grid shows resolution of GFDL CM3 coupled model cells. Red grid shows native resolution of CPC precipitation data cells. The shaded area indicates the ORB ($\sim$ 530 000 km^2) as defined by the USGS.

Lastly, we focus on the spring (Mar-Apr-May, MAM) season in the ORB (fig. 4.1), following the observation in *Nakamura et al.* (2013) that this is the dominant season for major regional

floods. Our historical study period is from 01 March 1950 through 30 May 2005, and our future study period is from 01 March 2006 through 30 May 2100. All anomalies are estimated relative to the historical monthly mean unless otherwise noted.

4.2.2 Regional Extreme Precipitation Days and Extreme Streamflow

We use the Climate Prediction Center (CPC) US unified gauge-based surface precipitation (P) data at horizontal resolution of 0.250° by 0.250° (*Chen et al.*, 2008). The data is defined as the precipitation accumulated in the prior 24 hours at 12 UTC and is available online from the International Research Institute for Climate and Society (IRI)'s Data library at `https://iridl.ldeo.columbia.edu/SOURCES/.NOAA/.NCEP/.CPC/.UNIFIED_PRCP/.GAUGE_BASED/.GLOBAL/.v1p0/`. We upscale the CPC precipitation data by taking the spatial average of the daily precipitation over the coarser horizontal grid of the dynamical climate model introduced below (2.50° longitude by 2.00° latitude). We refer to this upscaled CPC precipitation data as observed precipitation throughout the manuscript.

The 99th percentile precipitation exceedances, used to define the REP days, are defined from the full-year daily record for each individual grid cell within the region of interest. In this case, the region refers to all of the area covered by the blue and red grids in fig. 4.1. The 99th percentile thresholds used to derive the REP days are estimated separately for the observed and GCM records from the observational record (1950-2005) unless noted otherwise. This means that our REP record is insensitive to bias in the 99th percentile precipitation in the GCM, which in turn means that this work does not address GCM bias in precipitation intensity (such as in *Maraun et al.*, 2010). Using the available data shown in fig. 4.1, a REP day means that 4 or more of the region's 15 grid cells experience a 99th percentile exceedance of daily rainfall. We use the Hydro-Climatic Data Network streamflow data from the USGS data downloaded with the `dataRetrieval` package of the R statistical programming language, and retain only sites with drainage areas larger than 15 000 km^2 and with fewer than 25 missing days over the historical study period. Six streamflow stations in the ORB meet these criteria and are shown in fig. 4.2.

Our first goal is to investigate the relationship between the REP days and extreme stream-

flow days, the latter of which we define as streamflow greater than the 1 in 365 day streamflow (≈ 99.7th percentile), defined from each site's full record. We use the log odds ratio of eq. (4.1) to assess the extent to which REP day occurrence in the previous 15 days corresponds to enhanced probabilities of extreme streamflow at the six long record streamflow gauges.

$$(\mathrm{LOR}^s|\mathrm{REP}) = \ln\left[\frac{\mathrm{P}\left(S_t^s > S_{364/365}^s \,\middle|\, \sum_{t'=(t-15)}^{t} \mathrm{REP}_{t'} \geq 1\right) / \mathrm{P}\left(S_t^s \leq S_{364/365}^s \,\middle|\, \sum_{t'=(t-15)}^{t} \mathrm{REP}_{t'} \geq 1\right)}{\mathrm{P}\left(S_t^s > S_{364/365}^s \,\middle|\, \sum_{t'=(t-15)}^{t} \mathrm{REP}_{t'} = 0\right) / \mathrm{P}\left(S_t^s \leq S_{364/365}^s \,\middle|\, \sum_{t'=(t-15)}^{t} \mathrm{REP}_{t'} = 0\right)}\right] \quad (4.1)$$

where S_t^s is the streamflow at time step t and streamflow station s, $S_{364/365}^s$ is the 1 in 365 day streamflow at site s, and t' is a dummy variable to loop from $(t-15)$ to t.

4.2.3 Atmospheric Reanalysis for Event Diagnostics

We use atmospheric specific humidity (Q), geopotential height (Z), upward velocity (ω), and zonal wind (U) fields from the National Center for Environmental Prediction (NCEP)/National Center for Atmospheric Research (NCAR) reanalysis 1 data set (*Kalnay et al.*, 1996). The NCEP/NCAR reanalysis dataset has a horizontal resolution of 2.50° by 2.50° and 17 pressure levels. We download six hourly data and define each day as the average value between 12 UTC and 12 UTC to ensure that the atmospheric reanalysis data is on the same temporal grid as the CPC precipitation. The NCEP/NCAR Reanalysis 1 data is available from NOAA/OAR/ESRL PSD, Boulder, Colorado, USA, online at `http://www.esrl.noaa.gov/psd/`.

4.2.4 General Circulation Model

We use the P, Q, Z, ω, and U fields from the CM3 (*Donner et al.*, 2011). The surface and atmosphere in CM3 has a resolution of 2.50° longitude by 2.00° latitude (fig. 4.1). CM3 outputs are available online at `https://www.gfdl.noaa.gov/coupled-physical-model-cm3/`. Based on the atmospheric variables and daily resolution that we required for this work, we could only acquire two historic ensemble member simulations and one future simulation.

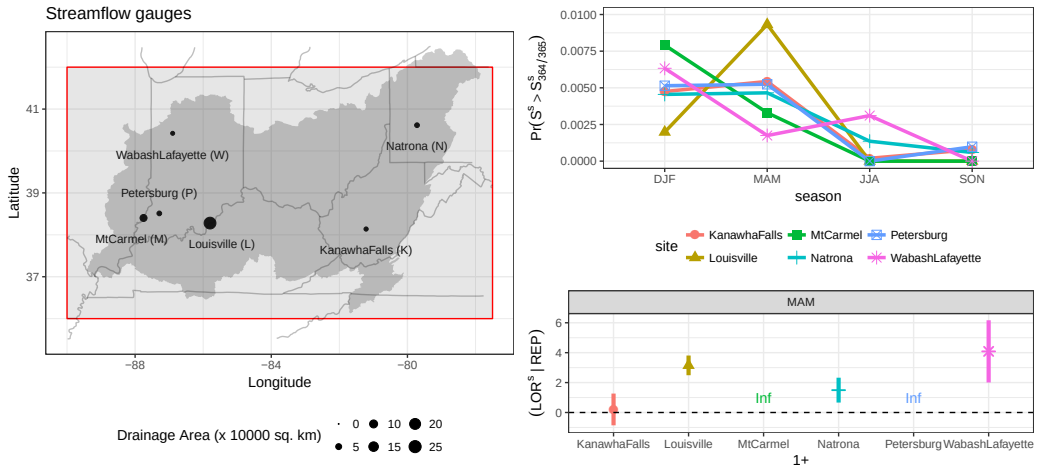

Figure 4.2: Relationship between streamflow and REP days. (Left) Locations and drainage areas of the six long record streamflow stations. (Top, right) The seasonality of extreme streamflow ($>\approx$ 99.7th percentile) for each site in colors as expressed through the probability of extreme streamflow occurrence during each season. (Bottom, right) The log odds ratio of eq. (4.1) and confidence interval associated with MAM days when one of more REP days have occurred in the previous fifteen days vs. those when no REP days have occurred in the previous 15 days and streamflow being above or below the $\approx$ 99.7th percentile. The odds ratio confidence interval was calculated via the unconditional maximum likelihood estimation (or the Wald method) via the `epitools` package of the R statistical programming language.

4.3 Regional Extreme Precipitation Days and Streamflow

Figure 4.2 highlights the positive relationship between REP incidence and subsequent extreme streamflows during MAM in the study basin. DJF and MAM dominate the record of extreme streamflows ($\approx$ 99.7th percentile) and the station with the largest drainage area (Louisville) shows a clear maximum in MAM. The estimated log odds ratio defined in eq. (4.1) is positive for all stations during MAM (fig. 4.2), a clear indication that the occurrence of REP days is strongly associated with the occurrence of extreme streamflows during MAM in the ORB. The extreme streamflow seasonality and enhanced odds of occurrence following REP days are similar when extreme streamflow is defined using the 99th and 99.9th percentiles, indicating that the relationship between high streamflows and antecedent REP events is not sensitive to the definition of extreme streamflow.

4.4 Regional Extreme Precipitation in a GCM and Observations

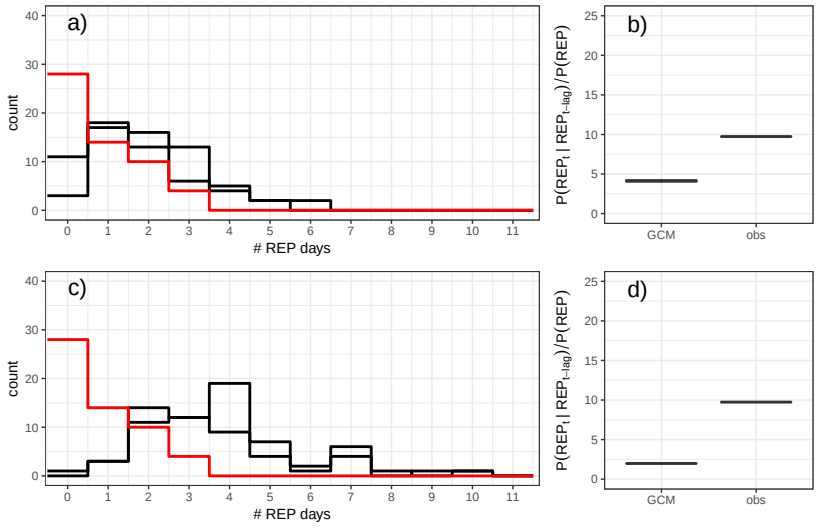

Figure 4.3: Frequency distribution of REP days in observations and GCM output. (a): The frequency distribution of the number of MAM REP days by year for the observed record (red solid line) and the two GFDL CM3 ensemble members (black solid lines). (b): The probability of a REP event on a day given that a REP event occurred the day prior divided by the marginal probability of a REP event for the MAM season for the observed record and the two ensemble members. (c,d): as (a,b) but with the observed 99th percentile precipitation thresholds used to derive the model REP records. The bottom panels show that the discrepancy between the GCM runs and the observed REP records is even more stark when the observed precipitation data is used to calculate the 99th percentile thresholds for the model and REP records, an indication of a significant positive bias with respect to the GCM's 99th percentile precipitation. In fact, the median of the study region's 99th percentiles is 31 mm/day in the GFDL CM3 model, and only 25 mm/day in the CPC data.

We next turn our attention to **Q1** by comparing REP day frequency and persistence in the observed and GCM records.

The CM3 model simulates too many MAM REP events in the study region and too few back-to-back MAM REP days when compared to the observed record (fig. 4.3). This is supported quantitatively by highly significant Wilcoxon rank sum tests in table 4.1. The MAM REP frequency bias stems from a seasonality bias in the GCM that results in too many (few) local extreme precipitation days in the spring (summer) and higher spatial coherence of local extreme precipitation days in the GCM. The origin of the persistence bias in the GCM appears to be related to faster storm propagation speeds due to bias in the climatological jet stream.

Table 4.1: The distributions of atmospheric indices in GCMs and reanalysis are more similar (per two-sample Wilcoxon rank sum tests) than the distributions of REP days per year based on the GCM and precipitation and the observed precipitation. The null hypothesis of this test is that it is equally likely that a randomly selected value from sample A (i.e., observations) is greater than or less than a randomly selected value from sample B (i.e., GCM ensemble member).

	Observed/Reanalysis & GCM ensemble member 1		Observed/Reanalysis & GCM ensemble member 2	
Variables being compared	W-statistic	p-value	W-statistic	p-value
# REPs (yearly)	2.2×10^3	1.8×10^{-4}	2.5×10^3	8.1×10^{-8}
Z_L (daily)	1.3×10^7	9.1×10^{-1}	1.3×10^7	8.7×10^{-1}
Z_H (daily)	1.3×10^7	8.1×10^{-1}	1.3×10^7	6.1×10^{-1}
Z_P (daily)	1.3×10^7	3.1×10^{-1}	1.3×10^7	4.6×10^{-1}
HUM (daily)	1.3×10^7	8.2×10^{-1}	1.3×10^7	8.8×10^{-1}
OMG (daily)	1.4×10^7	1.0×10^{-1}	1.4×10^7	9.6×10^{-2}

While the CM3 model exhibits a wet bias in the 99th percentile precipitation, the approach used to define REP events means that this does not explain the inflated MAM REP counts in the GCM. Since the total number of local (one cell) extreme precipitation days (i.e. $>$ 99th percentile) is the same for both the observed and GCM records, the REP frequency bias can stem from a bias in the seasonal distribution of the local extreme precipitation days or a bias in the spatial correlation across the study region.

There is clearly a bias in the seasonality of the extreme precipitation days, which contributes to the over-simulation of MAM REP days. The CM3 model ensemble members show 37 and 38 percent of their local (single-grid) extreme precipitation days occurring during MAM, while the observed record shows only 27 percent (see fig. 4.4). Conversely, the CM3 members simulate between 10 and 11 percent of local extreme precipitation days during June-August (JJA), less than the observed value of 26 percent. This seasonality bias is manifest in the REP climatology itself (fig. 4.5) with the GCM simulating relatively few REP days during JJA and relatively more during MAM. Deficiencies in simulating extreme precipitation during boreal mid-latitude summer has been observed and discussed for other models (e.g. *Durman et al.*, 2001) and may be attributable to parameterizations of sub-grid-scale convective processes (*Liang et al.*, 2006).

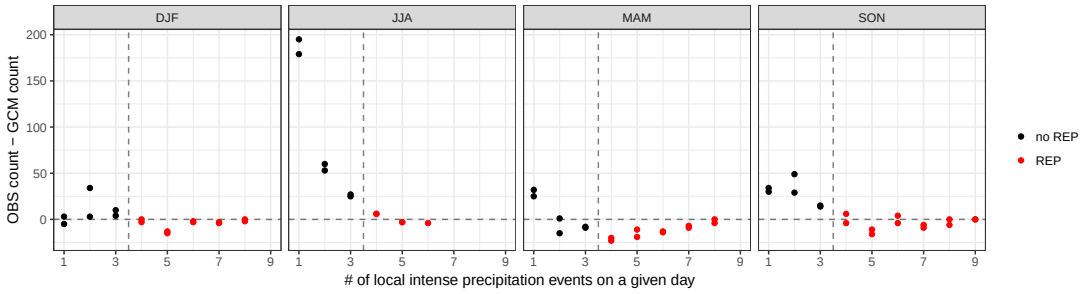

Figure 4.4: The difference of frequency distributions (between the observed and two GCM ensemble members) of local (one cell) extreme precipitation days by season (columns) over the observational record for all days with at least 1 local extreme precipitation event in the study region.

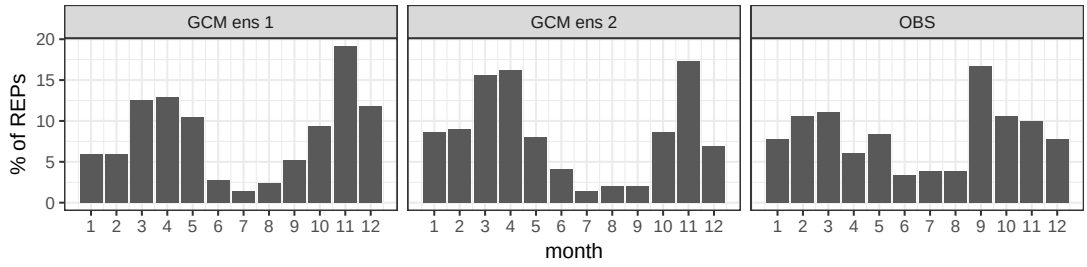

Figure 4.5: The distribution of the regional extreme precipitation days by month for the observed record and each of the two GCM ensemble members. Note that the GCM ensemble members are very similar and averaging across them does not significantly reduce the bias with respect to spring (MAM, or months 3, 4, and 5) and summer (JJA, or months 6, 7, and 8) REP frequency.

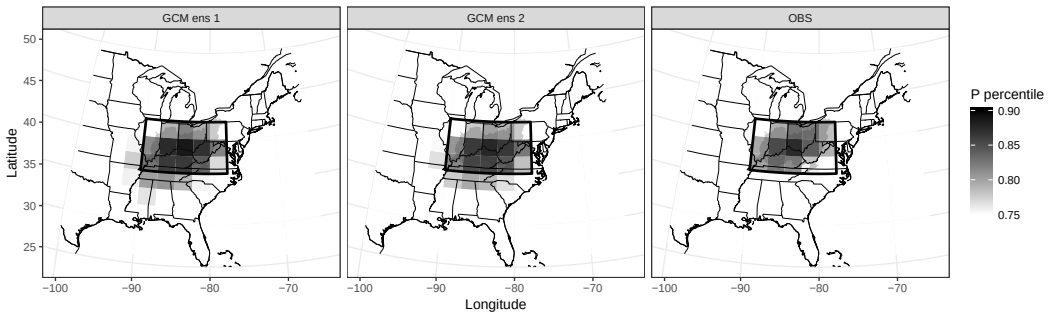

Figure 4.6: The precipitation percentiles (shading) averaged over all days when at least one of the 15 study area cells received rainfall greater than the 99th percentile for the observed and two GCM ensemble members. All cells with mean percentile less than the 75th are shaded white.

The second reason for the inflated MAM REP counts is a tendency of the CM3 model to produce too many co-occurring local extreme precipitation days. More precisely, REP days occur during 22 and 24 percent of all MAM days when there is at least one local extreme precipitation event in the two CM3 ensemble members, respectively, compared to just 11 percent in the observed records (see fig. 4.4). This indicates that when the model produces extreme precipitation in any part of the study region, it has a tendency to simultaneously produce extreme precipitation in several grid cells. This high regional covariance, or smearing, of the extreme precipitation can be seen in fig. 4.6. This high spatial covariance is not surprising given that the effective resolution of numerical models is known to be significantly greater than the grid spacing (e.g., *Grasso*, 2000). This point is noteworthy for any regional flood hazard assessment that uses GCMs.

In addition to the frequency bias, the CM3 model under-simulates the occurrence of back-to-back REP days (fig. 4.3, right panels). The probability of a REP day following the occurrence of a REP day is about 4 times more than the marginal probability of REP occurrence in the GCM, compared to about 10 times in the observed record. This appears to be related to representation of the storm tracks, which in CM3 propagate primarily from west to east, under-representing observed south to north movement. This causes the precipitation (particularly along cold fronts) to exit the study region more quickly (fig. 4.7). We conclude that the **relevant precipitation events are not well simulated by the CM3 model** (i.e. no to **Q1**) and turn our attention to **Q2** by investigating the atmospheric circulations associated with

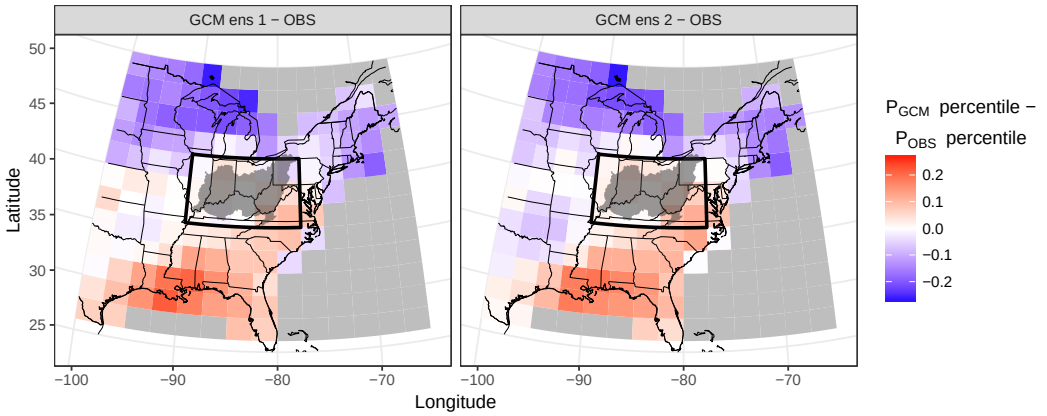

Figure 4.7: The difference between each GCM ensemble member and the observed record of precipitation percentiles (shading) averaged over all REP days.

REP days.

4.5 Circulation Patterns Associated with Regional Extreme Precipitation

The atmospheric circulation during the REP days is similar in the reanalysis record and the CM3 historical runs, aside from a modest southward shift in the composite storm location in the GCM that appears to be a manifestation of latitudinal bias in the jet.

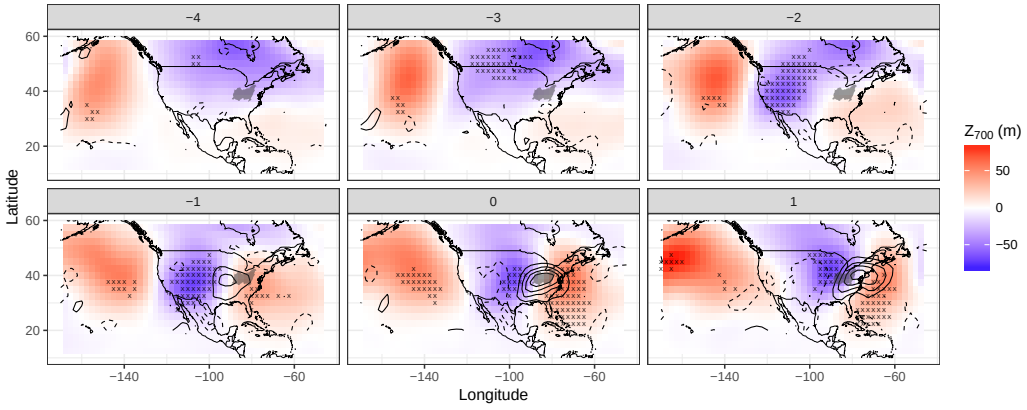

Figure 4.8: Daily composites of Z_{700} anomalies (shades) and Q_{700} (contours at 4×10^{-4} kg kg^{-1}) from four days before each MAM REP event to one day following the event for the observed-reanalysis record. Solid contours represent positive anomalies and dashed contours represent negative anomalies. An "X" indicates that at least 80% of composite members (i.e. at least 37 of the 46 REP events) had Z_{700} anomalies of the same sign in that location.

Figure 4.8 shows the composite time-lagged geopotential height and specific humidity anomalies at 700 hPa (Z_{700} and Q_{700}) preceding and during the MAM REP days for the observed record. The dominant features of the atmospheric development of the REP are similar to those found in *Nakamura et al.* (2013) for the top 20 floods in the ORB and include:

1. A zonal dipole pattern in the anomalous Z_{700} field at latitudes between about 35 °N to 45 °N preceding and accompanying the REP events
2. The dipole pattern migrates eastward beginning approximately three days prior to the REP events, accompanied by an intensification of the dipole and significant northward low-level wind anomalies (not shown)
3. A well-organized positive anomaly in the Q_{700} field over the ORB along the interface of low and high Z_{700} anomalies that peaks during the day of the event
4. An anomalous warm surface and low-level temperature anomaly that stretches from the Gulf of Mexico up to the Northeast US (not shown), indicating that the REP events are often associated with frontal systems which in turn are often coupled with extratropical cyclones (not shown)
5. An anomalous high pressure ridge in the northwest Pacific Ocean south of the Gulf of Alaska that starts to intensify at least 4 days prior to the REP day and persists through the day after the REP day. This north Pacific ridge appears to be a lower frequency pattern that together with the pressure dipole (noted above) forms a tripole structure spanning from the eastern Pacific to the western Atlantic during REP days that is reminiscent of the wavenumber 6 pattern.

The most consistent of the atmospheric features associated with the REP days is a high pressure system (Western Atlantic ridging) which is for some events related to an intensified and westward-extended subtropical high. Another consistent feature is the presence of a low pressure system in the western US that forms about 2-3 days prior to the REP days.

Despite the bias in the rainfall field, the CM3 ensemble member composites of Z_{700} (figs. 4.9 and 4.10) during MAM REP events show a similar pattern of troughing west of the basin and ridging east of the basin, compared to the reanalysis record. There are, however, a few subtle differences. The ridging patterns associated with REP days in the CM3

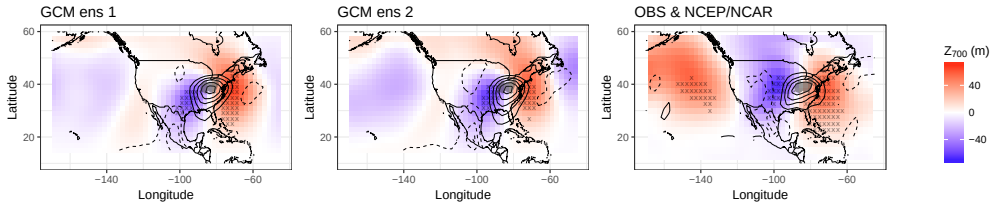

Figure 4.9: Same as fig. 4.8 but for the day of the REP event (lag = 0) and each of the GFDL CM3 GCM ensemble members and the observed-reanalysis record (panels). As in fig. 4.8, an "X" indicates that at least 80% of composite members had Z_{700} anomalies of the same sign in that location. This 80% criteria translates to at least 83 out of 103 REP events, 92 out of 115 REP events, and 37 out of 46 REP events, for the two CM3 ensemble members and the observed-reanalysis record, respectively.

model have a tendency to extend to the north-east of the study area, while in the reanalysis record the ridging tends to extend over locations to the south-east of the study area. The CM3 model also shows a southward displacement of the low pressure center relative to the reanalysis record, evident in the extent and location of precipitation during study region REP days (stronger/weaker southeast/northwest precipitation during GCM REP events can be seen in the difference between the GCM and observation percentile precipitation during REP events in fig. 4.6). This is likely related to a southward displacement of the storm tracks in the CM3 model, which can be seen in the enhanced (suppressed) standard deviation of MAM 700 hPa geopotential height to the south (north) of 30 °N to 35 °N in the GCM ensemble members compared to reanalysis (fig. 4.11) and the clear southward displacement of the springtime jet (fig. 4.12). We also note the absence of the REP-associated ridging in the north Pacific in the GCM, which along with the higher frequency wave train associated with REPs in the GCM, suggests that the GCM can produce REP days in the ORB without the presence of hemispherically organized flow compared to the observed-reanalysis record. Despite the modest latitudinal bias, and the lack of a clear tripole pattern, we highlight that the Z_{700} patterns associated with MAM REP events are largely similar between the GCM and reanalysis.

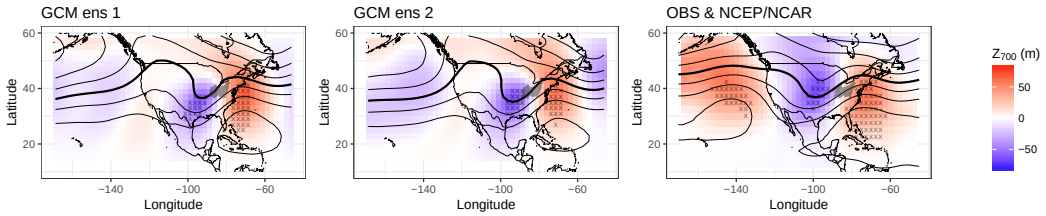

Figure 4.10: MAM REP day composites of Z_{700} anomalies (shading) and absolute Z_{700} (contours in 50 m increments with 3000 m marked with a thicker contour) for both the observed/reanalysis (i.e. reanalysis Z_{700} during observed REPs) and each of the two GCM ensemble members. Solid contours represent positive anomalies and dashed contours represent negative anomalies. An "X" indicates that at least 80% of composite members had Z_{700} anomalies of the same sign in that location. This 80% criteria translates to at least 83 out of 103 REP events, 92 out of 115 REP events, and 37 out of 46 REP events, for the two CM3 ensemble members and the observed-reanalysis record, respectively.

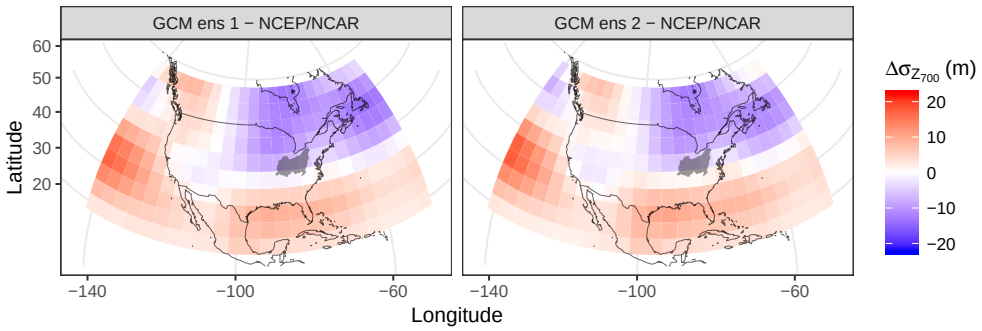

Figure 4.11: The difference in standard deviation of daily MAM geopotential height at 700 hPa for the reanalysis and each of the two GCM ensemble members. Note that the pattern associated with each ensemble member looks very similar, i.e. averaging across ensemble members does not meaningfully reduce the bias with respect to the reanalysis record.

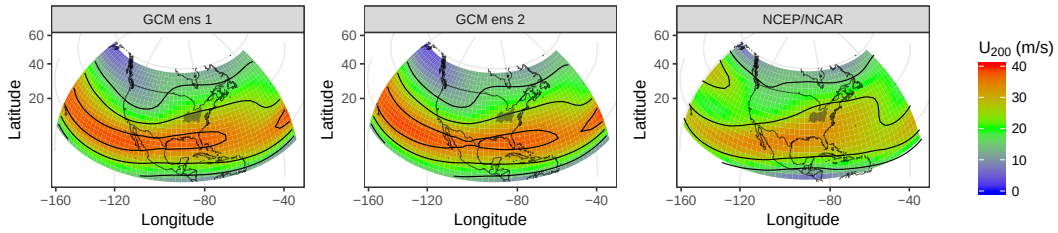

Figure 4.12: The climatological zonal wind 200 hPa (shading and contours) in m s^{-1} for the reanalysis and each of the two GCM ensemble members. The contours show 15 m s^{-1}, 25 m s^{-1} and 35 m s^{-1}. Note that the pattern associated with each ensemble member looks very similar, i.e. averaging across ensemble members does not meaningfully reduce the bias with respect to the reanalysis record.

4.6 Atmospheric Indices

In this section we show that the GCM appears to reasonably simulate the distributional and persistence features of five atmospheric indices that modulate the likelihood of REP events. This is critical to the conditional simulation strategy proposed in section 4.7.

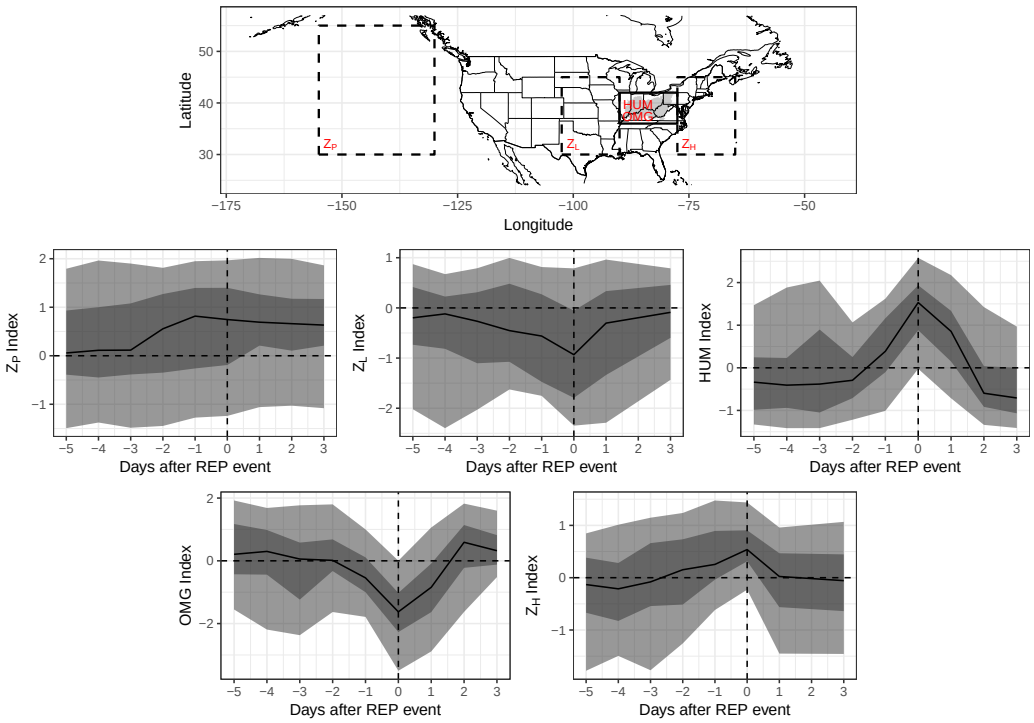

Figure 4.13: (Top) the regions that define each of the atmospheric indices. The index names are shown in red. The Ohio River basin, shown in more detail in fig. 4.1 is shaded in dark gray. The Z_P index is defined by the average Z_{700} within the area between 130 °W and 155 °W and 30 °N and 55 °N (leftmost dashed box), the Z_L index is defined by the average Z_{700} within the area between 87.5 °W and 103 °W and 30 °N and 45 °N (middle dashed box), and the Z_H index is defined by the average Z_{700} within the area between 62.5 °W and 77.5 °W and 30 °N and 45 °N (rightmost dashed box). The OMG and HUM indices are defined using the average atmospheric vertical velocity and specific humidity within the area between 77.5 °W and 90 °W and 36 °N and 42 °N (solid box). (Middle and bottom) The index values prior to and after the REP events. The black line shows the median index value. The dark shaded area shows the range capturing the middle 50% of days, while the light shaded area shows the range capturing the middle 90% of days. All panels use the observed REP record and the corresponding reanalysis-based atmospheric indices.

Given that the CM3 model credibly represents the pressure dipole associated with MAM REP events, we define two indices by geopotential heights in boxes to the east and west of the ORB. We call these indices the Z_L and Z_H (for the low and high pressure systems associated

with the REP days) and define them as the mean of Z_{700} in the western and eastern boxes, respectively, shown in fig. 4.13. The boxes have a large meridional extent to capture both the center of the low pressure storms in the GCM REP days and the observed REP days (fig. 4.9). We also define an index by the mean Z_{700} in the large box in the northwest Pacific during the three days prior to the current day. We call this index Z_P and include it to represent the impact of a strong wavetrain with a center of high pressure in the North Pacific on the probability of REP event (figs. 4.8 and 4.13). We also define two indices to capture the atmospheric conditions over the ORB. The first of these indices is defined as the mean of Q_{700} over the basin and is called HUM; we assume that higher values of moisture over the basin increase the probability of a REP day. The next of these indices is the mean of ω_{700} over the basin and is called OMG. This index is important since it represents the existent or absence of local convergence and uplift that is important for the occurrence of precipitation.

All five of these indices are defined as their standardized quantities (subtracting their seasonal mean and dividing by their seasonal standard deviation) following *Karl et al.* (1990). Most importantly, all five of these indices modulate the probability of REP occurrence (fig. 4.13). It should be noted, however, that the daily reanalysis-based indices have been defined by the 12 UTC to 12 UTC values to match the temporal grid of the CPC data while the CM3 indices have been defined on a standard daily grid that begins and ends with 0 UTC to match the daily temporal grid of the CM3 precipitation. We assume that the relationship between the indices and REP occurrence is insensitive to this temporal grid difference. Based on (fig. 4.13), we conclude that **indices that are associated with the onset of REP events can be identified from re-analysis** (i.e. yes to **Q2**) and turn our attention to **Q3** by investigating the atmospheric simulation of the indices in the CM3 GCM.

Figure 4.14 illustrates that the distributional and persistence properties of each of the indices are reasonably well simulated by the GCM (i.e. *yes* to **Q3**). Table 4.1 quantitatively illustrates (based on Wilcoxon rank sum tests) that the distributions of the atmospheric indices based on the GCM and reanalysis are more similar than the distributions of REP days per year based on the GCM precipitation and the observed precipitation. There are, however, a few differences between the GCM and reanalysis indices. These differences include slightly

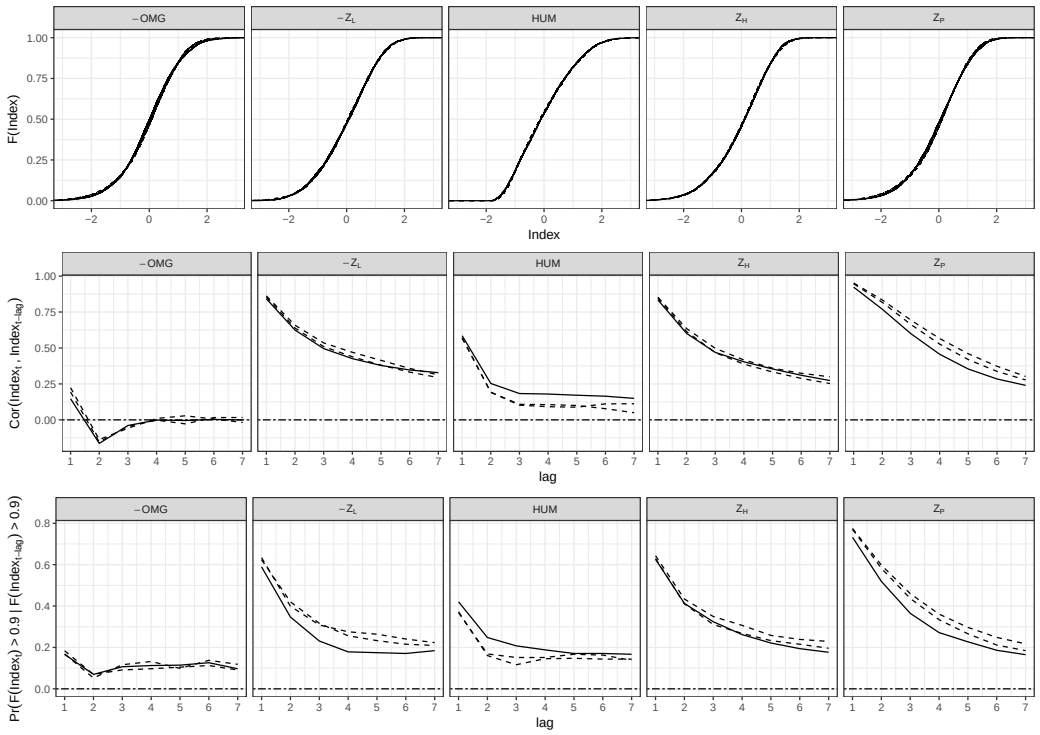

Figure 4.14: (Top) Cumulative distribution function for the MAM indices. (Middle) The serial correlation function for the MAM indices. (Bottom) The serial tail persistence of the MAM indices when in high states as shown by the probability of the index being above the 90th percentile on day t, given that the index was above that percentile on day t-lag, where lag values of 1 through 10 are shown along the x-axis. In all panels the solid line is the reanalysis-based indices and the dashed lines are the GCM ensemble member-based indices. Negative OMG and Z_L are shown for easier interpretation since low values of these two indices are associated with REP days.

lower HUM index autocorrelation, slightly higher Z_P autocorrelation, and higher persistence of extreme low values of Z_L for the GCM (fig. 4.14). It seems likely that the persistence bias of the HUM index partially explains the reduced persistence in the GCM-based REP days compared to the observed. On the other hand, the other notable persistence biases of the Z_L and Z_P indices should increase the probability of back-to-back REP days in the GCM compared to the observed record. Despite these minor differences, we conclude that **the atmospheric indices associated with REP events are credibly simulated by the GCM** (i.e. yes to **Q3**). We now turn our attention to the problem of directly using these indices to simulate the REP events (i.e. **Q4**).

4.7 Conditional Simulation

In this section we turn our attention to **Q4** and demonstrate that:

1. the conditional simulation of REP days based on a regression on the atmospheric indices addresses the bias in the observational record;
2. a future upward trend in REP day frequency is projected both when using the raw GCM precipitation fields and when using the conditional simulation model based on GCM-derived atmospheric indices;
3. this positive trend appears to be driven both by a trend in the moisture index (which is in turn at least partially the result of increasing temperatures), and by trends in the other indices.

To set up the logistic regression-based simulation model, with a binary response variable (REP or no REP), we assume that the Z_H, Z_L, Z_P, OMG, and HUM indices on day t linearly modulate the probability of REP occurrence on day t. Based on this assumption, we define a logistic regression model to estimate the probability of a REP day given the five indices (eq. (4.2)). We estimate $\alpha, \beta_{Z_L}, \beta_{Z_H}, \beta_{Z_P}, \beta_{HUM}, \beta_{OMG}$ from the observation-derived REPs and reanalysis-derived indices (eq. (4.2)). We refer to these parameter estimates as $a, b_{Z_L}, b_{Z_H}, b_{Z_P}, b_{HUM}, b_{OMG}$. We use a fully Bayesian model (*Jaynes*, 2003; *Gelman et al.*, 2014; *McElreath*, 2016) implemented in Stan (*Carpenter et al.*, 2017) in **R**. We use diffuse normal prior distributions with means of 0 and standard deviations of 25 and 5 for the α and β parameters, respectively.

$$P(REP_t^{obs} = 1) = \frac{\exp\left[\alpha + \beta_{Z_L}\left(Z_{L_{t+1}}^{reanal}\right) + \beta_{Z_H}\left(Z_{H_t}^{reanal}\right) + \beta_{Z_P}\left(Z_{P_t}^{reanal}\right) + \beta_{HUM}\left(HUM_t^{reanal}\right) + \beta_{OMG}\left(OMG_t^{reanal}\right)\right]}{1 + \exp\left[\alpha + \beta_{Z_L}\left(Z_{L_{t+1}}^{reanal}\right) + \beta_{Z_H}\left(Z_{H_t}^{reanal}\right) + \beta_{Z_P}\left(Z_{P_t}^{reanal}\right) + \beta_{HUM}\left(HUM_t^{reanal}\right) + \beta_{OMG}\left(OMG_t^{reanal}\right)\right]} \tag{4.2}$$

Where t is a time index and REP is the regional extreme precipitation indicator (either 0 or 1).

After fitting this model on the observed/reanalysis record, we are able to simulate REP days from the GCM-derived indices using eq. (4.3). Specifically, we sample from a Bernoulli distribution for each day with probability of a REP as computed from eq. (4.3). We retain 1000

samples for each day.

$$\widehat{\mathrm{P}(\mathrm{REP}_t^{\mathrm{mod}}=1)} = \frac{\exp\left[a + b_{\mathrm{Z_L}}\left(\mathrm{Z_L}_{t+1}^{\mathrm{mod}}\right) + b_{\mathrm{Z_H}}\left(\mathrm{Z_H}_t^{\mathrm{mod}}\right) + b_{\mathrm{Z_P}}\left(\mathrm{Z_P}_t^{\mathrm{mod}}\right) + b_{\mathrm{HUM}}\left(\mathrm{HUM}_t^{\mathrm{mod}}\right) + b_{\mathrm{OMG}}\left(\mathrm{OMG}_t^{\mathrm{mod}}\right)\right]}{1 + \exp\left[a + b_{\mathrm{Z_L}}\left(\mathrm{Z_L}_{t+1}^{\mathrm{mod}}\right) + b_{\mathrm{Z_H}}\left(\mathrm{Z_H}_t^{\mathrm{mod}}\right) + b_{\mathrm{Z_P}}\left(\mathrm{Z_P}_t^{\mathrm{mod}}\right) + b_{\mathrm{HUM}}\left(\mathrm{HUM}_t^{\mathrm{mod}}\right) + b_{\mathrm{OMG}}\left(\mathrm{OMG}_t^{\mathrm{mod}}\right)\right]} \quad (4.3)$$

4.7.1 Model Checking

To verify that our model captures a substantial portion of the variance in the record, we first evaluate the ability of our model to reproduce the observed record by fitting the model on the first 42 years (1950-1991; about three quarters of the data) and predicting the last 14 years. We use these time intervals so that the calibration sample contains at least several years of the relatively data rich period after the introduction of satellite observations systems in the late 1970s and early 1980s. The model is only able to capture a small portion of the day-to-day variation with daily hit rates of 12% and 11% for the calibration and testing samples, respectively, and false alarm rates of 88% for both the calibration and testing samples. If we allow the simulation to be off by one day in either direction, however, then we have hit rates of 22% and 14% and false alarm rates of 0%. Figures 4.15 and 4.16 show that the model captures a portion of the interannual variation, and has a negative bias with respect to representing the persistence of REP days. Lastly, the proposed model explains 33% of the deviance in the data and partially reproduces the spectral peaks at 3-4 years and 7-8 years when fit on the full historical data (fig. 4.17). In summary, the physical variables that we have identified only explain a portion of the variance in the REP record and can therefore be seen as necessary but not sufficient to predict day-to-day REP occurrence with high probability. This model is potentially useful, however, for understanding long-term changes in the REP frequency associated with changes to these underlying physical variables, as we show below.

4.7.2 Simulation Results

The results of our conditional simulation based on the GCM-derived atmospheric indices and the reanalysis-observation coefficient estimates for the historical record are shown in fig. 4.18. When the model is estimated based on the full historic reanalysis-observed record, the regression coefficient estimates for $\mathrm{b_{Z_L}}, \mathrm{b_{Z_H}}, \mathrm{b_{Z_P}}, \mathrm{b_{HUM}}, \mathrm{b_{OMG}}$ have means of -0.72, 0.65, 0.41, 0.90, and -1.11, and standard deviations of 0.18, 0.30, 0.18, 0.25, and 0.21. All coefficients are of their

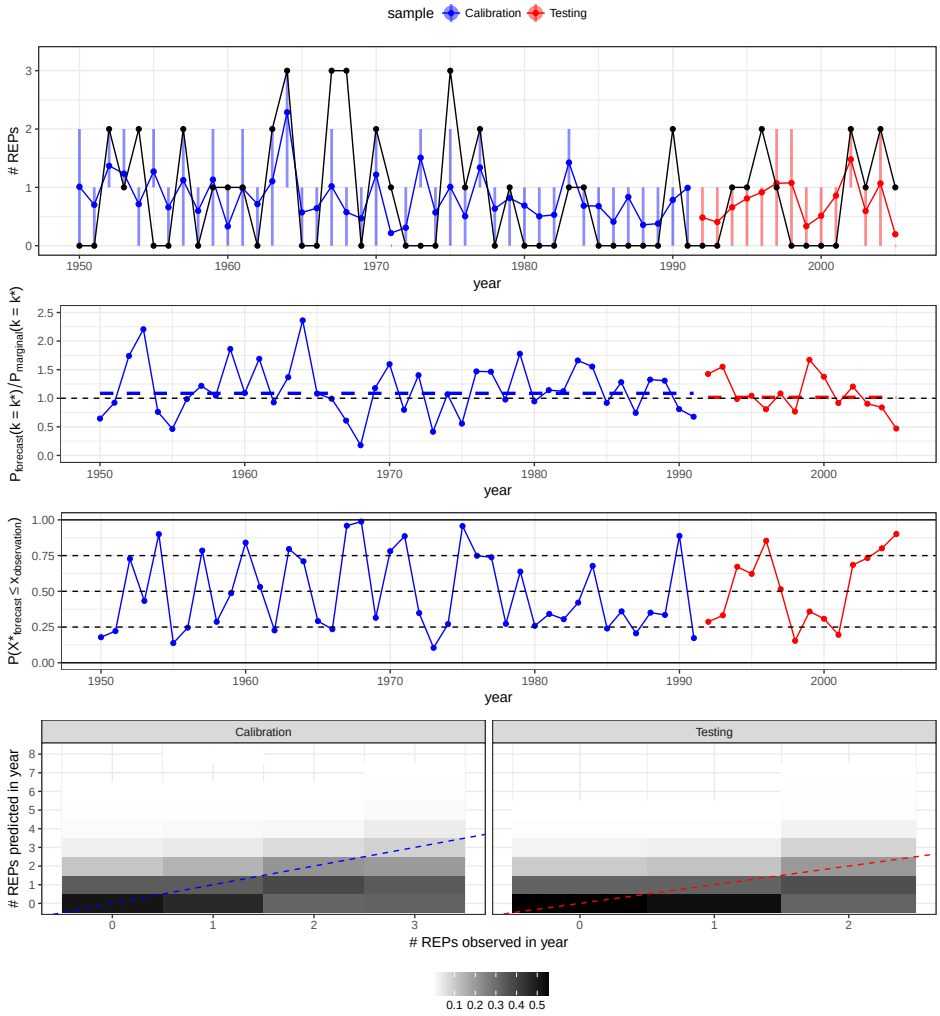

Figure 4.15: (Top) Yearly record of the number of REP days per year for the observed record (solid black points and line), the mean of the regression predicted record during the calibration period (solid blue points and line) and testing period (solid red points and line). The 50th percentile prediction intervals are also shown for each year with blue and red vertical lines for calibration and testing periods, respectively. (Second from top) The probability that the model simulates the observed number of REPs in a year divided by the calibration sample probability of observing that same number of REPs in a year for the calibration and testing samples (blue and red points and lines, respectively). A ratio greater than one indicates skill. The training and testing sample median ratios are shown with blue and red dashed lines. (Third from top) The probability that the simulated number of REPs in a year were less than the observed number of REPs in a year. Random noise with mean zero and standard deviation of 0.001 is added to the simulation derived yearly time-series to avoid the ties that result from the discrete nature of the data. (Bottom) The discrete probability distribution of simulated number of REP days for years where 0, 1, 2, or 3 REP days were observed. That is, each column of tiles sums to 1. A 1:1 line is shown via dashed lines.

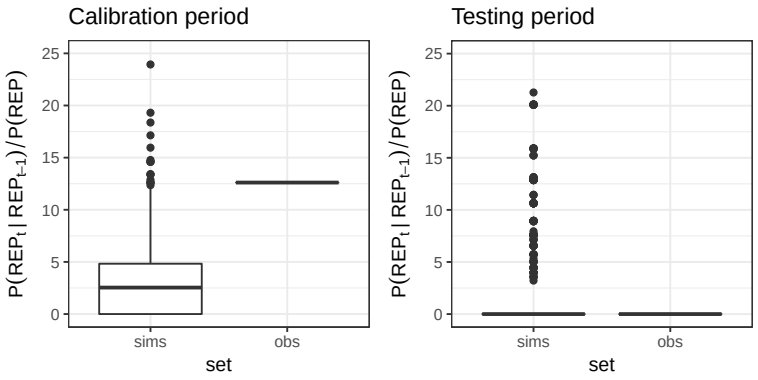

Figure 4.16: The probability of a REP event on a day given that a REP event occurred the day prior divided by the marginal probability of a REP event for the MAM season for the observed record (obs) and 1000 simulated records from the Bayesian regression model (sims) for the calibration (left) and testing (right) periods. The boxplot whiskers extend to points within 1.5 of the interquartile range, and any observation outside of this range is shown as a point.

Table 4.2: As table 4.1 but for the historical period observed REPs vs. mean of simulation model predicted REPs

	Observed & mean of model prediction	
Variables being compared	W-statistic	p-value
# REPs (yearly)	1.3×10^3	1.2×10^{-1}

expected sign and the HUM and OMG indices have the strongest effect on the probability of REP occurrence. The bias in the REP frequency is substantially reduced through the use of this simulation model (compare fig. 4.18 to the top panel of fig. 4.3), while the persistence bias is still significant. The bottom row of table 4.1 and table 4.2 quantitatively illustrate (based on Wilcoxon rank sum tests) that the distributions of GCM-index-based simulated REP days per year and observed REP days per year are more similar than the distributions of GCM-precipitation-based REP days per year and observed REP days per year.

We use a future simulation of the CM3 GCM under the RCP 8.5 forcing scenario to simulate daily REP records via our conditional simulation model for the years 2006 to 2100 and compare these projections against future daily REP records estimated directly from the GCM's precipitation field (fig. 4.19). The standardization of the indices was still based on the historical mean and standard deviation. We also compare our future simulations against projections based on a linear bias-corrected version of the GCM REPs where we assume that the

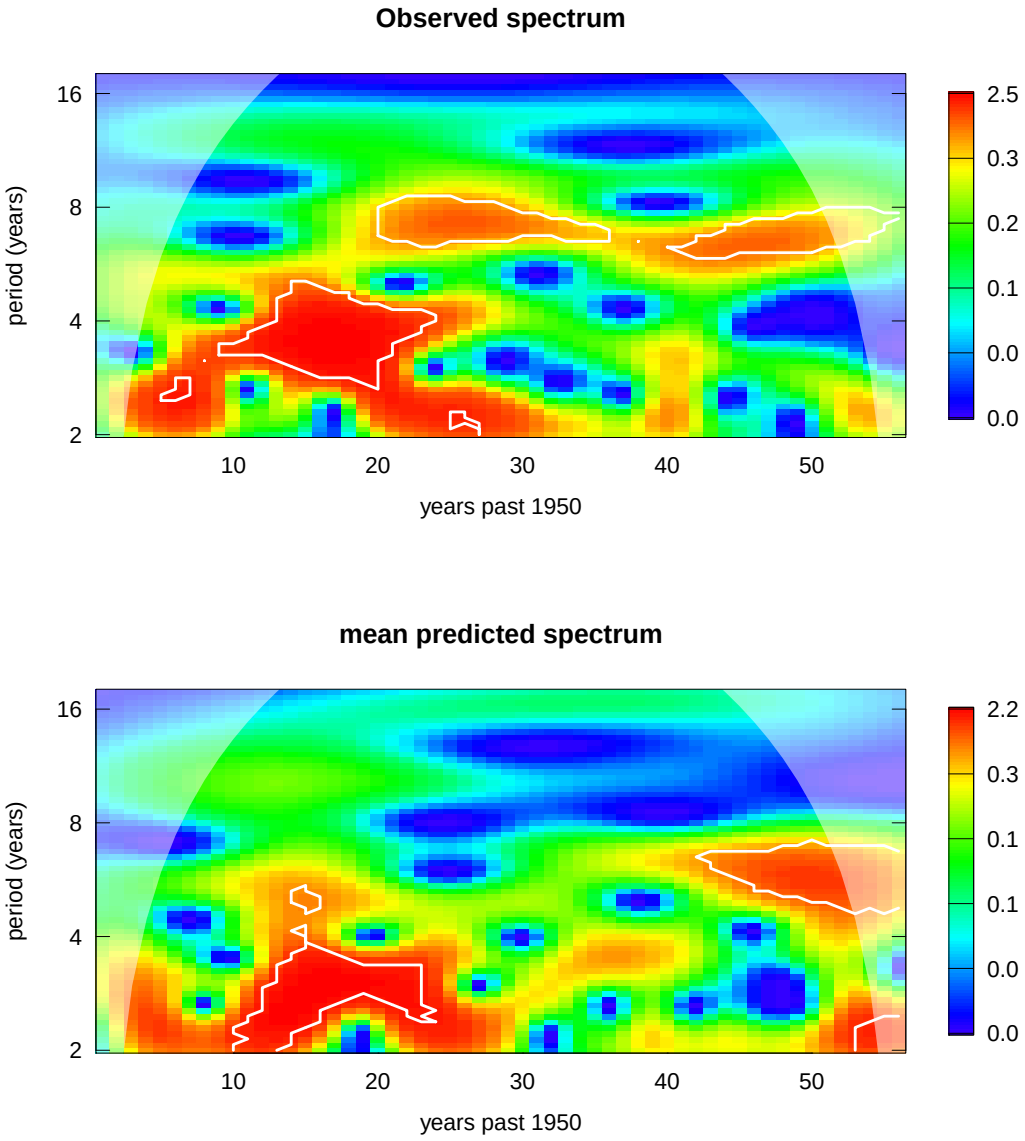

Figure 4.17: (Top) Wavelet power spectrum for the observed # of REP events by year. Color indicates power and regions inside of the white borders are significant at the 90% level as determined by shuffling the given time-series (i.e. bootstrapping). (Bottom) Same as (Top) but for the mean model predicted # REP by year.

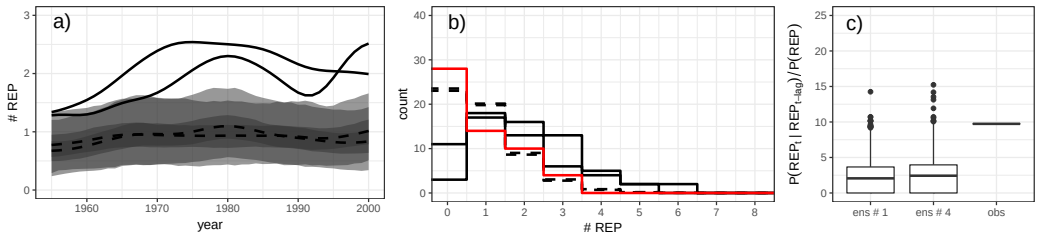

Figure 4.18: Comparison of REP day representation in observation and GCM simulation. (a) The number of MAM REP days by year based on the two GFDL CM3 ensemble member's precipitation fields (black solid lines), the mean of the simulated REP counts obtained via the regression on the indices derived from the two GFDL CM3 ensemble member's Z_{700}, Q_{700}, and ω_{700} fields (black dashed lines), and the 50th and 95th percentile prediction intervals based on the 1000 simulations (dark and light shaded regions, respectively). All data has been Gaussian kernel smoothed (bandwidth = 10 years) before the mean and prediction intervals are computed. The first and last 5 years of the smooths have been truncated from the figure to avoid edge effects. (b) The counts for the number of MAM REP days by year for the observed record (solid red line), the record derived from the GFDL GCM CM3 precipitation fields (solid black lines), and the mean of the simulations for each ensemble member (dashed black lines). (c) Probability of a MAM REP day on a day given that a REP day occurred the day prior divided by the marginal probability of a REP day for the observed record and the REP simulated records for the two ensemble members and the observed record. The boxplot whiskers extend to points within 1.5 times the interquartile range above the 75th percentile, and any observation outside of this range is shown as a point.

past frequency bias in the GCM REP record is multiplicative and representative of GCM REP frequency bias in the future. Our simulation model projects a significant increasing trend throughout much of the 21st century similar to that projected by the GCM precipitation fields, although the index-based projections show lower absolute REP frequency. The rescaled GCM precipitation field derived projection (blue line in fig. 4.19), i.e. the bias corrected GCM REP projection, deviates substantially from the mean index simulation projections in the late period of the 21st century. However, the rescaled projections do lie within the 95th percentile prediction interval of the simulation model projections. The observation that a positive, albeit weaker trend exists even after our conditional simulation provides some evidence that an increasing trend may occur. However, we emphasize restraint in this interpretation, since both approaches assume the RCP 8.5 forcing scenario and that the large-scale circulation patterns in the future are well-represented by the CM3 model physics.

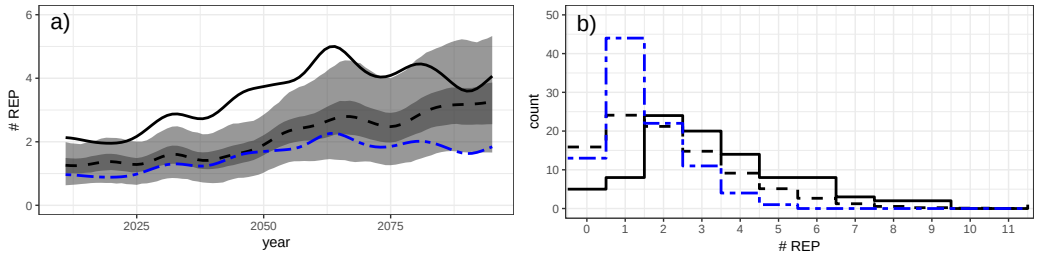

Figure 4.19: Projected number of MAM REP days using raw GCM output, a naive bias correction, and the Bayesian logistic regression model. (a) The projected number of MAM REP days by year based on the GFDL CM3 RCP 8.5 ensemble member precipitation field (black solid line), the mean of the simulated REP counts obtained via the regression on the GCM-based indices (black dashed lines), and the 50th and 95th percentile prediction intervals based on the 1000 simulations (dark and light shaded regions, respectively). The blue dashed line is the projected MAM REP record when we assume that the historical bias between the GCM and observed REP frequency is multiplicative and stationary and we rescale the projection based on the GCM precipitation field. In this case, this amounts to dividing the solid black line by about 2.2. All data has been Gaussian kernel smoothed (bandwidth = 10 years) before the mean and prediction intervals are computed. The first and last 5 years of the smooths have been truncated from the figure to avoid edge effects. (b) The counts for the number of MAM REP days by year with corresponding line colors and types as in (a).

4.7.3 Moisture Trend Contribution

It is notable that the increase in REP frequency estimated by our conditional sampling model is driven by a positive shift in the probability distribution of the as well as the other indices. To explore the relative contribution of the moisture changes (HUM) vs. changes in the other indices, we performed additional simulations using the last 30 years of GCM output from each of the twentieth and twentieth first centuries (1970-1999 and 2070-2099). We first compute the mean change in all GCM-derived indices between these two time periods (using the GCM ensemble mean for the historic period). We find that the mean MAM HUM increases by about 0.6 (i.e. about half a standard deviation). Then we use the regression estimates from the full observed historical record, but simulate REPs using three sets of predictors: 1) using the GCM indices for the 2070-2099 time period; 2) removing the trend in the HUM index by subtracting 0.6 from all HUM index values from 2070-2099 and then simulating the REPs for the 2070-2099 time period; 3) using the GCM indices for the 1970-1999 time period. We retain 1000 simulations for each of these scenarios and plot the resulting REP incidence in fig. 4.20. The median increase in the GCM simulations using our procedure from 1970-1999 to 2070-2099 is

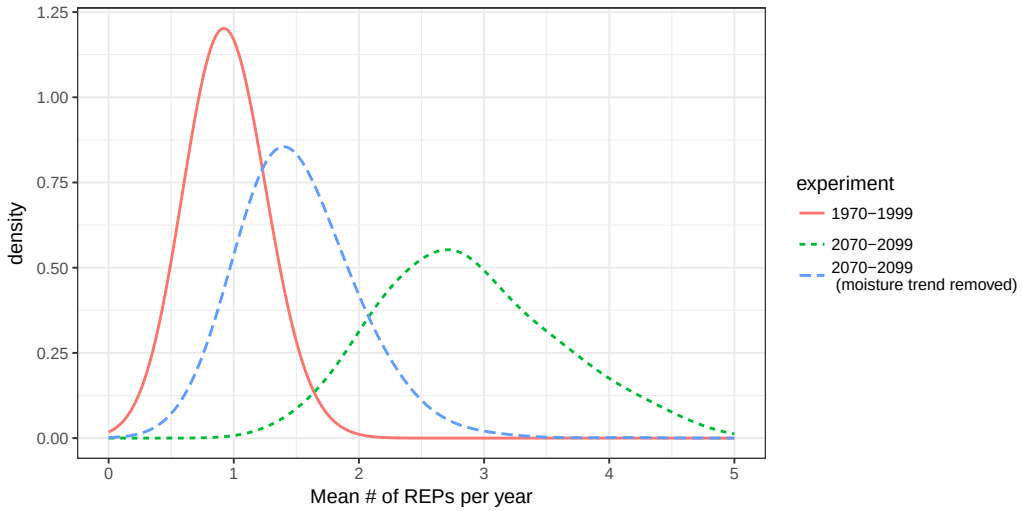

Figure 4.20: Kernel density smoothed PDFs showing the mean number of simulated MAM REP days over the 30 year periods of 1970-1999 (red line) and 2070-2099 (short-dashed green line) and 2070-2099 after the trend in the HUM index has been removed (long-dashed blue line). Each curve is composed from 1000 points that represent the mean # of REPs per year in a 30 year simulation.

about 200 percent when all index trends are included. It is only 60 percent when the trends in the HUM are removed. These results suggest that, given our model, about two-thirds of the future increase in MAM REPs is due to a humidity increase.

4.8 Summary and Discussion

4.8.1 Summary

Precipitation is the primary climate input into the modeling of extreme riverine floods. Consequently, hydrologists need to consider how to best use future predictions of regional climate in GCMs, given that many factors contribute to the well-documented biases in GCM based precipitation simulation. We were interested in an approach that provided a diagnostic of the physical factors associated with such biases. Next we were interested whether these factors could be used to achieve a better representation of the causal factors associated with extreme precipitation, and especially with regional extreme precipitation in a large river basin (the Ohio as the example), such that future GCM simulations could be used to statistically assess potential changes.

We began by defining a regional extreme precipitation index, illustrating its relationship to extreme streamflows in the study region, and investigating the dominant atmospheric circulation patterns associated with the precipitation events. Next we showed that the frequency and persistence properties of this regional extreme precipitation index are not well simulated by a GCM, but that the large scale atmospheric circulation indices (defined by large scale geopotential height, moisture, and vertical velocity fields) that are strongly associated with the extreme precipitation are credibly simulated by the same GCM. Then we constructed a logistic regression model to simulate the regional extreme precipitation index at the daily scale based on five atmospheric indices. This simulation framework greatly reduced the frequency bias in the observational record of the GCM REP days. Using this model for future projections we found that future GCM simulations likely overestimate the total number of regional extreme precipitation events out to the year 2100. However, an increasing trend in REP occurrence in the 21st century, attributed to trends in both the moisture index and other circulation indices, is still evident in our simulations. We acknowledge that our approach still relies on the assumptions that the relationship between the large-scale climate indices and the REP occurrence is stationary into the future and that our regression is valid over the ranges of the indices in the future GCM runs.

4.8.2 Relationship to Bias Correction and Downscaling Approaches

Like many bias correction and downscaling techniques, we assume that the GCM is deficient in its simulation of processes that link the global-synoptic scale circulations and the grid-scale processes that determine precipitation over a specific river basin which may represent just a few grid cells of the GCM. We developed our approach with the following common limitations of bias correction and downscaling approaches in mind. Using most bias-correction techniques (e.g. *Gutmann et al.*, 2014; *Piani et al.*, 2010; *Yang et al.*, 2005; *Friederichs and Hense*, 2007; *Goly et al.*, 2014; *Pierce et al.*, 2015) for extrapolation into the future projections is uncertain given that most approaches do not explicitly identify the underlying model deficiencies (*Ehret et al.*, 2012; *Dittes et al.*, 2018; *Bosshard et al.*, 2018). Many statistical downscaling schemes to recover precipitation estimates from large scale circulation features (e.g. (*Wilby*

et al., 2002)) have been proposed, including many tailored for use in future climate projection (see *Maraun et al.*, 2010, and references therein). However, it is often unclear how to adapt weather generator (e.g. (*Thorndahl et al.*, 2017)) and weather typing approaches (e.g. *Jacobeit et al.*, 2003; *Muñoz et al.*, 2015) in a non-stationary climate. Dynamical downscaling (e.g. *Schmidli et al.*, 2007)) is another option, but is computationally expensive (*Wilby et al.*, 2002), and is often sensitive to precipitation-related parameterizations and the size of the embedded domain used (*Liu et al.*, 2011; *Leduc and Laprise*, 2009). Regression downscaling (e.g *Wilby et al.*, 2002) is computationally cheap and is more able to deal with non-stationary conditions. However, the regressions often do not represent the extremes well and explain only a relatively small portion of the variance in the data (*Wilby et al.*, 2002). The latter point is particularly problematic if a goal of the downscaling is to estimate future precipitation conditions since it may be that the model sensitivity to future regional forcing is below the level of the noise (i.e. a signal in the precipitation may simply be an artifact of the model parameterization and estimation).

4.8.3 Caveats and Further Discussion

A shortcoming of our model is that it does not fully capture the serial correlation in the REP process, as represented by figs. 4.15 and 4.18. The negative persistence bias in the reconstruction of the observed-reanalysis record suggests that our model could be improved through the incorporation of other variables that inform the temporal clustering of the REP days. While the persistence bias can be partially mitigated by including lagged REP days as predictors, we chose not to include a lagged REP predictor because the predictor was not significant given the presence of the other predictors and the absence of a lagged REP predictor greatly reduces the computational cost of the simulation model.

As previously noted, our simulation method does not avoid a reliance on the assumption that circulation (and associated moisture) changes are well simulated into the future by the GCM. The frequency bias in the regional extreme precipitation record appears to be a manifestation of inflated spatial correlation of high intensity precipitation. The precipitation event persistence bias appears to be a manifestation of a strong and southerly displaced springtime

jet in the GCM that results in faster moving storms and lower autocorrelation in the humidity field over our study region. We were able to limit our simulation model's sensitivity to the southerly displacement bias by using standardized indices (i.e. a form of bias correction to translate the mean to be $\approx$0 and rescale the variance to be $\approx$1), but we did not fully address the persistence bias. Other approaches to handling biases in GCM circulation fields have been proposed when credible precipitation fields are the desired outcome; *Eden et al.* (2012) advocate for the approach of nudging GCM fields toward observed fields and then letting the GCM simulate the precipitation fields. Two deficiencies of this approach, however, are the reliance on the convective parameterization scheme of the GCM (which can be particularly problematic during summer), and an inability to project future precipitation events because there exists no future reanalysis field to nudge towards. Thus, it is difficult to avoid a reliance on GCM circulation fields when it comes to projecting regional scale precipitation events, and difficult to estimate the validity of the GCM under warming and other related and relevant changes such as changing mid-latitude meridional temperature gradients due to Arctic Amplification (*Barnes and Screen*, 2015). Finally, the simulation model presented in this paper has been shown to better predict the REP event frequency than do the GCM precipitation fields and is therefore plausibly useful for understanding the future trends in REP frequency. Having said that, the simulation model does not necessarily provide daily time sequences that are appropriate for impacts models given figs. 4.16 and 4.18.

Part II

Sequential Adaptation

The more you know, the harder it is to take decisive action. Once you are informed, you start seeing complexities and shades of gray. You realize nothing is as clear as it first appears. Ultimately, knowledge is paralyzing. Being a man of action, I cannot afford to take that risk.

Bill Watterson, The Authoritative Calvin and Hobbes

5

Review of Methods for Infrastructure Planning under Uncertainty

Whereas part I outlined a physical-dynamical approach to constraining future hydroclimate hazards, part II of this dissertation is concerned with using intrinsically uncertain projections to inform decisions and improve outcomes for local risk management and adaptation.

This chapter reviews approaches to planning and designing infrastructure systems under uncertainty. This is a field replete not only with competing methods but also deep philosophical disagreements. When should optimization be used when a system's objectives are unclear? How should probability be used to reason about uncertainties, including unknown unknowns? How can models inform decision-making for complex systems? What should decision-makers do when different models give different results? Who gets to decide the answers to these questions?

Though this chapter does not attempt to provide a definitive answer to these questions, it does seek to frame these debates and advocate a general perspective. First, section 5.1 reviews decision-theoretic approaches, focusing in particular on the uses and restrictions of rationality and optimization. Though rationality is found to be limited as a descriptive model of the world, it gives rise to useful notions of subjective probability and conditional optimization. Next, section 5.2 outlines approaches to decision-making for wicked problems under "true" uncertainty. In particular, widely sampling from possible outcomes, identifying fundamental tradeoffs, and representing path dependence can provide quantitative answers to qualitative questions. Finally, section 5.3 describes how engineering, policy, and financial instruments can support better outcomes. Since a decision framework is only as good as the decisions considered, "soft" instruments that improve the flexibility and performance of the system, evaluated using option theory and portfolio analysis, can lead to better outcomes.

5.1 Decision Theory

Decisions about climate adaptation, systems planning, and infrastructure operation draw upon theoretical frameworks for decision science developed in other fields, including economics, grand strategy, computer science, operations research, and business strategy. These theories emphasize that

1. the axioms of rationality and Bayesian decision theory provide a calculus for value and choice, conditional upon assessments of preference and belief (section 5.1.1);
2. many uncertainties that govern real-world planning problems cannot be described through a single objective probability distribution (section 5.1.2);
3. the design and management of infrastructure is intrinsically "wicked" because objectives cannot be clearly defined and conflict is intrinsic (section 5.1.3); and thus
4. the role of decision theory, and science more broadly, for wicked problems should be to transparently link assumptions, preferences, and outcomes (section 5.1.4).

5.1.1 Rationality, Decision Theory, and Optimization

The theory of rational decision making evolved in the middle of the 20th century in tandem with mathematical theories of probability and economics. In particular, *Von Neumann and Morgenstern* (1953) proposed four axioms for rational choice: (i) completeness of preference; (ii) transitivity of preference; (iii) continuity of preference, and (iv) independence of preference from the existence of irrelevant alternatives. *Von Neumann and Morgenstern* then proved that an individual or firm that follows these actions behaves as though maximizing the expectation of some function, which they called a utility function. Similarly, individuals and firms that do not follow these axioms can be systematically exploited (see the "Dutch book" arguments of *De Finetti*, 1972).

Over the next decades, the *descriptive* model of rationality used to study firms and individuals (see *Savage*, 1954; *Debreu*, 1959) became widely applied as a *normative* tool for planning. Efforts such as the Harvard Water Program (see *Maass et al.*, 1962) popularized the use of top-down rational planning approaches for water management (*Howe*, 1971) and other social planning problems. These methods used the vocabulary and mathematical framework of Bayesian decision theory (BDT) (*Gelman et al.*, 2014; *Savage*, 1954), bringing a formal mathematical treatment of these problems. Four elements define a formal decision problem in BDT:

- an action space $\mathcal{A}$ that describes all possible actions $a \in \mathcal{A}$ available to the decision-maker which, depending upon the problem at hand, may be continuous, discrete, multivariate, etc.;
- a state space $\mathcal{S}$, of potentially many dimensions, which specifies all the information available to the decision-maker;
- a reward function (alternatively called a utility function or objective and its negative as loss or cost function) $R : \mathcal{S} \times \mathcal{A} \to \mathbb{R}$ that maps information about the state of the world and a particular action taken to a real number; and
- a representation of uncertainty $p(s)$ that describes the probability that a given state of the world $s \in \mathcal{S}$ occurs.

These four elements can be combined to calculate the expected reward of taking a particular

action:

$$\mathbb{E}[R \mid a] = \int_{\mathcal{S}} R(a, s) p(s) \, \mathrm{d}s \,, \tag{5.1}$$

allowing the decision maker to select the best action

$$a^* \doteq \arg\max_{a \in \mathcal{A}} \mathbb{E}[R \mid a] \,. \tag{5.2}$$

In the case where the reward function is a discounted cash flow, eq. (5.1) is equivalent to classical cost-benefit analysis (CBA) or net present value (NPV) analysis using discounted cash flows. A key insight from eq. (5.1) is that

$$\mathbb{E}[R \mid a] \neq R(\mathbb{E}[s] \,, a), \tag{5.3}$$

meaning uncertainties must be fully described (see *Gelman et al.*, 2014, ch. 9, for simple examples in which these expectations diverge). For example, *Oddo et al.* (2017) revisit the point estimates used by *van Dantzig* (1956) to optimize levee heightening in the Netherlands and that show that considering uncertainties leads to substantially different decisions (this case study is revisited in chapter 7).

Many problems in infrastructure planning and management are sequential, meaning that (i) the goal is to solve for a policy $\pi : \mathcal{S} \to \mathcal{A}$ that maximizes expected future reward, and (ii) each action affects the decisions and rewards available in the future. For example, reservoir management, capacity expansion, and water quality control are all examples of sequential planning (see section 5.2.2 for further discussion). The extension of BDT to sequential decision problems is reinforcement learning (RL) (see *Sutton and Barto*, 2018, for a comprehensive review), in which the goal is to identify the action $a \in \mathcal{A}$ that maximizes, in expectation, the quantity

$$G_t = \gamma R_{t+1} + \gamma^2 R_{t+2} + \ldots \tag{5.4}$$

where $\gamma \in (0, 1)$ is a discount factor which is assumed constant (though it could depend on time or other factors; see *Arrow et al.*, 2013). A popular and widely used class of RL algorithms is dynamic programming (DP) (*Bellman*, 1954, 1957) and its extensions (*Bertsekas*, 1976; *Ste-*

dinger et al., 1984; *Faber and Stedinger*, 2001; *Lamontagne*, 2015). Another class of algorithms approximates the Q-function

$$\begin{aligned} q_\pi(s,a) &\doteq \mathbb{E}_\pi[G_t \mid S_t = s, A_t = a] \\ &= \mathbb{E}_\pi\left[\sum_{k=0}^{\infty} R_{t+k+1} \,\middle|\, S_t = s, A_t = a\right] \quad \forall s \in \mathcal{S}, a \in \mathcal{A}, \end{aligned} \tag{5.5}$$

which gives the expected discounted future rewards, conditional on being in state s, taking action a, and following an optimal strategy thereafter. Q learning, often using neural networks for function approximation (i.e., "deep Q learning"), has surpassed human performance in benchmarks including Atari video games (*Mnih et al.*, 2013, 2015; *Wang et al.*, 2016; *van Hasselt et al.*, 2015; *Schaul et al.*, 2015; *Fortunato et al.*, 2019; *Hessel et al.*, 2017). However, application to problems with complex action spaces or sparse rewards remains a challenge (*Doss-Gollin et al.*, 2019a). An alternative is to instead model the policy $\pi : \mathcal{S} \to \mathcal{A}$ as a function of parameters $\boldsymbol{\theta} \in \mathbb{R}^d$, and to search for approximately optimal $\boldsymbol{\theta}$ (*Schmidhuber*, 2001). This approach exploits theoretical properties such as the policy gradient theorem (*Sutton et al.*, 2000), and has been used in models like AlphaGo, which famously surpassed human performance at the game of Go (*Silver et al.*, 2017, 2018). Policy search methods are also used widely for multiobjective optimization (see section 5.2.3).

5.1.2 Epistemic Uncertainty and Subjective Probability

To implement an optimization procedure or calculate expected reward following eq. (5.1), one must first specify a probabilistic model for the probability of each state (or, in the case of sequential problems, for the evolution of states over time).

Projections of the relationship between decision and outcome depend upon complex dynamics, including human actions, that are intrinsically unpredictable, particularly in the distant future. In general, uncertainties can be grouped into four classes, describing those that are (i) purely stochastic with known parameters; (ii) stochastic with known model structure but unknown parameters; (iii) imaginable, with unknown model structure but a well characterized event space; and (iv) truly uncertain, in the sense that the events cannot even be imagined (*Walker et al.*, 2013b, fig. 1 divides these into five categories). The uncertainties

from categories (iii) and (iv) have been described as "deep uncertainty" (*Walker et al.*, 2013b,a; *Lempert*, 2002), "true uncertainty" (as opposed to categories (i) and (ii), termed "risk"; *Langlois and Cosgel*, 1993; *Knight*, 1921) and "black swans" (to refer specifically to events that cannot be proven impossible; *Taleb*, 2007). Uncertainties have also been characterized as epistemic if the modeler sees a possibility to reduce them by gathering more data or by refining models and aleatory otherwise.

There are many sources of deep and true uncertainty in projections of flood risk and its response to intervention. If risk is crudely defined as the product of hazard, meaning the probability that a particular event occurs (as discussed in chapter 2), and exposure, meaning the damage that will occur should the hazard arrive, total uncertainty stems from both (note that this definition of risk is unrelated to that of *Knight*, 1921).

Many of the physical dynamics discussed in part I lead large and deep uncertainties as to future hazard. Climate sensitivity, arctic amplification (AA) and the storm track response, and the response of clouds to warming illustrate the large uncertainties intrinsic to future climate. Hydroclimate extremes are also sensitive to anthropogenic climate change (ACC), and since future greenhouse gas emissions depend on political, economic, and technological factors, future hydroclimate extremes are themselves sensitive to these deep uncertainties. Humans also modify local environmental conditions in ways that affect hydroclimate hazard but are not readily quantifiable. For example, channelizing upstream portions of a river can reduce flood hazard upstream but increase it downstream (*Juan et al.*, 2020); these dynamics are therefore as much political and social as physical. Similarly, local land use change, including deforestation (*Lawrence and Vandecar*, 2015) and mangrove removal (*Hochard et al.*, 2019), can depend on deeply uncertain human actions, and the effect of these changes on hydroclimate hazard is often highly nonlinear.

Historical data also highlights the central role of exposure to total risk. For example, global exposure to river floods has grown exponentially since 1970, far outpacing increases in hazard (*Jongman et al.*, 2012). *Tedesco et al.* (2020) find that damage caused by Hurricane Florence was exacerbated by an increase in exposed property – from 10 to 52 billion dollars between 2000 and 2018 – and that while construction has slowed over the past decade, it has

nearly all occurred in low-lying and otherwise vulnerable areas. More generally, *Pielke et al.* (2008) attribute trends in loss to hurricanes over the past century in the United States (US) to changes in exposure, consistent with global analyses (*Peduzzi et al.*, 2012). This does not only lead to increased loss of property; *Di Baldassarre et al.* (2010) argue that increased exposure in vulnerable areas has increased flood mortality in sub-Saharan Africa. Economic risks can also cascade in non-intuitive ways through increasingly global supply chains (*Helbing*, 2013); both conceptual (*Inoue and Todo*, 2019) and observational (e.g. of Thailand's 2011 flood; *Haraguchi and Lall*, 2015) evidence suggests that supply chain interruptions can substantially exceed direct damage. A corollary to this point is that interventions to manage hydroclimate risk can have unintended consequences. For example, high traffic often motivates communities to widen and expand highways, but this can have the effect of decreasing the marginal cost of driving, thereby encouraging people to move their homes and workplaces farther apart and worsening traffic (*Lee et al.*, 1999). Similarly, the "safe development paradox" (*Haer et al.*, 2020) and "levee effect" (*Tobin*, 1995) describe the process by which structural flood protection can reduce minor floods and perceived risks, induce a sense of safety, motivate increased exposure, and thereby lead to greater losses when a large flood eventually occurs (*Barendrecht et al.*, 2017; *Merz et al.*, 2014; *Di Baldassarre et al.*, 2018a; *Aerts et al.*, 2018; *Kousky and Kunreuther*, 2010). Through a similar logic, measures to increase water supply can lead to higher water demand and thus greater vulnerability to droughts when they eventually occur (*Di Baldassarre et al.*, 2018b; *Srinivasan et al.*, 2017).

The observation that many of these mechanisms cannot be represented by a single objective probability density function (PDF) has motivated many criticisms of the application of BDT to planning problems. For example, *Shackle* (1972) argued probability to be an inappropriate calculus for true uncertainty, chiefly because the event space is model-dependent, and proposed an alternative calculus of surprise (see also *Derbyshire*, 2017). Yet while the lack of objective probabilities may merit alternative decision methodologies in practice, this theoretical argument is something of a straw man. In fact, BDT was conceived as a calculus for reasoning rather than for identifying objective truth; *De Finetti* often said that "probability does not exist" (*De Finetti*, 1972). *Savage* (1954) and *Ramsey* (2016), among others, also

viewed probability as "subjective," representing the state of belief of the decision-maker. The famous phrase "all models are wrong, but some are useful" (generally attributed to *Box*, 1976) also suggests that probability distributions and predictions ought to be viewed subjectively. More recent discussions of Bayesian philosophy (*Jaynes*, 2003; *McElreath*, 2016; *Gelman et al.*, 2014; *Bernardo*, 1994) also emphasize a philosophical view of probability as a language with which to reason about the unknown rather than a statement of objective truth (see *Gelman and Shalizi*, 2013, for a thorough discussion of Bayesian philosophy). As with decision theory, the true model is not known and inference should not be represented as objective.

That the theory of decisions and statistics were developed under the view of probability as a subjective assessment does negate the practical concerns raised by *Knight*, *Taleb*, *Shackle*, and others; techniques for planning under type (iii) and (iv) uncertainties are revisited in sections 5.2 and 5.3

5.1.3 Planning Problems are Wicked

A critical assumption of BDT, optimization, and RL is that the reward function is known *a priori*. However, specifying an objective for social planning problems is an intrinsically difficult task.

One approach to specifying an objective function comes from welfare economics and social choice theory, which are concerned with the aggregation of preferences (i.e., utility functions) across an economy (see *Arrow*, 1951; *Hindriks*, 2006). In theory, this may be done through a Cardinal welfare approach, assuming that individual welfare functions can be put on a common scale and aggregated so that the social welfare of a particular state is equal to some function (mean, minimum, etc.) of the individual welfares. However, this approach faces not only practical considerations (eliciting and scaling the utility functions of all individuals would require colossal effort) but also theoretical ones. For example, real-world decision-makers systematically violate the axioms of rational decision theory (see in particular *Ellsberg*, 1961; *Kahneman and Tversky*, 1979; *Machina*, 1987, 2014). More fundamentally, *Arrow* (1951, 1963) proved the impossibility of deterministic preferential voting mechanism that meets reasonable criteria for fairness and efficiency. This finding can be loosely inter-

preted as demonstrating that it is not only practically infeasible but also theoretically impossible to identify an objective social welfare function.

Another challenge to rational decision making in the domain of public planning is intrinsic conflict. *Barry* (1997) describes "levee patrols" of armed vigilantes who during the 1927 Mississippi River flood protected levee sections against saboteurs from the opposite riverbank. While the field of game theory (*Debreu*, 1959; *Von Neumann and Morgenstern*, 1953; *Nash*, 1951, 1950) provides a framework for descriptive understanding of the responses of different actors to planning decisions, it does not seek to provide a normative definition of the "best" policy, except where there is a role for an external facilitator to enforce "win-win" outcomes (see *Madani*, 2010, for examples including groundwater management as a prisoner's dilemma game).

In light of these challenges, *Rittel and Webber* (1973) argue that most problems in planning are "wicked," meaning that (i) the solution is sensitive to the problem definition and the problem definition to the solution; (ii) stakeholders have radically different world views and different frames for understanding the problem; (iii) the constraints to which that the problem is subject and the resources needed to solve it change over time; and (iv) the problem is never solved definitively. In particular, *Rittel and Webber* argue that the appealing notion of objective technocratic problem-solving is a myth, that there is not and cannot exist a true objective function, and that the expert is inevitably a player in a political game. This argument is bolstered by findings that *ex ante* analyses of infrastructure projects are systematically biased towards under-estimation of costs and over-estimation of benefits, reflecting that they are political documents rather than sincere attempts at objective truth (*Flyvbjerg et al.*, 2005; *Flyvbjerg*, 2009).

While many of the conflicts described by wicked problems are apparent during the planning process, intrinsic conflict across time is not. Inter-temporal choice is generally treated by discounting the future at a constant rate. A conceptual challenge is that discount rates are used both to represent opportunity cost (which is why they are often higher in developing nations than developed ones) and to represent the preference between the value of consumption today and consumption in the future (which, if it is assumed to be richer than the present,

can be discounted on grounds of decreasing marginal returns to money or other goods) (*Espinoza et al.*, 2019; *Arrow et al.*, 2013). For example, in the US the executive branch budgetary process assesses United States Army Corps of Engineers (USACE) projects at a discount rate of 7% on most projects, conceptually reflecting the opportunity cost of capital in the private sector, though many have argued for different approaches (*Carter and Nesbitt*, 2016). In general, planning decisions are quite sensitive to the choice of discount rate (*Weitzman*, 2007) and change when a distribution of discount rates are assumed relative to a single rate (*Zarekarizi et al.*, 2020). Estimating discount rates from past behavior is complicated because, among other reasons, many of the costs passed on to the future are opaque to the decision-makers who choose to pass them on (e.g., infrastructure maintenance costs; *Marohn*, 2019).

5.1.4 The Role of Decision Theory

The central message of this section is that while rationality is a helpful construct which gives rise to powerful optimization tools, there cannot exist an objective assessment of belief or preference. This is not to say that all beliefs are equally valid – some are more or less consistent with science and evidence than others – but rather that disagreement is inevitable. Given that planning problems, including flood risk management policies, confront deep uncertainties and are intrinsically wicked, a philosophical perspective on the role of science and decision theory is helpful.

Gilboa et al. (2018) suggest that decision theory should form the framework for a conversation between modelers and stakeholders. In this framework, the implications of different preferences and assumptions should be mapped clearly onto the likelihood of different outcomes. This approach is consistent with the *a posteriori* approach proposed by *Tsoukiàs* (2008), though it emphasizes an iterative process. One particular pitfall in stakeholder engagement for planning in wicked problems like flood risk management is that different stakeholders may have different preferences, and the preferences of the stakeholders "in the room" (often representing engineers, local government, utilities, and civic organizations) may not reflect the preferences of those not in the room. Thus, the scientist should provide a reproducible map from assumptions and preferences to outcomes so that others can explore the effect of

different preferences, assumptions, and beliefs.

5.2 Decision Frameworks for Planning under True Uncertainty

A variety of decision frameworks are used for problems in wicked systems under deep or true uncertainty. Despite important differences, these frameworks generally share

1. the use of system models to explore response to a wide range of plausible scenarios (section 5.2.1);
2. the formulation of adaptive and sequential plans to exploit new information as it emerges over time (section 5.2.2); and
3. an explicit quantification of tradeoffs between conflicting goals and outcomes (section 5.2.3).

5.2.1 Bottom-Up and Exploratory Modeling

A common approach across frameworks for planning under uncertainty is to invert standard "predict then plan" approaches in favor of "bottom-up" perspectives that use a system model to explore its response to a broad range of plausible scenarios *before* assessing how likely these scenarios are.

For example, *Bankes* (1993) distinguishes between consolidative modeling, which seeks to integrate all information about a particular system into a single model, and exploratory modeling, which is used to understand possible behavior. In particular, exploratory modeling can demonstrate the existence of particular outcomes, generate hypotheses, build qualitative insight, and identify scenarios worthy of further study. An explicit recognition that a modeling exercise is exploratory can help to limit the likelihood of over-interpreting mathematical models and drawing misleading conclusions (*Saltelli*, 2019). Frameworks for exploratory modeling (e.g., *Kwakkel and Pruyt*, 2013) are widely used in a variety of strategic planning fields.

The philosophical underpinnings of exploratory modeling are also evident in a variety of widely used frameworks for infrastructure systems planning under uncertainty. For example, decision scaling explores a system's "response surface" to forcing such as mean precipitation

and temperature (*Brown et al.*, 2012; *Steinschneider et al.*, 2015; *Poff et al.*, 2015). Once a system's essential fragilities have been identified, their likelihood is assessed using projections from a wide set of models. Derivative approaches, including the World Bank's decision tree framework (*Ray et al.*, 2018) and the resilience by design approach (*Brown et al.*, 2020), also emphasize bottom-up modeling or vulnerability assessment and consideration of a wide range of plausible scenarios.

Another framework for bottom-up analysis with wide application to infrastructure planning is robust decision making (RDM) (*Lempert et al.*, 2003). Like decision scaling, RDM uses an iterative process to identify potential strategies, characterize the vulnerabilities of such strategies, and evaluate the tradeoffs among them. For example, *Lempert et al.* (2012) run hundreds of CBAs for different plausible values of parameters, conduct scenario discovery through cluster analysis, and finally compare the groups of scenarios that lead to particularly good or poor outcomes with values from the scientific literature to assess how likely they are. Like exploratory modeling and decision scaling, RDM emphasizes an iterative process of engagement with stakeholders rather than a single prescriptive or normative solution; this process can lead to recognition of opportunities for collaboration rather than competition between stakeholders (e.g., between adjacent water uitilities; *Zeff et al.*, 2016; *Gorelick et al.*, 2019; *Herman et al.*, 2014; *Trindade et al.*, 2017, 2019).

5.2.2 Policies and Decision Pathways

Since infrastructure planning is a dynamic process, many decision support tools explicitly recognize the role of time.

For example, dynamic adaptive policy pathways (DAPP) is a qualitative framework (often implemented with quantitative modeling) emphasizing (i) that adaptation and investment decisions are sequential by nature, and (ii) that infrastructure and urban systems embody strong path dependence (*Haasnoot et al.*, 2012, 2013). Like RDM and decision scaling, DAPP emphasizes exploratory modeling and iterative stakeholder engagement (*Kwakkel et al.*, 2016, 2015), but DAPP particularly emphasizes the formulation of (i) candidate development pathways (*Wise et al.*, 2014) along which the system might develop, (ii) triggers or tipping points that

specify when particular actions will be taken, and (iii) signposts that allow proactive monitoring of key system variables (*Haasnoot et al.*, 2015; *Raso et al.*, 2019; *Lawrence and Haasnoot*, 2017). The methodology was originally developed for projects on the Thames Estuary and Dutch Delta, but has been applied to problems in water resources, regional planning, coastal planning, and heat risk management (see *Bloemen et al.*, 2018).

Alternatively, an optimization framework can solve sequential decision problems (see section 5.1.1). Since optimization models require a probabilistic representation of uncertainty, these often proceed by specifying a finite set of scenarios of deeper uncertainties, then developing scenario-dependent optimal policies (*Bertoni et al.*, 2017; *Kang and Lansey*, 2014). Often the probabilistic weighting of scenarios is implicitly a uniform distribution over an arbitrary set of scenarios considered (*Herman et al.*, 2020).

Like DAPP, sequential optimization and RL aim to exploit information as it emerges over time. For example, *Fletcher et al.* (2017) formulate the question of water system capacity expansion in Melbourne, Australia as a multistage decision and solve it using DP. Given an initial model for the evolution of reservoir inflows and population growth over time, the DP formulation enables learning. The analysis is repeated for several scenarios of electricity price, water shortage penalties, and demand per capita which are considered deeply uncertain. Similar approaches can inform reservoir planning (*Fletcher et al.*, 2019a), groundwater management (*Fletcher et al.*, 2019b), and coastal hurricane protection (*Lickley et al.*, 2014). Another DP model for coastal adaptation is discussed in chapter 7.

5.2.3 Tradeoff Quantification

In wicked problems for which no objective utility function can be formulated (section 5.1.3), it is common to use tradeoff analysis to compare how different actions or policies might affect a set of performance metrics chosen by a set of stakeholders. While these analyses do not yield a single optimal decision, they can narrow the set of decisions considered to a non-dominated, or Pareto-optimal, subset, meaning the set of decisions for which there is no way to improve one metric without making another worse. One approach to tradeoff analysis is multiobjective optimization, which searches directly for a non-dominated set of decisions. While

multiobjective methods have been used since the 1970s (*Geoffrion et al.*, 1972; *Benayoun et al.*, 1971) they introduce substantial computational cost and require sophisticated algorithms for non-trivial problems (*Reed et al.*, 2013; *Hadka and Reed*, 2012).

Multiobjective optimization is widely used for decision making under uncertainty, for example through the multiobjective robust decision-making (MORDM) framework which considers multiple objectives and a particular definition of robustness. First, a best estimate scenario is developed and an approximately pareto-optimal set of policies is generated for that scenario. Second, a large ensemble of alternative scenarios is generated and the performance of each policy is evaluated across these alternatives to ascertain robustness (*Kasprzyk et al.*, 2013, 2012; *Hadka et al.*, 2015). Different metrics of robustness are widely used and capture different metrics about the system's performance (*Herman et al.*, 2015; *McPhail et al.*, 2019) though measuring robustness over a set of scenarios requires weighting each scenario (often implicitly by a uniform distribution; *Herman et al.*, 2020).

In the sequential case, (section 5.2.2), dynamic policy search (DPS) is used to find a policy $\pi(a|s, \boldsymbol{\theta})$ (see section 5.1.1) that stochastically or deterministically maps a state s to an action a and is solved by identifying the set of $\boldsymbol{\theta}$ that lead to non-dominated policies (*Giuliani et al.*, 2016). RDM, MORDM, and DPS have been widely used in practice, including to inform long-term water resources planning in Lima (*Kalra et al.*, 2015), to identify cost-effective pathways for water system capacity expansion (*Trindade et al.*, 2019), to manage crop yield (*Yoon et al.*, 2019), and to identify a set of climate change mitigation strategies that perform well over a wide range of socioeconomic scenarios (*Lamontagne et al.*, 2019). Many other frameworks, including decision scaling (*Steinschneider et al.*, 2015), also incorporate multiobjective optimization or assessment.

Beyond assessing tradeoffs at the aggregate level, many frameworks also seek to quantify the sensitivity of different performance metrics to assumptions, parameters, and particular scenarios. For example, global sensitivity analysis (*Saltelli et al.*, 2010; *Herman and Usher*, 2017; *Sobol*, 2001), causality analysis (*Kumar and Gupta*, 2020; *Perdigão et al.*, 2020; *Weijs and Ruddell*, 2020; *Goodwell et al.*, 2020), clustering analysis, and induction rules (*Friedman and Fisher*, 1999) are used to identify scenarios or assumptions for which relevant system metrics

are particularly high or low.

5.3 Instrument Design for Resilient Systems

In conjunction with developing more transparent and effective tools for decision under uncertainty, science can help develop new instruments so that better options are available to decision-makers. Improving the quality and reducing the cost of these options can lead to better outcomes regardless of the formal decision framework used. In particular,

1. flexibility and optionality allow systems to manage changing conditions and generally increase robustness (section 5.3.1);
2. limiting exposure to hazards greatly reduces losses (section 5.3.2); and
3. financial instruments, in coordination with other policy tools, can support proactive risk management strategies (section 5.3.3)

5.3.1 Flexibility and Optionality

Rather than trying to design a static system which performs well over all plausible future states of the world, it is often preferable to design flexible and adaptive systems that adapt to new conditions and broaden the set of scenarios over which a system is able to perform well (*Gupta and Rosenhead*, 1968).

The value of flexibility is often quantified through real options analysis (ROA), which values the option, but not requirement, to take a particular action *Mun* (2006). ROA, sometimes called engineering options analysis to emphasize options that are incorporated into engineering design rather than financial contracts (*de Neufville et al.*, 2019; *de Neufville and Smet*, 2019), has been used in water system capacity expansion (*Erfani et al.*, 2018; *Fletcher et al.*, 2017, 2019b,a), coastal adaptation (*Prime et al.*, 2018; *Kim et al.*, 2018), flood risk management (*Hino and Hall*, 2017), and beyond to evaluate under what assumptions an early investment in flexibility pays off. In a didactic example, *de Neufville et al.* (2006) show that building a 5-story garage but paying extra to strengthen the foundations so that two additional levels can be added should the need arise is, under some assumptions about the future, preferable to building a 5-story (cheaper but no option value) or 7-story (more expensive up front) struc-

ture. ROA describes an approach rather than a particular solution methodology and the use of inappropriate solution methods will give poor results (*Schachter and Mancarella*, 2016; *Kind et al.*, 2018)

New technologies can also facilitate adaptive design. For example, decentralized and distributed infrastructure, including decentralized treatment and re-use (*Shannon et al.*, 2008; *Massoud et al.*, 2009; *Daigger et al.*, 2019; *Lackey Katy et al.*, 2020; *Biggs et al.*, 2010), rainwater harvesting (*Doss-Gollin et al.*, 2015; *Ennenbach et al.*, 2018; *Concha Larrauri et al.*, 2020; *World Bank*, 2018), and distributed solar electricity generation (*Hagerman et al.*, 2016; *Burger et al.*, 2019) can reduce the need for costly infrastructure expansion while improving resilience to physical hazards (*Talebiyan and Dueñas-Osorio*, 2020; *Paredes et al.*, 2019; *González et al.*, 2016). Further, distributed systems may be able to scale up and down to meet changing demand for infrastructure services (*Liu et al.*, 2020), unlike large static systems which often substitute size for scale and cannot scale down (*Ansar et al.*, 2017); this can be viewed as an option to scale down a system and reduce maintenance costs. This point is also discussed in section 9.3.

Although adaptive design is often assessed using multiple metrics, flexibility is a life-cycle system property of an engineering system that can be useful in achieving performance goals, not a performance metric itself, and should not be added as an objective to an optimization formulation (*Fletcher*, 2018; *Weck et al.*, 2011).

5.3.2 Exposure Reduction

Another broadly effective strategy for managing hydroclimate risks is to relentlessly lower exposure to extreme events.

As discussed in section 5.1.2, changes in exposure have outpaced changes in hazard for many risks including coastal and river flooding over the past several decades (see also *Jongman et al.*, 2012; *Pielke et al.*, 2008; *Tedesco et al.*, 2020). This effect has been described as an "expanding bullseye" to emphasize that increasing exposure dramatically expands the set of hazards that can cause significant damage (*Ashley et al.*, 2013). Limiting the growth of exposure is therefore a first-order lever for controlling future risk, regardless of projected future hazard, and, at the household and community level, requires new policies around land use,

transportation, and insurance. For the specific case of river floods, construction in low-lying areas and along riverbanks of wetlands and has not only increased exposure, but also altered hydrological dynamics to increase peak floods. This implies that reversing these trends through "green" infrastructure may lessen or reverse the impacts of land use change (*Jacob et al.*, 2014; *Brody et al.*, 2014), improve water quality and reliability (*Tellman et al.*, 2018; *Schmadel et al.*, 2019) and reduce both riverine and coastal flooding (*Gutman*, 2019; *Guannel et al.*, 2016; *Menéndez et al.*, 2020), though green and gray infrastructure often work best in tandem (*Du et al.*, 2020).

Exposure reduction is also a helpful paradigm for institutions with assets and supply chain spanning many locations. The spatial correlation of risk across locations (e.g., at a portfolio of assets owned by a mining company) leads to aggregate hazard that is not consistent with independent and identically distributed (IID) Poisson count models but instead fat-tailed (*Bonnafous and Lall*, 2020; *Bonnafous et al.*, 2017a,b). Spatially clustered risks can also arise from compound (*Zscheischler et al.*, 2018) and consecutive (*de Ruiter et al.*, 2020) events, complicating prediction. Similarly, mechanisms including the El Niño-Southern Oscillation (ENSO) (*Anderson et al.*, 2018), the Madden-Julien Oscillation (MJO) (*Anderson et al.*, 2020), Rossby waves (*Kornhuber et al.*, 2019b,a) and ACC (*Tigchelaar et al.*, 2018) can affect crop yields around the world and raise a possibility of global breadbasket failure; as *Taleb* (2007, 2012); *Taleb et al.* (2014) emphasize, not having observed this in the past is uninformative as to future risk. However, spatial correlation doesn't need to be a vulnerability; instead, large institutions can exploit negative correlations across space to diversify their exposure to physical risks (*Parhi*, 2020).

5.3.3 Financial Instruments

Another way to build adaptive, flexible, and robust infrastructure systems is through financial instruments. These can fund capital improvements, provide rapid funds for disaster response and recovery and align public and private incentives for risk-taking. Though they cannot solve every problem, financial instruments can improve the reliability and level of service of infrastructure systems while lessening the requirement for permanent and costly structures.

One class of instruments used to manage hydroclimate risks is comprised of products, like index insurance, whose aim is to facilitate rapid disaster response and recovery. An advantage of index insurance is that funds can be made available as soon as a disaster arrives, thereby funding immediate operational needs. This stands in contrast to reactive modes of disaster response in which funds for recovery must be requested from national governments or international organizations, often incurring significant delays at a critical juncture (*Clarke and Dercon*, 2016; *Wolfrom*, 2016; *World Bank*, 2015). Index insurance has been used to protect water utilities (*Zeff and Characklis*, 2013), hydropower operators (*Foster et al.*, 2015), and the shipping industry (*Meyer et al.*, 2016) from drought and for managing hydroclimate extremes in the developing world (*Khalil et al.*, 2007; *Barnett and Mahul*, 2007; *Carriquiry and Osgood*, 2012; *Greatrex et al.*, 2015). A central challenge is designing a suitable index, which must be closely related to the risk at hand, free from moral hazard, and triggered early enough to support risk management. When suitable indices can be identified (e.g., drought insurance for water utilities based on season-ahead snowpack measurements; *Hamilton et al.*, 2020) they can effectively mitigate financial risks and reduce the need for structural risk protection (*Zeff and Characklis*, 2013). Other financial instruments that are not based on indices but that also provide a nonstructural hedge against physical risk include option contracts such as a city purchasing the right to flood upstream farmers rather than raising urban levees (*Spence and Brown*, 2016).

Financial instruments can also reduce exposure to risk and incentivize risk-avoiding behavior. In general, flood insurance can be a valuable tool for risk management within a holistic policy framework and with the active involvement of financial institutions, builders, and government (*Kunreuther*, 1996; *Surminski et al.*, 2016; *Horn and McShane*, 2013). One challenge is that as a market player, the insurance industry has the option to raise rates or exit a market (*Cremades et al.*, 2018), which is not necessarily consistent with societal goals. Other challenges are social and political. A a study of flood insurance in St. Louis (*Kousky and Kunreuther*, 2010) demonstrated that (i) many property owners do not buy flood insurance; (ii) people underestimate flood risk (see also *Brody et al.*, 2017); (iii) flood maps are frequently inaccurate or biased (*Highfield and Brody*, 2017); (iv) many cities have a "love affair" with

levees (*Tobin*, 1995); (v) flood exposure is increasing over time; and (vi) communities take deep pride in rebuilding after a disaster, even when they are rebuilding in high-risk areas. Mechanisms of revenue collection and taxation can also disincentivize risk reduction: *Pinter* (2005) find that flood buyouts are often offset by construction in floodplains, which increases total risk, but this may be rational from the perspective of local leaders who need property tax revenue to fund critical services (*BenDor et al.*, 2020). On the other hand, there is evidence that where incentives are aligned risk, decreases: communities participating in the the Federal Emergency Management Agency (FEMA) community ratings program decreased flood losses by about 40% relative to those that did not (*Highfield and Brody*, 2017). These approaches illustrate how local communities can reduce flood losses without taking on costly debt and maintenance obligations (*Kunreuther and Heal*, 2012; *World Bank*, 2018; *Papakonstantinou et al.*, 2016).

El hombre, mis hijos – nos decía –, es como un río. Tiene barraca y orilla. Nace y desemboca en otros ríos. Alguna utilidad debe prestar. Mal río es el que muere en un estero.

Man, my sons – he told us –, is like a river, which has banks to keep it to its course, which is fed by other rivers, and which in turn feeds them. Men, like rivers, must serve some purpose. It is a bad river which ends up in a bog.

Augusto Antonio Roa Bastos, Hijo de Hombre

6

Robust Adaptation to Multiscale Climate Variability

This chapter begins with three assertions regarding the nature of climate risk, based on the findings presented in part I:

1. that different climate risk mitigation instruments have different planned lifespans;
2. that climate risk varies on many scales; and
3. that the processes which dominate this risk over the planning period depend on the planning period itself.

Defining M as the nominal design life of a structural or financial instrument and N as the length of the observational record (a proxy for total informational uncertainty), this chapter presents a series of stylized computational experiments to probe the implications of these

premises. Key findings are that:

1. quasi-periodic and secular climate signals, with different identifiability and predictability, control future uncertainty and risk;
2. adaptation strategies need to consider how uncertainties in risk projections influence success of decision pathways; and
3. stylized experiments reveal how bias and variance of climate risk projections influence risk mitigation over a finite planning period.

This chapter has been published as

> Doss-Gollin, J., D. J. Farnham, S. Steinschneider, and U. Lall (2019b), Robust adaptation to multiscale climate variability, *Earth's Future*, *7*(7), doi: 10.1029/2019EF001154

and is included with permission of all authors.

6.1 Introduction

Recent climate extremes such as floods, droughts, hurricanes, tornadoes, hailstorms, and heat waves have caused death and destruction, motivating investments in climate adaptation for the public and private sectors. Further, rapid and continuing changes to global climate hazard and exposure underscore the need for adaptation strategies. For example, population growth and urbanization have driven rapid increases in global exposure to events such as floods (*Jongman et al.*, 2012) and tropical cyclones (*Peduzzi et al.*, 2012). At the same time, anthropogenic modification of global and local climate processes affects the frequency, intensity, and location of extreme events (*IPCC*, 2012; *Milly et al.*, 2008; *Shaw et al.*, 2016). Even if future mitigation efforts are successful, existing levels of atmospheric CO_2 and ocean heat content necessitate the development of novel adaptation strategies.

This need has motivated a multitude of approaches for estimating the probability distribution of future climate risk, and for choosing between different risk mitigation instruments based on these estimates (see, e.g., *Merz et al.*, 2014). A typical goal is to create systems which are robust in the sense that they perform well over a wide range of plausible futures (*Lempert and Collins*, 2007; *Borgomeo et al.*, 2018) and which fail along non-catastrophic modes (*Brown*,

2010). Although climate risk has traditionally been managed with centrally planned structural instruments (e.g., a levee), the high price (*Papakonstantinou et al.*, 2016), environmental costs (*Dugan et al.*, 2010), and vulnerability to biased climate projections (*Lempert and Collins*, 2007) have recently dampened enthusiasm. Rather, actors such as New York City have turned to a combination of structural (e.g., stormwater barrier), operational (e.g., improved evacuation routes), and financial (e.g., a catastrophe bond) instruments for reducing vulnerability and increasing resilience to climate extremes (*Bloomberg*, 2013). These instruments are not typically implemented in isolation or statically. Instead, investment decisions made at each point in time affect the viability, costs, and benefits of future decisions, causing the system to trace a "pathway" through time (*Walker et al.*, 2013a; *Haasnoot et al.*, 2013, 2015).

Despite recent insights, important questions remain. How should a portfolio of risk mitigation instruments be optimized? How should one choose between permanent and transient instruments? Under what conditions is a permanent, large infrastructure investment required, and what information is needed to recognize this threshold? In this paper we focus more narrowly on the temporal structure of climate risk and how the uncertainty associated with its estimation influences the answers to these questions. We continue this section with three specific observations about climate risk which, while seemingly obvious, have important and subtle implications that we examine in sections 6.2 to 6.4.

6.1.1 Planning Decisions Are Made with Finite Horizons

Public or private sector investments in climate adaptation require not only the design of each potential instrument, but also selecting between instruments with vastly different operational planning periods. This project planning period, which we define as being M years, describes the nominal economic or physical lifespan of the structure or contract. Typical planning periods may vary from $M = 1$ year or less for a financial contract to $M = 100$ years or longer for a structural instrument, as illustrated in table 6.1. The planning period can also be interpreted as the finite period over which cost-benefit analysis (CBA) is conducted when assessing the project.

Typical climate risk management policies do not use a single risk mitigation instrument,

Location	Description	M	Reference
Iowa River	Purchase options for inundation of downstream agricultural lands to allow higher release flows from the flood control reservoir	1	*Spence and Brown* (2016)
New York City	Catastrophe bond for protection against storm surge caused by named storms and earthquakes	3	
County of Santa Barbara, California	Emergency improvements to portions of the Santa Maria Levee to reduce risk of levee failure	5	*USACE* (2007)
Iowa River	Raise levees by 6 feet	30	*Spence and Brown* (2016)
Dallas, TX	Evacuation of Rockefeller Boulevard	50	*USACE* (2014)
Central California	Tulare Lake storage and floodwater protection project	100	*GEI Consultants, Inc.* (2017)

Table 6.1: Six real-world risk mitigation instruments and the associated project planning period (M).

but rather build a portfolio of several instruments. Each has its own operational period, which may or may not match the planning horizon of the portfolio as a whole. This means that even if the portfolio has a long planning period, i.e. if long-term plans are a priority, this goal may be best accomplished through a series of flexible and adaptive instruments with short individual planning periods. For example, the optimal policy for New York City to manage uncertain hurricane risk in the 21st century might potentially be to keep areas devastated by hurricane Sandy zoned for low-impact development for the next 10 years. This would reduce future risk over all climate scenarios while postponing major investments until large uncertainties as to the magnitude of future sea level rise are resolved. The costs and benefits of each individual instrument will be assessed over its individual, finite planning period, but decisions about the portfolio structure are evaluated over the longer planning horizon.

The availability of precise climate information in the near future may significantly alter the choice between a large, long-duration instrument and a sequence of smaller, short duration instruments that can be executed quickly. For example, if above-average climate risk is projected over the next few years, a more costly project might be justified. However, in the plausible case of a long construction period for the large, permanent instrument, a financial risk mitigation instrument might be needed in the immediate term to cover potential losses before the large project is completed. Conversely, if the near-term risk is projected to be low,

then deferral of the large, potentially expensive instrument may be warranted. These cases highlight how the precision of short- and long-term climate risk projections plays directly into climate adaptation.

6.1.2 Climate Risk Varies on Many Scales

Climate risk is governed by a variety of physical processes which occur on scales ranging from local and transient to global and permanent. Of these processes, anthropogenic climate change (ACC) has received the most attention in the climate adaptation literature and its influence on some river floods, droughts, hurricanes, urban flooding, and many other climate hazards has been the subject of substantial investigation (e.g., *Coumou and Rahmstorf*, 2012; *Milly et al.*, 2008; *O'Gorman and Schneider*, 2009; *Trenberth et al.*, 2003). Human activities can also affect climate risk through modification of local land or river systems (see *Merz et al.*, 2014), and through changes in exposure to extremes (*Di Baldassarre et al.*, 2018a; *Jongman et al.*, 2012). In combination, these effects highlight that the past may not be an adequate representation of future climate risk (termed "nonstationarity" by *Milly et al.*, 2008).

Secular change is not the only mechanism which can cause historical records to provide a biased view of future risk. The Hurst phenomenon is a well-known mathematical relationship which describes the long memory of processes found in in geophysics, physics, biology, medicine, traffic, network dynamics, and finance (*O'Connell et al.*, 2016). The extensive observations of such behavior in hydrologic and climatic time series emphasize the need to consider such processes as underlying any discussion of climate change or nonstationarity (*Koutsoyiannis*, 2003; *Markonis and Koutsoyiannis*, 2013; *Palmer*, 1993). The Hurst phenomenon has also been connected to low frequency quasi-periodic phenomenon, especially where fractal scaling is expected. For example, wavelet methods have been used to estimate the Hurst exponent (*Simonsen et al.*, 1998; *Chamoli et al.*, 2007), and to design simulation algorithms that reproduce self-similarity, long range dependence and quasi-periodic regimes (*Kwon et al.*, 2007; *Bullmore et al.*, 2001; *Geweke and Porter-Hudak*, 1983; *Feng et al.*, 2005). The Hurst phenomenon also provides a link between catchment hydrology and global climate dynamics (*Blöschl and Montanari*, 2010; *Montanari*, 2003). The Hurst exponent is directly related

to the fractal dimension of a process, and there is a rich multi-disciplinary literature as to the process level and statistical justification of long memory and fractal processes in hydrology (*Mandelbrot*, 1985; *Mandelbrot and Wallis*, 1969; *Beran*, 1994). These processes have also been used to describe multi-scale dynamics of the climate (*Lovejoy and Schertzer*, 2012, 2013; *Lovejoy*, 2013; *Selvam*, 2017), including the El Niño-Southern Oscillation (ENSO) (*Maruyama*, 2018; *Živković and Rypdal*, 2013) and the Pacific Decadal Oscillation (PDO) (*Mantua et al.*, 1997).

External forcing from structured climate signals ("teleconnections"; *Ångström*, 1935) and catchment dynamics are both useful in explaining the low-frequency variability (LFV) observed in natural hydroclimate time series. We illustrate such LFV in fig. 6.1, which shows a 500 year drought reconstruction from the Living Blended Drought Analysis (LBDA) (*Cook et al.*, 2010), a 100 year record of annual maximum streamflow on the American River at Folsom, and the global wavelet power spectrum for both (*Torrence and Compo*, 1998; *Roesch and Schmidbauer*, 2016). Peaks for the American River time series are apparent at 2.3 and 15 years and in the LBDA time series at approximately 8, 20, and 64 years. This is illustrated by the blue line in fig. 6.1(b), which shows a 20 year moving average of the LBDA time series. A detailed analysis of these time series is beyond the scope of this paper, but we note that the high amplitude and long time periods of the quasi-periodic oscillations they exhibit are consistent with analyses of LFV in other hydroclimate systems (*Kiem et al.*, 2002; *Swierczynski et al.*, 2012; *Woollings et al.*, 2014b; *Hodgkins et al.*, 2017). The key implication is that the observations, (*Jain and Lall*, 2001), trends (*Bhattacharya et al.*, 1983), and frequencies (*Newman et al.*, 2016) observed in the past are often poor predictors of future behavior.

6.1.3 The Dominant Processes Depend on the Planning Period

Evaluating a particular risk mitigation instrument involves projecting climate risk over the M-year planning period. Consequently, the physical mechanisms which impart predictability on the system differ between projects with long and short planning periods. As illustrated in fig. 6.2 (a), the lifetime risk of a permanent structure with a 100 year planning period depends on the magnitude and extent of future human activities, with very large associated uncertainty. Even in the idealized and unrealistic case of a perfect climate model, these un-

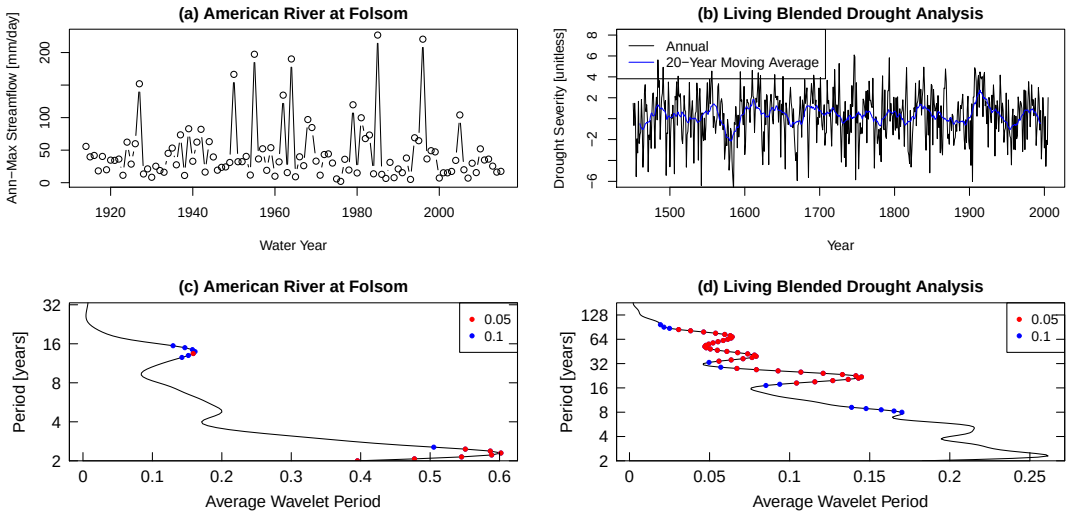

Figure 6.1: Hydroclimate time series vary on many time scales. (a) A 500 year reconstruction of summer rainfall over Arizona from the Living Blended Drought Analysis (LBDA). Lower values indicate more severe drought. A 20-year running mean is also shown in blue. (b) A 100 year record of annual-maximum streamflow for the American River at Folsom. Daily streamflow values were divided by the catchment area to yield a normalized flow in units of mm d^{-1}. (c) The global wavelet power spectrum of the LBDA time series (a). Blue (red) dots indicate frequencies which are significant at $\alpha = 0.10(0.05)$ compared to white noise. (d) Global wavelet power spectrum, like (c), for the American River data.

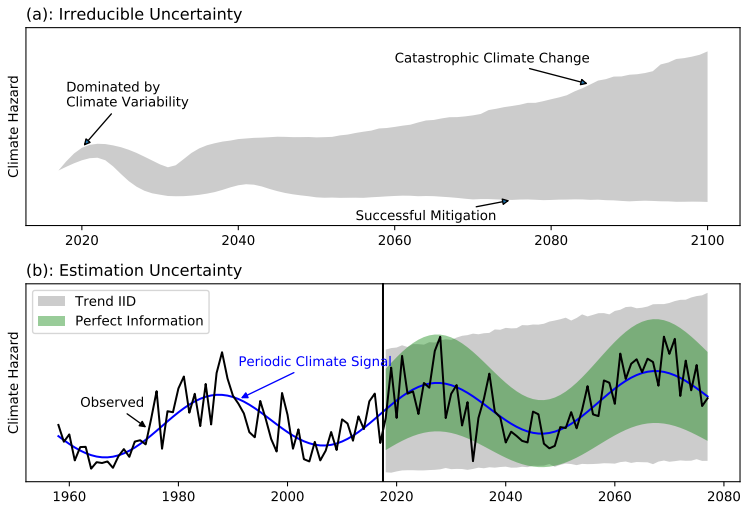

Figure 6.2: A stylized illustration of (a) irreducible and (b) estimation uncertainty. (a): Irreducible uncertainty cannot be resolved with better models or data and is dominated in the short term by chaotic behavior of the climate, and in the long term by the uncertainty in future anthropogenic climate change. (b): Informational uncertainty limits the potential to identify different climate signals. The blue line shows an idealized climate signal and the black line shows observations, which are scattered stochastically around the signal line. The green shading shows the true range within which observations will occur 95% of the time, while the gray shading the 95% confidence interval as estimated with a linear trend model.

certainties will be large. By contrast, this perfect climate model may usefully inform estimates of climate hazard over a three-year insurance contract with much less associated uncertainty.

Of course, scientists are not equipped with perfect models. Since different physical processes control climate risk at different timescales, successful integration of climate projections into decision frameworks depends on identifying, and subsequently predicting, these processes. A key question is whether the limited information in an N-year observational record permits the identification and projection of cyclical climate variability and secular change, and what the resulting bias and uncertainty portend for risk mitigation instruments with a planning period ranging from a few years to several decades. As shown in fig. 6.2 (b), the combination of LFV, stochastic variability, and secular change in a limited record can lead to large uncertainty in estimated future risk. Although fig. 6.2 focuses on physical processes, similar conclusions would also be valid for the socioeconomic processes which drive exposure to floods and other hydroclimate hazards.

6.2 Methods

We consider a set of stylized experiments to assess how well one can identify and predict risk associated with cyclical and secular climate signals for the M-year planning period and the probability of over- or under-design of a climate adaptation strategy based on these projections. We consider different temporal structures for the underlying risk which encompass quasi-periodic, regime-like, and secular change, as well as simple statistical models for estimating this risk from an N-year historical record. The relative importance of estimating the short- or long-term risk associated with these extremes depends on the design life M, but the potential to understand and predict these different types of variability depends on the informational uncertainty in the N-year historical record. Though we illustrate our findings with a simple flood risk example, the conclusions drawn apply to other hydroclimate hazards, and in particular those typically characterized through a time series of annual maxima or minima.

We consider three scenarios for climate risk, which we define by the structure of the underlying climate signal: (i) secular change only; (ii) LFV only; and (iii) LFV plus secular change. For each scenario, and for its identification from the N year length historical data, the bias and variance of the estimated flood risk over the M year design life relative to the "true model" are computed. We repeat the simulations $J = 1000$ times for each combination of experiment parameters to obtain estimates of the expected bias and variance for each scenario given M and N (section 6.2.3).

We caution the reader that the models for sampling climate risk (section 6.2.1) and for statistically projecting future risk (section 6.2.2) were chosen for their intuitive interpretation, rather than their general validity (see *Held*, 2005, for a thoughtful discussion of the value of simple models). We do not, in general, endorse these models for practical use but instead argue that the conclusions drawn from these simple models may be straightforwardly applied to more complex and realistic models. This discussion continues in section 6.4.

6.2.1 Sampling Climate Risk

The first step is to sample climate risk by generating synthetic streamflow sequences. To do this, we model annual-maximum flood peaks with a log-normal distribution, conditional on

a location parameter which varies in time:

$$\log Q(t) \sim \mathcal{N}(\mu(t), \sigma(t)). \tag{6.1}$$

We further assume a constant coefficient of variation of the log streamflow,

$$\sigma(t) = \xi\mu(t) \tag{6.2}$$

and apply a lower threshold on the standard deviation

$$\sigma(t) \geq \sigma_{\text{min}} > 0. \tag{6.3}$$

This formulation describes all scenarios for future climate considered in this paper within a single equation. To add climate variability to the system, the only component which needs to change is the dependence of $\mu(t)$ on time, which we parameterize as

$$\mu(t) = \mu_0 + \beta x(t) + \gamma(t - t_0), \tag{6.4}$$

where $x(t)$ represents a climate time series which itself exhibits LFV but not secular change. This parameterization is analogous to the "climate-informed" approach described in several studies for estimating climate risk (*Delgado et al.*, 2014; *Merz et al.*, 2014; *Farnham et al.*, 2018). Following eq. (6.4), when $\beta \neq 0$ there will be LFV, and when $\gamma \neq 0$ there will be secular change.

We represent the climate state variable $x(t)$ through an index for ENSO, which has been shown to impact flood risk around the world (*Ropelewski and Halpert*, 1987; *Ward et al.*, 2014) and has characteristic variability on timescales of 3 to 7 years (*Sarachik and Cane*, 2009) as well as a "staircase" of lower-frequency scales (*Jin et al.*, 1994). We model ENSO variability by taking a 20 000 year integration of the Cane-Zebiak model (*Zebiak and Cane*, 1987) to produce a monthly NINO3 index (*Ramesh et al.*, 2016). To create an annual time series, we average the October-December values of the NINO3 index for each year. Figure 6.3 shows a wavelet spectrum and time series plot of the resulting annual time series.

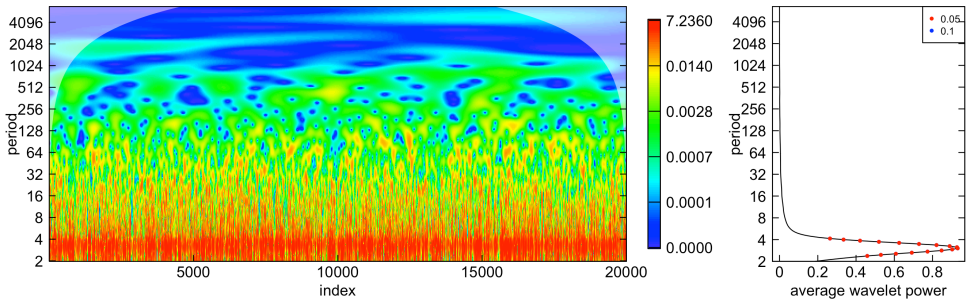

Figure 6.3: Wavelet analysis of the synthetic annual NINO3 time series. (L): wavelet power spectrum. Note that the color bar uses a quantile scale and is thus nonlinear. (R): global (average) power spectrum. Blue dots indicate frequencies which are significant at $\alpha = 0.10$ and red dots frequencies which are significant at $\alpha = 0.05$ compared to white noise.

To explore the sensitivity of our results to the assumed model structure, we also develop an alternative parameterization for $\mu(t)$ using a two-state Markov chain model. A Markov chain explicitly models transition between a fixed number of regimes, mimicking similar phenomena observed in nature. The transition matrix is given by

$$T = \begin{bmatrix} \pi_1 & 1-\pi_1 \\ 1-\pi_2 & \pi_2 \end{bmatrix}. \tag{6.5}$$

This transition matrix is first used to generate a sequence of states $S(t)$. The value $\mu(t)$ depends only on $S(t)$ and on time itself:

$$\mu(t) = \begin{cases} \mu_1 + \gamma_1(t - t_0) & \text{if} \quad S(t) = 1 \\ \mu_2 + \gamma_2(t - t_0) & \text{if} \quad S(t) = 2 \end{cases} \tag{6.6}$$

For simplicity, we assume that the coefficient of variation is the same for both states and that $\pi_1 = \pi_2$. We further impose $\mu_1 > \mu_2$ so that state 1 can be interpreted as the "wet" state and state 2 as the "dry" state.

6.2.2 Projecting Climate Risk over the Future M years

Once a synthetic streamflow sequence has been generated, we evaluate the identifiability and predictability of the dominant climate modes by fitting the sequence to statistical models and creating probabilistic projections of the future. We use three well-studied statistical methods for future flood risk, each of which parameterizes time in a different way. One is purely stationary, another captures LFV, and the third captures secular change. We choose these models for their interpretability and simplicity, rather than because of a belief that they are generally valid. For each synthetic flood sequence to be analyzed, the first N years are treated as observations. Once a statistical model is fit to these observations, then $K = 1000$ sequences of future annual-maximum streamflow over the future M-year record are generated from the fitted model using Monte Carlo simulation.

In the first case we fit a stationary model to the observed flood record, following classical assumptions of independent and identically distributed (IID) sequences. In this model annual-maximum streamflow are taken to follow a log-normal distribution with constant mean and variance. We refer to this model as "LN2 Stationary." The parameters of the model are fit in a Bayesian framework to fully represent the posterior uncertainty, using the stan probabilistic computing package (*Carpenter et al.*, 2017) with weakly informative priors (*Gelman et al.*, 2017; *Simpson et al.*, 2017). Equation (6.7) gives the full stationary model:

$$\begin{aligned} \log Q_{\text{hist}} &\sim \mathcal{N}(\mu,\ \sigma) \\ \mu &\sim \mathcal{N}(7, 1.5) \\ \sigma &\sim \mathcal{N}^{+}(1, 1) \end{aligned} \tag{6.7}$$

where $\mathcal{N}$ denotes the normal distribution and $\mathcal{N}^{+}$ denotes a half-normal distribution.

Next, we modify this stationary model to incorporate secular change. Many studies have done this by regressing certain parameters of the model on time (see *Salas et al.*, 2018, for a comprehensive review). We consider an extension of the stationary log-normal model by adding a time trend on the scale parameter and maintaining a constant coefficient of variation, as given in eq. (6.8). We refer to this model as "LN2 Linear Trend." This model gives a lower bound on total informational uncertainty because it correctly represents the trend's known

form, whereas in real-world analyses the form of the trend is unknown (and likely nonlinear). The full model, including priors, for the trend log-normal model is given by equation (6.8):

$$\begin{aligned} \mu &= \mu_0 + \beta_\mu (t - t_0) \\ \log Q_{\text{hist}} &\sim \mathcal{N}(\mu,\ \xi\mu) \\ \mu_0 &\sim \mathcal{N}(7, 1.5) \\ \beta_\mu &\sim \mathcal{N}(0, 0.1) \\ \log \xi &\sim \mathcal{N}(0.1, 0.1) \end{aligned} \tag{6.8}$$

where ξ is an estimated coefficient of variation. The stan models used are available with other codes at `https://github.com/jdossgollin/2018-robust-adaptation-cyclical-risk`.

Finally, we explicitly model LFV using a hidden Markov model (HMM). An HMM is a latent variable model in which the system being modeled is assumed to follow a Markov process with unobserved (i.e. hidden) states $S(t)$ (*Rabiner and Juang*, 1986). The (unobserved) states evolve following a first-order Markov process, and the observed variable (e.g. streamflow) depends only on the underlying state. HMMs have been widely used for modeling streamflow sequences (*Bracken et al.*, 2016) and ENSO (*Rojo Hernandez et al.*, 2017). We fit streamflow sequences using a HMM with two states. The model is fit using the Baum-Welch algorithm, assuming that the data follow a log-normal distribution that is conditional only on the unobserved state variables. This algorithm simultaneously estimates the transition matrix of the Markov process and the conditional parameters of each distribution. For simplicity, we fit only a two-state HMM to each sequence. Future floods are then estimated by simulating future states from the estimated transition matrix and then drawing $Q(t)$ conditional on the simulated state.

6.2.3 Evaluating Fitting Models

Both estimation bias and estimation uncertainty affect the utility of a climate risk projection. An instrument whose design was based on projections with overestimated variance or positive bias will be over-designed, either causing the risk manager to avoid the investment, given its higher cost, or will lead to unnecessary diversion of funds from other instruments.

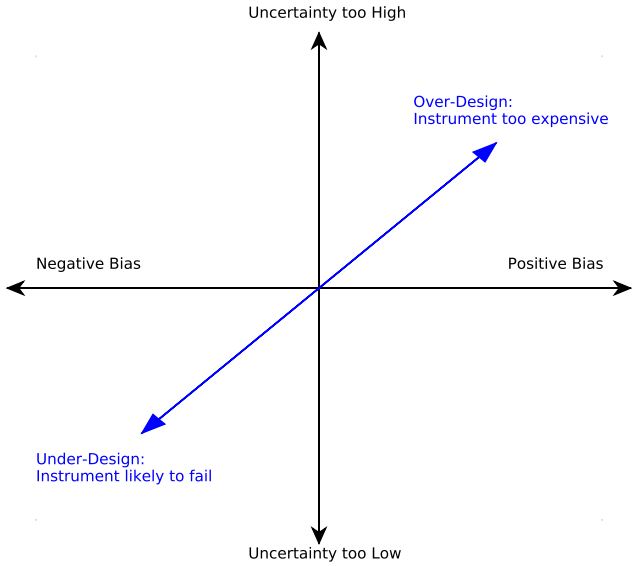

Figure 6.4: Consequences of model bias or incorrect model representation of uncertainty. If an estimate has a positive bias and overestimates uncertainty, the instrument may be too expensive. If an estimate has negative bias and underestimates uncertainty, it will be likely to fail.

Similarly, an instrument designed based on underestimated variance or negative bias may be under-designed, and thus fail to protect the public. This point is illustrated in fig. 6.4.

We evaluate both the estimation bias and estimation uncertainty. For a given choice of M, N, and generating model, we compare the synthetic streamflow sequence's N-year "historical record" and the $K = 1000$ posterior simulations of future flows. The quantity $\hat{p}_T$, the estimated expected number of floods per year, is taken by calculating, for each of the K posterior simulations, the number of exceedances of the flood design threshold, then dividing by M to get exceedances per year. We then compute the variance of these K estimates. We further calculate the bias of $\hat{p}_T$ by averaging it across the K samples and comparing this to the number of times the M-year "future period" of the synthetic streamflow sequence exceeds the flood design threshold. Since the "observed" number of flood exceedances from the generating model is inherently noisy for an M-year period, we average the bias and variance across $J = 1000$ different streamflow sequences to compute expected values of both. These sequences are generated with the same underlying parameters, but the specific synthetic NINO3 sequence (or set of Markov states) may differ between the J sequences.

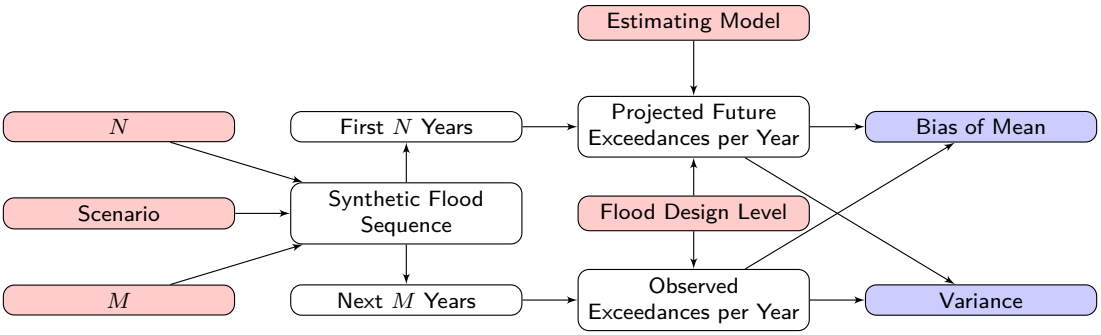

Figure 6.5: Flow chart describing experiment design. Parameters are shown in red. N denotes the informational uncertainty (length of historical record) and M the amount of extrapolation (project design life). Calculated quantities are shown in white. Quantities used for analysis are shown in blue.

6.2.4 Experiment design

Figure 6.5 describes the experimental design. We assess estimation bias and variance for three scenarios of future climate. First, we consider an idealized scenario where only secular change is present in the system and LFV is fully damped ("secular change only"). Next, we consider the "pre-industrial" case where there is no secular change but LFV modulates climate risk in time ("low-frequency variability only"). Finally, we consider a more realistic (though still idealized) case with both LFV and secular change ("low-frequency variability plus secular change").

Computation was carried out in the python programming language, making particular use of the matplotlib, numpy, pandas, pomegranate, scipy, and xarray libraries for scientific computing (*Hunter*, 2007; *van der Walt et al.*, 2011; *McKinney*, 2010; *Schreiber*, 2017; *Virtanen et al.*, 2020; *Hoyer and Hamman*, 2017). Wavelet analysis was conducted using the WaveletComp package (*Roesch and Schmidbauer*, 2016) in the R programming language. Bayesian models were written in the stan probabilistic programming language (*Carpenter et al.*, 2017) using the No U-Turn Sampler (*Hoffman and Gelman*, 2011; *Betancourt*, 2017). The codes used to generate the figures and text of this paper are available at on GitHub.

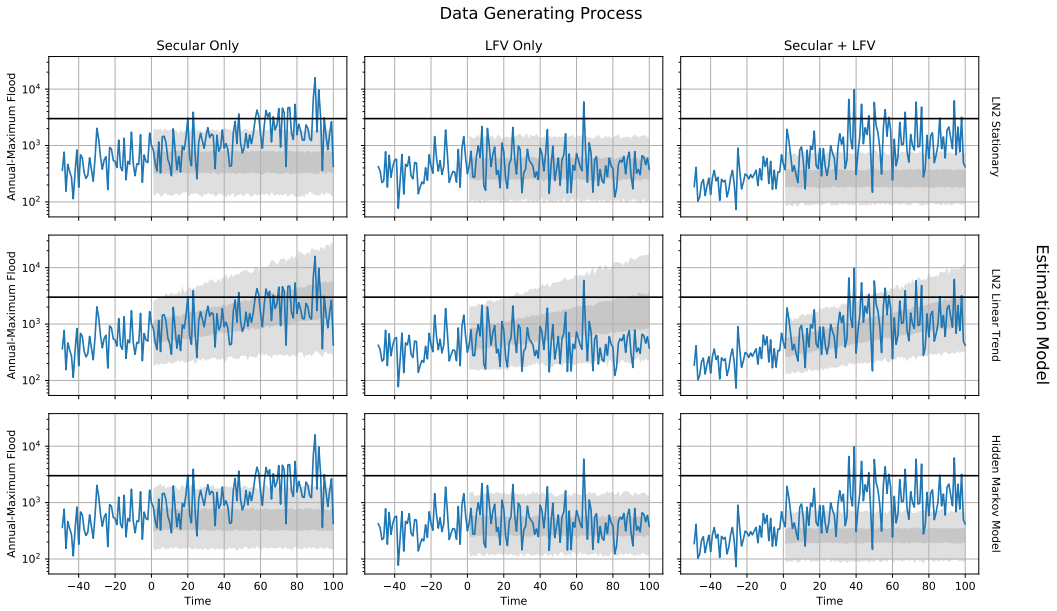

Figure 6.6: An illustration of the estimation procedure. A single streamflow sequence with $N = 50$ and $M = 100$ is shown for each of the three cases (secular only, LFV only, and secular plus LFV) considered. The blue line shows the observed sequence. The gray shading indicates the 50% and 95% confidence intervals using each of the three fitting methods discussed (rows). The horizontal black line indicates the flood threshold.

6.3 Results

These three scenarios for future climate considered are illustrated in fig. 6.6, which shows a single synthetic streamflow sequence generated with $N = 50$ and $M = 100$. We also show projected future climate risk with each of the three estimating models described in section 6.2.2. This figure highlights that even where projections of average streamflow are unbiased, if the spread is too large then projection of the threshold exceedance probability may be too large. In the remainder of this section we present a more systematic analysis of each of these three cases.

6.3.1 Secular Change Only

In the idealized case where only secular change exists, accurate climate predictions need to either use a long record to identify and model this trend, or to ignore the trend and predict only a few years ahead. This is shown in fig. 6.7, which depicts the estimation bias and variance for each of the three estimation models for many combinations of M and N.

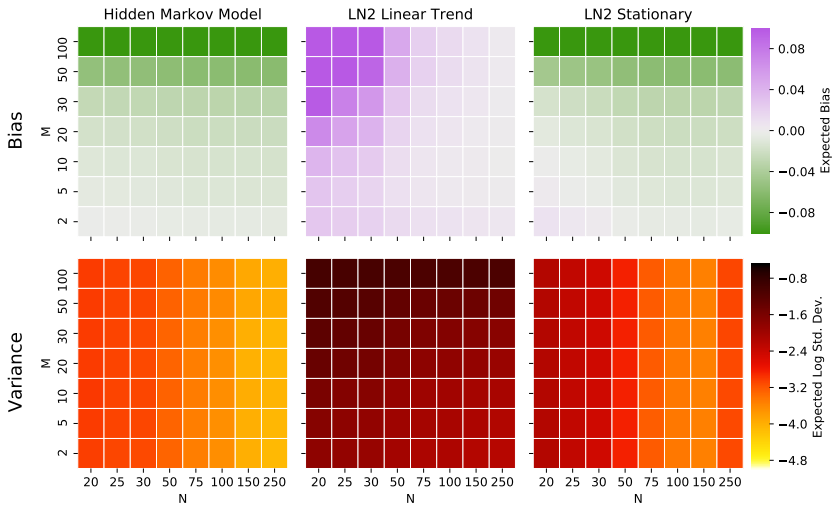

Figure 6.7: Expected estimation bias and variance for sequences generated with secular change only (no LFV). Sequences were fit to each of three statistical models (columns) for different N and M (x and y axis, respectively). Top row shows estimation bias and bottom row shows log standard deviation of estimates. Note the uneven spacing of the x and y axes.

The log-normal trend model tends to over-estimate risk (positive bias), except when N is large, because the model gives a non-zero probability to the trend being larger than it actually is. The variance of these estimates is also large. This again highlights the difficulty of fitting complex models for estimating risk when informational uncertainty is large. By contrast, the stationary log-normal model and HMM, which do not account for secular change, show relatively low variance of their estimates and exhibit low bias for short M. As $N \to \infty$, these (mis-specified) models can only represent the trend by setting the scale parameter very large, leading to high estimation variance and (as $M \to \infty$) also a large bias. This principle has prompted some to consider only the most recent years of the data, deliberately shortening N (i.e. *Müller et al.*, 2014). However, these results also highlight that the increase in variance as N is reduced may quickly outpace the utility of any bias reductions.

If the analyst could know *a priori* that secular change is present in a time series, and if M is long, then the use of a complex model which represents the processes causing this change is required. Here the log-normal linear trend model has the advantage of being correctly specified (both the generating and fitting processes assume a log-normal distribution conditional on a linear time trend), which is generally not the case in the real world (*Montanari and Koutsoyiannis*, 2014; *Serinaldi and Kilsby*, 2015). As a result, in real-world settings longer

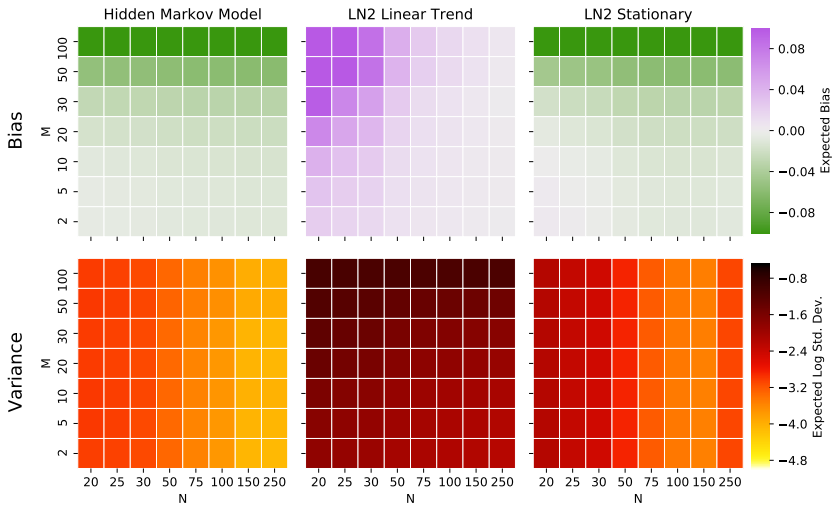

Figure 6.8: As fig. 6.7 for sequences generated with the two-state Markov chain model.

N may be required to identify trends whose exact form is not known. Alternatively, if M is small then it may be reasonable to use a stationary estimate, since the bias will be small and the variance substantially lower.

6.3.2 Low-Frequency Variability Only

We next turn to the idealized case where LFV is present but there is no secular change in the system. Figure 6.9 highlights that identification of nonexistent trends from limited data may lead to gross over-estimation of true risk through an increase in the variance of the estimated risk. As expected, the stationary log-normal model performs well overall, with low bias and low variance. The HMM actually out-performs the stationary model, with slightly lower variance than the stationary model, because it better captures the multimodal distribution that emerges from dependence on the ENSO index, which exhibits several regimes (fig. 6.3). By contrast, the linear trend model performs poorly for low N and high M because a positive probability is assigned to the existence of a positive trend.

Of particular relevance to analysis of real-world data sets is the ratio of the project planning period M to the characteristic periods of variability of the LFV. If this period is much larger than M, then a stationary assumption may provide reasonable estimates, and fewer observations may be required (shorter N). As shown in fig. 6.3, the ENSO time series is most

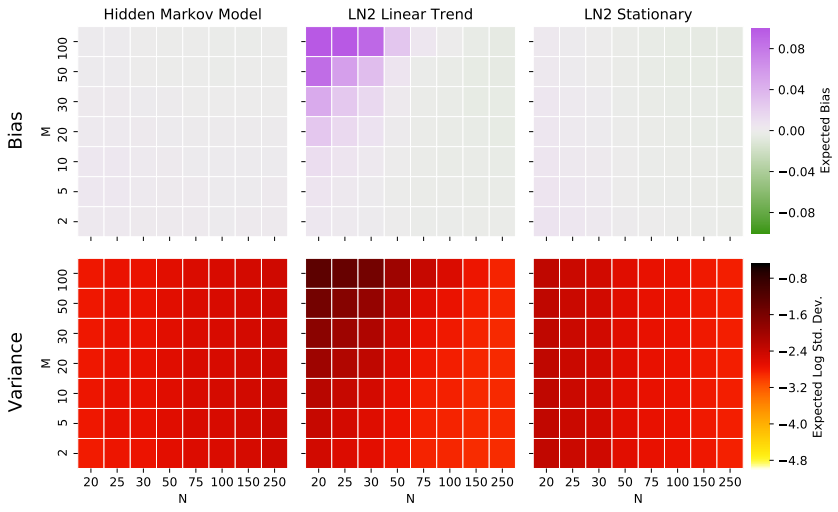

Figure 6.9: As fig. 6.7 but for sequences generated with zero secular change and strong LFV.

active in the 3 year to 6 year band. In the real world, however, many hydroclimate time series vary at multidecadal and longer frequencies. In this case, as illustrated in fig. 6.2, the characteristic periods may be as large or larger than M, particularly if multidecadal modes such as the PDO or Atlantic Meridional Oscillation (AMO) are involved, and the LFV must therefore be estimated explicitly. This in turn requires a longer observational record N in order to identify and predict these different signals.

6.3.3 Low-Frequency Variability and Secular Change

In the final and most realistic case, where both LFV and secular change are present, stationary models perform well for short M while for long M the trend must be identified from a long record and modeled explicitly.

Consistent with the conceptual illustration of fig. 6.2, the results of fig. 6.11 highlight that the relative importance of secular change and LFV depends on M. When M is long, climate risk is dominated by secular change and it becomes essential to model this risk explicitly with a more complex model (i.e., the linear trend model). Alternatively, when M is short, LFV dominates and the increased variance associated with estimating a trend is not worth the modest reduction in bias. As before, when the informational uncertainty is large (small N), the identifiability and predictability of the trend are limited.

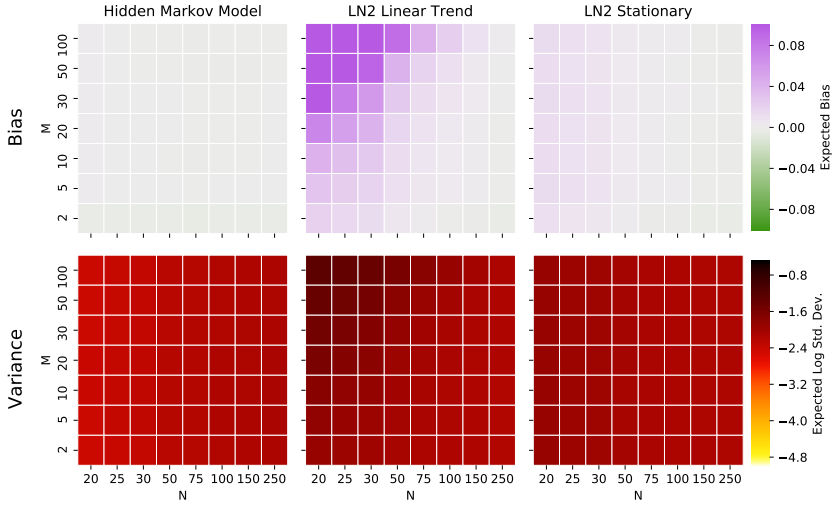

Figure 6.10: LFV only: as fig. 6.9 for sequences generated with the two-state Markov chain model.

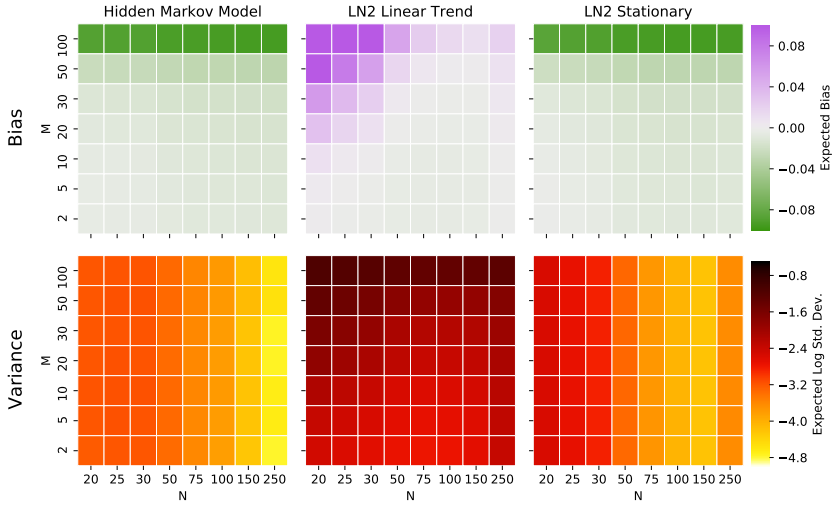

Figure 6.11: As fig. 6.7 but for sequences generated with both LFV and secular change.

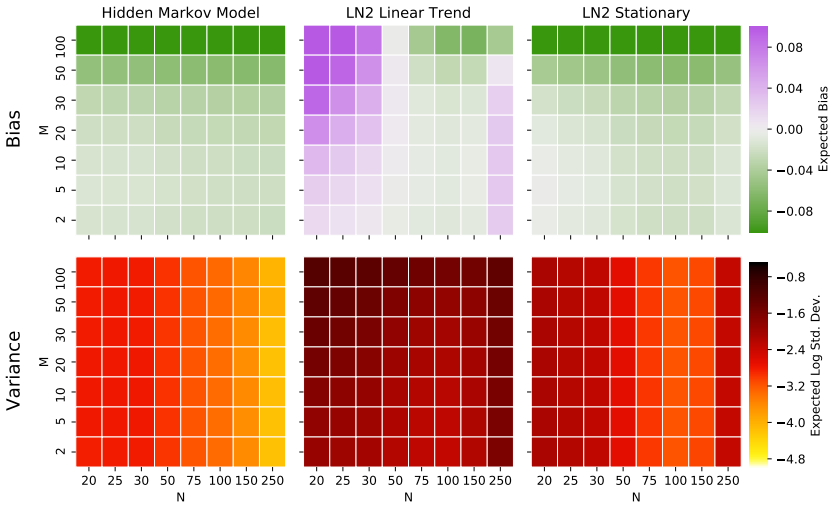

Figure 6.12: As fig. 6.11 for sequences generated with the two-state Markov chain model.

6.4 Discussion

Evaluating and implementing investments for climate risk mitigation involves making projections of climate risk, which generally exhibits both LFV and secular trends, over the M-year project life of the instrument. The success of this prediction will depend on the identifiability of different signals from limited information, the time scales of LFV relative to the project life of the instrument, and the degree of intrinsic uncertainty in the system. In this paper we took a synthetic data approach to explore the implications of varying M and N in stylized scenarios that represent important features of real-world hydroclimate systems.

Figures 6.7 and 6.11 show that for projects where M is sufficiently short, intrinsic uncertainty is low and cyclical climate variability is dominant over the project planning period (*Jain and Lall*, 2001; *Hodgkins et al.*, 2017). However, one's ability to identify and predict this variability depends on having a model of sufficient complexity to represent the processes that cause LFV, and the data to fit the model. In this case, the project may be in the "potential predictability zone" of fig. 6.13. If sufficient information is not available, however, then simple models which represent fewer processes may be preferred (the "rough guess zone").

For projects with longer M, our results highlight the importance of identifying and predicting secular change. As illustrated schematically in fig. 6.2, large uncertainties (e.g., as to future CO_2 concentrations and local climate impacts) lead to large intrinsic uncertainty in projections of future climate risk. As the physical mechanisms cascade from global (e.g., global mean surface temperature) to regional (e.g., storm track position; *Barnes and Screen*, 2015) and local (e.g., annual-maximum streamflows) scales, informational uncertainties also compound and increase (*Dittes et al.*, 2018; *Bosshard et al.*, 2018). With sufficient information (large N), this informational uncertainty may be reduced, but this data cannot address intrinsic uncertainty and this zone is thus named the "intrinsic uncertainty zone". Finally, if N is limited then there will be strong potential for misleading estimates and over-extrapolation (i.e. a "danger zone" for planning).

These findings were derived conceptually and through idealized computational experiments for simulating and predicting climate risk, but the principles are applicable to more complex, physically based methods. For example, flood frequency analysis may join observa-

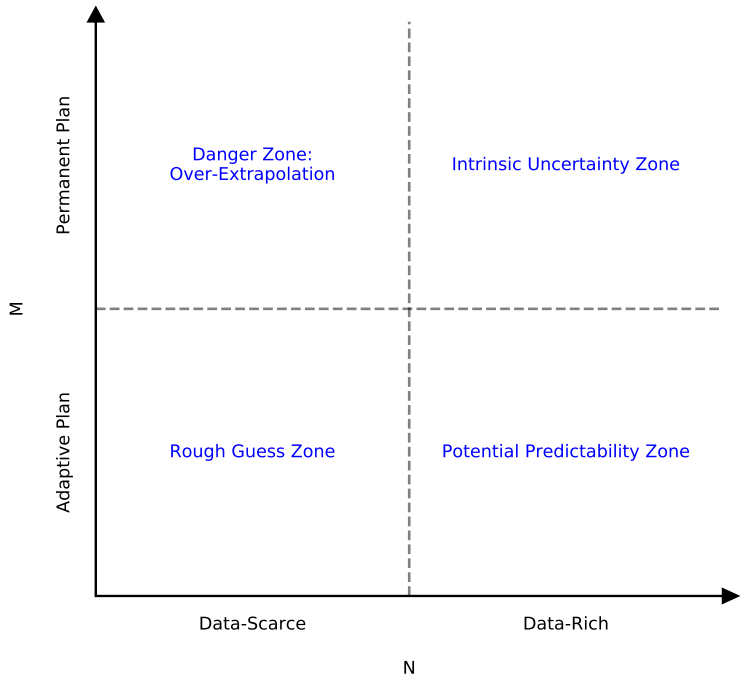

Figure 6.13: The importance of predicting different signals, and the identifiability and predictability of the signals, depends on the degree of informational uncertainty (N) and the project planning period (M).

tions across time and space (*Lima et al.*, 2016; *Merz and Blöschl*, 2008) or apply model chains based on general circulation models and hydrologic models (see *Merz et al.*, 2014) to increase N. We suggest that the sample size N defined in our experiments may be straightforwardly interpreted as a measure of the total informational uncertainty in the analysis; as N increases, informational uncertainty decreases.

Similarly, real-world climate adaptation plans will typically include multiple instruments which may be placed in different locations and times in a sequential fashion. Even if the planning period of a portfolio is long, the individual instruments within the portfolio may have short planning periods. Since section 6.3 shows that the bias and variance of climate risk projections tend to increase with M, the total bias and variance associated with sequencing 20 consecutive $M = 5$ year projects will be less than that associated with making a single $M = 100$ year project. This effect will be compounded by the fact that if the first $M = 5$ year project is based on estimates with informational uncertainty N, the second will have $N + 5$, the third $N + 10$, and so on.

The climate adaptation decisions which our analysis can inform are typically framed as economic cost-benefit analyses which discount future cash flows at some annual rate (*Sodastrom et al.*, 1999; *Powers*, 2003). The application of a positive discount rate, mandated for many public sector projects in the United States (*Powers*, 2003), further emphasizes the importance of predicting near-term risk. Projects with long planning periods must therefore overcome future discounting, the potential for large bias or variance, and that all estimates are made with informational uncertainty N. By contrast, the informational uncertainties for a sequence of short-term instruments are $N, N + M, N + 2M, \ldots$, potentially yielding improved identifiability and predictability of relevant climate signals.

6.5 Summary

In this paper we considered how the temporal structure of the climate affects the potential for successful prediction over a finite M-year future period. We began with three premises, or observations, about the nature of climate risk: (i) that different climate risk mitigation instruments have different planned lifespans; (ii) that climate risk varies on many scales;

and (iii) that the processes which dominate this risk over the planning period depend on the planning period itself. Although the simulations presented here are neatly divided into secular change, LFV only, and LFV plus secular change, real-world hydroclimate time series exhibit LFV on many timescales and several sources of (not necessarily linear) secular change, adding further informational and intrinsic uncertainties.

Depending on the specific climate mechanisms that impact a particular site, and the predictability thereof, the cost and risk associated with a sequence of short-term adaptation projects may be lower than with building a single, permanent structure to prepare for a worst-case scenario far into the future. For most large actors, a portfolio of both large M and small M projects will likely be necessary, none of which precludes the need for mitigation of global and local climate change and the development or the execution of vulnerability reduction strategies.

He who lives by the crystal ball soon learns to eat ground glass.

Edgar R. Fiedler

7

Near-Term Predictability Lowers Long-Term Adaptation Costs

Chapter 6 hypothesizes that a sequence of adaptation strategies with short project planning periods may more flexibly and robustly meet fast-changing societal needs than a single static investment. This chapter elaborates upon this hypothesis by identifying "optimal" sequences of levee heightening for a didactic case study in the Netherlands. By minimizing the joint costs of hard (levee construction) and soft (insurance for residual risk) instruments, this chapter shows that

1. large but distant and uncertain changes (e.g., sea level rise) should not necessarily motivate immediate investment in structural risk protection;
2. soft adaptation strategies are robust to different model structures and assumptions while hard instruments perform poorly under conditions for which they were not de-

signed; and

3. increasing the hypothetical predictability of near-term climate extremes significantly lowers long-term adaptation costs.

This chapter has not been published but is included with permission of coauthors Upmanu Lall and Jonathan Lamontagne.

7.1 Introduction

Large investment in civil infrastructure systems is a prerequisite to achieving key global objectives including deep decarbonization, mitigation of changing climate hazards, and universal access to sanitation, transit, and communication services. Three key factors impede progress. First, existing infrastructure is aging and deteriorating (*Ho et al.*, 2017; *Brown and Willis*, 2006), which increases the demand for limited resources and means that new projects must be evaluated within the context of decisions about whether to repair, replace, or abandon the inadequate structures already in place. Second, deep uncertainty as to future climate, technology, economics, and demographics means that design specifications formulated today are unlikely to meet the future needs of society, and that infrastructure will be asked to fulfill objectives for which it was not designed (*Chester et al.*, 2020; *Lempert et al.*, 2003). Finally, large and permanent infrastructure projects impose debt and maintenance payments, leaving the system fragile to population or revenue decline (*Ansar et al.*, 2017; *Taleb*, 2012). Failure to manage this triad of infrastructure challenges has led to widespread infrastructure decay, not only lowering economic productivity but disproportionately affecting the most vulnerable, as exemplified by lead poisoning in Flint and Washington, D.C. (*Roy and Edwards*, 2019), hookworm outbreaks in southern Alabama (*Albonico and Savioli*, 2017), and tailings dams failures around the world (*Santamarina et al.*, 2019; *Concha Larrauri and Lall*, 2018, 2020).

To manage these challenges, infrastructure owners and managers need to identify near-term actions that meet immediate needs while also ensuring reliable and cost-effective service in an uncertain future, taking into account that infrastructure planning is both sequential (*Fletcher et al.*, 2017; *Herman et al.*, 2020) and path-dependent (*Haasnoot et al.*, 2012, 2013; *Wise et al.*, 2014; *Zeff et al.*, 2016; *Trindade et al.*, 2019). In particular, while these policies

have historically relied heavily upon "hard" risk management with physical structures, they can also consider "soft" instruments that increase the productivity of existing resources and infrastructure (*Gleick*, 2003). For example, financial instruments (*Clarke and Dercon*, 2016; *Hamilton et al.*, 2020; *Meyer et al.*, 2016), operational improvements (*Bertoni et al.*, 2019; *Giuliani et al.*, 2018), index insurance (*Khalil et al.*, 2007; *Foster et al.*, 2015), demand management (*Zeff et al.*, 2020; *Lehe*, 2019), and distributed infrastructure (*Leigh and Lee*, 2019; *Burger et al.*, 2019) can all provide cost-effective service improvements without committing the system to a narrow and fragile path.

Climate information can also catalyze adaptive management of infrastructure systems. For example, predictive early warning systems for floods can save lives and reduce property damage (*Bedient et al.*, 2000; *Bischiniotis et al.*, 2020) while medium-range weather forecasts are used to inform decisions in agriculture, water management, and public health (*Nissan et al.*, 2019; *Vitart et al.*, 2016). Yet despite widespread recognition that organized low-frequency modes of variability, most famously the El Niño-Southern Oscillation (ENSO), dominate interannual variability of climate phenomena including Antarctic sea ice extent (*Jenkins et al.*, 2018), floods (*Hodgkins et al.*, 2017; *Swierczynski et al.*, 2012; *Ropelewski and Halpert*, 1987), droughts (*Cook et al.*, 2010; *Steiger et al.*, 2019), Atlantic hurricanes (*Lim et al.*, 2018; *Kossin*, 2017), and North Sea storm surges (*Chafik et al.*, 2017), seasonal to decadal (S2D) forecasts are rarely used to sequence and prioritize infrastructure investments.

We postulate that although projections of climate risk far into the future are deeply uncertain (*Wong and Keller*, 2017; *Ruckert et al.*, 2019; *Kopp et al.*, 2017), the substantial and improving skill of S2D models (*Kushnir et al.*, 2019; *Meehl et al.*, 2014; *Merryfield et al.*, 2020) can be used to improve the design and management of infrastructure systems. More specifically, we hypothesize that as the predictability of the climate system increases, soft adaptation policies with short planning periods can be more precisely designed, lowering their cost and thereby favoring policy portfolios with relatively more soft instruments (as articulated in *Doss-Gollin et al.*, 2019b).

In this paper we quantify the value of increased climate predictability for sequential planning, taking as a didactic example the co-optimization of levee heightening (a hard or struc-

tural instrument) and index insurance (a soft or nonstructral approach) in Delfzijl, Netherlands (*van Dantzig*, 1956; *Oddo et al.*, 2017; *Garner and Keller*, 2018; *Eijgenraam et al.*, 2014). In particular, we pose the following three questions.

1. What is the sensitivity of the optimal levee heightening to assumptions regarding near-term (seasonal to decadal) and long-term (century scale) sea level rise?
2. Is investing today in infrastructure designed for worst-case scenarios a robust response to large but distant and uncertain risks?
3. Can predictability of near-term risks lower the long-term costs of the adaptation pathway?

This general problem of combining hard and soft instruments to manage deep and dynamic uncertainties is relevant to a wide range of planning problems in infrastructure systems, and in particular coastal adaptation in the low-lying communities home to hundreds of millions of people worldwide (*Kulp and Strauss*, 2019).

7.2 Methods

We consider a didactic case study first developed by *van Dantzig* (1956) of levee heightening for a polder surrounded by a single reach of dike in the Netherlands. We frame this as an optimal control problem (*Herman et al.*, 2020) and use stochastic dynamic programming (SDP), which is a well-known exact solution method, to identify the decision for each time step (1 year) that, conditional on the observed state of the world, minimizes the expected future costs of constructing levees plus insuring residual risks. SDP can be used to compute exact and optimal policies given a representation of the environment as a finite Markov decision process (MDP), meaning that the state set $\mathcal{S}$, reward set $\mathcal{R}$, and action set $\mathcal{A}$ are each finite and that the state's dynamics are governed by a set of known probabilities $\mathrm{P}(s', r \mid s, a)$ for all $s \in \mathcal{S}$, $a \in \mathcal{A}(s)$, and $r \in \mathcal{R}$, where s' indicates the state at the next time step (following the notation of *Sutton and Barto*, 2018). SDP works by converting the *Bellman* equation for

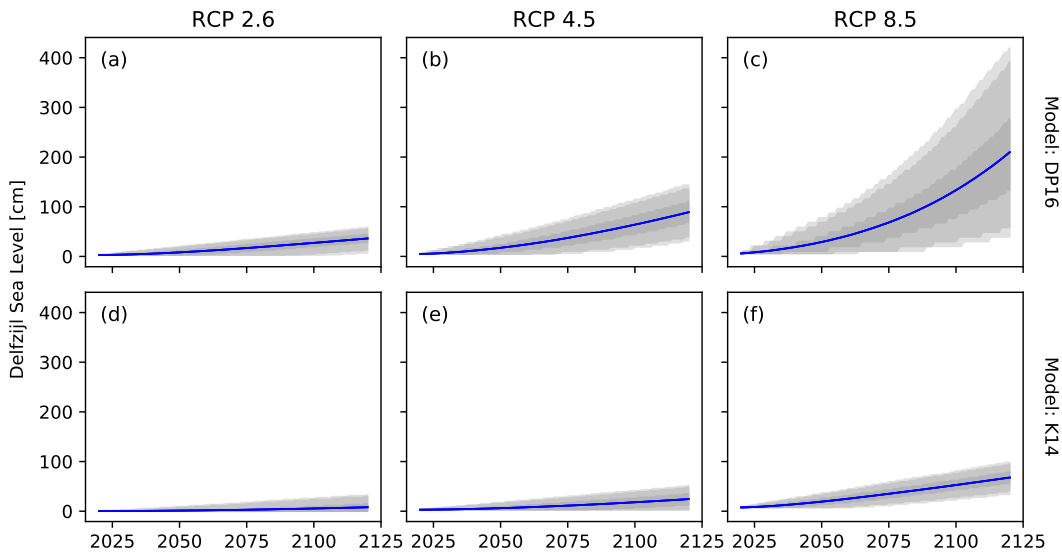

Figure 7.1: Different models and scenarios agree that local mean sea level at Delfzijl, Netherlands will rise over the next centuries but differ sharply on the magnitude and timing of this rise. Plot shows mean (blue line) and 50, 90, and 95 percent confidence intervals (gray shading) for lag-1 Markov models (eq. 7.2) fit to simulations of LSL at Delfzijl, Netherlands in cm for each of three RCP scenarios (columns) and each of two physical models described in *Kopp et al.* (2017): (i) the K14 model and (ii) the DP16 model (rows). The model described in eq. (7.2) credibly represents the complex dynamics from the K14 and DP16 models; simulations directly from these models are shown in figs. 7.2 and 7.3.

state-action value

$$q_*(s,a) = \sum_{s',r} \mathrm{P}(s', r \mid s, a) \left[r + \gamma \max_{a'} q_*(s', a') \right], \tag{7.1}$$

where γ is a discount rate and s' is the state at the next time step, into an optimal policy $a_* = \max_a q(s,a)$. The state-action value is solved by exhaustive recursive search described in algorithm 1. The remainder of this section defines the state space, reward function, and transition probabilities.

7.2.1 State Space and Transitions

The state space $\mathcal{S}$ consists of time t plus three additional variables, each with its own transition probability. At each time step the state space is fully described as a tuple $s = (t, \ell, x, h)$ giving the time, local sea level, low-frequency variability (LFV) state variable, and levee height,

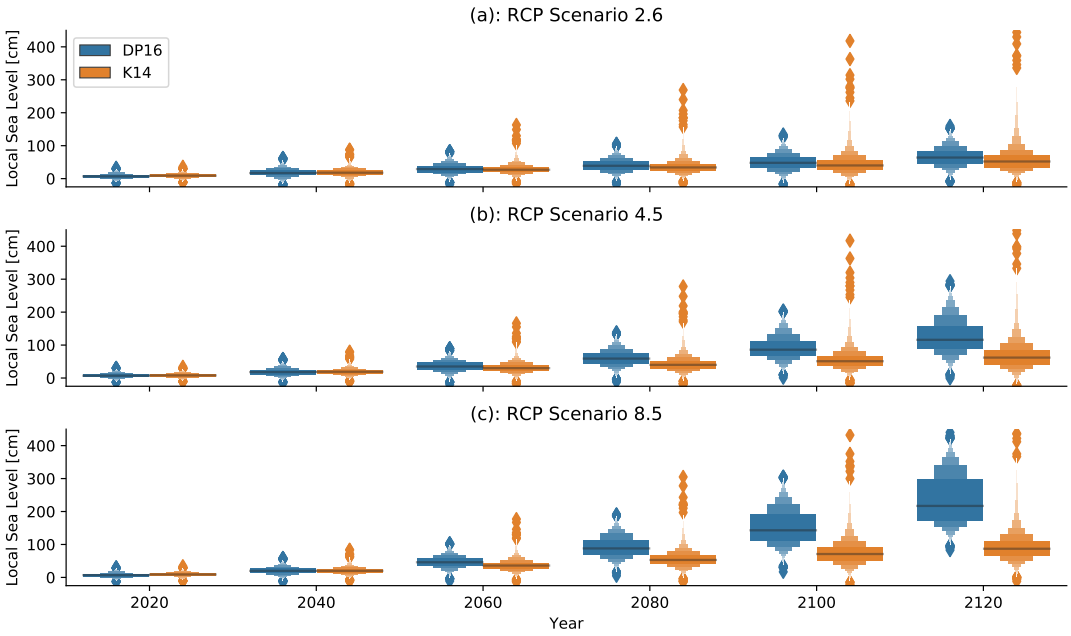

Figure 7.2: PDFs of simulated LSL at Delfzijl, Netherlands in cm in 2020, 2040, 2060, 2080, 2100, and 2120 (columns) for each of three RCP scenarios (columns) and each of two physical models: DP16 and K14 (colors) as outlined in *Kopp et al.* (2017). The PDFs are represented using a letter plot (*Hofmann et al.*, 2017); like boxplots, letter plots show only actual data values rather than smoothed values or estimated densities, but a broader set of quantiles can be presented. Distributions are estimated from 10 000 simulations for each model and each scenario.

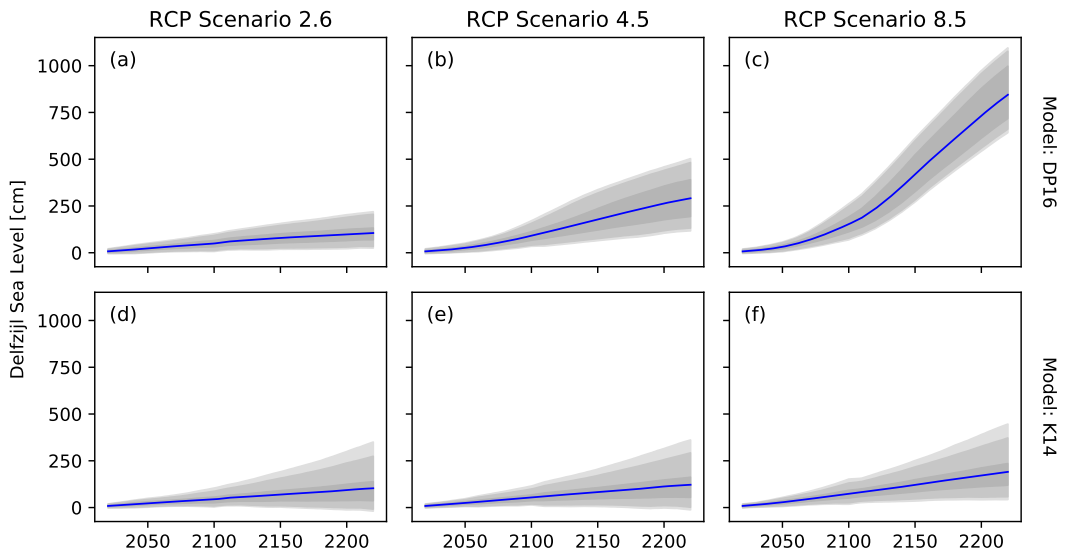

Figure 7.3: Different models and scenarios agree that local mean sea level at Delfzijl, Netherlands will rise over the next centuries but differ sharply on the magnitude and timing of this rise. Plot shows mean (blue line) and 50, 90, and 95 percent confidence intervals (gray shading) for simulations of LSL at Delfzijl, Netherlands in cm for each of three RCP scenarios (columns) and each of two physical models: DP16 and K14 (rows). Note that in contrast to figs. 7.1 and 7.2 the x axis on this plot goes to 2220.

respectively.

The annual-maximum flood in a particular year, y, is decomposed into an average value of LSL for that year ℓ and a superimposed storm surge y'. Figure 7.4 shows historical values of ℓ and y'.

The evolution of LSL (ℓ) was modeled using a first-order Markov transition model with n_L states (table 7.1). To estimate the corresponding Markov transition matrix $\mathbb{L}$, 10 000 simulations of LSL at Delfzijl were generated following the methodology of *Kopp et al.* (2017) for each of three RCP scenarios, and for each of two parameterizations of ice sheet dynamics: the more pessimistic assumptions of DP16 and the more optimistic assumptions of K14. These models produce estimates of LSL in 10 year increments, so the values were linearly interpolated to annual time steps. Transition probabilities were estimated empirically using observed counts of pairwise transitions for each of the 10 000 simulations. Given an estimate of this transition matrix, the transition probability for local sea level rise can be calculated (defining

an index i_L by $\ell = L_{i_L}$) as

$$\mathrm{P}(i'_L|s,a) = \mathrm{P}(i'_L|i_L) = \mathbb{L}_{i_L,i'_L}, \tag{7.2}$$

where n_L is the number of discrete states created for LSL. In total six separate transition matrices were created for LSL: the RCP scenarios and physical models used are summarized in table 7.2. For each transition matrix, LSL was discretized to n_L values (table 7.1). Figure 7.1 shows simulations of LSL from each of the six transition matrices; this lag-1 Markov model credibly represents the full model dynamics shown in figs. 7.2 and 7.3.

In addition to secular LSL rise, coastal floods depend on storm surges (y'). As shown in fig. 7.4, annual-maximum storm surges at Delfzijl exhibit some autocorrelation. This temporal structure was also modeled following a first-order Markov process for a LFV state variable x. Conditional on the state x, the storm surge y' was modeled following a Normal distribution with mean μ_x and standard deviation σ_x (exact values given in table 7.1). Rather than estimating an empirical transition matrix, however, a set of hypothetical transition matrices were generated, depending on a parameter $\tau \in (0, 1]$ governing the persistence of each LFV state:

$$\mathbb{X}_{ij}(\tau) = \frac{\tau^{(j-i+1) \bmod n_X}}{\sum_{i=1}^{n_X} \tau^i} \quad \text{for} \quad i,j = 1,\ldots,n_X \tag{7.3}$$

where mod indicates the modulo operator. Since eq. (7.3) matrix structure makes $\mathbb{X}$ quasi-periodic and symmetric, the marginal distribution of $\tilde{y}$ is independent of τ. As $\tau \to 0$, the persistence increases and the system evolves slowly and predictably; as $\tau \to 1$ the transitions become completely random. Thus, changing τ can be interpreted as a change in hypothetical medium-range climate predictability. The transition matrices shown are plotted in fig. 7.5 for all values of τ used in this study. Because of the assumed structure of the model, the formal transition probability for the LFV state depends only on x:

$$\mathrm{P}(x'|s,a) = \mathrm{P}(x'|x) = \mathbb{X}_{x,x'}. \tag{7.4}$$

The values of μ and σ shown in table 7.1 are based on values derived from a hidden Markov model (HMM) applied to observed storm surges (fig. 7.4b), but the HMM's transition matrix

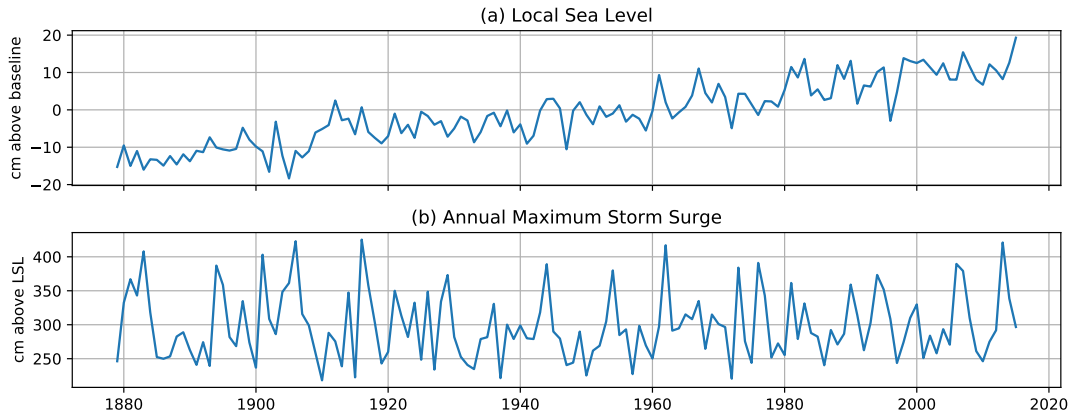

Figure 7.4: Historical flood data at Delfzijl, Netherlands (data adapted from *Oddo et al.*, 2017). (a): annual average of daily-mean sea level measurements, relative to baseline, in cm. (b): annual maximum of superimposed storm surges (calculated by subtracting the mean sea level from the maximum height recorded), also in cm.

was not used; instead $\mathbb{X}$ comes from eq. (7.3).

The last state variable is the levee height h. Possible levee heights are discretized to $0, 25, 50, \ldots, 1500$ cm. Although h is managed directly by the decision-maker, it is still stochastic: if a peak flood overtops the levee, the structure is destroyed and $h \leftarrow 0$, triggering a decision about whether (and how high) to rebuild. Since storm surges y' are modeled following a Normal distribution conditional on the LFV state, the probability of flooding is given by the Gaussian survival function

$$P_{\text{flood}}(s, a) = P_{\text{flood}}(h, \ell, x, a) = 1 - \frac{1}{2}\left[1 + \text{erf}\left(\frac{h + a - \ell - \mu_x}{\sigma\sqrt{2}}\right)\right], \tag{7.5}$$

where erf is the error function, h is the levee height, ℓ is the LSL, μ_x is the expected storm surge for LFV state x, and σ is the within-state standard deviation of storm surges. The levee height therefore evolves in time following

$$\text{P}(h'|s, a) = \text{P}(h'|h, \ell, x, a) = \begin{cases} 1 - P_{\text{flood}}(h, \ell, x) & h' = h + a \\ P_{\text{flood}}(h, \ell, x) & h' = 0 \\ 0 & \text{else.} \end{cases} \tag{7.6}$$

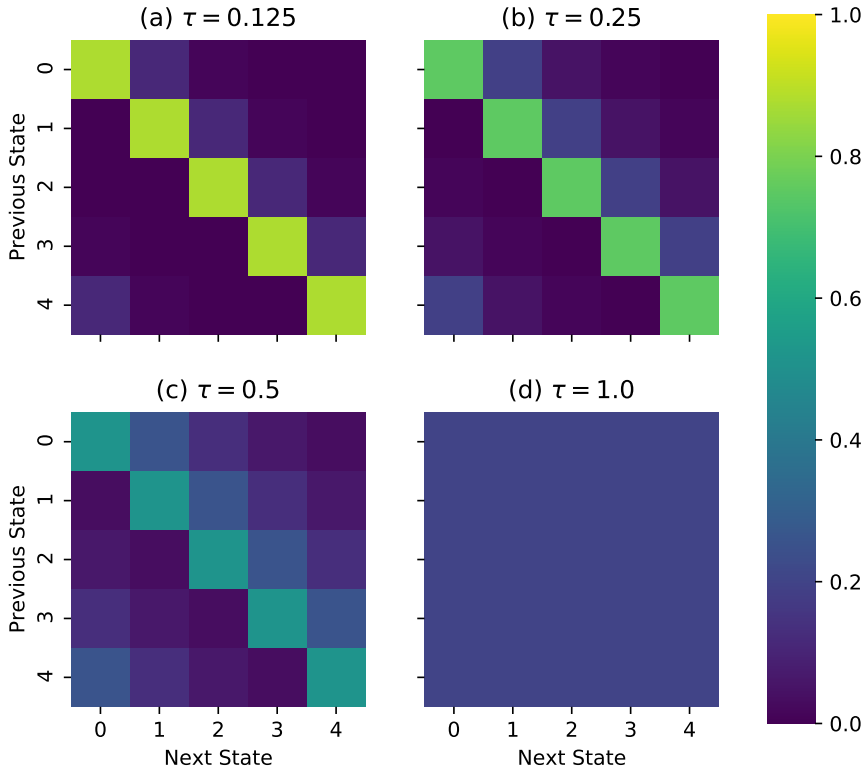

Figure 7.5: The transition matrices LX that specify $\mathrm{P}(x'|x,\tau)$ (eq. 7.4) for all value of τ.

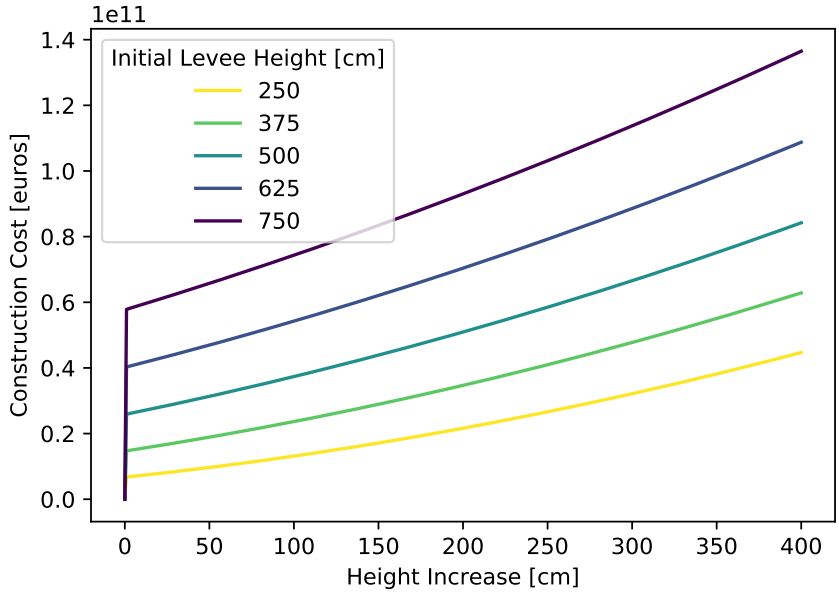

Figure 7.6: Construction costs increase quadratically with the initial levee height, in cm, and with the amount by which to raise the levee, and are discontinuous at zero. The exact equation is given by eq. (7.7) with parameters from table 7.1.

7.2.2 Cost Functions

At each time step, the decision-maker must decide whether to raise the levee, and if so by how much. The cost of raising the levee from h cm to $(h + a)$ cm is

$$c_c(s, a) = c_c(h, a) = \alpha_1 a^2 + \alpha_2 h + \alpha_3; \tag{7.7}$$

we use the values of $\{\alpha_1, \alpha_2, \alpha_3\}$ from *Eijgenraam et al.* (2012) for dike ring 16, as reproduced in table 7.1. Figure 7.6 plots this function for several values of h and for all $a \in \mathcal{A}$. Importantly, eq. (7.7) is discontinuous at $a = 0$; this reflects large fixed costs of construction such as permitting, equipment procural, engineering design, and covering the levee surface. Thus, a policy based on incrementally heightening the levee every few years is prohibitively expensive.

The second lever available to the decision-maker is implicit: the residual flood risk is covered through an index insurance contract which is renewed every year. Specifically, the

contract pays out v dollars:

$$v(t) = v_0(1 + \tau_v)^{t-t_0} \tag{7.8}$$

if the maximum flood height y overtops the levee. This makes the strong assumption that the value insured (representing the value of property lost and costs of evacuation) is unaffected by flood events. Although we assume that decisions are made every year and that insurance contracts are priced fairly, it is unreasonable to allow the insurance price to reflect concurrent climate information. The insurance rate is therefore assumed to reflect the distribution of floods by keeping sea level ℓ constant but looking forward one step in time for low-frequency variability x. In other words, the pricing of the next year's contract reflects a prediction of flood risk for the next year considering the levee height, the current sea level, and the full distribution for the next year's LFV index. The cost of insuring residual risk is therefore

$$c_i(s) = c_i(h, t, x) = v(t)\big\{\mathbb{E}\big[P'_{\text{flood}}\big] + \lambda\sigma\big[P'_{\text{flood}}\big]\big\}, \tag{7.9}$$

where

$$\mathbb{E}\big[P'_{\text{flood}}\big] = \sum_{x'=1}^{n_X} \mathrm{P}(x'|x) P_{\text{flood}}(h, \ell, x', a) \tag{7.10}$$

and

$$\sigma\big[P'_{\text{flood}}\big] = \left\{ \sum_{x'=1}^{n_X} \mathrm{P}(x'|x) \big[P_{\text{flood}}(h, \ell, x', a) - \mathbb{E}\big[P'_{\text{flood}}\big]\big]^2 \right\}^{1/2}. \tag{7.11}$$

The penalty in eq. (7.9) is equivalent to the Wang transform (*Wang*, 2002) if P_{flood} is assumed to be normally distributed; previous work on weather derivatives has found $\lambda = 0.25$ to be a reasonable value (*Hamilton et al.*, 2020; *Foster et al.*, 2015).

Combining these two costs, the total reward r at each time step is defined as $r = -c_c - c_i$.

7.2.3 Experiment Design

The state-value function eq. (7.1) was solved for each combination of structural or deep uncertainties, listed in table 7.2, using the recursive search approach of algorithm 1. The algorithm was implemented in python using efficient well-documented open-source libraries (*Lam et al.*, 2015; *Köster and Rahmann*, 2012; *Hunter*, 2007; *van der Walt et al.*, 2011; *Hoyer*

Symbol	Value	Description	Unit
α_1	0.102	Quadratic construction cost term	Million Euros per cm^2
α_2	3.20	Linear construction cost term	Million Euros per cm
α_3	319	Fixed cost of construction	Million Euros
v_0	22 700	Initial exposure	Million Euros
t_0	2020	Start year	year
τ_V	0.0100	Real exposure growth rate	year^{-1}
n_L	100	Number of discrete states for LSL	count
n_H	61	Number of possible levee heights	count
n_X	5	Number of discrete LFV states	count
h_0	425	Initial levee height	cm
μ_1	242	Expected storm surge in state 1	cm
μ_2	278	Expected storm surge in state 2	cm
μ_3	287	Expected storm surge in state 3	cm
μ_4	326	Expected storm surge in state 4	cm
μ_5	386	Expected storm surge in state 5	cm
σ_1	12.0	Standard deviation of storm surge for state 1	cm
σ_1	16.2	Standard deviation of storm surge for state 2	cm
σ_1	12.6	Standard deviation of storm surge for state 3	cm
σ_1	21.2	Standard deviation of storm surge for state 4	cm
σ_1	23.4	Standard deviation of storm surge for state 5	cm
λ	0.250	Risk premium for insurance contract	

Table 7.1: Exact value of parameters used

and Hamman, 2017); codes are available at `https://github.com/jdossgollin/2020-sequential-adaptation`. Rather than assigning a terminal value to the final state, the model was run to the year 2220 and all results after 2120 were discarded.

Description	Values used
Physical model for LSL	DP16, K14
RCP scenario	2.6, 4.5, 8.6
Discount rate $1 - \gamma$	1%, 4%, 7%
Climate predictability parameter τ	0.125, 0.25, 0.5, 1.0

Table 7.2: Deep uncertainties and model structural uncertainties were treated by calculating the state-value function separately for each combination of parameters (i.e., the outer product).

Algorithm 1: Exact solution method for discretized state-value function.

Input: Vector T of length n_T giving time steps in 1 year increments
Input: Vector H of length n_H giving possible levee heights
Input: Vector L of length n_L giving possible local mean sea levels
Input: Vector M of length n_X giving mean storm surge for each LFV state
Input: Real σ giving state-conditional standard deviation of storm surge
Input: Matrix $\mathbb{X}$ of shape $n_X \times n_X$ giving LFV state transition probabilities
Input: Matrix $\mathbb{L}$ of shape $n_L \times n_L$ giving LSL transition probabilities
Input: Real discount rate $1 - \gamma$
Output: State-value function V of shape $[n_T, n_H, n_L, n_X]$
Initialize state-value $V = 0$;
for $i_T = n_T - 1, n_T - 2, \ldots, 1$ **do**
  Assign $t = T_{n_{i_T}}$;
  Calculate $v(t)$ following eq. (7.8);
  for $i_H = 1, \ldots, n_H$ **do**
    Assign $h = H_{i_H}$;
    Define possible levee increases: $A = H_{i_H + i_A} - H_{i_H}$ for $i_A = 0, \ldots, n_H - i_H$;
    for $i_L = 1, \ldots, n_L$ **do**
      Assign $\ell = L_{i_L}$;
      for $i_X = 1, \ldots, n_X$ **do**
        Assign $x = X_{i_X}$;
        Define $s = \{t, h, \ell, x\}$;
        Initialize state-action values $Q = 0$;
        for $i_A = 0, \ldots, n_H - i_H$: **do**
          Assign $a = A_{i_A}$;
          Calculate $c_c(h, a)$ from eq. (7.7);
          Calculate $c_i(s, a)$ from eq. (7.9);
          $r \leftarrow -c_c - c_i$;
          for h' *in* H **do**
            Calculate $\mathrm{P}(h'|s, a)$ from eq. (7.6);
            for ℓ' *in* L **do**
              Calculate $\mathrm{P}(\ell'|s, a)$ from eq. (7.2);
              for x' *in* X **do**
                Calculate $\mathrm{P}(x'|s, a)$ from eq. (7.4);
                $\mathrm{P}(s'|s, a) \leftarrow P(h'|s, a)P(\ell'|s, a)P(x'|s, a)$;
                $Q_{i_A} \leftarrow r + \gamma P(s'|s, a)V_{t+1,h',\ell',x'}$;
        $V_{t,h,\ell,x} \leftarrow \max Q$;

7.3 Results and Discussion

The SDP model identifies the optimal (cost-minimizing) levee heightening each year, as a function of levee height, sea level, and LFV state.

7.3.1 Optimal Levee Heightening

The first question considered is the sensitivity of the optimal levee heightening to assumptions regarding long-term sea level rise. One way to answer this question is to extract from the full solution the optimal amount by which to heighten the levee at the first time step (in 2020), shown for different assumptions in table 7.3. This table generally indicates that it is optimal to not increase the levee height, though for the lowest discount rate and the most extreme LFV state it does advise to heighten the levee by an amount that depends mainly on the scenario of sea level rise considered. Interestingly, the one scenario for which the model does not recommend heightening the levee – even in the highest-risk LFV state – is the DP16 RCP 8.5 scenario shown in fig. 7.1c. This reflects that while this is the scenario with the highest eventual sea level rise, it is also that with the greatest intra-scenario uncertainty. It is therefore advantageous to defer investment until this uncertainty is partially resolved.

Similarly, fig. 7.7(d-f) shows simulations of levee height as a function of time for different simulations from the DP16 model with a 4% discount rate. In these simulations all levees are eventually heightened to a level specific to the RCP scenario and physical model. However, the timing of these height increases varies widely between different simulations. Results are qualitatively similar for different values of τ and discount rate and for the other physical model (see figs. 7.8 to 7.10). These illustrate that deferring an investment in physical infrastructure does not preclude its eventual implementation, but merely defers it until a later date, partially discounting construction costs on the grounds of opportunity cost: resources invested in levees are not improving schools, supporting public health programs, or alleviating poverty. Once the near-term benefits (here lower insurance premiums) of heightening outweigh the costs, the levee is raised. If the levee height were lower ($h_0 = 375\,\text{cm}$), the model recommends immediate heightening as shown in table 7.4.

This model's guidance to not raise levees in 2020 should not be interpreted as implying

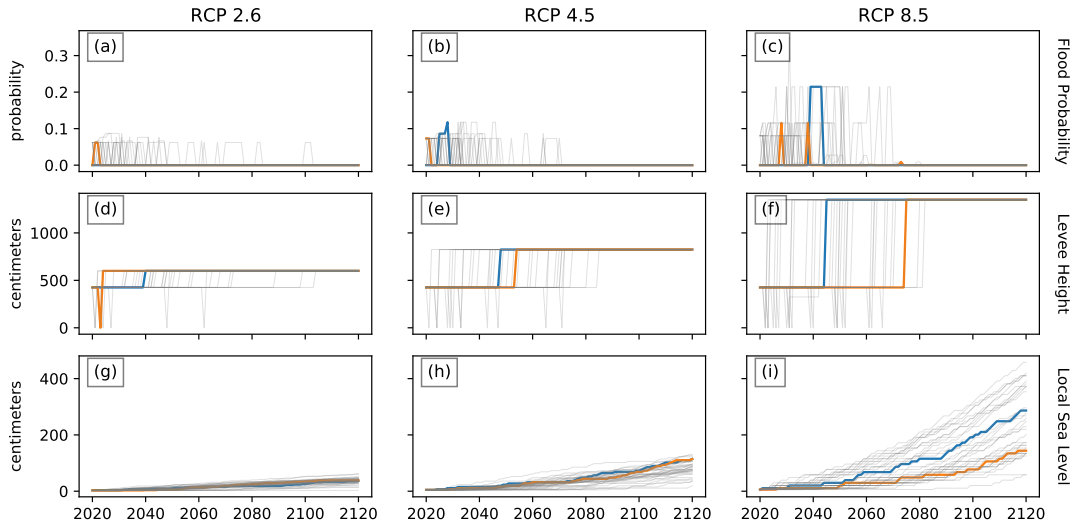

Figure 7.7: Simulations from the SDP model show that the optimal amount by which to heighten the levee is dominated by assumed future LSL conditions, but that levee heightening should be delayed. This (i) delays construction costs until the future, which is discounted, and (ii) allows some uncertainties to resolve over time. All simulations shown are exchangeable – two are highlighted (one blue and one orange) at random in order to more easily visualize specific trajectories. Results shown here for DP16 model with $\tau = 0.25$ and a 4% discount rate.

that communities should do nothing in the face of long-term climate challenges, but reflects that the only levers available in this model are levees and insurance. Real-world communities have many other levers available for flood risk management, including land use management (*Blum et al.*, 2020), buyouts (*BenDor et al.*, 2020), early warning systems (*Bedient et al.*, 2000), and exposure management (particularly important since structural risk management can increase exposure via the "levee effect"; *Barendrecht et al.*, 2017; *Di Baldassarre et al.*, 2018a; *Tobin*, 1995).

7.3.2 Robustness of Over- or Under-Design

We next turn to the question of whether making immediate capital investments in anticipation of the eventual emergence of worst-case scenarios is a robust response to large but distant and uncertain risks. In this model sea level rise is large and inevitable, but its timing and magnitude vary dramatically between the most optimistic (fig. 7.1d) and pessimistic (fig. 7.1c) scenarios. The possibility of this scenario motivates the consideration of building large levees

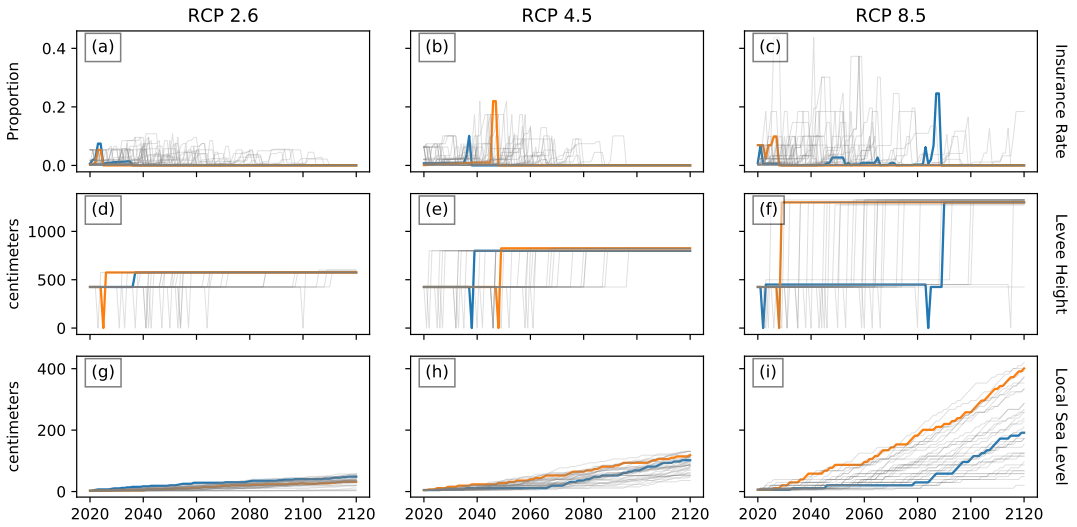

Figure 7.8: As fig. 7.7 (using the DP16 model and $\tau = 0.25$) but with a 7% discount rate.

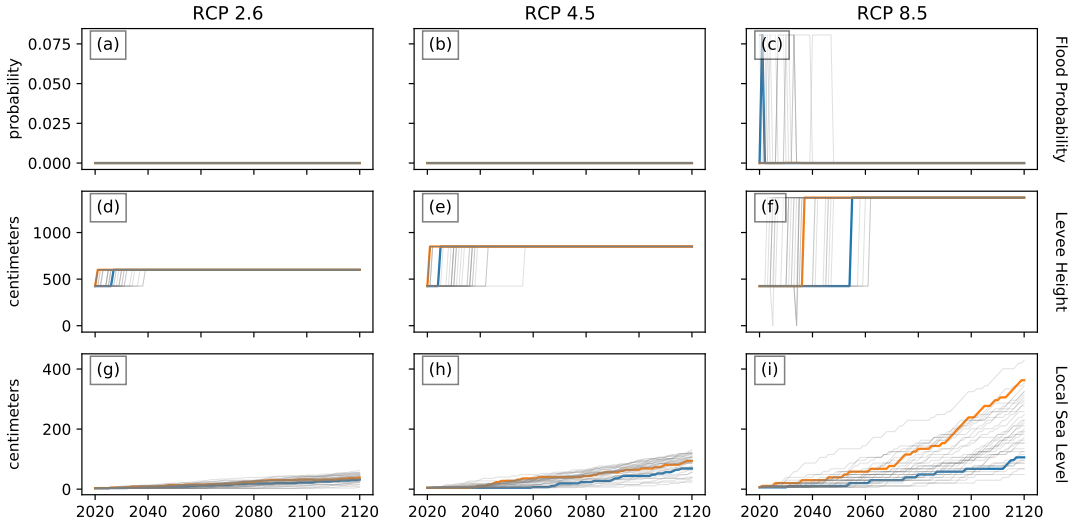

Figure 7.9: As fig. 7.7 (using the DP16 model and $\tau = 0.25$) but with a 1% discount rate.

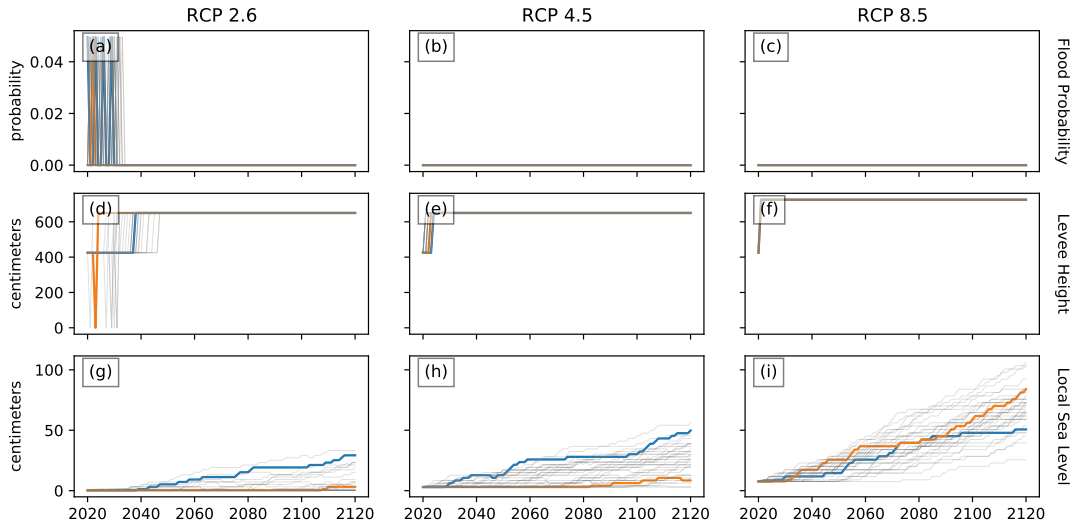

Figure 7.10: As fig. 7.7 but for the K14 model, $\tau = 1.0$, and a 1% discount rate.

today in order to be protected against all plausible scenarios.

Yet this approach is in fact highly fragile to the choice of scenario used. Figure 7.11 shows the expected scenario-conditional regret as a function of levee height increase for each RCP scenario, discount rate, and physical model, fixing τ and x. The scenario-conditional regret is defined as the difference in expected discounted costs over the adaptation pathway between (i) raising the levee by a given amount in 2020, then following the optimal investment strategy for a given strategy thereafter; and (ii) raising the levee in 2020 by the optimal amount. This value therefore answers the question "what is the expected cost penalty, for a particular probabilistic model of sea level rise, of raising the levee by a given amount?" It implicitly assumes that the optimal investment policy, for each scenario, is known after the first time step – in other words, in 2021 the decision-maker knows which RCP scenario and model govern the system and is able to optimize accordingly. By definition, the optimal action for a given scenario has an expected scenario-conditional regret of 0.

Like table 7.3, fig. 7.11 shows that the optimal decision, if you know you are in a particular scenario, is sometimes to raise the levee. However, raising the levee is not a robust strategy (as defined in *Herman et al.*, 2015): the optimal heightening for a moderate climate scenario ($<$ 250 cm) has very high regret for a more extreme scenario (c), and vice-versa. This is because under construction cost function used (eq. (7.7) and fig. 7.6), it is more costly to build

incrementally than to build just once. If the levee is raised too high, resources are wasted, but if the levee is raised too little it will need to be raised again in the future, incurring additional costs. This illustrates that under deep uncertainty, deferring large static expenditures – when this preserves the flexibility and adaptive capacity of the system – can be a robust decision. Results for different values of τ, and for different initial LFV states, are qualitatively similar (figs. 7.12 and 7.14).

It is also informative to examine when the model does recommend heightening. Figures 7.9 and 7.10 shows simulations from the K14 model with $\tau = 1.0$ and a 1% discount rate. In this case near-term risks are high (because the of initial LFV state), there is zero predictability ($\tau = 1.0$), and uncertainties as to future sea level rise are small (because it uses the K14 model). Under these conditions, the model recommends early heightening. However, fig. 7.11 shows that even though heightening is the optimal choice if the RCP scenario and model are known, deferring heightening is robust to model structure uncertainty.

7.3.3 Reducing Costs Through Near-Term Predictability

We finally consider whether improving the potential predictability of flood risk can reduce long-term adaptation costs.

The simulations shown in fig. 7.7 indicate that flood risk varies significantly from year to year (a-c), reflecting the changing LFV state over time. The different distribution of storm surges in each state leads to very different flood probabilities in each, and this is also reflected in the insurance premium (not shown). This suggests that being able to predict these variations could inform timing decisions for levee heightening: if the climate is in a low-risk state and likely to remain in one for the foreseeable future, there is no need to raise the levee but if the climate is in a high-risk state the levee should be heightened.

We explore this quantitatively by varing τ, a parameter that describes the intrinsic persistence and predictability of the LFV state: as $\tau \to 0$ the climate becomes highly persistent and predictable and as $\tau \to 1$ the state-conditional distribution of storm surges converges to the marginal distribution (eqs. (7.3) and (7.4)). Figure 7.15 shows the expected costs over the adaptation pathway of being in a particular state as a function of the initial LFV state

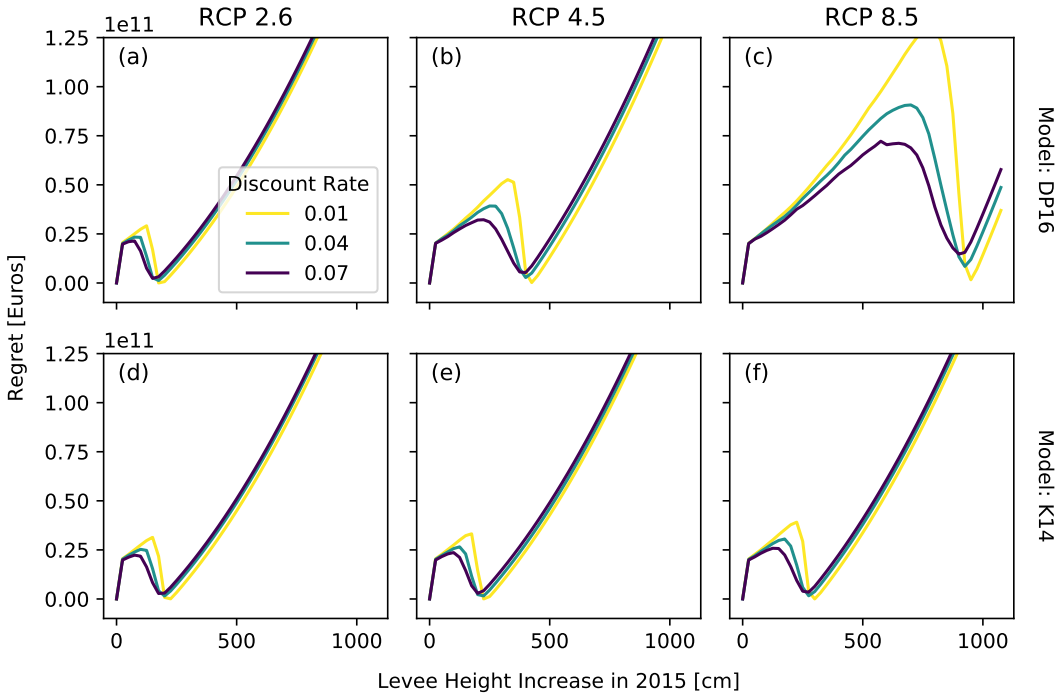

Figure 7.11: Under deep and model structure uncertainty, deferring capital expenses can be a robust solution. The y-axis shows the expected scenario-conditional regret as a function of levee height increase in 2020 for each physical model, RCP scenario, and discount rate. Although a height increase of 0 (deferring construction) is not the optimal solution for all scenarios, it has low regret for all; conversely heightening the levee by an amount which is optimal for one scenario may have very high regret in another. Here $\tau = 1.0$ and $x_0 = 4$.

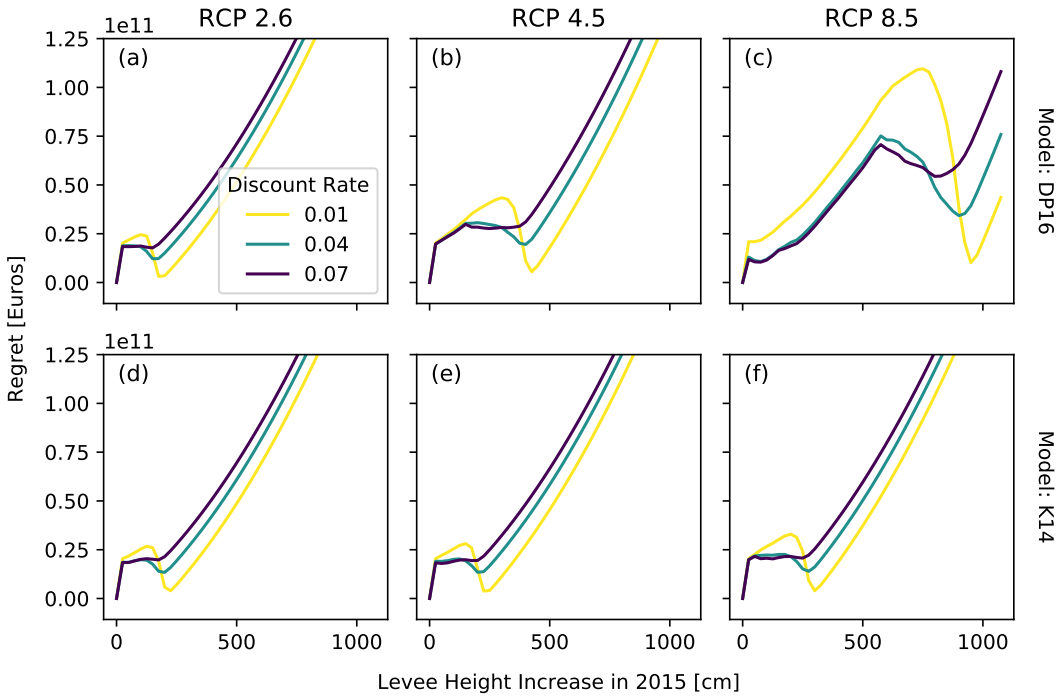

Figure 7.12: As fig. 7.11 but for $\tau = 0.125$ and initial LFV state 0.

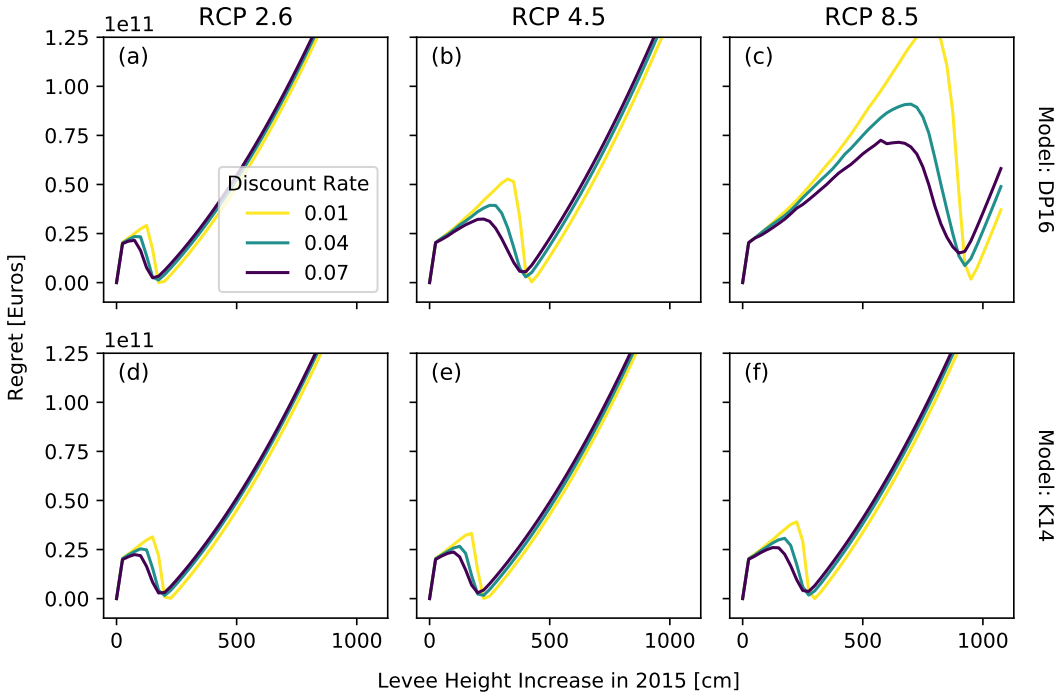

Figure 7.13: As fig. 7.11 ($\tau = 1.0$) but for initial LFV state 0.

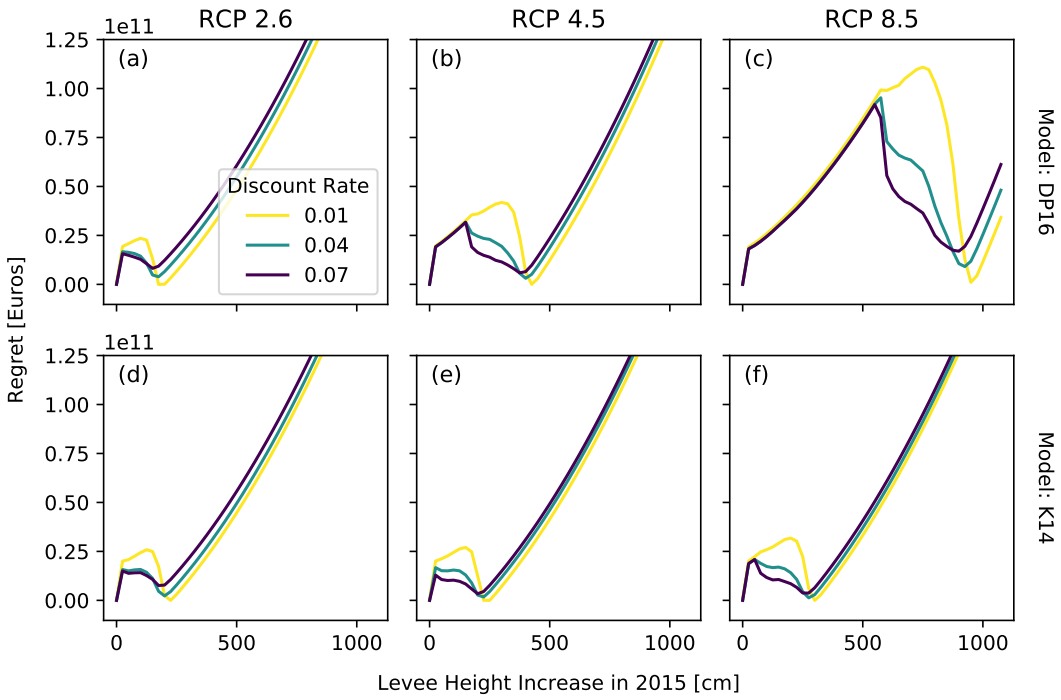

Figure 7.14: As fig. 7.11 (initial LFV state 4) but for $\tau = 0.125$.

and of τ for different RCP scenarios. If $\tau < 1$ then the expected costs over the adaptation pathway are less for low-risk LFV states than for high risk LFV states. Further, for all but the highest-risk LFV state, the savings resulting from increased predictability (lower τ) are of order 5×10^9 Euro, which is comparable to the cost difference between RCP 4.5 and RCP 2.6.

Unsurprisingly, more severe climate scenarios lead to higher costs over the adaptation pathway. This underscores that the value of deferring capital investments in this study, which considers adaptation under exogenous and dynamic uncertainty, does not imply a high value deferring investments in climate change mitigation. In particular, increasing the severity of the sea level rise scenario reduces flexibility and optionality for the decision-maker. Since climate mitigation reduces the uncertainty in future climate risk (*Daniel et al.*, 2019), our results emphasize that mitigation creates value by increasing the options available to decision-makers.

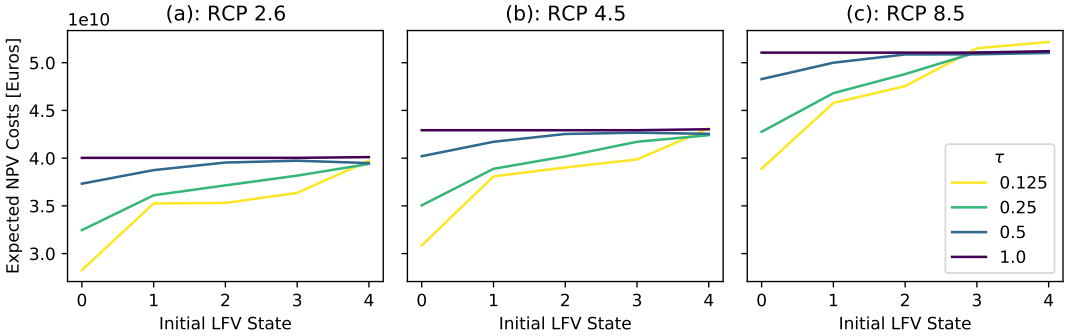

Figure 7.15: Increasing climate predictability dramatically lowers expected costs over the adaptation pathway. Shown are expected discounted total costs over the adaptation pathway as a function of RCP scenario, initial LFV state, and degree of climate predictability (τ). Results are shown for K14 model and intermediate discount rate (4%). When starting at RCP 4.5 with $\tau = 0.5$ in initial LFV state 2, the decrease in expected future costs by increasing predictability so that $\tau = 0.25$ is approximately equal to that of leaving $\tau = 0.5$ but moving to RCP 2.6.

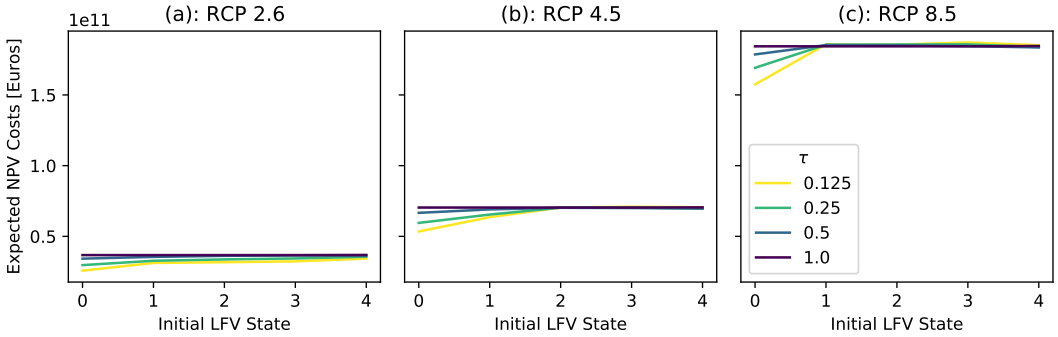

Figure 7.16: As fig. 7.15 (discount rate 4%) but for DP16 model.

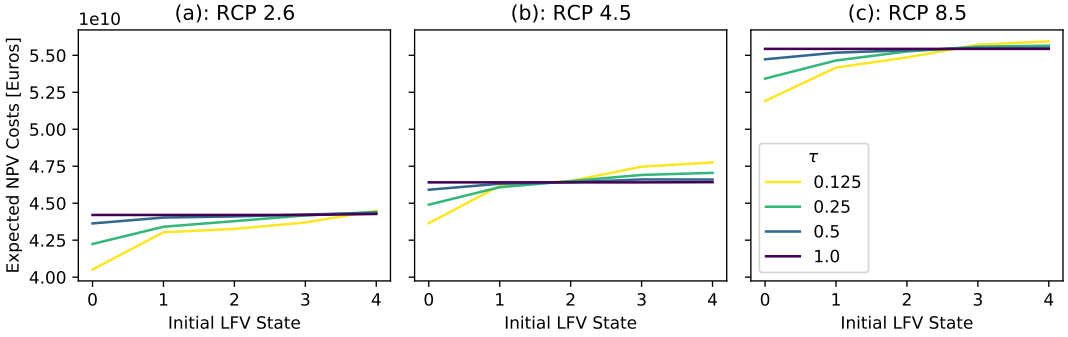

Figure 7.17: As fig. 7.15 (K14 model) but for 1% discount rate.

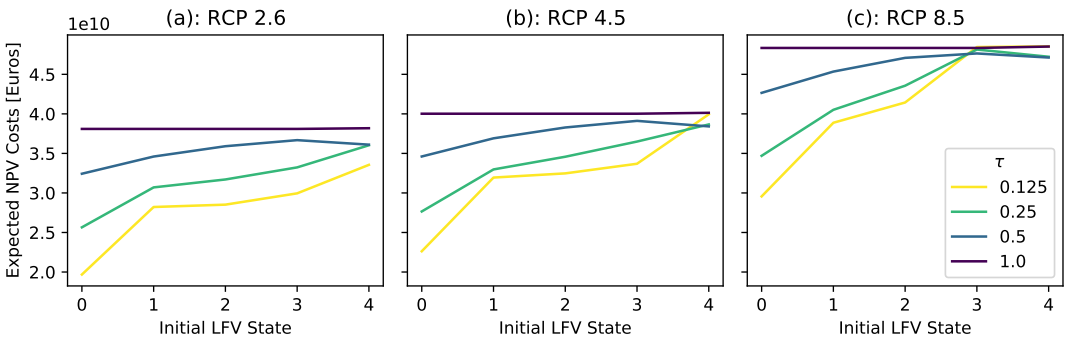

Figure 7.18: As fig. 7.15 (K14 model) but for 7% discount rate.

7.4 Summary and Implications

Coastal communities around the world facing inevitable but uncertain sea level rise face a challenging decision: build infrastructure today that is robust to worst-case scenarios of sea level rise over its design life, or instead build cheaper infrastructure that may not perform acceptably under all scenarios. This is, however, a false dichotomy: adaptation is sequential, and so decision-makers who choose not to build today can – in an idealized world free of time-sensitive funding mechanisms – instead build tomorrow. In this paper we consider a didactic case study in the Netherlands and identify the cost-minimizing levee heightening as a function of time, levee height, local sea level, and LFV state for each of several RCP scenarios, discount rates, physical models of sea level rise, and degrees of intrinsic predictability of the climate system that governs storm surges. We find that

1. even when large sea level rise is anticipated for the future, the decision to invest in structural risk protection is dominated by near-term risks;
2. soft risk protection instruments preserve options and performance over a wide range of future scenarios while hard instruments designed for one scenario perform poorly in another; and
3. as the potential predictability of near-term hydroclimate risk increases, soft adaptation strategies can be more precisely designed to manage near-term risks, thereby lowering long-term adaptation costs.

In this paper we considered only uncertainty in sea level rise. Real-world planners must

confront deep uncertainties including levee strength and failure probability (physical), the future rate of growth and vulnerability within the polder and the recovery after a flood event (socio-economic), future technologies for structural flood risk protection (technological), and the costs of capital finance, insurance premiums, infrastructure maintenance, and construction (financial). Our results show that in general, increasing the magnitude of dynamic uncertainties leads to a greater preference for deferring static investments, and so our results are likely a lower bound on the preference for not raising the levees today.

Although we find that making large investments today to protect against risks that will emerge only after several decades does not, in general, justify the opportunity costs associated, this does not imply that climate change should be neglected in engineering design. First, we show that as climate change worsens, adaptation costs grow. This emphasizes the value of early and decisive action for climate change mitigation. Second, we show that when large investments are eventually made, they need to take climate change into consideration so that expensive retrofitting is not required.

Our findings are relevant for a broad range of problems in climate adaptation and infrastructure transformation where (i) credible probabilistic S2D climate risk forecasts are available; and (ii) uncertainties are deep and dynamic; (iii) fixed capital costs are high. Of course, the financial and regulatory processes governing levee heightening in most parts of the world are slow and deliberative by design, complicating efforts to develop adaptive plans. These findings underscore a need for adaptive regulatory frameworks, possibly by granting permits and funds for future structural investments to be made when fixed conditions (i.e., "signposts" *Raso et al.*, 2019; *Haasnoot et al.*, 2013) are met. These results can also directly inform decision problems in the private sector, including home elevation and other building-scale flood resilience problems that are not "wicked" (*Rittel and Webber*, 1973) and where deliberative political processes are not required.

Table 7.3: Cost-minimizing first-year (2020) height increases for initial levee height 425 cm above sea level for different combinations of (columns) the physical model for local sea level rise and RCP scenario and (rows) discount rate, rate parameter describing low-frequency variability, and storm surge (mean, standard deviation).

		LSL Model	DP16			K14		
		RCP Scenario	2.6	4.5	8.5	2.6	4.5	8.5
Discount Rate	LFV Rate τ	Storm Surge						
0.01	0.125	(241.6, 12.0)	0	0	0	0	0	0
		(278.3, 16.2)	0	0	0	0	0	0
		(287.1, 12.6)	0	0	0	0	0	0
		(325.9, 21.2)	0	0	0	0	0	0
		(386.3, 23.4)	175	425	0	225	250	300
	0.250	(241.6, 12.0)	0	0	0	0	0	0
		(278.3, 16.2)	0	0	0	0	0	0
		(287.1, 12.6)	0	0	0	0	0	0
		(325.9, 21.2)	0	0	0	0	0	0
		(386.3, 23.4)	175	425	0	225	225	300
	0.500	(241.6, 12.0)	0	0	0	0	0	0
		(278.3, 16.2)	0	0	0	0	0	0
		(287.1, 12.6)	0	0	0	0	0	0
		(325.9, 21.2)	175	0	0	0	225	300
		(386.3, 23.4)	175	425	0	225	225	300
	1.000	(241.6, 12.0)	175	0	0	0	0	300
		(278.3, 16.2)	175	0	0	0	0	300
		(287.1, 12.6)	175	0	0	0	0	300
		(325.9, 21.2)	175	0	0	0	0	300
		(386.3, 23.4)	175	0	0	0	225	300
0.04	0.125	(241.6, 12.0)	0	0	0	0	0	0
		(278.3, 16.2)	0	0	0	0	0	0
		(287.1, 12.6)	0	0	0	0	0	0
		(325.9, 21.2)	0	0	0	0	0	0
		(386.3, 23.4)	0	0	0	0	0	0
	0.250	(241.6, 12.0)	0	0	0	0	0	0
		(278.3, 16.2)	0	0	0	0	0	0
		(287.1, 12.6)	0	0	0	0	0	0
		(325.9, 21.2)	0	0	0	0	0	0
		(386.3, 23.4)	0	0	0	0	0	0
	0.500	(241.6, 12.0)	0	0	0	0	0	0
		(278.3, 16.2)	0	0	0	0	0	0
		(287.1, 12.6)	0	0	0	0	0	0
		(325.9, 21.2)	0	0	0	0	0	0
		(386.3, 23.4)	0	0	0	0	0	0
	1.000	(241.6, 12.0)	0	0	0	0	0	0
		(278.3, 16.2)	0	0	0	0	0	0

Continued on next page

Discount Rate	LFV Rate τ	LSL Model / RCP Scenario / Storm Surge	DP16 2.6	DP16 4.5	DP16 8.5	K14 2.6	K14 4.5	K14 8.5
		(287.1, 12.6)	0	0	0	0	0	0
		(325.9, 21.2)	0	0	0	0	0	0
		(386.3, 23.4)	0	0	0	0	0	0
0.07	0.125	(241.6, 12.0)	0	0	0	0	0	0
		(278.3, 16.2)	0	0	0	0	0	0
		(287.1, 12.6)	0	0	0	0	0	0
		(325.9, 21.2)	0	0	0	0	0	0
		(386.3, 23.4)	0	0	0	0	0	0
	0.250	(241.6, 12.0)	0	0	0	0	0	0
		(278.3, 16.2)	0	0	0	0	0	0
		(287.1, 12.6)	0	0	0	0	0	0
		(325.9, 21.2)	0	0	0	0	0	0
		(386.3, 23.4)	0	0	0	0	0	0
	0.500	(241.6, 12.0)	0	0	0	0	0	0
		(278.3, 16.2)	0	0	0	0	0	0
		(287.1, 12.6)	0	0	0	0	0	0
		(325.9, 21.2)	0	0	0	0	0	0
		(386.3, 23.4)	0	0	0	0	0	0
	1.000	(241.6, 12.0)	0	0	0	0	0	0
		(278.3, 16.2)	0	0	0	0	0	0
		(287.1, 12.6)	0	0	0	0	0	0
		(325.9, 21.2)	0	0	0	0	0	0
		(386.3, 23.4)	0	0	0	0	0	0

Table 7.4: Cost-minimizing first-year (2020) height increases for initial levee height 375 cm above sea level for different combinations of (columns) the physical model for local sea level rise and RCP scenario and (rows) discount rate, rate parameter describing low-frequency variability, and storm surge (mean, standard deviation).

		LSL Model	DP16			K14		
		RCP Scenario	2.6	4.5	8.5	2.6	4.5	8.5
Discount Rate	LFV Rate τ	Storm Surge						
0.01	0.125	(241.6, 12.0)	0	0	0	0	0	0
		(278.3, 16.2)	0	0	0	0	0	0
		(287.1, 12.6)	225	475	0	275	275	350
		(325.9, 21.2)	225	475	1000	275	275	350
		(386.3, 23.4)	225	475	1000	275	300	350
	0.250	(241.6, 12.0)	0	0	0	0	0	0
		(278.3, 16.2)	225	0	0	275	275	350
		(287.1, 12.6)	225	475	0	275	275	350
		(325.9, 21.2)	225	475	1000	275	275	350
		(386.3, 23.4)	225	475	1000	275	275	350
	0.500	(241.6, 12.0)	225	475	0	275	275	350
		(278.3, 16.2)	225	475	1000	275	275	350
		(287.1, 12.6)	225	475	1000	275	275	350
		(325.9, 21.2)	225	475	1000	275	275	350
		(386.3, 23.4)	225	475	1000	275	275	350
	1.000	(241.6, 12.0)	225	475	1000	275	275	350
		(278.3, 16.2)	225	475	1000	275	275	350
		(287.1, 12.6)	225	475	1000	275	275	350
		(325.9, 21.2)	225	475	1000	275	275	350
		(386.3, 23.4)	225	475	1000	275	275	350
0.04	0.125	(241.6, 12.0)	0	0	0	0	0	0
		(278.3, 16.2)	0	0	0	0	0	0
		(287.1, 12.6)	0	0	0	0	0	0
		(325.9, 21.2)	225	450	0	250	275	325
		(386.3, 23.4)	225	450	975	250	275	325
	0.250	(241.6, 12.0)	0	0	0	0	0	0
		(278.3, 16.2)	0	0	0	0	0	0
		(287.1, 12.6)	0	0	0	0	0	0
		(325.9, 21.2)	225	450	0	250	275	325
		(386.3, 23.4)	225	450	975	250	275	325
	0.500	(241.6, 12.0)	0	0	0	0	0	0
		(278.3, 16.2)	225	0	0	250	275	325
		(287.1, 12.6)	225	450	0	250	275	325
		(325.9, 21.2)	225	450	0	250	275	325
		(386.3, 23.4)	225	450	975	250	275	325
	1.000	(241.6, 12.0)	225	450	0	250	275	325
		(278.3, 16.2)	225	450	0	250	275	325

Continued on next page

Discount Rate	LFV Rate τ	LSL Model RCP Scenario Storm Surge	DP16 2.6	 4.5	 8.5	K14 2.6	 4.5	 8.5
		(287.1, 12.6)	225	450	0	250	275	325
		(325.9, 21.2)	225	450	0	250	275	325
		(386.3, 23.4)	225	450	0	250	275	325
0.07	0.125	(241.6, 12.0)	0	0	0	0	0	0
		(278.3, 16.2)	0	0	0	0	0	0
		(287.1, 12.6)	0	0	0	0	0	0
		(325.9, 21.2)	0	0	0	225	250	300
		(386.3, 23.4)	200	425	0	225	250	325
	0.250	(241.6, 12.0)	0	0	0	0	0	0
		(278.3, 16.2)	0	0	0	0	0	0
		(287.1, 12.6)	0	0	0	0	0	0
		(325.9, 21.2)	200	0	0	225	250	300
		(386.3, 23.4)	200	425	0	225	250	300
	0.500	(241.6, 12.0)	0	0	0	0	0	0
		(278.3, 16.2)	0	0	0	0	0	0
		(287.1, 12.6)	200	0	0	225	250	300
		(325.9, 21.2)	200	425	0	225	250	300
		(386.3, 23.4)	200	425	0	225	250	300
	1.000	(241.6, 12.0)	200	450	0	225	250	325
		(278.3, 16.2)	200	450	0	225	250	325
		(287.1, 12.6)	200	450	0	225	250	325
		(325.9, 21.2)	200	450	0	225	250	325
		(386.3, 23.4)	200	450	0	225	250	325

Part III

Discussion and Conclusions

What's the use of having developed a science well enough to make predictions if, in the end, all we're willing to do is stand around and wait for them to come true?

F. Sherwood Rowland

8

Policy Implications

The preceding chapters have laid out evidence for a set of specific hypotheses describing sequential climate adaptation and presented idealized experiments to probe these hypotheses. The intended audience of those chapters is scholars and researchers developing methodologies for engineering and planning practice. This chapter seeks to distill insight from the previous chapters into simple recommendations for professional engineers and policy-makers involved with infrastructure systems planning. This chapter has been published as

> Doss-Gollin, J., D. J. Farnham, M. Ho, and U. Lall (2020), Adaptation over fatalism: Leveraging high-impact climate disasters to boost societal resilience, *Journal of Water Resources Planning and Management*, *146*(4), doi: 10.1061/(ASCE)WR.1943-5452.0001190

and is reproduced with permission of all authors.

8.1 Introduction

The property damaged and the lives disrupted by recent hurricanes, floods, droughts, and water quality violations highlight the inadequacy of water infrastructure in the United States and around the world. Decisions about managing these infrastructure systems are strongly informed by societal perceptions of risk, which in turn are shaped through narratives of high-impact events in academic, governmental, commercial, and popular media.

In recent years, post-hoc analyses of high-impact water and climate disasters have increasingly focused on the role of anthropogenic climate change (ACC). This is a welcome development which helps to build support for much-needed mitigation of global greenhouse gas emissions and pushes companies, governments, and aid agencies to prepare for a changing environment. Yet climate *impacts* require a confluence of physical hazards and societal vulnerabilities, and so narratives centered only on the role of ACC can neglect the aging infrastructure, increasing development with exposure to climate risks, and inadequate maintenance that set the stage for meteorological and hydrological events to become humanitarian disasters. The fatalistic narratives that emerge, which often imply that because an event was exacerbated by climate change its consequences could not have been averted, discourage adaptive planning.

8.2 How Climate Disasters Emerge

Climate risk is defined as the product of hazard, or the probability that a particular event occurs, and exposure, which encompasses vulnerability and resilience to describe the damage that will result if the event does occur. ACC causes dynamic and thermodynamic changes that have already altered the intensity, seasonality, frequency, and location of water-related climate extremes, thereby shifting climate hazard, and further changes are anticipated. Yet analysis of recent high-impact water and climate disasters reveals that avoidable planning decisions including poor land use policy, misaligned incentives for risk taking, and inadequate physical infrastructure dramatically amplify the impact of climate hazards. Systematic analysis of global changes in exposure to floods (*Jongman et al.*, 2012) and hurricanes (*Peduzzi*

et al., 2012) emphasize that changing exposure far outpaces changing hazard in the historical record.

For example, failure of the primary and auxiliary spillways at the Oroville dam in 2017, which prompted an evacuation of the Feather River (California) basin, was widely blamed on ACC in popular and scientific (e.g., *Huang et al.*, 2018) media, despite an absence of such claims by the state management agency. While ACC may have contributed to this event both directly, by increasing the moisture-holding capacity of the atmosphere, and indirectly, by possibly favoring the persistence of the wet regime, the flows over the two spillways at the time of their failures were only 18% and 3% of the design capacities, respectively (*France et al.*, 2018). Further, continued development of highly vulnerable downstream communities increased the number of individuals and the total value of property exposed to potential flooding even though the structural deficiencies had been known and documented for several decades. Thus, while the rainy spring may have been exacerbated by ACC, the resulting flood *risk* was dominated by inadequate system planning and investment.

Recent hurricanes also illustrate the importance of local decisions in high-impact events. For example, while ACC made Hurricane Harvey's precipitation approximately 15% more intense (*Emanuel*, 2017b), unmanaged sprawl and the destruction of Bayou wetlands increased peak runoff volume and the total value of property exposed to flooding (*Jacob et al.*, 2014). Even worse, forensic infrastructure inspection in New Orleans following Hurricane Katrina revealed that unrealistic design assumptions and inadequate maintenance caused several levees to fail before design levels were reached (*Sills et al.*, 2008). Even though hurricane intensity is anticipated to increase under ACC (*Knutson et al.*, 2010), the first lesson of New Orleans and Houston is that human error, inadequate infrastructure maintenance, and inadequate risk zoning for regional growth dominate observed changes in many climate risks.

These factors have also turned unexceptional hydrological droughts into severe water shortages. For example, the 2015-17 "day zero" drought in Cape Town was described as unprecedented and linked to ACC in the public narrative. While Cape Town's reservoirs were designed primarily to supply urban demand, the government approved withdrawals for irrigation following a long wet period. These agricultural releases were maintained through

much of the drought, contributing to day zero. Although ACC is projected to increase the frequency of multi-year droughts (*Otto et al.*, 2018), similar droughts were observed in the late 1930s and early 1970s, and hydrologists had warned that they could occur again (*Muller*, 2018). Recent water crises in Mexico City, São Paulo, and Barcelona also occurred during meteorological droughts that had close analogs within the historical record. In all these cases, predictable water shortages were exacerbated by unmanaged consumption, leakage losses (in the case of Mexico City as much as 130 liters per person per day, or 40% of total supply; *Tortajada*, 2006), poor water allocation, and new agricultural water consumption. Although it is tempting to use ACC as a scapegoat, responsible authorities must better communicate to the public the ways in which short-sighted planning dramatically increases long-term risk.

8.3 Towards Constructive Narratives

Despite clear risks from ACC, local resource and infrastructure systems management still drive societal resilience to water and climate risks. Improving these built and social systems requires developing consensus for large investments and management shifts, which may be easier if ACC is presented as one of many stress factors challenging our water infrastructure. In this section we offer some suggestions for ways in which researchers and practitioners working on water infrastructure systems can discuss ACC in ways that emphasize both the need for improved local resilience, and also the need for mitigation of global greenhouse emissions.

DO discuss specific ways in which the local environment has changed over the design life of existing infrastructure. Even where detailed attribution studies that assess the causal effect of specific forcings are not available, observational evidence can be connected to collective memory. For example, changes in snow frequency have already been observed in many parts of New England (*Huntington et al.*, 2004), which has implications not only for snow management but also for stormwater design and reservoir operation. Communicating ACC by relating history and local memories to rigorous science can build credibility and help frame discussion of future changes.

DO describe how uncertainties including the extent of future greenhouse emissions, global climate dynamics, and local environment challenge long-term planning. Making costly investments for a specific, possibly worst-case, scenario that does not arrive (i.e. "over-preparation") leads to significant opportunity costs relative to other activities that may require a more immediate response. For example, while rising sea levels threaten coastal communities, it may not be financially or physically prudent to build storm walls around every continent – particularly for worst-case scenarios of sea level rise. Instead, it is important to help communities develop flexible and adaptive policies that make use of climate and demographic forecasts at many timescales.

DO NOT conflate "deep uncertainty" as to the distant future with uncertainty as to the near future. There has been successful identification and prediction of climate on sub-seasonal to decadal time scales, and this can be used to inform the development of tools to alleviate the impact of weather and climate hazards. For example, skillful prediction of the North Atlantic Oscillation could inform hurricane risk and coastal adaptation decisions along the Susquehanna river (*Toomey et al.*, 2019) or financial preparedness and disaster allocation for floods in Europe (*Zanardo et al.*, 2019). In order to use these forecasts, however, planners must embrace uncertainty and develop decision frameworks that make use of probabilistic information at many timescales.

DO talk about how local changes in development, land use, and disaster readiness have changed the consequences of a given storm. For example, better early warnings and early action plans have dramatically reduced the number of lives lost to land-falling tropical cyclones even in very poor regions (*Kumar et al.*, 2019). However, as development along waterfronts has grown, the value of property damaged for a given storm has risen dramatically. While ideas like risk, exposure, and vulnerability can seem abstract, contextualizing them within the local environment can bring them to life.

DO talk about the original design considerations relative to current needs. It is natural to pay water infrastructure little attention until something goes wrong. However, tens of thousands of dams in the United States that put life and property at risk are well beyond

their original design age, and their maintenance status is generally poor or unknown (*Ho et al.*, 2017). While recent dam failures have not had an impact as significant as the Johnstown floods of 1889 and 1977, dam failure remains a risk for many communities. Further, as the case of Cape Town illustrates, past and future changes in demographics, regulations, funding, technology, and resource management often demand that our critical infrastructure perform tasks for which was never designed.

DO NOT assume that construction is sufficient to solve infrastructure systems challenges. Well-recognized paradoxes include the "levee effect" or "safe development paradox," which describe the mechanism by which new flood protection infrastructure can lead to low perceived risk, increased development, and thus amplified impacts when extremes eventually occur. Analogs to this effect exist in water storage (increased water availability can lead to increased water demand), transportation (building highways can lower the marginal cost of driving and induce greater traffic), and many other applications. This does not imply that new structures are never needed, but rather emphasizes the need to couple them with strong governance. For example, the construction of flood protection infrastructure could be accompanied by zoning regulations that limit development in the floodplain it protects. This sort of comprehensive planning can impose order on the complex feedbacks between humans, the environment, and infrastructure systems that the safe development paradox describes.

DO consider how financial, regulatory, and technological advances can help water systems "fail safely" (*Brown*, 2010) and support resilience. Strict zoning policies can limit future sprawl and ensure that new construction in high-risk areas like the New York City waterfront can withstand anticipated storms. Decentralized water re-use networks can provide clean drinking water without requiring costly public investments in water treatment facilities, conveyance, and source development. Parametric and forecast insurance can provide funds for rapid response and recovery (*Clarke and Dercon*, 2016). The particular circumstances of each place are unique, but a public discourse that transparently evaluates a wide range of options should be promoted.

DO NOT fall back on fatalist narratives in the aftermath of natural disasters. Fatalist climate narratives divert attention from productive discussions about the use of adaptive planning and management strategies to decrease damages from similar events in the future. Promoting policies that curb excessive exposure and promote responsible upkeep of critical infrastructure may be particularly constructive.

8.4 Final Word

Deep uncertainty caused by ACC, the unpredictable performance of aging infrastructure, changing social and economic conditions, and a myriad of other factors have motivated the integration of structural and non-structural adaptation strategies for managing water infrastructure systems. These instruments represent creative and resilient solutions for climate risk adaptation, transcending traditional infrastructure design and build approaches to more integrally consider land use and financial instruments as part of a strategy for response and recovery. By communicating the challenges of climate change adaptation through a systems lens, the public can more readily assess which strategies make sense in their specific context.

Of course, the execution of thoughtful local climate adaptation plans can by no means preclude the need for dramatic action to mitigate global greenhouse gas emissions.

I changed what I could, and what I couldn't, I endured.

Dorothy Vaughan

9 Summary, Discussion, and Future Work

This chapter summarizes the key findings, discusses strengths and limitations of the approaches taken, and suggests directions for future research, focusing on real-world applications of the conceptual framework developed here.

9.1 Summary

Floods are a leading cause of death and destruction, resulting in global losses worth over $USD 60 billion in 2016 alone (*Munich Re*, 2017) and displacing at least 55 million people between 2010 and 2018 (*Brakenridge*, 2018). Historical and projected changes to both the physical mechanisms that generate floods and the socio-techno-demographic processes that control vulnerability and exposure are expected to worsen future flood losses.

This dissertation began with the premise that mechanistic understanding of the drivers

of floods in a particular location could be used to constrain and evaluate projections of future risk. Chapter 2 reviewed the literature on flood-generating mechanisms, focusing mainly on riverine floods in large mid-latitude basins. The key argument advanced in chapter 2 was that the intrinsic limitations of generic black-box modeling approaches, including general circulation models (GCMs) and local statistical distributions, limit their suitability for projecting future risks, and that mechanistic understanding is necessary to further evaluate and constrain projections. Chapter 3 illustrates this framework by exploring the climatological drivers of heavy rainfall in the Lower Paraguay River Basin (LPRB) and the sub-seasonal to seasonal (S2S) factors responsible for persistent rainfall and flooding. Rainfall forecasts from numerical models are shown to exhibit significant deficiencies in simulation of the South American Low-Level Jet (SALLJ) and its relationship with large-scale flood-generating mechanisms. However, multiple sources of predictability, including the El Niño-Southern Oscillation (ENSO), the Madden-Julien Oscillation (MJO), and the South Central Atlantic Dipole (SCAD) could inform future flood risks. Chapter 4 illustrates how mechanistic understanding might constrain projections of future hydroclimate hazard, taking as a case study regional extreme rainfall in the Ohio River Basin (ORB). Although a GCM was found not to simulate regional extreme precipitation (REP) days credibly, the model was found to credibly simulate five climate indices representing the synoptic circulations that were responsible for them, and this relationship was used to develop a probabilistic regression model. This approach can be applied to generic hydroclimate hazards around the world, though it relies on having process-based understanding of the drivers of the hazard and sufficient observational data to assess the credibility of GCM simulations.

Part II turns to the question of how one should use projections that are intrinsically uncertain and imperfect to inform risk management plans in the public and private sectors. Chapter 5 reviews the literature on planning under uncertainty and describes a philosophy for using imperfect models to inform choice in "wicked" (*Rittel and Webber*, 1973) problems embedded within complex systems. The philosophy advanced draws from the *Savage* (1954) notion of subjective probability, the *Bankes* (1993) framework of exploratory modeling, and the *Weinberg* (1972) idea of trans-science to advocate the exploration of the implications and

tradeoffs of different possible actions, *conditional* on modeling choices and assumptions that are known to be wrong (*Gelman and Shalizi*, 2013) but potentially useful (*Box*, 1976). A second premise of this chapter is that improving civil infrastructure *services* does not always require new physical structures, and that long-term planning needs to account for (i) a portfolio of different tools and strategies, (ii) evaluated within a sequential planning framework, and (iii) subject to path dependence. Chapter 6 focuses on a key distinction between "hard" and "soft" adaptation strategies, which is that the former, in general, commit resources and are exposed to uncertainty over a longer time horizon than the latter. Since the bias and variance of risk projections increase with time, as demonstrated through numerical experiments, hard instruments must contend with larger and deeper uncertainties than soft ones. This implies a cost penalty for static instruments and that, under some circumstances, a sequence of adaptive instruments tailored to evolving conditions may be more cost-effective than a single static one designed to meet performance specifications over all plausible states of the world. Chapter 7 illustrates this concept through a didactic case study of levee heightening under uncertain sea level rise. Scenario-conditional optimization illustrates (i) that deferring permanent investments can be a robust response to deep uncertainty, particularly if the near-term benefits of construction are small, and (ii) that skillful projections of near-term climate variability can inform the design of soft instruments, thereby reducing long-term adaptation costs.

Parts I and II use observational analyses and numerical experiments to explore conceptual advances. Because of the breadth and novelty of the perspectives, the examples advanced are generally conceptual. Chapter 8 concludes by considering their implications for general planning problems in the public and private sector. Chapter 8 focuses particularly on ways to frame constructive narratives around anthropogenic climate change (ACC) with the goal of clearly communicating uncertainties and tradeoffs instead of relying on the lazy and fatalistic narrative that ACC renders losses inevitable. At a moment in which fatalistic narratives regarding COVID-19 prevail, the generality of this point appears particularly salient.

9.2 Discussion

A central assumption of part I is that the mechanistic causal chain for a particular event is insensitive to ACC and other secular trends. This assumption is most explicit in the statistical model developed in chapter 4, which hypothesizes a stationary relationship between large-scale climate indices and REP events (see section 4.8.3). This assumption is approximately valid if sufficient conditioning information is included within the predictive variables. Since these physical processes are relatively well understood, this is a reasonable assumption; however, great care must be taken to develop a statistical model that truly represents well-understood physical processes and to avoid "data mining" which may perform well over the historical record but extrapolate poorly. Further, limited historical records cannot rule out the possibility of impactful events driven by other mechanisms. However, running GCM experiments under a wide range of possible boundary forcing and model structures to explore what *could* be possible, and subsequently assessing probability in the spirit of bottom-up modeling approaches discussed in part II, could reduce vulnerability to "black swan" events (i.e., those that have not been observed but cannot be proven impossible *Taleb*, 2007).

A secondary, mostly implicit, assumption of part I is that increasing model skill due to improved resolution (*Cook et al.*, 2020; *Wehner et al.*, 2010; *Kendon et al.*, 2012; *Muller et al.*, 2011) and parameterization (*Rasp et al.*, 2018; *Gentine et al.*, 2018; *Wong et al.*, 2017; *Liu et al.*, 2011; *Pithan et al.*, 2016) will not, alone, be adequate to overcome the limitations of GCMs for simulating hydroclimate variables at spatiotemporal scales relevant to decision makers. As improved representation of clouds, aerosols, and land feedbacks enable GCMs more credibly simulate local hydroclimate processes, the set of uses for which GCM rainfall fields can be used "out of the box" will increase. At the same time, fundamental limitations arise from the (i) discretization and approximation of the continuous equations of motion, (ii) damping of low-frequency modes of variability (*Palmer*, 1999), and (iii) finite set of processes represented in the model, and these limitations are most noticeable for the extreme events of the greatest importance to societal decision-making. It is therefore reasonable to assume that hybrid models or model output statistics (MOS) of some form will be needed for the foreseeable future, though the set of variables used to inform these models and the statistical model's

structure should evolve. Of course, neither improved model skill nor statistical-dynamical models address deep uncertainties in boundary forcing and other human activities.

Chapter 6 bridges the work on understanding and predicting hydroclimate variability with the work on sequential planning. The forms of uncertainty considered in this chapter are parametric and structural, but the set of model structures considered is finite (i.e. the $\mathcal{M}$-closed case defined by *Bernardo*, 1994). In the real world, uncertainties are far deeper and the structure is not known (the $\mathcal{M}$-open case). Although experiments were conducted within the context of this strong assumption, increasing degrees of parametric uncertainty were taken as a proxy for epistemic or deep uncertainties. Thus, as deep and structural uncertainties increase, the cost of extrapolation should increase. This might imply, for example, that if the model of chapter 7 were extended to consider additional sources of uncertainty including population and land value, construction costs, the cost of capital, and the value of various alternatives (including managed retreat, hardening properties within the dike ring, etc.) then the preference for deferring large capital costs might again increase.

The argument that large, static, and centrally planned, designed, managed, and funded infrastructure tends to be cost-ineffective is not entirely new. For example, China's large infrastructure projects may have traded short-term benefit for excessive debt (*Ansar et al.*, 2016). This type of investment strategy is fragile (as defined by *Taleb*, 2012) as these static infrastructure systems cannot readily scale up or down (*Ansar et al.*, 2017, notes that they trade size for scalability). *Marohn* (2019) makes a similar argument, calling development-driven sprawling development in the United States (US) a Ponzi scheme argues and that the value generated doesn't justify the long-term maintenance, repair, and replacement obligations. As discussed in chapter 5, engineers should, in general, embrace the fact that complex problems are political. Yet the gap between how prospective investments in infrastructure are described and their actual performance (*Flyvbjerg et al.*, 2005; *Flyvbjerg*, 2009; *Ansar et al.*, 2014) emphasizes a need for science to more transparently *inform* political decisions.

9.3 Future Work

Adaptive plans that evaluate and optimize over different sources of uncertainty on different timescales can be used to inform climate adaptation and infrastructure transformation at the household, community, company, and national scales. Key actors have already committed substantial resources to climate adaptation, and more is expected. For example, at the federal scale, the United States Army Corps of Engineers (USACE) has proposed structural flood protection projects across the US including a possible $USD 100 billion floodwall along the New York / New Jersey coast (*USACE*, 2019). At local scales, cities including New York (*Bloomberg*, 2013), Houston (*City of Houston*, 2020), and Chicago (*Chicago Climate Task Force*, 2008) have developed resilience or climate adaptation plans. And the private sector is increasingly coming to view climate as a financial risk rather than a reputational one (such as Oliver Wyman, a multinational management consulting company with particular expertise in finance and technology; *Colas et al.*, 2019). Recognition of the need for improved infrastructure to manage climate risks, decarbonize the economy, generate wealth, and improve quality of life implies a critical role for science-based analysis to inform the sequencing and prioritization of different projects.

This dissertation focused on water and floods, but there are related problems in many areas of infrastructure systems planning. For example, deep decarbonization of the electricity and energy sectors is a critical step towards mitigating global greenhouse gas emissions. A number of plans have been put forth suggesting different pathways towards this goal (e.g., *Davis et al.*, 2018; *Jacobson et al.*, 2017). Yet investments in the energy sector face deep and dynamic uncertainties, including (i) the price and efficiency of solar panels, wind turbines, and batteries (technological uncertainty), (ii) the timing and occurrence of carbon tax or other regulations (political uncertainty), and (iii) demand for electricity (economic uncertainty). Planning in the energy sector must also account for the potential emergence of new technologies such as safe next-generation nuclear power and closed-loop liquid carbon fuels. The decision problem is therefore quite complex: optimizing for energy system safety, reliability, cost, and carbon emissions, to prioritize investments in energy storage (*Arbabzadeh et al.*, 2019), transmission (*MacDonald et al.*, 2016), and different generation technologies across

large areas.

The approaches developed in this dissertation can help in two ways. First, decision models used for long-term planning are generally run on time steps of one or more years. This requires parameterizing generation and demand at shorter time scales (e.g., *Su et al.*, 2020; *Chowdhury et al.*, 2019). Parametric space-time models that capture the availability of correlated electricity sources (such as complementary solar and wind availability in Texas; *Slusarewicz and Cohan*, 2018) over long time scales can be used to inform the sequencing and location of transmission and generation projects. Second, it is likely that the learning rate of uncertainties like renewable energy costs will be quite rapid. Like the problem of confronting uncertain sea level rise (chapter 7), sequential planning in the electricity sector needs to account for learning over time, model structure uncertainty, and stochastic uncertainties.

Another application is in urban planning and land use. Observational data (*Pielke et al.*, 2008; *Jongman et al.*, 2012; *Peduzzi et al.*, 2012; *Tedesco et al.*, 2020; *Ashley et al.*, 2013) and modeling efforts (*Haer et al.*, 2020; *Srikrishnan and Keller*, 2019; *Barendrecht et al.*, 2019) emphasize that changing exposure is a dominant driver of total flood risk. At the same time, the actions that affect exposure – construction and development in floodplains – can also change flood hazard, particularly in downstream locations. For example, *Blum et al.* (2020) find that, on average, a one percentage point increase in impervious basin cover causes a 3.3% increase in annual flood magnitude. This is in agreement with findings that land use changes (*Sebastian et al.*, 2019) and river channelization (*Juan et al.*, 2020) significantly increased peak streamflows in recent Houston floods. Yet while it is easy to advise cities to restrict development in areas that generate substantial risk (hazard or exposure), cities are heavily reliant on near-term tax revenues, and development offers immediate resources even if it increases long-term risks and obligations. To manage these risks, cities need coherent land use policies that balance tax revenue, long-term expenses and fragilities, equity, and scalability (*BenDor et al.*, 2020). Improving policies to allocate resources, across space, between levers like centralized drainage, managed retreat (*Hino et al.*, 2017), resilience bonds (*Ruggeri*, 2017), and green infrastructure (*Ochoa-Tocachi et al.*, 2019) and home elevation (*Zarekarizi et al.*, 2020) can help cities better navigate tradeoffs between revenue and risk. Tools for spatial policy

search, planning under uncertainty, and modeling the local correlation structure of hydroclimate extremes will be particularly helpful.

A third application is in distributed water-energy systems. As briefly mentioned in section 5.3.1, distributed resources offer important advantages in scale and reliability. This is not an entirely novel approach; as the United States Environmental Protection Agency (EPA) notes, decentralized wastewater treatment systems (e.g., septic tanks) served 25% of the US population and were used in one-third of all new housing and commercial developments in 1997 (*USEPA*, 2005). Yet cities and utilities increasingly recognize the cost and scale issues detailed in chapter 1 (*Broaddus*, 2019; *Jones et al.*, 2012). Since landscapes and yards are a major consumer of urban water, findings that rainwater harvesting can supply up to 50% of the annual demand for traditional landscaping and over 100% of the water-smart landscaping in Colorado (*Gilliom et al.*, 2019) suggest that utilities may be able to manage growth and increased water usage without costly capital expenditures (see *Trindade et al.*, 2019, for an example of these costs). Distributed water resources may also manage the flashiness of pluvial floods (*Jamali et al.*, 2020) and protect fragile ecosystems from stormwater extremes (*Cunningham and Gharipour*, 2018), and optimization models suggest that while the optimal degree of centralization is site-specific, the calculated optimal degree of centralization is substantially lower than the current level (for a case study in Switzerland *Eggimann et al.*, 2015, 2016). However, studies of distribution in the energy sector have identified challenges as well as opportunities – particularly around the incentive of the wealthy to contribute to centralized systems, the need for monitoring and local system control, and local efficiencies (*Burger et al.*, 2019; *MIT Energy Initiative*, 2016). A comprehensive research agenda for decentralized water infrastructure that develops engineering component designs, digital monitoring, and regulatory and management frameworks, and that matches different technologies to different use cases, can drastically improve the set of levers available to decision-makers with significant potential to improve outcomes.

Bibliography

Aerts, J. C. J. H., W. J. W. Botzen, K. C. Clarke, S. L. Cutter, J. W. Hall, B. Merz, E. Michel-Kerjan, J. Mysiak, S. Surminski, and H. Kunreuther (2018), Integrating human behaviour dynamics into flood disaster risk assessment, *Nature Climate Change*, *8*(3), 193–199, doi: 10.1038/s41558-018-0085-1.

Agel, L., M. Barlow, S. B. Feldstein, and W. J. J. Gutowski (2018), Identification of large-scale meteorological patterns associated with extreme precipitation in the US northeast, *Climate Dynamics*, *50*(5-6), 1819–1839, doi: 10.1007/s00382-017-3724-8.

Albonico, M., and L. Savioli (2017), Hookworm: A neglected resurgent infection, *BMJ*, *359*, doi: 10.1136/bmj.j4813.

Anderson, W., R. Seager, W. E. Baethgen, and M. A. Cane (2018), Trans-Pacific ENSO teleconnections pose a correlated risk to agriculture, *Agricultural and Forest Meteorology*, *262*, 298–309, doi: 10.1016/j.agrformet.2018.07.023.

Anderson, W. B., Han, Eunjin, Baethgen, Walter, Goddard, Lisa, Muñoz, Ángel G., and Robertson Andrew W. (2020), The Madden-Julian Oscillation affects crop yields around the world, *Earth and Space Science Open Archive*, doi: 10.1002/essoar.10501965.1.

Ångström, A. (1935), Teleconnections of Climatic Changes in Present Time, *Geografiska Annaler*, *17*(3-4), 242–258, doi: 10.1080/20014422.1935.11880600.

Ansar, A., B. Flyvbjerg, A. Budzier, and D. Lunn (2014), Should we build more large dams? The actual costs of hydropower megaproject development, *Energy Policy*, *69*, 43–56, doi: 10.1016/j.enpol.2013.10.069.

Ansar, A., B. Flyvbjerg, A. Budzier, and D. Lunn (2016), Does Infrastructure Investment Lead to Economic Growth or Economic Fragility? Evidence from China, *Oxford Review of Economic Policy*, *32*(3), 360–390, doi: 10.1093/oxrep/grw022.

Ansar, A., B. Flyvbjerg, A. Budzier, and D. Lunn (2017), Big is Fragile: An Attempt at Theorizing Scale, *arXiv:1603.01416 [q-fin]*.

Arbabzadeh, M., R. Sioshansi, J. X. Johnson, and G. A. Keoleian (2019), The role of energy storage in deep decarbonization of electricity production, *Nature Communications*, *10*(1), 3413, doi: 10.1038/s41467-019-11161-5.

Arrow, K., M. Cropper, C. Gollier, B. Groom, G. Heal, R. Newell, W. Nordhaus, R. Pindyck, W. Pizer, P. Portney, T. Sterner, R. S. J. Tol, and M. Weitzman (2013), Determining benefits and costs for future generations, *Science*, *341*(6144), 349–350, doi: 10.1126/science.1235665.

Arrow, K. J. (1951), *Social Choice and Individual Values*, Wiley, New York.

Arrow, K. J. (1963), *Social Choice and Individual Values*, Yale Univeristy Press, New Haven, CT.

Ashley, W. S., S. Strader, T. Rosencrants, and A. J. Krmenec (2013), Spatiotemporal changes in tornado Hazard exposure: The case of the expanding bull's-eye effect in Chicago, Illinois, *Weather, Climate, and Society*, *6*(2), 175–193, doi: 10.1175/WCAS-D-13-00047.1.

Ayyub, B. M. (2018), *Climate-Resilient Infrastructure: Adaptive Design and Risk Management*, American Society of Civil Engineers, Reston, Virginia.

Bankes, S. (1993), Exploratory Modeling for Policy Analysis, *Operations Research*, *41*(3), 435–449, doi: 10.1287/opre.41.3.435.

Bao, J.-W., S. A. Michelson, P. J. Neiman, F. M. Ralph, and J. M. Wilczak (2006), Interpretation of Enhanced Integrated Water Vapor Bands Associated with Extratropical Cyclones: Their Formation and Connection to Tropical Moisture, *Monthly Weather Review*, *134*(4), 1063–1080, doi: 10.1175/MWR3123.1.

Barendrecht, M. H., A. Viglione, and G. Blöschl (2017), A dynamic framework for flood risk, *Water Security*, *1*, 3–11, doi: 10.1016/j.wasec.2017.02.001.

Barendrecht, M. H., A. Viglione, H. Kreibich, B. Merz, S. Vorogushyn, and G. Blöschl (2019), The Value of Empirical Data for Estimating the Parameters of a Sociohydrological Flood Risk Model, *Water Resources Research*, *55*(2), 1312–1336, doi: 10.1029/2018WR024128.

Barnes, E. A., and J. A. Screen (2015), The impact of Arctic warming on the midlatitude jetstream: Can it? Has it? Will it?, *Wiley Interdisciplinary Reviews-Climate Change*, *6*(3), 277–286, doi: 10.1002/wcc.337.

Barnett, B. J., and O. Mahul (2007), Weather index insurance for agriculture and rural areas in lower-income countries, *American Journal of Agricultural Economics*, *89*(5), 1241–1247, doi: 10.1111/j.1467-8276.2007.01091.x.

Barnston, A. G., and C. F. Ropelewski (1992), Prediction of ENSO Episodes Using Canonical Correlation Analysis, *Journal of Climate*, *5*(11), 1316–1345, doi: 10.1175/1520-0442(1992)005<1316:POEEUC>2.0.CO;2.

Barnston, A. G., S. Li, S. J. Mason, D. G. DeWitt, L. Goddard, and X. Gong (2010), Verification of the First 11 Years of IRIs Seasonal Climate Forecasts, *Journal of Applied Meteorology and Climatology*, *49*(3), 493–520, doi: 10.1175/2009jamc2325.1.

Barnston, A. G., M. K. Tippett, M. L. LHeureux, S. Li, and D. G. DeWitt (2012), Skill of Real-Time Seasonal ENSO Model Predictions During 2002–11: Is Our Capability Increasing?, *Bulletin of the American Meteorological Society*, *93*(5), ES48–ES50, doi: 10.1175/bams-d-11-00111.2.

Barreiro, M. (2017), Interannual variability of extratropical transient wave activity and its influence on rainfall over Uruguay, *International Journal of Climatology*, *37*(12), 4261–4274, doi: 10.1002/joc.5082.

Barros, V. R., L. Chamorro, G. Coronel, and J. Baez (2004), The major discharge events in the Paraguay River: Magnitudes, source regions, and climate forcings, *Journal of Hydrometeorology*, *5*(6), 1161–1170, doi: 10.1175/JHM-378.1.

Barry, J. M. (1997), *Rising Tide : The Great Mississippi Flood of 1927 and How It Changed America*, Simon & Schuster, New York.

Bedient, P. B., B. C. Hoblit, D. C. Gladwell, and B. E. Vieux (2000), NEXRAD radar for flood prediction in Houston, *Journal of Hydrologic Engineering*, *5*(3), 269–277, doi: 10.1061/(ASCE)1084-0699(2000)5:3(269).

Bellman, R. (1954), The theory of dynamic programming, *Bulletin of the American Mathematical Society*, *60*(6), 503–515, doi: 10.1090/S0002-9904-1954-09848-8.

Bellman, R. (1957), *Dynamic Programming*, Princeton University Press, Princeton, New Jersey.

Benayoun, R., J. de Montgolfier, J. Tergny, and O. Laritchev (1971), Linear programming with multiple objective functions: Step method (stem), *Mathematical Programming*, *1*(1), 366–375, doi: 10.1007/BF01584098.

BenDor, T. K., D. Salvesen, C. Kamrath, and B. Ganser (2020), Floodplain buyouts and municipal finance, *Natural Hazards Review*, *21*(3), 04020,020, doi: 10.1061/(ASCE)NH.1527-6996.0000380.

Beran, J. (1994), *Statistics for Long-Memory Processes*, Chapman & Hall, New York.

Berg, P., C. Moseley, and J. O. Haerter (2013), Strong increase in convective precipitation in response to higher temperatures, *Nature Geoscience*, *6*(3), 181–185, doi: 10.1038/ngeo1731.

Bernardo, J. M. (1994), *Bayesian Theory*, Wiley, New York.

Bertoni, F., M. Giuliani, and A. Castelletti (2017), Scenario-based fitted Q-iteration for adaptive control of water reservoir systems under uncertainty, *IFAC-PapersOnLine*, *50*(1), 3183–3188, doi: 10.1016/j.ifacol.2017.08.340.

Bertoni, F., A. Castelletti, M. Giuliani, and P. M. Reed (2019), Discovering dependencies, tradeoffs, and robustness in joint dam design and operation: An ex-post assessment of the Kariba Dam, *Earth's Future*, *7*(12), 1367–1390, doi: 10.1029/2019EF001235.

Bertsekas, D. P. (1976), *Dynamic Programming and Stochastic Control*, no. 125 in Mathematics in Sciencce and Engineering, Academic Press.

Betancourt, M. (2017), A Conceptual Introduction to Hamiltonian Monte Carlo, *Methodology (stat.ME)*.

Bhattacharya, R. N., V. K. Gupta, and E. Waymire (1983), The Hurst effect under trends, *Journal of Applied Probability*, *20*(3), 649–662, doi: 10.2307/3213900.

Biggs, C., C. Ryan, and J. Wiseman (2010), Distributed Systems: A design model for sustainable and resilient infrastructure, *Tech. Rep. 3*, Victorian Eco-Innovation Lab.

Bischiniotis, K., H. de Moel, M. van den Homberg, A. Couasnon, J. Aerts, G. Guimarães Nobre, E. Zsoter, and B. van den Hurk (2020), A framework for comparing permanent and forecast-based flood risk-reduction strategies, *Science of The Total Environment*, *720*, 137,572, doi: 10.1016/j.scitotenv.2020.137572.

Bissolli, P., K. Friedrich, J. Rapp, and M. Ziese (2011), Flooding in eastern central Europe in May 2010 – reasons, evolution and climatological assessment, *Weather*, *66*(6), 147–153, doi: 10.1002/wea.759.

Block, P. J., F. A. S. Filho, L. Sun, and H.-H. Kwon (2009), A streamflow forecasting framework using multiple climate and hydrological models, *JAWRA Journal of the American Water Resources Association*, *45*(4), 828–843, doi: 10.1111/j.1752-1688.2009.00327.x.

Bloemen, P., T. Reeder, C. Zevenbergen, J. Rijke, and A. Kingsborough (2018), Lessons learned from applying adaptation pathways in flood risk management and challenges for the further development of this approach, *Mitigation and Adaptation Strategies for Global Change*, *23*(7), 1083–1108, doi: 10.1007/s11027-017-9773-9.

Bloomberg, M. (2013), A Stronger, More Resilient New York, *Tech. rep.*, City of New York, New York.

Blöschl, G., and A. Montanari (2010), Climate change impacts—throwing the dice?, *Hydrological Processes*, *24*(3), 374–381, doi: 10.1002/hyp.7574.

Blum, A. G., P. J. Ferraro, S. A. Archfield, and K. R. Ryberg (2020), Causal Effect of Impervious Cover on Annual Flood Magnitude for the United States, *Geophysical Research Letters*, *47*(5), doi: 10.1029/2019GL086480.

Bock, A. R., L. E. Hay, G. J. McCabe, S. L. Markstrom, and R. D. Atkinson (2018), Do Downscaled General Circulation Models Reliably Simulate Historical Climatic Conditions?, *Earth Interactions*, *22*(10), 1–22, doi: 10.1175/EI-D-17-0018.1.

Boers, N., B. Bookhagen, N. Marwan, J. Kurths, and J. Marengo (2013), Complex networks identify spatial patterns of extreme rainfall events of the South American Monsoon System, *Geophysical Research Letters*, *40*(16), 4386–4392, doi: 10.1002/grl.50681.

Boers, N., B. Bookhagen, H. M. J. Barbosa, N. Marwan, J. Kurths, and J. A. Marengo (2014), Prediction of extreme floods in the eastern Central Andes based on a complex networks approach, *Nature Communications*, *5*(1), 5199, doi: 10.1038/ncomms6199.

Bonnafous, L., and U. Lall (2020), Space-time clustering of climate extremes amplify global climate impacts, leading to fat-tailed risk, *Natural Hazards and Earth System Sciences Discussions*, pp. 1–19, doi: 10.5194/nhess-2019-405.

Bonnafous, L., U. Lall, and J. Siegel (2017a), A water risk index for portfolio exposure to climatic extremes: Conceptualization and an application to the mining industry, *Hydrology and Earth System Sciences*, *21*(4), 2075–2106, doi: 10.5194/hess-21-2075-2017.

Bonnafous, L., U. Lall, and J. Siegel (2017b), An index for drought induced financial risk in the mining industry, *Water Resources Research*, *53*(2), 1509–1524, doi: 10.1002/2016WR019866.

Borgomeo, E., M. Mortazavi-Naeini, J. W. Hall, and B. P. Guillod (2018), Risk, Robustness and Water Resources Planning Under Uncertainty, *Earth's Future*, *6*(3), 468–487, doi: 10.1002/2017EF000730.

Bosshard, T., M. Carambia, K. Goergen, S. Kotlarski, P. Krahe, M. Zappa, and C. Schär (2018), Quantifying uncertainty sources in an ensemble of hydrological climate-impact projections, *Water Resources Research*, pp. 1523–1536, doi: 10.1029/2011WR011533@10.1002/(ISSN)1944-7973.IMPACRIVR1.

Box, G. E. P. (1976), Science and Statistics, *Journal of the American Statistical Association*, *71*(356), 791–799, doi: 10.1080/01621459.1976.10480949.

Bracken, C., B. Rajagopalan, and C. Woodhouse (2016), A Bayesian hierarchical nonhomogeneous hidden Markov model for multisite streamflow reconstructions, *Water Resources Research*, *52*(10), 7837–7850, doi: 10.1002/2016WR018887.

Brakenridge, G. R. (2018), Global Active Archive of Large Flood Events, http://floodobservatory.colorado.edu/Archives/index.html.

Branstator, G. (2002), Circumglobal Teleconnections, the Jet Stream Waveguide, and the North Atlantic Oscillation, *Journal of Climate*, *15*(14), 1893–1910, doi: 10.1175/1520-0442(2002)015<1893:cttjsw>2.0.co;2.

Bravo, J. M., D. Allasia, A. R. Paz, W. Collischonn, and C. E. M. Tucci (2012), Coupled Hydrologic-Hydraulic Modeling of the Upper Paraguay River Basin, *Journal of Hydrologic Engineering*, *17*(5), 635–646, doi: 10.1061/(ASCE)HE.1943-5584.0000494.

British Broadcasting Corporation (2015), Flooding 'Worst in 50 Years', as 150,000 Flee in Paraguay, Argentina, Brazil and Uruguay, *BBC News*.

Broaddus, L. E. (2019), Distributed Infrastructure, *Tech. rep.*, Broadview Collaborative.

Bröcker, J., and L. A. Smith (2007), Scoring Probabilistic Forecasts: The Importance of Being Proper, *Weather and Forecasting*, *22*(2), 382–388, doi: 10.1175/WAF966.1.

Brody, S., R. Blessing, A. Sebastian, and P. Bedient (2014), Examining the impact of land use/land cover characteristics on flood losses, *Journal of Environmental Planning and Management*, *57*(8), 1252–1265, doi: 10.1080/09640568.2013.802228.

Brody, S. D., W. E. Highfield, M. Wilson, M. K. Lindell, and R. Blessing (2017), Understanding the motivations of coastal residents to voluntarily purchase federal flood insurance, *Journal of Risk Research*, *20*(6), 760–775, doi: 10.1080/13669877.2015.1119179.

Brown, C., F. Boltz, S. Freeman, J. Tront, and D. Rodriguez (2020), Resilience by design: A deep uncertainty approach for water systems in a changing world, *Water Security*, *9*, 100,051, doi: 10.1016/j.wasec.2019.100051.

Brown, C. M. (2010), The End of Reliability, *Journal of Water Resources Planning and Management*, *136*(2), 143–145, doi: 10.1061/(ASCE)WR.1943-5452.65.

Brown, C. M., Y. Ghile, M. Laverty, and K. Li (2012), Decision scaling: Linking bottom-up vulnerability analysis with climate projections in the water sector, *Water Resources Research*, *48*(9), doi: 10.1029/2011WR011212.

Brown, R., and H. Willis (2006), The economics of aging infrastructure, *IEEE Power and Energy Magazine*, *4*(3), 36–43, doi: 10.1109/MPAE.2006.1632452.

Bullmore, E., C. Long, J. Suckling, J. Fadili, G. Calvert, F. Zelaya, T. A. Carpenter, and M. Brammer (2001), Colored noise and computational inference in neurophysiological (fMRI) time series analysis: Resampling methods in time and wavelet domains, *Human Brain Mapping*, *12*(2), 61–78, doi: 10.1002/1097-0193(200102)12:2<61::AID-HBM1004>3.0.CO;2-W.

Burger, S. P., J. D. Jenkins, S. C. Huntington, and I. J. Perez-Arriaga (2019), Why distributed? A critical review of the tradeoffs between centralized and decentralized resources, *IEEE Power and Energy Magazine*, *17*(2), 16–24, doi: 10.1109/MPE.2018.2885203.

Byrne, M. P., and P. A. O'Gorman (2015), The Response of Precipitation Minus Evapotranspiration to Climate Warming: Why the "Wet-Get-Wetter, Dry-Get-Drier" Scaling Does Not Hold over Land, *Journal of Climate*, *28*(20), 8078–8092, doi: 10.1175/JCLI-D-15-0369.1.

Cai, W., M. J. McPhaden, A. M. Grimm, R. R. Rodrigues, A. S. Taschetto, R. D. Garreaud, B. Dewitte, G. Poveda, Y.-G. Ham, A. Santoso, B. Ng, W. Anderson, G. Wang, T. Geng, H.-S. Jo, J. A. Marengo, L. M. Alves, M. Osman, S. Li, L. Wu, C. Karamperidou, K. Takahashi, and C. Vera (2020), Climate impacts of the El Niño–Southern Oscillation on South America, *Nature Reviews Earth & Environment*, *1*(4), 215–231, doi: 10.1038/s43017-020-0040-3.

Campetella, C. M., and C. S. Vera (2002), The influence of the Andes mountains on the South American low-level flow, *Geophysical Research Letters*, *29*(17), 7–1–7–4, doi: 10.1029/2002GL015451.

Capotondi, A., A. T. Wittenberg, M. Newman, E. Di Lorenzo, J.-Y. Yu, P. Braconnot, J. Cole, B. Dewitte, B. Giese, E. Guilyardi, F.-F. Jin, K. Karnauskas, B. Kirtman, T. Lee, N. Schneider, Y. Xue, and S.-W. Yeh (2015), Understanding ENSO Diversity, *Bulletin of the American Meteorological Society*, *96*(6), 921–938, doi: 10.1175/BAMS-D-13-00117.1.

Carbin, G. W., M. K. Tippett, S. P. Lillo, and H. E. Brooks (2016), Visualizing Long-Range Severe Thunderstorm Environment Guidance from CFSv2, *Bulletin of the American Meteorological Society*, *97*(6), 1021–1031, doi: 10.1175/BAMS-D-14-00136.1.

Carpenter, B., A. Gelman, M. D. Hoffman, D. Lee, B. Goodrich, M. Betancourt, M. A. Brubaker, J. Guo, P. Li, and A. Riddell (2017), Stan: A Probabilistic Programming Language, *Journal Of Statistical Software*, *76*(1), 1–29, doi: 10.18637/jss.v076.i01.

Carriquiry, M. A., and D. E. Osgood (2012), Index insurance, probabilistic climate forecasts, and production, *Journal of Risk and Insurance*, *79*(1), 287–300, doi: 10.1111/j.1539-6975.2011.01422.x.

Carter, N. T., and A. C. Nesbitt (2016), Discount rates in the economic evaluation of U.S. Army Corps of Engineers projects, *CRS Report R44594*, Congressional Research Service.

Carvalho, L. M. V., C. Jones, and B. Liebmann (2004), The South Atlantic convergence zone: Intensity, form, persistence, and relationships with intraseasonal to interannual activity and extreme rainfall, *Journal of Climate*, *17*(1), 88–108, doi: 10.1175/1520-0442(2004)017<0088:TSACZI>2.0.CO;2.

Carvalho, L. M. V., A. E. Silva, C. Jones, B. Liebmann, P. L. Silva Dias, and H. R. Rocha (2010a), Moisture transport and intraseasonal variability in the South America monsoon system, *Climate Dynamics*, *36*(9-10), 1865–1880, doi: 10.1007/s00382-010-0806-2.

Carvalho, L. M. V., C. Jones, A. E. Silva, B. Liebmann, and P. L. Silva Dias (2010b), The South American Monsoon System and the 1970s climate transition, *International Journal of Climatology*, *31*(8), 1248–1256, doi: 10.1002/joc.2147.

Cassou, C., Y. Kushnir, E. Hawkins, A. Pirani, F. Kucharski, I.-S. Kang, and N. Caltabiano (2018), Decadal Climate Variability and Predictability: Challenges and Opportunities, *Bulletin of the American Meteorological Society*, *99*(3), 479–490, doi: 10.1175/BAMS-D-16-0286.1.

Castillo, R., R. Nieto, A. Drumond, and L. Gimeno (2014), The role of the ENSO cycle in the modulation of moisture transport from major oceanic moisture sources, *Water Resources Research*, *50*(2), 1046–1058, doi: 10.1002/2013WR013900.

Catto, J. L., and S. Pfahl (2013), The importance of fronts for extreme precipitation, *Journal of Geophysical Research: Atmospheres*, *118*(19), 10, 791–10, 801, doi: 10.1002/jgrd.50852.

Center for International Earth Science Information Network (2016), Gridded Population of the World, Version 4 (GPWv4): Population Density Adjusted to Match 2015 Revision UN WPP Country Totals, Revision 10, *Tech. rep.*, Gridded Population of the World, Version 4 (GPWv4): Population Density Adjusted to Match 2015 Revision UN WPP Country Totals, Revision 10.

Chafik, L., J. E. Ø. Nilsen, and S. Dangendorf (2017), Impact of North Atlantic teleconnection patterns on northern European sea level, *Journal of Marine Science and Engineering*, *5*(3), 43, doi: 10.3390/jmse5030043.

Chamoli, A., A. Ram Bansal, and V. P. Dimri (2007), Wavelet and rescaled range approach for the Hurst coefficient for short and long time series, *Computers & Geosciences*, *33*(1), 83–93, doi: 10.1016/j.cageo.2006.05.008.

Chang, W., M. L. Stein, J. Wang, V. R. Kotamarthi, and E. J. Moyer (2016), Changes in spatiotemporal precipitation patterns in changing climate conditions, *Journal of Climate*, *29*(23), 8355–8376, doi: 10.1175/JCLI-D-15-0844.1.

Chattopadhyay, A., P. Hassanzadeh, and S. Pasha (2020), Predicting clustered weather patterns: A test case for applications of convolutional neural netwcorks to spatio-temporal climate data, *Scientific Reports*, *10*(1), 1–13, doi: 10.1038/s41598-020-57897-9.

Chen, M., W. Shi, P. Xie, V. B. S. Silva, V. E. Kousky, R. Wayne Higgins, and J. E. Janowiak (2008), Assessing objective techniques for gauge-based analyses of global daily precipitation, *Journal of Geophysical Research*, *113*(D4), 1147, doi: 10.1029/2007JD009132.

Cheng, D., Y. Cui, F. Su, Y. Jia, and C. E. Choi (2018), The characteristics of the Mocoa compound disaster event, Colombia, *Landslides*, *10*(6), 1–1232, doi: 10.1007/s10346-018-0969-1.

Chester, M. V., B. S. Underwood, and C. Samaras (2020), Keeping infrastructure reliable under climate uncertainty, *Nature Climate Change*, pp. 1–3, doi: 10.1038/s41558-020-0741-0.

Chicago Climate Task Force (2008), Chicago Climate Action Plan, *Tech. rep.*, Chicago.

Chowdhury, A. K., J. Kern, T. D. Dang, and S. Galelli (2019), PowNet: A power systems analysis model for large-scale water-energy nexus studies, *arXiv:1909.12529 [physics]*.

Cioffi, F., F. Conticello, and U. Lall (2016), Projecting changes in Tanzania rainfall for the 21st century, *International Journal of Climatology*, *36*(13), 4297–4314, doi: 10.1002/joc.4632.

Cioffi, F., F. Conticello, U. Lall, L. Marotta, and V. Telesca (2017), Large scale climate and rainfall seasonality in a Mediterranean Area: Insights from a non-homogeneous Markov model applied to the Agro-Pontino plain, *Hydrological Processes*, *31*(3), 668–686, doi: 10.1002/hyp.11061.

City of Houston (2020), Resilient Houston, *Tech. rep.*, Houston, TX.

Clarke, D. J., and S. Dercon (2016), *Dull Disasters? How Planning Ahead Will Make a Difference*, Oxford University Press, doi: 10.1093/acprof:oso/9780198785576.001.0001.

Cohen, J., J. A. Screen, J. C. Furtado, M. Barlow, D. Whittleston, D. Coumou, J. Francis, K. Dethloff, D. Entekhabi, J. Overland, and J. Jones (2014), Recent Arctic amplification and extreme mid-latitude weather, *Nature Geoscience*, *7*(9), 627–637, doi: 10.1038/ngeo2234.

Cohn, T. A., and H. F. Lins (2005), Nature's style: Naturally trendy, *Geophysical Research Letters*, *32*(23), 393, doi: 10.1029/2005GL024476.

Colas, J., I. Khaykin, and A. Pyanet (2019), Climate Change - Managing a New Financial Risk, *Tech. rep.*, Oliver Wyman.

Collischonn, W., C. Tucci, and R. T. Clarke (2001), Further evidence of changes in the hydrological regime of the River Paraguay: Part of a wider phenomenon of climate change?, *Journal of Hydrology*, *245*(1-4), 218–238, doi: 10.1016/S0022-1694(01)00348-1.

Concha Larrauri, P., and U. Lall (2018), Tailings dams failures: Updated statistical model for discharge volume and runout, *Environments*, *5*(2), 28, doi: 10.3390/environments5020028.

Concha Larrauri, P., and U. Lall (2020), Assessing the exposure of critical infrastructure and other assets to the climate induced failure of aging dams in the US, *Tech. rep.*, Columbia Water Center.

Concha Larrauri, P., J. P. C. Gutierrez, U. Lall, and M. Ennenbach (2020), A City Wide Assessment of the Financial Benefits of Rainwater Harvesting in Mexico City, *JAWRA Journal of the American Water Resources Association*, doi: 10.1111/1752-1688.12823.

Conticello, F., F. Cioffi, B. Merz, and U. Lall (2017), An event synchronization method to link heavy rainfall events and large-scale atmospheric circulation features, *International Journal of Climatology*, *38*(3), 1421–1437, doi: 10.1002/joc.5255.

Conticello, F. R., F. Cioffi, U. Lall, and B. Merz (2020), Synchronization and delay between circulation patterns and high streamflow events in Germany, *Water Resources Research*, p. e2019WR025598, doi: 10.1029/2019WR025598.

Cook, E. R., R. Seager, R. R. Heim Jr, R. S. Vose, C. Herweijer, and C. Woodhouse (2010), Megadroughts in North America: Placing IPCC projections of hydroclimatic change in a long-term palaeoclimate context, *Journal of Quaternary Science*, *25*(1), 48–61, doi: 10.1002/jqs.1303.

Cook, L. M., S. McGinnis, and C. Samaras (2020), The effect of modeling choices on updating intensity-duration-frequency curves and stormwater infrastructure designs for climate change, *Climatic Change*, *159*(2), 289–308, doi: 10.1007/s10584-019-02649-6.

Corti, S., F. Molteni, and T. N. Palmer (1999), Signature of recent climate change in frequencies of natural atmospheric circulation regimes, *Nature*, *398*(6730), 799–802, doi: 10.1038/19745.

Coumou, D., and S. Rahmstorf (2012), A decade of weather extremes, *Nature Climate Change*, *10*(7), P100,013–496, doi: 10.1038/nclimate1452.

Coumou, D., V. Petoukhov, S. Rahmstorf, S. Petri, and H. J. Schellnhuber (2014), Quasi-resonant circulation regimes and hemispheric synchronization of extreme weather in boreal summer, *Proceedings of the National Academy of Sciences of the United States of America*, *111*(34), 12,331–12,336, doi: 10.1073/pnas.1412797111.

Coumou, D., G. Di Capua, S. Vavrus, L. Wang, and S. Wang (2018), The influence of Arctic amplification on mid-latitude summer circulation, *Nature Communications*, *9*(1), 501, doi: 10.1038/s41467-018-05256-8.

Cremades, R., S. Surminski, M. Máñez Costa, P. Hudson, P. Shrivastava, and J. Gascoigne (2018), Using the adaptive cycle in climate-risk insurance to design resilient futures, *Nature Climate Change*, *8*(1), 4–7, doi: 10.1038/s41558-017-0044-2.

Cunningham, C., and M. Gharipour (2018), Pipe Dreams: Urban Wastewater Treatment for Biodiversity Protection, *Urban Science*, *2*(1), 10, doi: 10.3390/urbansci2010010.

Dacre, H. F., P. A. Clark, O. Martinez-Alvarado, M. A. Stringer, and D. A. Lavers (2015), How Do Atmospheric Rivers Form?, *Bulletin of the American Meteorological Society*, *96*(8), 1243–1255, doi: 10.1175/BAMS-D-14-00031.1.

Dai, A. (2006), Precipitation characteristics in eighteen coupled climate models, *Journal of Climate*, *19*(18), 4605–4630, doi: 10.1175/JCLI3884.1.

Daigger, G. T., N. Voutchkov, U. Lall, and W. Sarni (2019), The future of water: A collection of essays on "disruptive" technologies that may transform the water sector in the next 10 years, *Tech. Rep. IDB-DP-657*, Interamerican Development Bank Water and Sanitation Division.

Daniel, K. D., R. B. Litterman, and G. Wagner (2019), Declining CO2 price paths, *Proceedings of the National Academy of Sciences*, p. 201817444, doi: 10.1073/pnas.1817444116.

Davis, N. A., and S. M. Davis (2018), Reconciling Hadley Cell Expansion Trend Estimates in Reanalyses, *Geophysical Research Letters*, doi: 10.1029/2018GL079593.

Davis, S. J., N. S. Lewis, M. Shaner, S. Aggarwal, D. Arent, I. L. Azevedo, S. M. Benson, T. Bradley, J. Brouwer, Y.-M. Chiang, C. T. M. Clack, A. Cohen, S. Doig, J. Edmonds, P. Fennell, C. B. Field, B. Hannegan, B.-M. Hodge, M. I. Hoffert, E. Ingersoll, P. Jaramillo, K. S. Lackner, K. J. Mach, M. Mastrandrea, J. Ogden, P. F. Peterson, D. L. Sanchez, D. Sperling, J. Stagner, J. E. Trancik, C.-J. Yang, and K. Caldeira (2018), Net-zero emissions energy systems, *Science*, *360*(6396), eaas9793, doi: 10.1126/science.aas9793.

Dawson, A. (2016), Windspharm: A High-Level Library for Global Wind Field Computations Using Spherical Harmonics, *Journal of Open Research Software*, *4*(1), 751, doi: 10.5334/jors.129.

De Finetti, B. (1972), *Probability, Induction and Statistics; the Art of Guessing*, J. Wiley, New York.

de Neufville, R., and K. Smet (2019), Engineering Options Analysis (EOA), in *Decision Making under Deep Uncertainty: From Theory to Practice*, edited by V. A. W. J. Marchau, W. E. Walker, P. J. T. M. Bloemen, and S. W. Popper, pp. 117–132, Springer International Publishing, Cham, doi: 10.1007/978-3-030-05252-2_6.

de Neufville, R., S. Scholtes, and T. Wang (2006), Real Options by Spreadsheet: Parking Garage Case Example, *Journal of Infrastructure Systems*, *12*(2), 107–111, doi: 10.1061/(ASCE)1076-0342(2006)12:2(107).

de Neufville, R., K. Smet, M.-A. Cardin, and M. Ranjbar-Bourani (2019), Engineering Options Analysis (EOA): Applications, in *Decision Making under Deep Uncertainty: From Theory to Practice*, edited by V. A. W. J. Marchau, W. E. Walker, P. J. T. M. Bloemen, and S. W. Popper, pp. 223–252, Springer International Publishing, Cham, doi: 10.1007/978-3-030-05252-2_11.

de Ruiter, M. C., A. Couasnon, M. J. C. van den Homberg, J. E. Daniell, J. C. Gill, and P. J. Ward (2020), Why we can no longer ignore consecutive disasters, *Earth's Future*, *8*(3), e2019EF001,425, doi: 10.1029/2019EF001425.

Debreu, G. (1959), *Theory of Value; an Axiomatic Analysis of Economic Equilibrium*, Yale Univeristy Press, New Haven, CT.

Delgado, J. M., B. Merz, and H. Apel (2012), A climate-flood link for the lower Mekong River, *Hydrology and Earth System Sciences*, *16*(5), 1533–1541, doi: 10.5194/hess-16-1533-2012.

Delgado, J. M., B. Merz, and H. Apel (2014), Projecting flood hazard under climate change: An alternative approach to model chains, *Natural Hazards and Earth System Science*, *14*(6), 1579–1589, doi: 10.5194/nhess-14-1579-2014.

Derbyshire, J. (2017), Potential surprise theory as a theoretical foundation for scenario planning, *Technological Forecasting and Social Change*, *124*, 77–87, doi: 10.1016/j.techfore.2016.05.008.

Dettinger, M. D., F. M. Ralph, T. Das, P. J. Neiman, and D. R. Cayan (2011), Atmospheric Rivers, Floods and the Water Resources of California, *Water*, *3*(2), 445–478, doi: 10.3390/w3020445.

Dezfuli, A. (2019), Rare atmospheric river caused record floods across the Middle East, *Bulletin of the American Meteorological Society*, doi: 10.1175/BAMS-D-19-0247.1.

Di Baldassarre, G., A. Montanari, H. Lins, D. Koutsoyiannis, L. Brandimarte, and G. Blöschl (2010), Flood fatalities in Africa: From diagnosis to mitigation, *Geophysical Research Letters*, *37*(22), doi: 10.1029/2010GL045467.

Di Baldassarre, G., H. Kreibich, S. Vorogushyn, J. Aerts, K. Arnbjerg-Nielsen, M. Barendrecht, P. Bates, M. Borga, W. Botzen, P. Bubeck, B. D. Marchi, C. Llasat, M. Mazzoleni, D. Molinari, E. Mondino, J. Mård, O. Petrucci, A. Scolobig, A. Viglione, and P. J. Ward (2018a), Hess Opinions: An interdisciplinary research agenda to explore the unintended consequences of structural flood protection, *Hydrology and Earth System Sciences*, *22*(11), 5629–5637, doi: 10.5194/hess-22-5629-2018.

Di Baldassarre, G., N. Wanders, A. AghaKouchak, L. Kuil, S. Rangecroft, T. I. E. Veldkamp, M. Garcia, P. R. van Oel, K. Breinl, and A. F. Loon (2018b), Water shortages worsened by reservoir effects, *Nature Sustainability*, *1*(11), 617, doi: 10.1038/s41893-018-0159-0.

Dirmeyer, P. A., and J. L. Kinter (2010), Floods over the U.S. Midwest: A Regional Water Cycle Perspective, *Journal of Hydrometeorology*, *11*(5), 1172–1181, doi: 10.1175/2010JHM1196.1.

Dirmeyer, P. A., and J. L. Kinter (2011), The "Maya Express": Floods in the U.S. Midwest, *EOS, Transactions American Geophysical Union*, *90*(12), 101–102, doi: 10.1029/2009EO120001.

Dittes, B., O. Špačková, L. Schoppa, and D. Straub (2018), Managing uncertainty in flood protection planning with climate projections, *Hydrology and Earth System Sciences*, *22*(4), 2511–2526, doi: 10.5194/hess-22-2511-2018.

Donner, L. J., B. L. Wyman, R. S. Hemler, L. W. Horowitz, Y. Ming, M. Zhao, J.-C. Golaz, P. Ginoux, S.-J. Lin, M. D. Schwarzkopf, J. Austin, G. Alaka, W. F. Cooke, T. L. Delworth, S. M. Freidenreich, C. T. Gordon, S. M. Griffies, I. M. Held, W. J. Hurlin, S. A. Klein, T. R. Knutson, A. R. Langenhorst, H.-C. Lee, Y. Lin, B. I. Magi, S. L. Malyshev, P. C. D. Milly, V. Naik, M. J. Nath, R. Pincus, J. J. Ploshay, V. Ramaswamy, C. J. Seman, E. Shevliakova, J. J. Sirutis, W. F. Stern, R. J. Stouffer, R. J. Wilson, M. Winton, A. T. Wittenberg, and F. Zeng (2011), The Dynamical Core, Physical Parameterizations, and Basic Simulation Characteristics of the Atmospheric Component AM3 of the GFDL Global Coupled Model CM3, *Journal of Climate*, *24*(13), 3484–3519, doi: 10.1175/2011JCLI3955.1.

Doss-Gollin, J., F. d. A. de Souza Filho, and F. O. E. da Silva (2015), Analytic modeling of rainwater harvesting in the Brazilian Semiarid Northeast, *Journal of the American Water Resources Association*, *52*(1), 129–137, doi: 10.1111/1752-1688.12376.

Doss-Gollin, J., Á. G. Muñoz, S. J. Mason, and M. Pastén (2018), Heavy rainfall in Paraguay during the 2015-2016 austral summer: Causes and sub-seasonal-to-seasonal predictive skill, *Journal of Climate*, *31*(17), 6669–6685, doi: 10.1175/JCLI-D-17-0805.1.

Doss-Gollin, J., U. Lall, and J. Lamontagne (2019a), Towards adaptive resilience: Managing uncertainties and exploiting predictability across timescales, in *American Geophsyical Union Fall Meeting*, San Francisco, CA, doi: 10.6084/m9.figshare.11397936.v1.

Doss-Gollin, J., D. J. Farnham, S. Steinschneider, and U. Lall (2019b), Robust adaptation to multiscale climate variability, *Earth's Future*, *7*(7), doi: 10.1029/2019EF001154.

Doss-Gollin, J., D. J. Farnham, M. Ho, and U. Lall (2020), Adaptation over fatalism: Leveraging high-impact climate disasters to boost societal resilience, *Journal of Water Resources Planning and Management*, *146*(4), doi: 10.1061/(ASCE)WR.1943-5452.0001190.

Du, S., P. Scussolini, P. J. Ward, M. Zhang, J. Wen, L. Wang, E. Koks, A. Diaz-Loaiza, J. Gao, Q. Ke, and J. C. J. H. Aerts (2020), Hard or soft flood adaptation? Advantages of a hybrid strategy for Shanghai, *Global Environmental Change*, *61*, 102,037, doi: 10.1016/j.gloenvcha.2020.102037.

Duchez, A., E. Frajka-Williams, S. A. Josey, D. G. Evans, J. P. Grist, R. Marsh, G. D. McCarthy, B. Sinha, D. I. Berry, and J. J.-M. Hirschi (2016), Drivers of exceptionally cold North Atlantic Ocean temperatures and their link to the 2015 European heat wave, *Environmental Research Letters*, *11*(7), 074,004, doi: 10.1088/1748-9326/11/7/074004.

Dugan, P. J., C. Barlow, A. A. Agostinho, E. Baran, G. F. Cada, D. Chen, I. G. Cowx, J. W. Ferguson, T. Jutagate, M. Mallen-Cooper, G. Marmulla, J. Nestler, M. Petrere, R. L. Welcomme, and K. O. Winemiller (2010), Fish Migration, Dams, and Loss of Ecosystem Services in the Mekong Basin, *AMBIO*, *39*(4), 344–348, doi: 10.1007/s13280-010-0036-1.

Durman, C. F., J. M. Gregory, D. C. Hassell, R. G. Jones, and J. M. Murphy (2001), A comparison of extreme European daily precipitation simulated by a global and a regional climate model for present and future climates, *Quarterly Journal of the Royal Meteorological Society*, *127*(573), 1005–1015, doi: 10.1002/qj.49712757316.

Eden, J. M., M. Widmann, D. Grawe, and S. Rast (2012), Skill, Correction, and Downscaling of GCM-Simulated Precipitation, *Journal of Climate*, *25*(11), 3970–3984, doi: 10.1175/JCLI-D-11-00254.1.

Eggimann, S., B. Truffer, and M. Maurer (2015), To connect or not to connect? Modelling the optimal degree of centralisation for wastewater infrastructures, *Water Research*, *84*, 218–231, doi: 10.1016/j.watres.2015.07.004.

Eggimann, S., B. Truffer, and M. Maurer (2016), Economies of density for on-site waste water treatment, *Water Research*, *101*, 476–489, doi: 10.1016/j.watres.2016.06.011.

Ehret, U., E. Zehe, V. Wulfmeyer, K. Warrach-Sagi, and J. Liebert (2012), Should we apply bias correction to global and regional climate model data?, *Hydrology and Earth System Sciences*, *16*(9), 3391–3404, doi: 10.5194/hess-16-3391-2012.

Eijgenraam, C., R. Brekelmans, D. den Hertog, and K. Roos (2012), Flood prevention by optimal dike heightening.

Eijgenraam, C., J. Kind, C. Bak, R. Brekelmans, D. den Hertog, M. Duits, K. Roos, P. Vermeer, and W. Kuijken (2014), Economically Efficient Standards to Protect the Netherlands Against Flooding, *INFORMS Journal on Applied Analytics*, *44*(1), 7–21, doi: 10.1287/inte.2013.0721.

El Adlouni, S.-E., B. Bobée, and T. B. M. J. Ouarda (2008), On the tails of extreme event distributions in hydrology, *Journal of Hydrology*, *355*(1-4), 16–33, doi: 10.1016/j.jhydrol.2008.02.011.

Ellsberg, D. (1961), Risk, Ambiguity, and the Savage Axioms, *The Quarterly Journal of Economics*, *75*(4), 643–669, doi: 10.2307/1884324.

Emanuel, K. (2017a), Will Global Warming Make Hurricane Forecasting More Difficult?, *Bulletin of the American Meteorological Society*, *98*(3), 495–501, doi: 10.1175/BAMS-D-16-0134.1.

Emanuel, K. (2017b), Assessing the present and future probability of Hurricane Harvey's rainfall, *Proceedings of the National Academy of Sciences*, *114*(48), 12,681–12,684, doi: 10.1073/pnas.1716222114.

Emanuel, K. A. (1988), The maximum intensity of hurricanes, *Journal of the Atmospheric Sciences*, *45*(7), 1143–1155, doi: 10.1175/1520-0469(1988)045<1143:TMIOH>2.0.CO;2.

Ennenbach, M. W., P. C. Larrauri, and U. Lall (2018), County-Scale Rainwater Harvesting Feasibility in the United States: Climate, Collection Area, Density, and Reuse Considerations, *Journal of the American Water Resources Association*, *54*(1), 255–274, doi: 10.1111/1752-1688.12607.

Erfani, T., K. Pachos, and J. J. Harou (2018), Real-Options Water Supply Planning: Multistage Scenario Trees for Adaptive and Flexible Capacity Expansion Under Probabilistic Climate Change Uncertainty, *Water Resources Research*, *54*(7), 5069–5087, doi: 10.1029/2017WR021803.

Escobar, H. (2015), Drought triggers alarms in Brazil's biggest metropolis, *Science*, *347*(6224), 812–812, doi: 10.1126/science.347.6224.812.

Espinoza, D., J. Morris, H. Baroud, M. Bisogno, A. Cifuentes, A. Gentzoglanis, L. Luccioni, J. Rojo, and F. Vahedifard (2019), The role of traditional discounted cash flows in the tragedy of the horizon: Another inconvenient truth, *Mitigation and Adaptation Strategies for Global Change*, doi: 10.1007/s11027-019-09884-3.

Espinoza, V., D. E. Waliser, B. Guan, D. A. Lavers, and F. M. Ralph (2018), Global Analysis of Climate Change Projection Effects on Atmospheric Rivers, *Geophysical Research Letters*, *47*(3), 514, doi: 10.1029/2017GL076968.

Faber, B. A., and J. R. Stedinger (2001), Reservoir optimization using sampling SDP with ensemble streamflow prediction (ESP) forecasts, *Journal of Hydrology*, *249*(1), 113–133, doi: 10.1016/S0022-1694(01)00419-X.

Faranda, D., J. M. Freitas, V. Lucarini, G. Turchetti, and S. Vaienti (2013), Extreme value statistics for dynamical systems with noise, *Nonlinearity*, *26*(9), 2597–2622, doi: 10.1088/0951-7715/26/9/2597.

Faranda, D., G. Messori, and P. Yiou (2017), Dynamical proxies of North Atlantic predictability and extremes, *Scientific reports*, *7*, 41,278, doi: 10.1038/srep41278.

Farnham, D. J., S. Steinschneider, and U. Lall (2017), Zonal Wind Indices to Reconstruct CONUS Winter Precipitation, *Geophysical Research Letters*, *44*(24), 12, 236–12, 243, doi: 10.1002/2017GL075959.

Farnham, D. J., J. Doss-Gollin, and U. Lall (2018), Regional extreme precipitation events: Robust inference from credibly simulated GCM variables, *Water Resources Research*, *54*(6), doi: 10.1002/2017wr021318.

Feng, H., T. R. Willemain, and N. Shang (2005), Wavelet-Based Bootstrap for Time Series Analysis, *Communications in Statistics - Simulation and Computation*, *34*(2), 393–413, doi: 10.1081/SAC-200055722.

Feng, J., T. Lian, J. Ying, J. Li, and G. Li (2019), Do CMIP5 models show El Niño diversity?, *Journal of Climate*, doi: 10.1175/JCLI-D-18-0854.1.

Fletcher, S., M. Lickley, and K. Strzepek (2019a), Learning about climate change uncertainty enables flexible water infrastructure planning, *Nature Communications*, *10*(1), 1782, doi: 10.1038/s41467-019-09677-x.

Fletcher, S., K. Strzepek, A. Alsaati, and O. de Weck (2019b), Learning and flexibility for water supply infrastructure planning under groundwater resource uncertainty, *Environmental Research Letters*, *14*(11), 114,022, doi: 10.1088/1748-9326/ab4664.

Fletcher, S. M. (2018), Learning and flexibility for water supply infrastructure planning under diverse uncertainties, Ph.D. Thesis, Massachusetts Institute of Technology.

Fletcher, S. M., M. Miotti, S. Jaichander, M. M. Klemun, K. Strzepek, and A. Siddiqi (2017), Water Supply Infrastructure Planning: Decision-Making Framework to Classify Multiple Uncertainties and Evaluate Flexible Design, *Journal of Water Resources Planning and Management*, *143*(10), 04017,061, doi: 10.1061/(ASCE)WR.1943-5452.0000823.

Flyvbjerg, B. (2009), Survival of the unfittest: Why the worst infrastructure gets built-and what we can do about it, *Oxford Review of Economic Policy*, *25*(3), 344–367, doi: 10.1093/oxrep/grp024.

Flyvbjerg, B., M. K. S. Holm, and S. L. Buhl (2005), How (in)accurate are demand forecasts in public works projects?: The case of transportation, *Journal of the American Planning Association*, *71*(2), 131–146, doi: 10.1080/01944360508976688.

Fortunato, M., M. G. Azar, B. Piot, J. Menick, I. Osband, A. Graves, V. Mnih, R. Munos, D. Hassabis, O. Pietquin, C. Blundell, and S. Legg (2019), Noisy Networks for Exploration, *arXiv:1706.10295 [cs.LG]*.

Foster, B. T., J. D. Kern, and G. W. Characklis (2015), Mitigating hydrologic financial risk in hydropower generation using index-based financial instruments, *Water Resources and Economics*, *10*, 45–67, doi: 10.1016/j.wre.2015.04.001.

France, J. W., I. A. Alvi, P. A. Dickson, H. T. Falvery, S. J. Rigbey, and J. Trojanowski (2018), Independent Forensic Team Report Oroville Dam Spillway Incident, *Tech. rep.*, California Institution of Water Resources.

Francis, J. A., and S. J. Vavrus (2012), Evidence linking Arctic amplification to extreme weather in mid-latitudes, *Geophysical Research Letters*, *39*(6), doi: 10.1029/2012GL051000.

Friederichs, P., and A. Hense (2007), Statistical Downscaling of Extreme Precipitation Events Using Censored Quantile Regression, *Monthly Weather Review*, *135*(6), 2365–2378, doi: 10.1175/MWR3403.1.

Friedman, J. H., and N. I. Fisher (1999), Bump hunting in high-dimensional data, *Statistics and Computing*, *9*(2), 123–143, doi: 10.1023/A:1008894516817.

Fritz, A. (2016), 'Omega block' will create warmth and sun for some, feet of snow for others, *The Washington Post*.

Gale, E. L., and M. A. Saunders (2013), The 2011 Thailand flood: Climate causes and return periods, *Weather*, *68*(9), 233–237, doi: 10.1002/wea.2133.

Garner, G. G., and K. Keller (2018), Using direct policy search to identify robust strategies in adapting to uncertain sea-level rise and storm surge, *Environmental Modelling & Software*, *107*, 96–104, doi: 10.1016/j.envsoft.2018.05.006.

GEI Consultants, Inc. (2017), Tulare Lake Storage and Floodwater Protection Feasibility Report, *Tech. rep.*, California Water Comission.

Gelman, A., and E. Loken (2013), The garden of forking paths: Why multiple comparisons can be a problem, even when there is no "fishing expedition" or "p-hacking" and the research hypothesis ….

Gelman, A., and C. R. Shalizi (2013), Philosophy and the practice of Bayesian statistics, *British Journal of Mathematical and Statistical Psychology*, *66*(1), 8–38, doi: 10.1111/j.2044-8317.2011.02037.x.

Gelman, A., J. B. Carlin, H. S. Stern, and D. B. Rubin (2014), *Bayesian Data Analysis*, third ed., Chapman & Hall/CRC Boca Raton, FL, USA.

Gelman, A., D. Simpson, and M. Betancourt (2017), The Prior Can Often Only Be Understood in the Context of the Likelihood, *Entropy*, *19*(10), 555, doi: 10.3390/e19100555.

Gentine, P., M. Pritchard, S. Rasp, G. Reinaudi, and G. Yacalis (2018), Could machine learning break the convection parameterization deadlock?, *Geophysical Research Letters*, *45*(11), 5742–5751, doi: 10.1029/2018GL078202.

Geoffrion, A. M., J. S. Dyer, and A. Feinberg (1972), An Interactive Approach for Multi-Criterion Optimization, with an Application to the Operation of an Academic Department, *Management Science*, *19*(4), 357–368, doi: 10.1287/mnsc.19.4.357.

Geweke, J., and S. Porter-Hudak (1983), The Estimation and Application of Long Memory Time Series Models, *Journal of Time Series Analysis*, *4*(4), 221–238, doi: 10.1111/j.1467-9892.1983.tb00371.x.

Ghil, M. (2020), Hilbert problems for the geosciences in the 21st century – 20 years later, *Nonlinear Processes in Geophysics Discussions*, pp. 1–30, doi: 10.5194/npg-2020-13.

Ghil, M., P. Yiou, S. Hallegatte, B. D. Malamud, P. Naveau, A. Soloviev, P. Friederichs, V. Keilis-Borok, D. Kondrashov, V. Kossobokov, O. Mestre, C. Nicolis, H. W. Rust, P. Shebalin, M. Vrac, A. Witt, and I. Zaliapin (2011), Extreme events: Dynamics, statistics and prediction, *Nonlinear Processes in Geophysics*, *18*(3), 295–350, doi: 10.5194/npg-18-295-2011.

Gilboa, I., M. Rouziou, and O. Sibony (2018), Decision theory made relevant: Between the software and the shrink, *Research in Economics*, *72*(2), 240–250, doi: 10.1016/j.rie.2018.01.001.

Gilliom, R. L., C. D. Bell, T. S. Hogue, and J. E. McCray (2019), A Rainwater Harvesting Accounting Tool for Water Supply Availability in Colorado, *Water*, *11*(11), 2205, doi: 10.3390/w11112205.

Gimeno, L., A. Drumond, R. Nieto, R. M. Trigo, and A. Stohl (2010), On the origin of continental precipitation, *Geophysical Research Letters*, *37*(13), doi: 10.1029/2010GL043712.

Gimeno, L., R. Nieto, M. Vázquez, and D. A. Lavers (2014), Atmospheric rivers: A mini-review, *Frontiers in Earth Science*, *2*, 1063, doi: 10.3389/feart.2014.00002.

Giuliani, M., A. Castelletti, F. Pianosi, E. Mason, and P. M. Reed (2016), Curses, Tradeoffs, and Scalable Management: Advancing Evolutionary Multiobjective Direct Policy Search to Improve Water Reservoir Operations, *Journal of Water Resources Planning and Management*, *142*(2), 04015,050, doi: 10.1061/(ASCE)WR.1943-5452.0000570.

Giuliani, M., J. D. Quinn, J. D. Herman, A. Castelletti, and P. M. Reed (2018), Scalable multiobjective control for large-scale water resources systems under uncertainty, *IEEE Transactions on Control Systems Technology*, *26*(4), 1492–1499, doi: 10.1109/TCST.2017.2705162.

Glahn, H. R., and D. A. Lowry (1972), The Use of Model Output Statistics (MOS) in Objective Weather Forecasting, *Journal of Applied Meteorology*, *11*(8), 1203–1211, doi: 10.1175/1520-0450(1972)011<1203:tuomos>2.0.co;2.

Gleick, P. H. (2003), Global freshwater resources: Soft-path solutions for the 21st century, *Science*, *302*(5650), 1524–1528, doi: 10.1126/science.1089967.

Goddard, L., W. E. Baethgen, H. Bhojwani, and A. W. Robertson (2014), The International Research Institute for Climate & Society: Why, what and how, *Earth Perspectives*, *1*(1), 10, doi: 10.1186/2194-6434-1-10.

Goly, A., R. S. V. Teegavarapu, and A. Mondal (2014), Development and Evaluation of Statistical Downscaling Models for Monthly Precipitation, *Earth Interactions*, *18*(18), 1–28, doi: 10.1175/EI-D-14-0024.1.

González, A. D., L. Dueñas-Osorio, M. Sánchez-Silva, and A. L. Medaglia (2016), The interdependent network design problem for optimal infrastructure system restoration, *Computer-Aided Civil and Infrastructure Engineering*, *31*(5), 334–350, doi: 10.1111/mice.12171.

Gonzalez, P. L. M., and L. Goddard (2015), Long-lead ENSO predictability from CMIP5 decadal hindcasts, *Climate Dynamics*, *46*(9-10), 3127–3147, doi: 10.1007/s00382-015-2757-0.

Good, I. J. (1952), Rational Decisions, *Journal of the Royal Statistical Society. Series B (Methodological)*, *14*(1), 107–114, doi: 10.1111/j.2517-6161.1952.tb00104.x.

Goodwell, A. E., P. Jiang, B. L. Ruddell, and P. Kumar (2020), Debates: Does information theory provide a new paradigm for earth science? Causality, interaction, and feedback, *Water Resources Research*, *56*(2), e2019WR024,940, doi: 10.1029/2019WR024940.

Gorelick, D. E., L. Lin, Zeff, Y. Kim, J. Vose, J. Coulston, D. Wear, L. Band, P. M. Reed, and G. W. Characklis (2019), Accounting for adaptive water supply management when quantifying climate and landcover change vulnerability, *Water Resources Research*, doi: 10.1029/2019WR025614.

Grams, C. M., H. Binder, S. Pfahl, N. Piaget, and H. Wernli (2014), Atmospheric processes triggering the central European floods in June 2013, *Natural Hazards and Earth System Science*, *14*(7), 1691–1702, doi: 10.5194/nhess-14-1691-2014.

Grasso, L. D. (2000), The Differentiation between Grid Spacing and Resolution and Their Application to Numerical Modeling, *Bulletin of the American Meteorological Society*, *81*(3), 579–586, doi: 10.1175/1520-0477(2000)081<0579:CAA>2.3.CO;2.

Greatrex, H., J. Hansen, S. Garvin, R. Diro, L. G. M, B. S, R. Kolli, and D. E. Osgood (2015), Scaling up index insurance for smallholder farmers: Recent evidence and insights, *Report*, CGIAR Research Program on Climate Change, Agriculture and Food Security (CCAFS).

Green, J. K., A. G. Konings, S. H. Alemohammad, J. Berry, D. Entekhabi, J. Kolassa, J.-E. Lee, and P. Gentine (2017), Regionally strong feedbacks between the atmosphere and terrestrial biosphere, *Nature Geoscience*, *10*(6), 410–+, doi: 10.1038/NGEO2957.

Greene, A. M., and A. W. Robertson (2017), Interannual and low-frequency variability of Upper Indus Basin winter/spring precipitation in observations and CMIP5 models, *Climate Dynamics*, *49*(11-12), 4171–4188, doi: 10.1007/s00382-017-3571-7.

Greenland, S. (2008), Invited Commentary: Variable Selection versus Shrinkage in the Control of Multiple Confounders, *American Journal of Epidemiology*, *167*(5), 523–529, doi: 10.1093/aje/kwm355.

Grimm, A. M. (2003), The El Niño Impact on the Summer Monsoon in Brazil: Regional Processes versus Remote Influences, *Journal of Climate*, *16*(2), 263–280, doi: 10.1175/1520-0442(2003)016<0263:teniot>2.0.co;2.

Grimm, A. M., and R. G. Tedeschi (2009), ENSO and Extreme Rainfall Events in South America, *Journal of Climate*, *22*(7), 1589–1609, doi: 10.1175/2008JCLI2429.1.

Grimm, A. M., and M. T. Zilli (2009), Interannual Variability and Seasonal Evolution of Summer Monsoon Rainfall in South America, *Journal of Climate*, *22*(9), 2257–2275, doi: 10.1175/2008JCLI2345.1.

Grimm, A. M., V. R. Barros, and M. E. Doyle (2000), Climate variability in southern South America associated with El Nino and La Nina events, *Journal of Climate*, *13*(1), 35–58, doi: 10.1175/1520-0442(2000)013<0035:CVISSA>2.0.CO;2.

Grimm, A. M., J. S. Pal, and F. Giorgi (2007), Connection between Spring Conditions and Peak Summer Monsoon Rainfall in South America: Role of Soil Moisture, Surface Temperature, and Topography in Eastern Brazil, *Journal of Climate*, *20*(24), 5929–5945, doi: 10.1175/2007JCLI1684.1.

Guannel, G., K. Arkema, P. Ruggiero, and G. Verutes (2016), The Power of Three: Coral Reefs, seagrasses and mangroves protect coastal regions and increase their resilience, *PLOS ONE*, *11*(7), e0158,094, doi: 10.1371/journal.pone.0158094.

Gudmundsson, L., J. B. Bremnes, J. E. Haugen, and T. Engen-Skaugen (2012), Technical Note: Downscaling RCM precipitation to the station scale using statistical transformations – a comparison of methods, *Hydrology and Earth System Sciences*, *16*(9), 3383–3390, doi: 10.5194/hess-16-3383-2012.

Gupta, S. K., and J. Rosenhead (1968), Robustness in Sequential Investment Decisions, *Management Science*, *15*(2), B18–B29, doi: 10.1287/mnsc.15.2.B18.

Gutman, J. (2019), Commentary: Urban wetlands restoration as NBS for flood risk mitigation: From positive case to legitimate practice, in the view of evidence-based flood risk policy making, in *Nature-Based Flood Risk Management on Private Land: Disciplinary Perspectives on a Multidisciplinary Challenge*, edited by T. Hartmann, L. Slavíková, and S. McCarthy, pp. 127–134, Springer International Publishing, Cham, doi: 10.1007/978-3-030-23842-1_13.

Gutmann, E., T. Pruitt, M. P. Clark, L. Brekke, J. R. Arnold, D. A. Raff, and R. M. Rasmussen (2014), An intercomparison of statistical downscaling methods used for water resource assessments in the United States, *Water Resources Research*, *50*(9), 7167–7186, doi: 10.1002/2014WR015559.

Haasnoot, M., H. Middelkoop, A. Offermans, E. van Beek, and W. P. A. van Deursen (2012), Exploring pathways for sustainable water management in river deltas in a changing environment, *Climatic Change*, *115*(3), 795–819, doi: 10.1007/s10584-012-0444-2.

Haasnoot, M., J. H. Kwakkel, W. E. Walker, and J. ter Maat (2013), Dynamic adaptive policy pathways: A method for crafting robust decisions for a deeply uncertain world, *Global Environmental Change*, *23*(2), 485–498, doi: 10.1016/j.gloenvcha.2012.12.006.

Haasnoot, M., J. Schellekens, J. J. Beersma, H. Middelkoop, and J. C. J. Kwadijk (2015), Transient scenarios for robust climate change adaptation illustrated for water management in The Netherlands, *Environmental Research Letters*, *10*(10), 105,008, doi: 10.1088/1748-9326/10/10/105008.

Hadka, D., and P. Reed (2012), Borg: An Auto-Adaptive Many-Objective Evolutionary Computing Framework, *Evolutionary Computation*, *21*(2), 231–259, doi: 10.1162/EVCO_a_00075.

Hadka, D., J. Herman, P. Reed, and K. Keller (2015), An open source framework for many-objective robust decision making, *Environmental Modelling & Software*, *74*, 114–129, doi: 10.1016/j.envsoft.2015.07.014.

Haer, T., T. G. Husby, W. J. W. Botzen, and J. C. J. H. Aerts (2020), The safe development paradox: An agent-based model for flood risk under climate change in the European Union, *Global Environmental Change*, *60*, 102,009, doi: 10.1016/j.gloenvcha.2019.102009.

Hagerman, S., P. Jaramillo, and M. G. Morgan (2016), Is rooftop solar PV at socket parity without subsidies?, *Energy Policy*, *89*, 84–94, doi: 10.1016/j.enpol.2015.11.017.

Ham, Y.-G., J.-H. Kim, and J.-J. Luo (2019), Deep learning for multi-year ENSO forecasts, *Nature*, pp. 1–5, doi: 10.1038/s41586-019-1559-7.

Hamilton, A., G. W. Characklis, and P. M. Reed (2020), Managing financial risk tradeoffs for hydropower generation using snowpack-based index contracts, *Earth and Space Science Open Archive*, doi: 10.1002/essoar.10502068.1.

Hannachi, A., and N. Trendafilov (2017), Archetypal Analysis: Mining Weather and Climate Extremes, *Journal of Climate*, *30*(17), 6927–6944, doi: 10.1175/JCLI-D-16-0798.1.

Hannachi, A., T. Woollings, and K. Fraedrich (2011), The North Atlantic jet stream: A look at preferred positions, paths and transitions, *Quarterly Journal of the Royal Meteorological Society*, *138*(665), 862–877, doi: 10.1002/qj.959.

Hannachi, A., D. M. Straus, C. L. E. Franzke, S. Corti, and T. Woollings (2017), Low-frequency nonlinearity and regime behavior in the Northern Hemisphere extratropical atmosphere, *Reviews of Geophysics*, *55*(1), 199–234, doi: 10.1002/2015RG000509.

Haraguchi, M., and U. Lall (2015), Flood risks and impacts: A case study of Thailand's floods in 2011 and research questions for supply chain decision making, *International Journal of Disaster Risk Reduction*, *14*, 256–272, doi: 10.1016/j.ijdrr.2014.09.005.

Harsha, J. (2019), Ageing large dams and future water crisis, *Economic and Political Weekly*, *54*(26-27), 7–8.

Hassanzadeh, P., Z. Kuang, and B. F. Farrell (2014), Responses of midlatitude blocks and wave amplitude to changes in the meridional temperature gradient in an idealized dry GCM, *Geophysical Research Letters*, *41*(14), 5223–5232, doi: 10.1002/2014GL060764.

Hawkins, E., and R. Sutton (2012), Time of emergence of climate signals, *Geophysical Research Letters*, *39*(1), doi: 10.1029/2011GL050087.

Heinze, G., and D. Dunkler (2017), Five myths about variable selection, *Transplant International*, *30*(1), 6–10, doi: 10.1111/tri.12895.

Heinze, G., C. Wallisch, and D. Dunkler (2018), Variable selection – A review and recommendations for the practicing statistician, *Biometrical Journal*, *60*(3), 431–449, doi: 10.1002/bimj.201700067.

Helbing, D. (2013), Globally networked risks and how to respond, *Nature*, *497*(7447), 51–59, doi: 10.1038/nature12047.

Held, I. M. (2005), The Gap between Simulation and Understanding in Climate Modeling, *Bulletin of the American Meteorological Society*, *86*(11), 1609–1614, doi: 10.1175/BAMS-86-11-1609.

Held, I. M., and A. Y. Hou (1980), Nonlinear Axially Symmetric Circulations in a Nearly Inviscid Atmosphere, *Journal of the Atmospheric Sciences*, *37*(3), 515–533, doi: 10.1175/1520-0469(1980)037<0515:nascia>2.0.co;2.

Held, I. M., and B. J. Soden (2006), Robust Responses of the Hydrological Cycle to Global Warming, *Journal of Climate*, *19*(21), 5686–5699, doi: 10.1175/JCLI3990.1.

Hellmuth, M. E., S. J. Mason, C. Vaughan, M. van Aalst, and R. Choularton (2011), *A Better Climate for Disaster Risk Management*, International Research Institute for Climate and Society, Palisades.

Herdies, D. L., A. da Silva, M. A. F. Silva Dias, and R. Nieto Ferreira (2002), Moisture budget of the bimodal pattern of the summer circulation over South America, *Journal of Geophysical Research: Atmospheres*, pp. LBA 42–1, doi: 10.1029/2001JD000997.

Herman, J., and W. Usher (2017), SALib: An open-source Python library for Sensitivity Analysis, *Journal of Open Source Software*, *2*(9), 97, doi: 10.21105/joss.00097.

Herman, J. D., H. B. Zeff, P. M. Reed, and G. W. Characklis (2014), Beyond optimality: Multistakeholder robustness tradeoffs for regional water portfolio planning under deep uncertainty, *Water Resources Research*, *50*(10), 7692–7713, doi: 10.1002/2014WR015338.

Herman, J. D., P. M. Reed, H. B. Zeff, and G. W. Characklis (2015), How Should Robustness Be Defined for Water Systems Planning under Change?, *Journal of Water Resources Planning and Management*, *141*(10), 04015,012, doi: 10.1061/(ASCE)WR.1943-5452.0000509.

Herman, J. D., J. D. Quinn, S. Steinschneider, M. Giuliani, and S. Fletcher (2020), Climate adaptation as a control problem: Review and perspectives on dynamic water resources planning under uncertainty, *Water Resources Research*, p. e24389, doi: 10.1029/2019WR025502.

Hessel, M., J. Modayil, H. van Hasselt, T. Schaul, G. Ostrovski, W. Dabney, D. Horgan, B. Piot, M. Azar, and D. Silver (2017), Rainbow: Combining Improvements in Deep Reinforcement Learning, *arXiv:1710.02298 [cs.AI]*.

Highfield, W. E., and S. D. Brody (2017), Determining the effects of the FEMA Community Rating System program on flood losses in the United States, *International Journal of Disaster Risk Reduction*, *21*, 396–404, doi: 10.1016/j.ijdrr.2017.01.013.

Hindriks, J. (2006), *Intermediate Public Economics*, MIT Press, Cambridge, Mass.

Hino, M., and J. W. Hall (2017), Real Options Analysis of Adaptation to Changing Flood Risk: Structural and Nonstructural Measures, *ASCE-ASME Journal of Risk and Uncertainty in Engineering Systems, Part A: Civil Engineering*, *3*(3), 04017,005, doi: 10.1061/AJRUA6.0000905.

Hino, M., C. B. Field, and K. J. Mach (2017), Managed retreat as a response to natural hazard risk, *Nature Climate Change*, *7*(5), 364–370, doi: 10.1038/nclimate3252.

Hirabayashi, Y., R. Mahendran, S. Koirala, L. Konoshima, D. Yamazaki, S. Watanabe, H. Kim, and S. Kanae (2013), Global flood risk under climate change, *Nature Climate Change*, *3*(9), 816–821, doi: 10.1038/nclimate1911.

Ho, M., U. Lall, M. Allaire, N. Devineni, H.-H. Kwon, I. Pal, D. Raff, and D. Wegner (2017), The future role of dams in the United States of America, *Water Resources Research*, *53*(2), 982–998, doi: 10.1002/2016WR019905.

Hochard, J. P., S. Hamilton, and E. B. Barbier (2019), Mangroves shelter coastal economic activity from cyclones, *Proceedings of the National Academy of Sciences*, *116*(25), 12,232–12,237, doi: 10.1073/pnas.1820067116.

Hodgkins, G. A., P. H. Whitfield, D. H. Burn, J. Hannaford, B. Renard, K. Stahl, A. K. Fleig, H. Madsen, L. Mediero, J. Korhonen, C. Murphy, and D. Wilson (2017), Climate-driven variability in the occurrence of major floods across North America and Europe, *Journal of Hydrology*, *552*, 704–717, doi: 10.1016/j.jhydrol.2017.07.027.

Hoerling, M., J. Eischeid, A. Kumar, R. Leung, A. Mariotti, K. Mo, S. Schubert, and R. Seager (2014), Causes and predictability of the 2012 Great Plains drought, *Bulletin of the American Meteorological Society*, *95*(2), 269–282, doi: 10.1175/BAMS-D-13-00055.1.

Hoffman, M. D., and A. Gelman (2011), The No-U-Turn Sampler: Adaptively Setting Path Lengths in Hamiltonian Monte Carlo, *arXiv:1111.4246 [stat.CO]*.

Hofmann, H., H. Wickham, and K. Kafadar (2017), Letter-Value Plots: Boxplots for Large Data, *Journal of Computational and Graphical Statistics*, *26*(3), 469–477, doi: 10.1080/10618600.2017.1305277.

Holsclaw, T., A. M. Greene, A. W. Robertson, and P. Smyth (2015), A Bayesian Hidden Markov Model of Daily Precipitation over South and East Asia, *Journal of Hydrometeorology*, *17*(1), 3–25, doi: 10.1175/JHM-D-14-0142.1.

Horn, D., and M. McShane (2013), Flooding the market, *Nature Climate Change*, *3*(11), 945–947, doi: 10.1038/nclimate2025.

Hoskins, B., and T. Woollings (2015), Persistent Extratropical Regimes and Climate Extremes, *Current Climate Change Reports*, *1*(3), 115–124, doi: 10.1007/s40641-015-0020-8.

Howe, C. W. (1971), *Benefit-Cost Analysis for Water System Planning*, American Geophysical Union, Washington.

Hoyer, S., and J. Hamman (2017), Xarray: N-D labeled Arrays and Datasets in Python, *Journal of Open Research Software*, *5*(1), 304, doi: 10.5334/jors.148.

Huang, H.-P., R. Seager, and Y. Kushnir (2005), The 1976/77 transition in precipitation over the Americas and the influence of tropical sea surface temperature, *Climate Dynamics*, *24*(7), 721–740, doi: 10.1007/s00382-005-0015-6.

Huang, X., A. D. Hall, and N. Berg (2018), Anthropogenic Warming Impacts on Today's Sierra Nevada Snowpack and Flood Risk, *Geophysical Research Letters*, *45*(12), 6215–6222, doi: 10.1029/2018GL077432.

Hughes, J. P., P. Guttorp, and S. P. Charles (1999), A non-homogeneous hidden Markov model for precipitation occurrence, *Journal of the Royal Statistical Society: Series C (Applied Statistics)*, *48*(1), 15–30, doi: 10.1111/1467-9876.00136.

Hunter, J. D. (2007), Matplotlib: A 2D graphics environment, *Computing in Science & Engineering*, *9*(3), 90–95, doi: 10.1109/MCSE.2007.55.

Huntingford, C., D. Mitchell, K. Kornhuber, D. Coumou, S. Osprey, and M. Allen (2019), Assessing changes in risk of amplified planetary waves in a warming world, *Atmospheric Science Letters*, doi: 10.1002/asl.929.

Huntington, T. G., G. A. Hodgkins, B. D. Keim, and R. W. Dudley (2004), Changes in the Proportion of Precipitation Occurring as Snow in New England (1949–2000), *Journal of Climate*, *17*(13), 2626–2636, doi: 10.1175/1520-0442(2004)017<2626:CITPOP>2.0.CO;2.

Inoue, H., and Y. Todo (2019), Firm-level propagation of shocks through supply-chain networks, *Nature Sustainability*, *2*(9), 841–847, doi: 10.1038/s41893-019-0351-x.

IPCC (2012), *Managing the Risks of Extreme Events and Disasters to Advance Climate Change Adaptation*, Cambridge University Press, Cambridge, UK.

Jacob, J. S., K. Pandian, R. Lopez, and H. Biggs (2014), Houston-Area Freshwater Wetland Loss, 1992-2010, *Tech. Rep. TAMU-SG-14-303*, The Texas A&M University System.

Jacobeit, J., H. Wanner, J. Luterbacher, C. Beck, A. Philipp, and K. Sturm (2003), Atmospheric circulation variability in the North-Atlantic-European area since the mid-seventeenth century, *Climate Dynamics*, *20*(4), 341–352, doi: 10.1007/s00382-002-0278-0.

Jacobson, M. Z., M. A. Delucchi, Z. A. F. Bauer, S. C. Goodman, W. E. Chapman, M. A. Cameron, C. Bozonnat, L. Chobadi, H. A. Clonts, P. Enevoldsen, J. R. Erwin, S. N. Fobi, O. K. Goldstrom, E. M. Hennessy, J. Liu, J. Lo, C. B. Meyer, S. B. Morris, K. R. Moy, P. L. O'Neill, I. Petkov, S. Redfern, R. Schucker, M. A. Sontag, J. Wang, E. Weiner, and A. S. Yachanin (2017), 100% Clean and Renewable Wind, Water, and Sunlight All-Sector Energy Roadmaps for 139 Countries of the World, *Joule*, *1*(1), 108–121, doi: 10.1016/j.joule.2017.07.005.

Jain, S., and U. Lall (2001), Floods in a changing climate: Does the past represent the future?, *Water Resources Research*, *37*(12), 3193–3205, doi: 10.1029/2001WR000495.

Jamali, B., P. M. Bach, and A. Deletic (2020), Rainwater harvesting for urban flood management – An integrated modelling framework, *Water Research*, *171*, 115,372, doi: 10.1016/j.watres.2019.115372.

Jaynes, E. T. (2003), *Probability Theory: The Logic of Science*, Cambridge University Press, New York, NY.

Jenkins, A., D. Shoosmith, P. Dutrieux, S. Jacobs, T. W. Kim, S. H. Lee, H. K. Ha, and S. Stammerjohn (2018), West Antarctic Ice Sheet retreat in the Amundsen Sea driven by decadal oceanic variability, *Nature Geoscience*, *11*(10), 733–738, doi: 10.1038/s41561-018-0207-4.

Jin, F. F., J. D. Neelin, and M. Ghil (1994), El-Nino on the Devils Staircase - Annual Subharmonic Steps to Chaos, *Science*, *264*(5155), 70–72, doi: 10.1126/science.264.5155.70.

Johnson, F., and A. Sharma (2012), A nesting model for bias correction of variability at multiple time scales in general circulation model precipitation simulations, *Water Resources Research*, *48*(1), 1, doi: 10.1029/2011WR010464.

Jolliffe, I. T., and D. B. Stephenson (2012), *Forecast Verification: A Practitioner's Guide in Atmospheric Science*, 2nd ed ed., John Wiley & Sons.

Jones, C., and L. M. V. Carvalho (2002), Active and Break Phases in the South American Monsoon System, *Journal of Climate*, *15*(8), 905–914, doi: 10.1175/1520-0442(2002)015<0905:aabpit>2.0.co;2.

Jones, K. J., A. Ravichandran, and M. J. Rolen (2012), Decentralized wastewater treatment in the City of Sugar Land and Sugar Land's extra territorial jurisdictions, *Tech. Rep. 1148311259*, Texas Water Development Board.

Jongman, B., P. J. Ward, and J. C. J. H. Aerts (2012), Global exposure to river and coastal flooding: Long term trends and changes, *Global Environmental Change*, *22*(4), 823–835, doi: 10.1016/j.gloenvcha.2012.07.004.

Juan, A., A. Gori, and A. Sebastian (2020), Comparing floodplain evolution in channelized and unchannelized urban watersheds in Houston, Texas, *Journal of Flood Risk Management*, p. e12604, doi: 10.1111/jfr3.12604.

Kahneman, D., and A. Tversky (1979), Prospect Theory: An Analysis of Decision under Risk, *Econometrica*, *47*(2), 263–291, doi: 10.2307/1914185.

Kalchbrenner, N., and C. Sønderby (2020), A neural weather model for eight-hour precipitation forecasting.

Kalnay, E., M. Kanamitsu, R. Kistler, W. Collins, D. Deaven, L. Gandin, M. Iredell, S. Saha, G. White, J. Woollen, Y. Zhu, M. Chelliah, W. Ebisuzaki, W. Higgins, J. Janowiak, K. C. Mo, C. Ropelewski, J. Wang, A. Leetmaa, R. Reynolds, R. Jenne, and D. Joseph (1996), The NCEP/NCAR 40-year reanalysis project, *Bulletin of the American Meteorological Society*, *77*(3), 437–471, doi: 10.1175/1520-0477(1996)077<0437:TNYRP>2.0.CO;2.

Kalra, N. R., D. G. Groves, L. Bonzanigo, E. Molina Perez, C. Ramos, C. J. Brandon, and I. Rodriguez Cabanillas (2015), Robust decision-making in the water sector: A strategy for implementing Lima's long-term water resources master plan, *Tech. Rep. WPS7439*, The World Bank.

Kanamitsu, M., W. Ebisuzaki, J. Woollen, S.-K. Yang, J. J. Hnilo, M. Fiorino, and G. L. Potter (2002), NCEP–DOE AMIP-II Reanalysis (R-2), *Bulletin of the American Meteorological Society*, *83*(11), 1631–1643, doi: 10.1175/bams-83-11-1631(2002)083<1631:nar>2.3.co;2.

Kang, D., and K. Lansey (2014), Multiperiod Planning of Water Supply Infrastructure Based on Scenario Analysis, *Journal of Water Resources Planning and Management*, *140*(1), 40–54, doi: 10.1061/(ASCE)WR.1943-5452.0000310.

Kaplan, A., M. A. Cane, Y. Kushnir, A. C. Clement, M. B. Blumenthal, and B. Rajagopalan (1998), Analyses of global sea surface temperature 1856-1991, *Journal of Geophysical Research: Oceans*, *103*(C9), 18,567–18,589, doi: 10.1029/97JC01736.

Karl, T. R., W.-C. Wang, M. E. Schlesinger, R. W. Knight, and D. Portman (1990), A Method of Relating General Circulation Model Simulated Climate to the Observed Local Climate. Part I: Seasonal Statistics, *Journal of Climate*, *3*(10), 1053–1079, doi: 10.1175/1520-0442(1990)003<1053:AMORGC>2.0.CO;2.

Kaspi, Y., and T. Schneider (2013), The Role of Stationary Eddies in Shaping Midlatitude Storm Tracks, *Journal of the Atmospheric Sciences*, *70*(8), 2596–2613, doi: 10.1175/JAS-D-12-082.1.

Kasprzyk, J. R., P. M. Reed, G. W. Characklis, and B. R. Kirsch (2012), Many-objective de Novo water supply portfolio planning under deep uncertainty, *Environmental Modelling & Software*, *34*, 87–104, doi: 10.1016/j.envsoft.2011.04.003.

Kasprzyk, J. R., S. Nataraj, P. M. Reed, and R. J. Lempert (2013), Many objective robust decision making for complex environmental systems undergoing change, *Environmental Modelling & Software*, *42*, 55–71, doi: 10.1016/j.envsoft.2012.12.007.

Kendon, E. J., N. M. Roberts, C. A. Senior, and M. J. Roberts (2012), Realism of Rainfall in a Very High-Resolution Regional Climate Model, *Journal of Climate*, *25*(17), 5791–5806, doi: 10.1175/JCLI-D-11-00562.1.

Khalil, A. F., H.-H. Kwon, U. Lall, M. J. Miranda, and J. Skees (2007), El Niño–Southern Oscillation–based index insurance for floods: Statistical risk analyses and application to Peru, *Water Resources Research*, *43*(10), doi: 10.1029/2006WR005281.

Kiem, A. S., S. W. Franks, and G. Kuczera (2002), Multi-decadal variability of flood risk, *Geophysical Research Letters*, *30*(2), 3, doi: 10.1029/2002GL015992.

Kim, H., J. M. Caron, J. H. Richter, and I. R. Simpson (2020), The lack of QBO-MJO connection in CMIP6 models, *Geophysical Research Letters*, p. e2020GL087295, doi: 10.1029/2020GL087295.

Kim, M.-J., R. J. Nicholls, J. M. Preston, and G. A. M. de Almeida (2018), An assessment of the optimum timing of coastal flood adaptation given sea-level rise using real options analysis, *Journal of Flood Risk Management*, *0*(0), e12,494, doi: 10.1111/jfr3.12494.

Kimoto, M., and M. Ghil (1993), Multiple Flow Regimes in the Northern Hemisphere Winter. Part I: Methodology and Hemispheric Regimes, *Journal of the Atmospheric Sciences*, *50*(16), 2625–2644, doi: 10.1175/1520-0469(1993)050<2625:MFRITN>2.0.CO;2.

Kind, J. M., J. H. Baayen, and W. J. W. Botzen (2018), Benefits and Limitations of Real Options Analysis for the Practice of River Flood Risk Management, *Water Resources Research*, *95*(6144), 76, doi: 10.1002/2017WR022402.

Knight, F. H. (1921), *Risk, Uncertainty and Profit*, Boston ; New York : Hougthon Mifflin Company, Place of publication not identified.

Knippertz, P., and H. Wernli (2010), A Lagrangian Climatology of Tropical Moisture Exports to the Northern Hemispheric Extratropics, *Journal of Climate*, *23*(4), 987–1003, doi: 10.1175/2009JCLI3333.1.

Knippertz, P., H. Wernli, and G. Gläser (2013), A Global Climatology of Tropical Moisture Exports, *Journal of Climate*, *26*(10), 3031–3045, doi: 10.1175/JCLI-D-12-00401.1.

Knutson, T. R., J. L. McBride, J. Chan, K. Emanuel, G. Holland, C. Landsea, I. Held, J. P. Kossin, A. K. Srivastava, and M. Sugi (2010), Tropical cyclones and climate change, *Nature Geoscience*, *3*(3), 157–163, doi: 10.1038/ngeo779.

Kopp, R. E., R. M. DeConto, D. A. Bader, C. C. Hay, R. M. Horton, S. Kulp, M. Oppenheimer, D. Pollard, and B. H. Strauss (2017), Evolving Understanding of Antarctic Ice-Sheet Physics and Ambiguity in Probabilistic Sea-Level Projections, *Earth's Future*, *5*(12), 1217–1233, doi: 10.1002/2017EF000663.

Kornhuber, K., V. Petoukhov, S. Petri, S. Rahmstorf, and D. Coumou (2016), Evidence for wave resonance as a key mechanism for generating high-amplitude quasi-stationary waves in boreal summer, *Climate Dynamics*, *49*(5-6), 1961–1979, doi: 10.1007/s00382-016-3399-6.

Kornhuber, K., S. Osprey, D. Coumou, S. Petri, V. Petoukhov, S. Rahmstorf, and L. Gray (2019a), Extreme weather events in early summer 2018 connected by a recurrent hemispheric wave-7 pattern, *Environmental Research Letters*, *14*(5), 054,002, doi: 10.1088/1748-9326/ab13bf.

Kornhuber, K., D. Coumou, E. Vogel, C. Lesk, J. F. Donges, J. Lehmann, and R. M. Horton (2019b), Amplified Rossby waves enhance risk of concurrent heatwaves in major breadbasket regions, *Nature Climate Change*, pp. 1–6, doi: 10.1038/s41558-019-0637-z.

Kossin, J. P. (2017), Hurricane intensification along United States coast suppressed during active hurricane periods, *Nature*, *541*(7637), 390–393, doi: 10.1038/nature20783.

Köster, J., and S. Rahmann (2012), Snakemake: A scalable bioinformatics workflow engine, *Bioinformatics*, *28*(19), 2520–2522, doi: 10.1093/bioinformatics/bts480.

Koster, R. D., P. A. Dirmeyer, Z. Guo, G. Bonan, E. Chan, P. Cox, C. T. Gordon, S. Kanae, E. Kowalczyk, D. Lawrence, P. Liu, C.-H. Lu, S. Malyshev, B. McAvaney, K. Mitchell, D. Mocko, T. Oki, K. Oleson, A. Pitman, Y. C. Sud, C. M. Taylor, D. Verseghy, R. Vasic, Y. Xue, and T. Yamada (2004), Regions of Strong Coupling Between Soil Moisture and Precipitation, *Science*, *305*(5687), 1138–1140, doi: 10.1126/science.1100217.

Kousky, C., and H. Kunreuther (2010), Improving Flood Insurance and Flood-Risk Management: Insights from St. Louis, Missouri, *Natural Hazards Review*, *11*(4), 162–172, doi: 10.1061/(ASCE)NH.1527-6996.0000021.

Koutsoyiannis, D. (2003), Climate change, the Hurst phenomenon, and hydrological statistics, *Hydrological Sciences Journal*, *48*(1), 3–24, doi: 10.1623/hysj.48.1.3.43481.

Kravtsov, S., C. Grimm, and S. Gu (2018), Global-scale multidecadal variability missing in state-of-the-art climate models, *npj Climate and Atmospheric Science*, *1*(1), 34, doi: 10.1038/s41612-018-0044-6.

Kulp, S. A., and B. H. Strauss (2019), New elevation data triple estimates of global vulnerability to sea-level rise and coastal flooding, *Nature Communications*, *10*(1), 1–12, doi: 10.1038/s41467-019-12808-z.

Kumar, H., J. Gettleman, and S. Yasir (2019), How Do You Save a Million People From a Cyclone? Ask a Poor State in India, *The New York Times*.

Kumar, P., and H. V. Gupta (2020), Debates: Does information theory provide a new paradigm for earth science?, *Water Resources Research*, *56*(2), e2019WR026,398, doi: 10.1029/2019WR026398.

Kundzewicz, Z. W., N. Lugeri, R. Dankers, Y. Hirabayashi, P. Döll, I. Pińskwar, T. Dysarz, S. Hochrainer, and P. Matczak (2010), Assessing river flood risk and adaptation in Europe—review of projections for the future, *Mitigation and Adaptation Strategies for Global Change*, *15*(7), 641–656, doi: 10.1007/s11027-010-9213-6.

Kundzewicz, Z. W., S. Kanae, S. I. Seneviratne, J. Handmer, N. Nicholls, P. Peduzzi, R. Mechler, L. M. Bouwer, N. Arnell, K. Mach, R. Muir-Wood, G. R. Brakenridge, W. Kron, G. Benito, Y. Honda, K. Takahashi, and B. Sherstyukov (2013), Flood risk and climate change: Global and regional perspectives, *Hydrological Sciences Journal*, *59*(1), 1–28, doi: 10.1080/02626667.2013.857411.

Kunreuther, H. (1996), Mitigating disaster losses through insurance, *Journal of Risk and Uncertainty*, *12*(2-3), 171–187, doi: 10.1007/BF00055792.

Kunreuther, H., and G. Heal (2012), Managing Catastrophic Risk, *Working Paper 18136*, National Bureau of Economic Research, doi: 10.3386/w18136.

Kushnir, Y., A. A. Scaife, R. Arritt, G. Balsamo, G. Boer, F. Doblas-Reyes, E. Hawkins, M. Kimoto, R. K. Kolli, A. Kumar, D. Matei, K. Matthes, W. A. Müller, T. O'Kane, J. Perlwitz, S. Power, M. Raphael, A. Shimpo, D. Smith, M. Tuma, and B. Wu (2019), Towards operational predictions of the near-term climate, *Nature Climate Change*, p. 1, doi: 10.1038/s41558-018-0359-7.

Kwakkel, J. H., and E. Pruyt (2013), Exploratory modeling and analysis, an approach for model-based foresight under deep uncertainty, *Technological Forecasting and Social Change*, *80*(3), 419–431, doi: 10.1016/j.techfore.2012.10.005.

Kwakkel, J. H., M. Haasnoot, and W. E. Walker (2015), Developing dynamic adaptive policy pathways: A computer-assisted approach for developing adaptive strategies for a deeply uncertain world, *Climatic Change*, *132*(3), 373–386, doi: 10.1007/s10584-014-1210-4.

Kwakkel, J. H., M. Haasnoot, and W. E. Walker (2016), Comparing Robust Decision-Making and Dynamic Adaptive Policy Pathways for model-based decision support under deep uncertainty, *Environmental Modelling & Software*, *86*, 168–183, doi: 10.1016/j.envsoft.2016.09.017.

Kwon, H.-H., U. Lall, and A. F. Khalil (2007), Stochastic simulation model for nonstationary time series using an autoregressive wavelet decomposition: Applications to rainfall and temperature, *Water Resources Research*, *43*(5), 287, doi: 10.1029/2006WR005258.

Kwon, H.-H., U. Lall, and J. Obeysekera (2009), Simulation of daily rainfall scenarios with interannual and multidecadal climate cycles for South Florida, *Stochastic Environmental Research and Risk Assessment*, *23*(7), 879–896, doi: 10.1007/s00477-008-0270-2.

Lackey Katy, Sharkey Suzanne, Sharvelle Sybil, Kehoe Paula, and Chang Taylor (2020), Decentralized water reuse: Implementing and regulating onsite nonpotable water wystems, *Journal of Sustainable Water in the Built Environment*, *6*(1), 02519,001, doi: 10.1061/JSWBAY.0000891.

Lall, U. (1986), Project Risk Considering Samplng Uncertainties and a Finite Project Operation Period, in *Proceedings of the International Symposium on Flood Frequency and Risk Analyses*, pp. 305–318, Baton Rouge, U.S.A.

Lam, S. K., A. Pitrou, and S. Seibert (2015), Numba: A LLVM-based Python JIT compiler, in *Proceedings of the Second Workshop on the LLVM Compiler Infrastructure in HPC*, LLVM '15, pp. 1–6, Association for Computing Machinery, Austin, Texas, doi: 10.1145/2833157.2833162.

Lamontagne, J. (2015), Representation of uncertainty and corridor DP for hydropower optimization, Ph.D Thesis, Cornell University.

Lamontagne, J. R., P. M. Reed, G. Marangoni, K. Keller, and G. G. Garner (2019), Robust abatement pathways to tolerable climate futures require immediate global action, *Nature Climate Change*, *9*(4), 290–294, doi: 10.1038/s41558-019-0426-8.

Langlois, R. N., and M. M. Cosgel (1993), Frank Knight on Risk, Uncertainty, and the Firm: A New Interpretation, *Economic Inquiry*, *31*(3), 456–465, doi: 10.1111/j.1465-7295.1993.tb01305.x.

Lanzante, J. R., K. W. Dixon, M. J. Nath, C. E. Whitlock, and D. Adams-Smith (2018), Some Pitfalls in Statistical Downscaling of Future Climate, *Bulletin of the American Meteorological Society*, *99*(4), 791–803, doi: 10.1175/BAMS-D-17-0046.1.

Lau, W. K. M., and K.-M. Kim (2012), The 2010 Pakistan Flood and Russian Heat Wave: Teleconnection of Hydrometeorological Extremes, *Journal of Hydrometeorology*, *13*(1), 392–403, doi: 10.1175/JHM-D-11-016.1.

Lavers, D. A., and G. Villarini (2013a), The nexus between atmospheric rivers and extreme precipitation across Europe, *Geophysical Research Letters*, *40*(12), 3259–3264, doi: 10.1002/grl.50636.

Lavers, D. A., and G. Villarini (2013b), Atmospheric Rivers and Flooding over the Central United States, *Journal of Climate*, *26*(20), 7829–7836, doi: 10.1175/JCLI-D-13-00212.1.

Lavers, D. A., R. P. Allan, E. F. Wood, G. Villarini, D. J. Brayshaw, and A. J. Wade (2011), Winter floods in Britain are connected to atmospheric rivers, *Geophysical Research Letters*, *38*(23), doi: 10.1029/2011GL049783.

Lawrence, D., and K. Vandecar (2015), Effects of tropical deforestation on climate and agriculture, *Nature Climate Change*, *5*(1), 27–36, doi: 10.1038/nclimate2430.

Lawrence, J., and M. Haasnoot (2017), What it took to catalyse uptake of dynamic adaptive pathways planning to address climate change uncertainty, *Environmental Science & Policy*, *68*, 47–57, doi: 10.1016/j.envsci.2016.12.003.

Leduc, M., and R. Laprise (2009), Regional climate model sensitivity to domain size, *Climate Dynamics*, *32*(6), 833–854, doi: 10.1007/s00382-008-0400-z.

Lee, C. C., and S. C. Sheridan (2018), Trends in weather type frequencies across North America, *npj Climate and Atmospheric Science*, *1*(1), 41, doi: 10.1038/s41612-018-0051-7.

Lee, D., L. Klein, and G. Camus (1999), Induced Traffic and Induced Demand, *Transportation Research Record: Journal of the Transportation Research Board*, *1659*, 68–75, doi: 10.3141/1659-09.

Lehe, L. (2019), Downtown congestion pricing in practice, *Transportation Research Part C: Emerging Technologies*, *100*, 200–223, doi: 10.1016/j.trc.2019.01.020.

Lehmann, J., and D. Coumou (2015), The influence of mid-latitude storm tracks on hot, cold, dry and wet extremes, *Scientific reports*, *5*(1), 3220, doi: 10.1038/srep17491.

Lehner, B., P. Döll, J. Alcamo, T. Henrichs, and F. Kaspar (2006), Estimating the Impact of Global Change on Flood and Drought Risks in Europe: A Continental, Integrated Analysis, *Climatic Change*, *75*(3), 273–299, doi: 10.1007/s10584-006-6338-4.

Leigh, N. G., and H. Lee (2019), Sustainable and Resilient Urban Water Systems: The Role of Decentralization and Planning, *Sustainability*, *11*(3), 918, doi: 10.3390/su11030918.

Lempert, R. J. (2002), A new decision sciences for complex systems, *Proceedings of the National Academy of Sciences*, *99*(suppl 3), 7309–7313, doi: 10.1073/pnas.082081699.

Lempert, R. J., and M. T. Collins (2007), Managing the Risk of Uncertain Threshold Responses: Comparison of Robust, Optimum, and Precautionary Approaches, *Risk Analysis*, *27*(4), 1009–1026, doi: 10.1111/j.1539-6924.2007.00940.x.

Lempert, R. J., S. W. Popper, and S. C. Bankes (2003), Shaping the next one hundred years: New methods for quantitative, long-term policy analysis, *Tech. Rep. MR-1626-RPC*, RAND Corporation, Santa Monica, CA.

Lempert, R. J., R. L. Sriver, and K. Keller (2012), Characterizing Uncertain Sea Level Rise Projections to Support Investment Decisions, *Product Page*, RAND.

Liang, X.-Z., J. Pan, J. Zhu, K. E. Kunkel, J. X. L. Wang, and A. Dai (2006), Regional climate model downscaling of the U.S. summer climate and future change, *Journal of Geophysical Research: Atmospheres*, *111*(D10), doi: 10.1029/2005JD006685.

Lickley, M. J., N. Lin, and H. D. Jacoby (2014), Analysis of coastal protection under rising flood risk, *Climate Risk Management*, *6*, 18–26, doi: 10.1016/j.crm.2015.01.001.

Liebmann, B., G. N. Kiladis, C. S. Vera, A. C. Saulo, and L. M. V. Carvalho (2004), Subseasonal variations of rainfall in South America in the vicinity of the low-level jet east of the Andes and comparison to those in the South Atlantic convergence zone, *Journal of Climate*, *17*(19), 3829–3842, doi: 10.1175/1520-0442(2004)017<3829:SVORIS>2.0.CO;2.

Lim, Y.-K., S. D. Schubert, R. Kovach, A. M. Molod, and S. Pawson (2018), The roles of climate change and climate variability in the 2017 Atlantic hurricane season, *Scientific Reports*, *8*(1), 1–10, doi: 10.1038/s41598-018-34343-5.

Lima, C. H. R., and U. Lall (2010), Spatial scaling in a changing climate: A hierarchical bayesian model for non-stationary multi-site annual maximum and monthly streamflow, *Journal of Hydrology*, *383*(3-4), 307–318, doi: 10.1016/j.jhydrol.2009.12.045.

Lima, C. H. R., U. Lall, T. Troy, and N. Devineni (2016), A hierarchical Bayesian GEV model for improving local and regional flood quantile estimates, *Journal of Hydrology*, *541*, 816–823, doi: 10.1016/j.jhydrol.2016.07.042.

Lin, N., and K. Emanuel (2016), Grey swan tropical cyclones, *Nature Climate Change*, *6*(1), 106–111, doi: 10.1038/nclimate2777.

Liu, C., K. Ikeda, G. Thompson, R. Rasmussen, and J. Dudhia (2011), High-Resolution Simulations of Wintertime Precipitation in the Colorado Headwaters Region: Sensitivity to Physics Parameterizations, *Monthly Weather Review*, *139*(11), 3533–3553, doi: 10.1175/MWR-D-11-00009.1.

Liu, L., E. Lopez, L. Dueñas-Osorio, L. Stadler, Y. Xie, P. J. J. Alvarez, and Q. Li (2020), The importance of system configuration for distributed direct potable water reuse, *Nature Sustainability*, pp. 1–8, doi: 10.1038/s41893-020-0518-5.

Loader, C. (1999), *Local Regression and Likelihood*, Springer,, New York :.

Lopez-Cantu, T., and C. Samaras (2018), Temporal and spatial evaluation of stormwater engineering standards reveals risks and priorities across the United States, *Environmental Research Letters*, *13*(7), doi: 10.1088/1748-9326/aac696.

Lorenz, E. N. (1963), Deterministic Nonperiodic Flow, *Journal of the Atmospheric Sciences*, *20*(2), 130–141, doi: 10.1175/1520-0469(1963)020<0130:DNF>2.0.CO;2.

Lorenz, E. N. (1984), Irregularity: A fundamental property of the atmosphere, *Tellus A*, *36A*(2), 98–110, doi: 10.1111/j.1600-0870.1984.tb00230.x.

Loucks, D. P. (2017), *Water Resource Systems Planning and Management: An Introduction to Methods, Models, and Applications*, Imprint: Springer, Cham.

Lovejoy, S. (2013), What Is Climate?, *EOS, Transactions American Geophysical Union*, *94*(1), 1–2, doi: 10.1002/2013EO010001.

Lovejoy, S., and D. Schertzer (2012), Low-Frequency Weather and the Emergence of the Climate, in *Extreme Events and Natural Hazards: The Complexity Perspective*, pp. 231–254, American Geophysical Union (AGU), doi: 10.1029/2011GM001087.

Lovejoy, S., and D. Schertzer (Eds.) (2013), *The Weather and Climate Emergent Laws and Multifractal Cascades*, Cambridge University Press,, Cambridge :.

Lu, J., G. A. Vecchi, and T. Reichler (2007), Expansion of the Hadley cell under global warming, *Geophysical Research Letters*, *34*(6), doi: 10.1029/2006GL028443.

Lu, M., U. Lall, A. Schwartz, and H. Kwon (2013), Precipitation predictability associated with tropical moisture exports and circulation patterns for a major flood in France in 1995, *Water Resources Research*, *49*(10), 6381–6392, doi: 10.1002/wrcr.20512.

Lu, M., M. Tippett, and U. Lall (2015), Changes in the seasonality of tornado and favorable genesis conditions in the central United States, *Geophysical Research Letters*, *42*(10), 4224–4231, doi: 10.1002/2015GL063968.

Lucarini, V., D. Faranda, J. Wouters, and T. Kuna (2014), Towards a General Theory of Extremes for Observables of Chaotic Dynamical Systems, *Journal of Statistical Physics*, *154*(3), 723–750, doi: 10.1007/s10955-013-0914-6.

Lyu, K., X. Zhang, J. A. Church, A. B. A. Slangen, and J. Hu (2014), Time of emergence for regional sea-level change, *Nature Climate Change*, *4*(11), 1006–1010, doi: 10.1038/nclimate2397.

Maass, A., M. M. Hufschmidt, R. Dorfman, H. A. Thomas Jr., S. A. Marglin, and G. M. Fair (1962), *Design of Water Resource Systems*, Harvard University Press, Cambridge, MA.

MacDonald, A. E., C. T. M. Clack, A. Alexander, A. Dunbar, J. Wilczak, and Y. Xie (2016), Future cost-competitive electricity systems and their impact on US CO2 emissions, *Nature Climate Change*, *6*(5), 526–531, doi: 10.1038/nclimate2921.

MacGillivray, B. H. (2019), Null Hypothesis Testing $\neq$ scientific inference: A critique of the shaky premise at the heart of the science and values debate, and a defense of value-neutral risk assessment, *Risk Analysis*, *0*(0), doi: 10.1111/risa.13284.

Machina, M. (2014), *Handbook of the Economics of Risk and Uncertainty*, Elsevier, Oxford.

Machina, M. J. (1987), Choice under Uncertainty: Problems Solved and Unsolved, *Journal of Economic Perspectives*, *1*(1), 121–154, doi: 10.1257/jep.1.1.121.

Madani, K. (2010), Game theory and water resources, *Journal of Hydrology*, *381*(3), 225–238, doi: 10.1016/j.jhydrol.2009.11.045.

Mallakpour, I., and G. Villarini (2015), The changing nature of flooding across the central United States, *Nature Climate Change*, *5*(3), 250–254, doi: 10.1038/nclimate2516.

Mandelbrot, B. B. (1985), Self-Affine Fractals and Fractal Dimension, *Physica Scripta*, *32*(4), 257–260, doi: 10.1088/0031-8949/32/4/001.

Mandelbrot, B. B., and J. R. Wallis (1969), Robustness of the rescaled range R/S in the measurement of noncyclic long run statistical dependence, *Water Resources Research*, *5*(5), 967–988, doi: 10.1029/WR005i005p00967.

Mann, M. E., S. Rahmstorf, K. Kornhuber, B. A. Steinman, S. K. Miller, S. Petri, and D. Coumou (2018), Projected changes in persistent extreme summer weather events: The role of quasi-resonant amplification, *Science Advances*, *4*(10), eaat3272, doi: 10.1126/sciadv.aat3272.

Mantua, N. J., S. R. Hare, Y. Zhang, J. M. Wallace, and R. C. Francis (1997), A Pacific interdecadal climate oscillation with impacts on salmon production, *Bulletin of the American Meteorological Society*, *78*(6), 1069–1079, doi: 10.1175/1520-0477(1997)078<1069:APICOW>2.0.CO;2.

Maraun, D., and M. Widmann (2018), Cross-validation of bias-corrected climate simulations is misleading, *Hydrology and Earth System Sciences*, *22*(9), 4867–4873, doi: 10.5194/hess-22-4867-2018.

Maraun, D., F. Wetterhall, A. M. Ireson, R. E. Chandler, E. J. Kendon, M. Widmann, S. Brienen, H. W. Rust, T. Sauter, M. Themeßl, V. K. C. Venema, K. P. Chun, C. M. Goodess, R. G. Jones, C. Onof, M. Vrac, and I. Thiele-Eich (2010), Precipitation downscaling under climate change: Recent developments to bridge the gap between dynamical models and the end user, *Reviews of Geophysics*, *48*(3), doi: 10.1029/2009RG000314.

Marengo, J. A., W. R. Soares, C. Saulo, and M. Nicolini (2004), Climatology of the Low-Level Jet East of the Andes as Derived from the NCEP–NCAR Reanalyses: Characteristics and Temporal Variability, *Journal of Climate*, *17*(12), 2261–2280, doi: 10.1175/1520-0442(2004)017<2261:cotlje>2.0.co;2.

Marengo, J. A., B. Liebmann, A. M. Grimm, V. Misra, P. L. Silva Dias, I. F. A. Cavalcanti, L. M. V. Carvalho, E. H. Berbery, T. Ambrizzi, C. S. Vera, A. C. Saulo, J. Nogues Paegle, E. Zipser, A. Seth, and L. M. Alves (2012), Recent developments on the South American monsoon system, *International Journal of Climatology*, *32*(1), 1–21, doi: 10.1002/joc.2254.

Markonis, Y., and D. Koutsoyiannis (2013), Climatic Variability Over Time Scales Spanning Nine Orders of Magnitude: Connecting Milankovitch Cycles with Hurst–Kolmogorov Dynamics, *Surveys in Geophysics*, *34*(2), 181–207, doi: 10.1007/s10712-012-9208-9.

Markonis, Y., M. Hanel, P. Máca, J. Kyselý, and E. R. Cook (2018), Persistent multi-scale fluctuations shift European hydroclimate to its millennial boundaries, *Nature Communications*, *9*(1), 17, doi: 10.1038/s41467-018-04207-7.

Marohn, C. (2019), *Strong Towns: A Bottom-Up Revolution to Rebuild American Prosperity*, 1st edition ed., John Wiley & Sons.

Maruyama, F. (2018), The Relation among the Solar Activity, the Total Ozone, QBO, NAO, and ENSO by Wavelet-Based Multifractal Analysis, *Journal of Applied Mathematics and Physics*, *06*, 1301, doi: 10.4236/jamp.2018.66109.

Marwan, N., and J. Kurths (2015), Complex network based techniques to identify extreme events and (sudden) transitions in spatio-temporal systems, *Chaos: An Interdisciplinary Journal of Nonlinear Science*, *25*(9), 097,609, doi: 10.1063/1.4916924.

Mason, S. J., and O. Baddour (2008), Statistical Modelling, in *Seasonal Climate: Forecasting and Managing Risk*, edited by A. Troccoli, M. Harrison, D. L. T. Anderson, and S. J. Mason, NATO Science Series, pp. 163–201, Springer Netherlands, Dordrecht, doi: 10.1007/978-1-4020-6992-5_7.

Mason, S. J., and M. K. Tippett (2017), Climate Predictability Tool Version 15.5.10.

Mason, S. J., and A. P. Weigel (2009), A Generic Forecast Verification Framework for Administrative Purposes, *Monthly Weather Review*, *137*(1), 331–349, doi: 10.1175/2008MWR2553.1.

Massoud, M. A., A. Tarhini, and J. A. Nasr (2009), Decentralized approaches to wastewater treatment and management: Applicability in developing countries, *Journal of Environmental Management*, *90*(1), 652–659, doi: 10.1016/j.jenvman.2008.07.001.

Matalas, N. C. (2012), Comment on the Announced Death of Stationarity, *Journal of Water Resources Planning and Management*, *138*(4), 311–312, doi: 10.1061/(ASCE)WR.1943-5452.0000215.

Matalas, N. C., and M. B. Fiering (1977), 6. Water-Resource Systems Planning., in *Climate, Climatic Change, and Water Supply*, pp. 99–110, The National Academies Press, Washington, DC.

McElreath, R. (2016), *Statistical Rethinking: A Bayesian Course with Examples in R and Stan*, RC Press Taylor & Francis Group, Boca Raton.

McKinney, W. (2010), Data Structures for Statistical Computing in Python, in *Proceedings of the 9th Python in Science Ldots*.

McPhail, C., H. R. Maier, J. H. Kwakkel, M. Giuliani, A. Castelletti, and S. Westra (2019), Robustness Metrics: How Are They Calculated, When Should They Be Used and Why Do They Give Different Results?, *Earth's Future*, pp. 169–191, doi: 10.1002/2017EF000649.

McShane, B. B., D. Gal, A. Gelman, C. Robert, and J. L. Tackett (2017), Abandon Statistical Significance, *arXiv:1709.07588 [stat.ME]*.

Meehl, G. A., L. Goddard, G. Boer, R. Burgman, G. Branstator, C. Cassou, S. Corti, G. Danabasoglu, F. Doblas-Reyes, E. Hawkins, A. Karspeck, M. Kimoto, A. Kumar, D. Matei, J. Mignot, R. Msadek, A. Navarra, H. Pohlmann, M. Rienecker, T. Rosati, E. Schneider, D. M. Smith, R. Sutton, H. Teng, G. J. van Oldenborgh, G. A. Vecchi, and S. Yeager (2014), Decadal Climate Prediction: An Update from the Trenches, *Bulletin of the American Meteorological Society*, *95*(2), 243–267, doi: 10.1175/BAMS-D-12-00241.1.

Menéndez, P., I. J. Losada, S. Torres-Ortega, S. Narayan, and M. W. Beck (2020), The global flood protection benefits of mangroves, *Scientific Reports*, *10*(1), 1–11, doi: 10.1038/s41598-020-61136-6.

Merryfield, W. J., J. Baehr, L. Batté, E. J. Becker, A. H. Butler, C. A. S. Coelho, G. Danabasoglu, P. A. Dirmeyer, F. J. Doblas-Reyes, D. I. V. Domeisen, L. Ferranti, T. Ilynia, A. Kumar, W. A. Müller, M. Rixen, A. W. Robertson, D. M. Smith, Y. Takaya, M. Tuma, F. Vitart, C. J. White, M. S. Alvarez, C. Ardilouze, H. Attard, C. Baggett, M. A. Balmaseda, A. F. Beraki, P. S. Bhattacharjee, R. Bilbao, F. M. de Andrade, M. J. DeFlorio, L. B. Díaz, M. A. Ehsan, G. Fragkoulidis, S. Grainger, B. W. Green, M. C. Hell, J. M. Infanti, K. Isensee, T. Kataoka, B. P. Kirtman, N. P. Klingaman, J.-Y. Lee, K. Mayer, R. McKay, J. V. Mecking, D. E. Miller, N. Neddermann, C. H. Justin Ng, A. Ossó, K. Pankatz, S. Peatman, K. Pegion, J. Perlwitz, G. C. Recalde-Coronel, A. Reintges, C. Renkl, B. Solaraju-Murali, A. Spring, C. Stan, Y. Q. Sun, C. R. Tozer, N. Vigaud, S. Woolnough, and S. Yeager (2020), Current and emerging developments in subseasonal to decadal prediction, *Bulletin of the American Meteorological Society*, doi: 10.1175/BAMS-D-19-0037.1.

Merz, B., J. C. J. H. Aerts, K. Arnbjerg-Nielsen, M. Baldi, A. Becker, A. Bichet, G. Blöschl, L. M. Bouwer, A. Brauer, F. Cioffi, J. M. Delgado, M. Gocht, F. Guzzetti, S. Harrigan, K. Hirschboeck, C. Kilsby, W. Kron, H. H. Kwon, U. Lall, R. Merz, K. Nissen, P. Salvatti, T. Swierczynski, U. Ulbrich, A. Viglione, P. J. Ward, M. Weiler, B. Wilhelm, and M. Nied (2014), Floods and climate: Emerging perspectives for flood risk assessment and management, *Natural Hazards and Earth System Science*, *14*(7), 1921–1942, doi: 10.5194/nhess-14-1921-2014.

Merz, R., and G. Blöschl (2008), Flood frequency hydrology: 1. Temporal, spatial, and causal expansion of information, *Water Resources Research*, *44*(8), 3, doi: 10.1029/2007WR006744.

Messner, J. W., G. J. Mayr, A. Zeileis, and D. S. Wilks (2014), Heteroscedastic Extended Logistic Regression for Postprocessing of Ensemble Guidance, *Monthly Weather Review*, *142*(1), 448–456, doi: 10.1175/MWR-D-13-00271.1.

Messori, G., R. Caballero, and D. Faranda (2017), A dynamical systems approach to studying midlatitude weather extremes, *Geophysical Research Letters*, *44*(7), 3346–3354, doi: 10.1002/2017GL072879.

Meyer, E. S., G. W. Characklis, C. M. Brown, and P. Moody (2016), Hedging the financial risk from water scarcity for Great Lakes shipping, *Water Resources Research*, *52*(1), 227–245, doi: 10.1002/2015WR017855.

Michelangeli, P. A., R. Vautard, and B. Legras (1995), Weather Regimes - Recurrence and Quasi Stationarity, *Journal of the Atmospheric Sciences*, *52*(8), 1237–1256, doi: 10.1175/1520-0469(1995)052<1237:WRRAQS>2.0.CO;2.

Milly, P. C. D., J. Betancourt, M. Falkenmark, R. M. Hirsch, Z. W. Kundzewicz, D. P. Lettenmaier, and R. J. Stouffer (2008), Stationarity Is Dead: Whither Water Management?, *Science*, *319*(5863), 573–574, doi: 10.1126/science.1151915.

MIT Energy Initiative (2016), Utility of the future, *Tech. rep.*, Massachusetts Institute of Technology, Cambridge, MA.

Mnih, V., K. Kavukcuoglu, D. Silver, A. Graves, I. Antonoglou, D. Wierstra, and M. Riedmiller (2013), Playing Atari with Deep Reinforcement Learning, *arXiv:1312.5602 [cs.LG]*.

Mnih, V., K. Kavukcuoglu, D. Silver, A. A. Rusu, J. Veness, M. G. Bellemare, A. Graves, M. Riedmiller, A. K. Fidjeland, G. Ostrovski, S. Petersen, C. Beattie, A. Sadik, I. Antonoglou, H. King, D. Kumaran, D. Wierstra, S. Legg, and D. Hassabis (2015), Human-level control through deep reinforcement learning, *Nature*, *518*(7540), 529–533, doi: 10.1038/nature14236.

Montanari, A. (2003), Long-range dependence in hydrology, in *Theory and Applications of Long-Range Dependence*, edited by P. Doukhan, G. Oppenheim, and M. Taqqu, pp. 461–472, Birkhäuser Basel, Basel, Switzerland.

Montanari, A., and D. Koutsoyiannis (2014), Modeling and mitigating natural hazards: Stationarity is immortal!, *Water Resources Research*, *50*(12), 9748–9756, doi: 10.1002/2014WR016092.

Moon, H., L. Gudmundsson, and S. I. Seneviratne (2018), Drought Persistence Errors in Global Climate Models, *Journal of Geophysical Research: Atmospheres*, *50*(20), 7541–3496, doi: 10.1002/2017JD027577.

MOPC (2016), Evaluación Del Impacto de El Niño 2015-2016 En Sector Transporte y Comunicación Paraguay, *Tech. rep.*, Ministerio de Obras Públicas y Comunicación.

Moron, V., A. W. Robertson, J.-H. Qian, and M. Ghil (2015), Weather types across the Maritime Continent: From the diurnal cycle to interannual variations, *Frontiers in Environmental Science*, *2*, 163, doi: 10.3389/fenvs.2014.00065.

Müller, B., M. Wild, A. Driesse, and K. Behrens (2014), Rethinking solar resource assessments in the context of global dimming and brightening, *Solar Energy*, *99*, 272–282, doi: 10.1016/j.solener.2013.11.013.

Muller, C. J., P. A. O, and L. E. Back (2011), Intensification of Precipitation Extremes with Warming in a Cloud-Resolving Model, *Journal of Climate*, *24*(11), 2784–2800, doi: 10.1175/2011JCLI3876.1.

Muller, M. (2018), Cape Town's drought: Don't blame climate change, *Nature*, *559*(7713), 174–176, doi: 10.1038/d41586-018-05649-1.

Mun, J. (2006), *Real Options Analysis : Tools and Techniques for Valuing Strategic Investments and Decisions*, John Wiley & Sons, Hoboken, N.J.

Munich Re (2017), Natural catastrophe losses at their highest for four years, *Tech. rep.*, Munic RE.

Muñoz, Á. G., L. Goddard, A. W. Robertson, Y. Kushnir, and W. E. Baethgen (2015), CrossTime Scale Interactions and Rainfall Extreme Events in Southeastern South America for the Austral Summer. Part I: Potential Predictors, *Journal of Climate*, *28*(19), 7894–7913, doi: 10.1175/JCLI-D-14-00693.1.

Muñoz, Á. G., J. Díaz-Lobatón, X. Chourio, and M. J. Stock (2016a), Seasonal Prediction of Lightning Activity in North Western Venezuela: Large-Scale versus Local Drivers, *Atmospheric Research*, *172173*, 147–162, doi: 10.1016/j.atmosres.2015.12.018.

Muñoz, Á. G., L. Goddard, S. J. Mason, and A. W. Robertson (2016b), CrossTime Scale Interactions and Rainfall Extreme Events in Southeastern South America for the Austral Summer. Part II: Predictive Skill, *Journal of Climate*, *29*(16), 5915–5934, doi: 10.1175/JCLI-D-15-0699.1.

Muñoz, Á. G., X. Yang, G. A. Vecchi, A. W. Robertson, and W. F. Cooke (2017), A Weather-Type-Based Cross-Time-Scale Diagnostic Framework for Coupled Circulation Models, *Journal of Climate*, *30*(22), 8951–8972, doi: 10.1175/jcli-d-17-0115.1.

Najibi, N., N. Devineni, M. Lu, and R. A. P. Perdigão (2019), Coupled flow accumulation and atmospheric blocking govern flood duration, *npj Climate and Atmospheric Science*, *2*(1), 19, doi: 10.1038/s41612-019-0076-6.

Nakamura, J., U. Lall, Y. Kushnir, A. W. Robertson, and R. Seager (2013), Dynamical Structure of Extreme Floods in the U.S. Midwest and the United Kingdom, *Journal of Hydrometeorology*, *14*(2), 485–504, doi: 10.1175/JHM-D-12-059.1.

Nakamura, J., U. Lall, Y. Kushnir, and B. Rajagopalan (2015), HITS: Hurricane Intensity and Track Simulator with North Atlantic Ocean Applications for Risk Assessment, *Journal of Applied Meteorology and Climatology*, *54*(7), 1620–1636, doi: 10.1175/JAMC-D-14-0141.1.

Nash, J. (1951), Non-Cooperative Games, *Annals of Mathematics*, *54*(2), 286–295, doi: 10.2307/1969529.

Nash, J. F. (1950), Equilibrium points in n-person games, *Proceedings of the National Academy of Sciences*, *36*(1), 48–49, doi: 10.1073/pnas.36.1.48.

Newman, M., M. A. Alexander, T. R. Ault, K. M. Cobb, C. Deser, E. Di Lorenzo, N. J. Mantua, A. J. Miller, S. Minobe, H. Nakamura, N. Schneider, D. J. Vimont, A. S. Phillips, J. D. Scott, and C. A. Smith (2016), The Pacific Decadal Oscillation, Revisited, *Journal of Climate*, *29*(12), 4399–4427, doi: 10.1175/JCLI-D-15-0508.1.

Ng, C. H. J., and G. A. Vecchi (2020), Large-scale environmental controls on the seasonal statistics of rapidly intensifying North Atlantic tropical cyclones, *Climate Dynamics*, doi: 10.1007/s00382-020-05207-4.

Nie, J., P. Dai, and A. H. Sobel (2020), Dry and moist dynamics shape regional patterns of extreme precipitation sensitivity, *Proceedings of the National Academy of Sciences*, doi: 10.1073/pnas.1913584117.

Nissan, H., L. Goddard, E. C. de Perez, J. Furlow, W. Baethgen, M. C. Thomson, and S. J. Mason (2019), On the use and misuse of climate change projections in international development, *Wiley Interdisciplinary Reviews: Climate Change*, *0*(0), 579, doi: 10.1002/wcc.579.

Nogués-Paegle, J., and K. C. Mo (1997), Alternating wet and dry conditions over South America during summer, *Monthly Weather Review*, *125*(2), 279–291, doi: 10.1175/1520-0493(1997)125<0279:AWADCO>2.0.CO;2.

Obeysekera, J., and J. D. Salas (2016), Frequency of Recurrent Extremes under Nonstationarity, *Journal of Hydrologic Engineering*, *21*(5), 04016,005, doi: 10.1061/(ASCE)HE.1943-5584.0001339.

Obeysekera, J., J. D. Salas, and J. D. Salas (2014), Quantifying the Uncertainty of Design Floods under Nonstationary Conditions, *Journal of Hydrologic Engineering*, *19*(7), 1438–1446, doi: 10.1061/(ASCE)HE.1943-5584.0000931.

Ochoa-Tocachi, B. F., J. D. Bardales, J. Antiporta, K. Pérez, L. Acosta, F. Mao, Z. Zulkafli, J. Gil-Ríos, O. Angulo, S. Grainger, G. Gammie, B. D. Bièvre, and W. Buytaert (2019), Potential contributions of pre-Inca infiltration infrastructure to Andean water security, *Nature Sustainability*, *2*(7), 584–593, doi: 10.1038/s41893-019-0307-1.

O'Connell, P. E., D. Koutsoyiannis, H. F. Lins, Y. Markonis, A. Montanari, and T. Cohn (2016), The scientific legacy of Harold Edwin Hurst (1880–1978), *Hydrological Sciences Journal*, *61*(9), 1571–1590, doi: 10.1080/02626667.2015.1125998.

Oddo, P. C., B. S. Lee, G. G. Garner, V. Srikrishnan, P. M. Reed, C. E. Forest, and K. Keller (2017), Deep Uncertainties in Sea-Level Rise and Storm Surge Projections: Implications for Coastal Flood Risk Management, *Risk Analysis*, *0*(0), doi: 10.1111/risa.12888.

O'Gorman, P. A. (2015), Precipitation Extremes Under Climate Change, *Current Climate Change Reports*, *1*(2), 49–59, doi: 10.1007/s40641-015-0009-3.

O'Gorman, P. A., and T. Schneider (2009), The physical basis for increases in precipitation extremes in simulations of 21st-century climate change, *Proceedings of the National Academy of Sciences of the United States of America*, *106*(35), 14,773–14,777, doi: 10.1073/pnas.0907610106.

Otto, F. E. L., P. Wolski, F. Lehner, C. Tebaldi, G. J. van Oldenborgh, S. Hogesteeger, R. Singh, P. Holden, N. S. Fučkar, R. C. Odoulami, and M. New (2018), Anthropogenic influence on the drivers of the Western Cape drought 2015–2017, *Environmental Research Letters*, *13*(12), 124,010, doi: 10.1088/1748-9326/aae9f9.

Paegle, J. N., L. A. Byerle, and K. C. Mo (2000), Intraseasonal modulation of South American summer precipitation, *Monthly Weather Review*, *128*(3), 837–850, doi: 10.1175/1520-0493(2000)128<0837:IMOSAS>2.0.CO;2.

Pall, P., M. R. Allen, and D. A. Stone (2007), Testing the Clausius–Clapeyron constraint on changes in extreme precipitation under CO2 warming, *Climate Dynamics*, *28*(4), 351–363, doi: 10.1007/s00382-006-0180-2.

Palmer, T. N. (1993), A nonlinear dynamical perspective on climate change, *Weather*, *48*(10), 314–326, doi: 10.1002/j.1477-8696.1993.tb05802.x.

Palmer, T. N. (1999), A Nonlinear Dynamical Perspective on Climate Prediction, *Journal of Climate*, *12*(2), 575–591, doi: 10.1175/1520-0442(1999)012<0575:ANDPOC>2.0.CO;2.

Palmer, T. N. (2013), Climate extremes and the role of dynamics, *Proceedings of the National Academy of Sciences of the United States of America*, *110*(14), 5281–5282, doi: 10.1073/pnas.1303295110.

Papakonstantinou, V., T. Maier, R. R. Kaldany, A. Belelieu, and M. Drexler (2016), Risk Mitigation Instruments in Infrastructure, *Tech. rep.*, World Economic Forum.

Paredes, R., L. Dueñas-Osorio, K. S. Meel, and M. Y. Vardi (2019), Principled network reliability approximation: A counting-based approach, *Reliability Engineering & System Safety*, *191*, 106,472, doi: 10.1016/j.ress.2019.04.025.

Parhi, P. (2020), Utility of climate forecast insurance as a pre-hazard risk reduction funding tool.

Payne, A. E., M.-E. Demory, L. R. Leung, A. M. Ramos, C. A. Shields, J. J. Rutz, N. Siler, G. Villarini, A. Hall, and F. M. Ralph (2020), Responses and impacts of atmospheric rivers to climate change, *Nature Reviews Earth & Environment*, *1*(3), 143–157, doi: 10.1038/s43017-020-0030-5.

Pedregosa, F., G. Varoquaux, A. Gramfort, V. Michel, B. Thirion, O. Grisel, M. Blondel, P. Prettenhofer, R. Weiss, V. Dubourg, J. Vanderplas, A. Passos, D. Cournapeau, M. Brucher, M. Perrot, and É. Duchesnay (2011), Scikit-learn: Machine Learning in Python, *Journal of Machine Learning Research*, *12*(1), 2825–2830, doi: 10.18637/jss.v033.i01.

Peduzzi, P., B. Chatenoux, H. Dao, A. De Bono, C. Herold, J. Kossin, F. Mouton, and O. Nordbeck (2012), Global trends in tropical cyclone risk, *Nature Climate Change*, *2*(4), 289–294, doi: 10.1038/nclimate1410.

Pendergrass, A. G., and R. Knutti (2018), The uneven nature of daily precipitation and its change, *Geophysical Research Letters*, *0*(ja), doi: 10.1029/2018GL080298.

Perdigão, R. A. P., U. Ehret, K. H. Knuth, and J. Wang (2020), Debates: Does information theory provide a new paradigm for earth science? Emerging concepts and pathways of information physics, *Water Resources Research*, *56*(2), e2019WR025,270, doi: 10.1029/2019WR025270.

Perry, C. A. (2000), Significant floods in the United States during the 20th century: USGS measures a century of floods, *Tech. Rep. USGS Fact Sheet 024–00*, United States Geological Survey.

Petoukhov, V., S. Rahmstorf, S. Petri, and H. J. Schellnhuber (2013), Quasiresonant Amplification of Planetary Waves and Recent Northern Hemisphere Weather Extremes, *Proceedings of the National Academy of Sciences of the United States of America*, *110*(14), 5336–5341, doi: 10.1073/pnas.1222000110.

Pfahl, S., P. A. O'Gorman, and E. M. Fischer (2017), Understanding the regional pattern of projected future changes in extreme precipitation, *Nature Climate Change*, *7*(6), 423–427, doi: 10.1038/nclimate3287.

Pfleiderer, P., C.-F. Schleussner, K. Kornhuber, and D. Coumou (2019), Summer weather becomes more persistent in a 2 °C world, *Nature Climate Change*, pp. 1–6, doi: 10.1038/s41558-019-0555-0.

Piani, C., J. O. Haerter, and E. Coppola (2010), Statistical bias correction for daily precipitation in regional climate models over Europe, *Theoretical and Applied Climatology*, *99*(1), 187–192, doi: 10.1007/s00704-009-0134-9.

Pielke, R. A., G. Joel, C. Landsea, C. Douglas, M. A. Saunders, and M. Rade (2008), Normalized Hurricane Damage in the United States: 1900–2005, *Natural Hazards Review*, *9*(1), 29–42, doi: 10.1061/(ASCE)1527-6988(2008)9:1(29).

Pierce, D. W., D. R. Cayan, E. P. Maurer, J. T. Abatzoglou, and K. C. Hegewisch (2015), Improved Bias Correction Techniques for Hydrological Simulations of Climate Change, *Journal of Hydrometeorology*, *16*(6), 2421–2442, doi: 10.1175/JHM-D-14-0236.1.

Pinter, N. (2005), One Step Forward, Two Steps Back on U.S. Floodplains, *Science*, *308*(5719), 207–208, doi: 10.1126/science.1108411.

Pithan, F., T. G. Shepherd, G. Zappa, and I. Sandu (2016), Climate model biases in jet streams, blocking and storm tracks resulting from missing orographic drag, *Geophysical Research Letters*, *43*(13), 7231–7240, doi: 10.1002/2016GL069551.

Pizarro, G. (2006), Instruments for Managing Seasonal Flood Risk Using Climate Forecasts, Ph.D. thesis, Columbia University / Columbia University, United States – New York.

Poff, N. L., C. M. Brown, T. E. Grantham, J. H. Matthews, M. A. Palmer, C. M. Spence, R. L. Wilby, M. Haasnoot, G. F. Mendoza, K. C. Dominique, and A. Baeza (2015), Sustainable water management under future uncertainty with eco-engineering decision scaling, *Nature Climate Change*, *6*(1), 25–34, doi: 10.1038/nclimate2765.

Powers, K. (2003), Benefit-Cost Analysis and the Discount Rate for the Corps of Engineers' Water Resource Projects: Theory and Practice, *Tech. Rep. RL31976*, Congressional Research Service, Washington, DC.

Prime, T., K. Morrissey, J. Brown, and A. Plater (2018), Protecting Energy Infrastructure against the Uncertainty of Future Climate Change: A Real Options Approach, *Journal of Ocean and Coastal Economics*, *5*(1), doi: 10.15351/2373-8456.1075.

Rabiner, L., and B. Juang (1986), An Introduction to Hidden Markov Models, *IEEE ASSP Magazine*, *3*(1), 4–16, doi: 10.1109/MASSP.1986.1165342.

Rädler, A. T., P. H. Groenemeijer, E. Faust, R. Sausen, and T. Púčik (2019), Frequency of severe thunderstorms across Europe expected to increase in the 21st century due to rising instability, *npj Climate and Atmospheric Science*, *2*(1), 1–5, doi: 10.1038/s41612-019-0083-7.

Rahmstorf, S., J. E. Box, G. Feulner, M. E. Mann, A. Robinson, S. Rutherford, and E. J. Schaffernicht (2015), Exceptional twentieth-century slowdown in Atlantic Ocean overturning circulation, *Nature Climate Change*, *5*(5), 475–480, doi: 10.1038/nclimate2554.

Rajczak, J., S. Kotlarski, and C. Schär (2016), Does Quantile Mapping of Simulated Precipitation Correct for Biases in Transition Probabilities and Spell Lengths?, *Journal of Climate*, *29*(5), 1605–1615, doi: 10.1175/JCLI-D-15-0162.1.

Ralph, F. M., and M. D. Dettinger (2011), Storms, floods, and the science of atmospheric rivers, *EOS, Transactions American Geophysical Union*, *92*(32), 265, doi: 10.1029/2011EO320001.

Ramesh, N., M. A. Cane, R. Seager, and D. E. Lee (2016), Predictability and prediction of persistent cool states of the Tropical Pacific Ocean, *Climate Dynamics*, *49*(7-8), 2291–2307, doi: 10.1007/s00382-016-3446-3.

Ramsey, F. P. (2016), Truth and Probability, in *Readings in Formal Epistemology*, edited by H. Arló-Costa, V. F. Hendricks, and J. van Benthem, Springer Graduate Texts in Philosophy, pp. 21–45, Springer International Publishing, Cham, doi: 10.1007/978-3-319-20451-2_3.

Raso, L., J. Kwakkel, J. Timmermans, and G. Panthou (2019), How to evaluate a monitoring system for adaptive policies: Criteria for signposts selection and their model-based evaluation, *Climatic Change*, doi: 10.1007/s10584-018-2355-3.

Rasp, S., M. S. Pritchard, and P. Gentine (2018), Deep learning to represent subgrid processes in climate models, *Proceedings of the National Academy of Sciences*, *115*(39), 9684–9689, doi: 10.1073/pnas.1810286115.

Ray, P. A., M. Ü. Taner, K. E. Schlef, S. Wi, H. F. Khan, S. S. G. Freeman, and C. M. Brown (2018), Growth of the Decision Tree: Advances in Bottom-Up Climate Change Risk Management, *Journal of the American Water Resources Association*, *0*(0), doi: 10.1111/1752-1688.12701.

Read, L. K., and R. M. Vogel (2016a), Hazard function theory for nonstationary natural hazards, *Natural Hazards and Earth System Science*, *16*(4), 915–925, doi: 10.5194/nhess-16-915-2016.

Read, L. K., and R. M. Vogel (2016b), Hazard function analysis for flood planning under nonstationarity, *Water Resources Research*, *52*(5), 4116–4131, doi: 10.1002/2015WR018370.

Reed, P. M., D. Hadka, J. D. Herman, J. R. Kasprzyk, and J. B. Kollat (2013), Evolutionary multiobjective optimization in water resources: The past, present, and future, *Advances in Water Resources*, *51*, 438–456, doi: 10.1016/j.advwatres.2012.01.005.

Reinhold, B. B., and R. T. Pierrehumbert (1982), Dynamics of Weather Regimes - Quasi-Stationary Waves and Blocking, *Monthly Weather Review*, *110*(9), 1105–1145, doi: 10.1175/1520-0493(1982)110<1105:DOWRQS>2.0.CO;2.

Reynolds, R. W., N. A. Rayner, T. M. Smith, D. C. Stokes, and W. Wang (2002), An Improved In Situ and Satellite SST Analysis for Climate, *Journal of Climate*, *15*(13), 1609–1625, doi: 10.1175/1520-0442(2002)015<1609:AIISAS>2.0.CO;2.

Rittel, H. W. J., and M. M. Webber (1973), Dilemmas in a general theory of planning, *Policy Sciences*, *4*(2), 155–169, doi: 10.1007/BF01405730.

Roa Bastos, A. A. (1961), *Hijo de Hombre*, Editorial Losada, Buenos Aires.

Robertson, A. W., S. Kirshner, and P. Smyth (2004), Downscaling of Daily Rainfall Occurrence over Northeast Brazil Using a Hidden Markov Model, *Journal of Climate*, *17*(22), 4407–4424, doi: 10.1175/JCLI-3216.1.

Rocheta, E., J. P. Evans, and A. Sharma (2017), Can Bias Correction of Regional Climate Model Lateral Boundary Conditions Improve Low-Frequency Rainfall Variability?, *Journal of Climate*, *30*(24), 9785–9806, doi: 10.1175/JCLI-D-16-0654.1.

Roesch, A., and H. Schmidbauer (2016), WaveletComp: Computational wavelet analysis. R package version 1.1.

Rojo Hernandez, J. D., U. Lall, and O. J. Mesa (2017), ENSO Dynamics and Trends, an Alternate View, *AGU Fall Meeting Abstracts*, *41*.

Ropelewski, C. F., and M. S. Halpert (1987), Global and Regional Scale Precipitation Patterns Associated with the El-Nino Southern Oscillation, *Monthly Weather Review*, *115*(8), 1606–1626, doi: 10.1175/1520-0493(1987)115<1606:GARSPP>2.0.CO;2.

Rothlisberger, M., S. Pfahl, and O. Martius (2016), Regional-Scale Jet Waviness Modulates the Occurrence of Mid-Latitude Weather Extremes, *Geophysical Research Letters*, *43*(20), 2016GL070,944–10, 997, doi: 10.1002/2016GL070944.

Roulston, M. S., and L. A. Smith (2002), Evaluating Probabilistic Forecasts Using Information Theory, *Monthly Weather Review*, *130*(6), 1653–1660, doi: 10.1175/1520-0493(2002)130<1653:EPFUIT>2.0.CO;2.

Roy, S., and M. A. Edwards (2019), Preventing another lead (Pb) in drinking water crisis: Lessons from the Washington D.C. and Flint MI contamination events, *Current Opinion in Environmental Science & Health*, *7*, 34–44, doi: 10.1016/j.coesh.2018.10.002.

Roy, T., J. A. Martinez, J. E. Herrera-Estrada, Y. Zhang, F. Dominguez, A. Berg, M. Ek, and E. F. Wood (2018), Role of moisture transport and recycling in characterizing droughts: Perspectives from two recent U.S. droughts and the CFSv2 system, *Journal of Hydrometeorology*, *20*(1), 139–154, doi: 10.1175/JHM-D-18-0159.1.

Ruckert, K. L., V. Srikrishnan, and K. Keller (2019), Characterizing the deep uncertainties surrounding coastal flood hazard projections: A case study for Norfolk, VA, *Scientific Reports*, *9*(1), 1–12, doi: 10.1038/s41598-019-47587-6.

Ruggeri, A. (2017), 'Resilience bonds': A secret weapon against catastrophe, *BBC Future*.

Sadoff, C. W., E. Borgomeo, and S. Uhlenbrook (2020), Rethinking water for SDG 6, *Nature Sustainability*, pp. 1–2, doi: 10.1038/s41893-020-0530-9.

Salas, J. D., J. D. Salas, and J. Obeysekera (2014), Revisiting the Concepts of Return Period and Risk for Nonstationary Hydrologic Extreme Events, *Journal of Hydrologic Engineering*, *19*(3), 554–568, doi: 10.1061/(ASCE)HE.1943-5584.0000820.

Salas, J. D., J. Obeysekera, and R. M. Vogel (2018), Techniques for assessing water infrastructure for nonstationary extreme events: A review, *Hydrological Sciences Journal*, *63*(3), 325–352, doi: 10.1080/02626667.2018.1426858.

Salio, P., M. Nicolini, and A. C. Saulo (2002), Chaco low-level jet events characterization during the austral summer season, *Journal of Geophysical Research*, *107*(D24), doi: 10.1029/2001JD001315.

Salio, P., M. Nicolini, and E. J. Zipser (2007), Mesoscale convective systems over southeastern South America and their relationship with the South American low-level jet, *Monthly Weather Review*, *135*(4), 1290–1309, doi: 10.1175/MWR3305.1.

Saltelli, A. (2019), A short comment on statistical versus mathematical modelling, *Nature Communications*, *10*(1), 1–3, doi: 10.1038/s41467-019-11865-8.

Saltelli, A., P. Annoni, I. Azzini, F. Campolongo, M. Ratto, and S. Tarantola (2010), Variance based sensitivity analysis of model output. Design and estimator for the total sensitivity index, *Computer Physics Communications*, *181*(2), 259–270, doi: 10.1016/j.cpc.2009.09.018.

Santamarina, J. C., L. A. Torres-Cruz, and R. C. Bachus (2019), Why coal ash and tailings dam disasters occur, *Science*, *364*(6440), 526–528, doi: 10.1126/science.aax1927.

Santer, B. D., S. Po-Chedley, M. D. Zelinka, I. Cvijanovic, C. Bonfils, P. J. Durack, Q. Fu, J. Kiehl, C. Mears, J. Painter, G. Pallotta, S. Solomon, F. J. Wentz, and C.-Z. Zou (2018), Human influence on the seasonal cycle of tropospheric temperature, *Science*, *361*(6399), doi: 10.1126/science.aas8806.

Sarachik, E. S., and M. A. Cane (2009), *The El Niño–Southern Oscillation Phenomenon*, Cambridge University Press, Cambridge.

Saulo, C., J. Ruiz, and Y. G. Skabar (2007), Synergism between the low-level jet and organized convection at its exit region, *Monthly Weather Review*, *135*(4), 1310–1326, doi: 10.1175/MWR3317.1.

Savage, L. (1954), *Foundations of Statistics.*, Wiley, New York.

Schachter, J. A., and P. Mancarella (2016), A critical review of Real Options thinking for valuing investment flexibility in Smart Grids and low carbon energy systems, *Renewable and Sustainable Energy Reviews*, *56*, 261–271, doi: 10.1016/j.rser.2015.11.071.

Schaul, T., J. Quan, I. Antonoglou, and D. Silver (2015), Prioritized Experience Replay, *arXiv:1511.05952 [cs.LG]*.

Schmadel, N. M., J. W. Harvey, G. E. Schwarz, R. B. Alexander, J. D. Gomez-Velez, D. Scott, and S. W. Ator (2019), Small ponds in headwater catchments are a dominant influence on regional nutrient and sediment budgets, *Geophysical Research Letters*, *0*, doi: 10.1029/2019GL083937.

Schmidhuber, J. (2001), Sequential Decision Making Based on Direct Search, in *Sequence Learning: Paradigms, Algorithms, and Applications*, edited by R. Sun and C. L. Giles, Lecture Notes in Computer Science, pp. 213–240, Springer, Berlin, Heidelberg, doi: 10.1007/3-540-44565-X_10.

Schmidli, J., C. M. Goodess, C. Frei, M. R. Haylock, Y. Hundecha, J. Ribalaygua, and T. Schmith (2007), Statistical and dynamical downscaling of precipitation: An evaluation and comparison of scenarios for the European Alps, *Journal of Geophysical Research: Atmospheres*, *112*(D4), doi: 10.1029/2005JD007026.

Schreiber, J. (2017), Pomegranate: Fast and Flexible Probabilistic Modeling in Python, *Journal of Machine Learning Research*, *18*(1), 5992–5997.

Schubert, S. D., Y. Chang, H. Wang, R. Koster, and M. Suarez (2016), A Modeling Study of the Causes and Predictability of the Spring 2011 Extreme U.S. Weather Activity, *Journal of Climate*, *29*(21), 7869–7887, doi: 10.1175/JCLI-D-15-0673.1.

Screen, J. A., and I. Simmonds (2014), Amplified Mid-Latitude Planetary Waves Favour Particular Regional Weather Extremes, *Nature Climate Change*, *4*(8), 704–709, doi: 10.1038/nclimate2271.

Seager, R., M. Hoerling, S. D. Schubert, H. Wang, B. Lyon, A. Kumar, J. Nakamura, and N. H. Henderson (2014), Causes and predictability of the 2011-14 California Drought : Assessment report, *Tech. rep.*, NOAA Modeling, Analysis, Predictions, and Projections.

Sebastian, A., A. Gori, R. B. Blessing, K. van der Wiel, and B. Bass (2019), Disentangling the impacts of human and environmental change on catchment response during Hurricane Harvey, *Environmental Research Letters*, *14*(12), 124,023, doi: 10.1088/1748-9326/ab5234.

Seidel, D. J., Q. Fu, W. J. Randel, and T. J. Reichler (2007), Widening of the tropical belt in a changing climate, *Nature Geoscience*, *1*(1), 21–24, doi: 10.1038/ngeo.2007.38.

Seluchi, M. E., R. Garreaud, F. A. Norte, and A. C. Saulo (2006), Influence of the Subtropical Andes on Baroclinic Disturbances: A Cold Front Case Study, *Monthly Weather Review*, *134*(11), 3317–3335, doi: 10.1175/MWR3247.1.

Selvam, A. M. (2017), Universal Inverse Power-Law Distribution for Fractal Fluctuations in Dynamical Systems: Applications for Predictability of Inter-Annual Variability of Indian and USA Region Rainfall, *Pure and Applied Geophysics*, *174*(1), 413–426, doi: 10.1007/s00024-016-1394-9.

Serinaldi, F., and C. G. Kilsby (2015), Stationarity Is Undead: Uncertainty Dominates the Distribution of Extremes, *Advances in Water Resources*, *77*, 17–36, doi: 10.1016/j.advwatres.2014.12.013.

Seth, A., K. Fernandes, and S. J. Camargo (2015), Two Summers of São Paulo Drought: Origins in the Western Tropical Pacific, *Geophysical Research Letters*, *42*(24), 2015GL066,314–10,823, doi: 10.1002/2015GL066314.

Shackle, G. L. S. (1949), *Expectation in Economics*, University Press, Cambridge, UK.

Shackle, G. L. S. G. L. S. (1972), *Epistemics and Economics: A Critique of Economic Doctrines*, Cambridge University Press, Cambridge, UK.

Shannon, M. A., P. W. Bohn, M. Elimelech, J. G. Georgiadis, B. J. Mariñas, and A. M. Mayes (2008), Science and technology for water purification in the coming decades, *Nature*, *452*(7185), 301–310, doi: 10.1038/nature06599.

Sharmila, S., and K. J. E. Walsh (2018), Recent poleward shift of tropical cyclone formation linked to Hadley cell expansion, *Nature Climate Change*, *8*(8), 730–736, doi: 10.1038/s41558-018-0227-5.

Shaw, T. A., M. Baldwin, E. A. Barnes, R. Caballero, C. I. Garfinkel, Y. T. Hwang, C. Li, P. A. O'Gorman, G. Rivière, I. R. Simpson, and A. Voigt (2016), Storm Track Processes and the Opposing Influences of Climate Change, *Nature Geoscience*, *9*(9), 656–664, doi: 10.1038/ngeo2783.

Sills, G. L., N. D. Vroman, R. E. Wahl, and N. T. Schwanz (2008), Overview of New Orleans Levee Failures: Lessons Learned and Their Impact on National Levee Design and Assessment, *Journal of Geotechnical and Geoenvironmental Engineering*, *134*(5), 556–565, doi: 10.1061/(ASCE)1090-0241(2008)134:5(556).

Silver, D., J. Schrittwieser, K. Simonyan, I. Antonoglou, A. Huang, A. Guez, T. Hubert, L. Baker, M. Lai, A. Bolton, Y. Chen, T. Lillicrap, F. Hui, L. Sifre, G. van den Driessche, T. Graepel, and D. Hassabis (2017), Mastering the game of Go without human knowledge, *Nature*, *550*(7676), 354–359, doi: 10.1038/nature24270.

Silver, D., T. Hubert, J. Schrittwieser, I. Antonoglou, M. Lai, A. Guez, M. Lanctot, L. Sifre, D. Kumaran, T. Graepel, T. Lillicrap, K. Simonyan, and D. Hassabis (2018), A general reinforcement learning algorithm that masters chess, shogi, and Go through self-play, *Science*, *362*(6419), 1140–1144, doi: 10.1126/science.aar6404.

Simonsen, I., A. Hansen, and O. M. Nes (1998), Determination of the Hurst exponent by use of wavelet transforms, *Physical Review E*, *58*(3), 2779–2787, doi: 10.1103/PhysRevE.58.2779.

Simpson, D., H. Rue, A. Riebler, T. G. Martins, and S. H. Sørbye (2017), Penalising Model Component Complexity: A Principled, Practical Approach to Constructing Priors, *Statistical Science*, *32*(1), 1–28, doi: 10.1214/16-STS576.

Slusarewicz, J. H., and D. S. Cohan (2018), Assessing solar and wind complementarity in Texas, *Renewables: Wind, Water, and Solar*, *5*(1), 7, doi: 10.1186/s40807-018-0054-3.

Smith, A., N. Lott, T. Houston, K. Shein, J. Crouch, and J. Enloe (2016), U.S. billion-dollar weather & climate disasters 1980-2016, *Tech. rep.*, NOAA National Centers for Environmental Information.

Smith, J. A., A. A. Cox, M. L. Baeck, L. Yang, and P. Bates (2018), Strange floods: The upper tail of flood peaks in the United States, *Water Resources Research*, *54*(9), 6510–6542, doi: 10.1029/2018WR022539.

Sobol, I. M. (2001), Global sensitivity indices for nonlinear mathematical models and their Monte Carlo estimates, *Mathematics and Computers in Simulation*, *55*(1), 271–280, doi: 10.1016/S0378-4754(00)00270-6.

Sodastrom, E., J. Sokolove, and S. K. Fairfax (1999), Federal Reserved Water Rights Applied to School Trust Lands Land and Water Division: Article, *Land and Water Law Review*, *34*, 1–38.

Sodemann, H., and A. Stohl (2013), Moisture Origin and Meridional Transport in Atmospheric Rivers and Their Association with Multiple Cyclones, *Monthly Weather Review*, *141*(8), 2850–2868, doi: 10.1175/MWR-D-12-00256.1.

Spence, C. M., and C. M. Brown (2016), Nonstationary Decision Model for Flood Risk Decision Scaling, *Water Resources Research*, *52*(11), 8650–8667, doi: 10.1002/2016WR018981.

Srikrishnan, V., and K. Keller (2019), Small increases in agent-based model complexity can result in large increases in required calibration data, *arXiv:1811.08524 [stat]*.

Srinivasan, V., M. Konar, and M. Sivapalan (2017), A dynamic framework for water security, *Water Security*, *1*, 12–20, doi: 10.1016/j.wasec.2017.03.001.

Stadtherr, L., D. Coumou, V. Petoukhov, S. Petri, and S. Rahmstorf (2016), Record Balkan Floods of 2014 Linked to Planetary Wave Resonance, *Science Advances*, *2*(4), e1501,428–e1501,428, doi: 10.1126/sciadv.1501428.

Stainforth, D. A., T. E. Downing, R. Washington, A. Lopez, and New, Mark (2007), Issues in the interpretation of climate model ensembles to inform decisions, *Philosophical Transactions of the Royal Society A: Mathematical, Physical and Engineering Sciences*, *365*(1857), 2163–2177, doi: 10.1098/rsta.2007.2073.

Stedinger, J. R. (1997), Expected probability and annual damage estimators, *Journal of Water Resources Planning and Management*, *123*(2), 125–135, doi: 10.1061/(ASCE)0733-9496(1997)123:2(125).

Stedinger, J. R., B. F. Sule, and D. P. Loucks (1984), Stochastic dynamic programming models for reservoir operation optimization, *Water Resources Research*, *20*(11), 1499–1505, doi: 10.1029/WR020i011p01499.

Steiger, N. J., J. E. Smerdon, B. I. Cook, R. Seager, A. P. Williams, and E. R. Cook (2019), Oceanic and radiative forcing of medieval megadroughts in the American Southwest, *Science Advances*, *5*(7), eaax0087, doi: 10.1126/sciadv.aax0087.

Steinschneider, S., and C. Brown (2013), A semiparametric multivariate, multisite weather generator with low-frequency variability for use in climate risk assessments, *Water Resources Research*, *49*(11), 7205–7220, doi: 10.1002/wrcr.20528.

Steinschneider, S., and U. Lall (2015a), Daily Precipitation and Tropical Moisture Exports across the Eastern United States: An Application of Archetypal Analysis to Identify Spatiotemporal Structure, *Journal of Climate*, *28*(21), 8585–8602, doi: 10.1175/JCLI-D-15-0340.1.

Steinschneider, S., and U. Lall (2015b), A hierarchical Bayesian regional model for nonstationary precipitation extremes in Northern California conditioned on tropical moisture exports, *Water Resources Research*, *51*(3), 1472–1492, doi: 10.1002/2014WR016664.

Steinschneider, S., and U. Lall (2016), Spatiotemporal Structure of Precipitation Related to Tropical Moisture Exports over the Eastern United States and Its Relation to Climate Teleconnections, *Journal of Hydrometeorology*, *17*(3), 897–913, doi: 10.1175/JHM-D-15-0120.1.

Steinschneider, S., R. McCrary, S. Wi, K. Mulligan, L. O. Mearns, and C. M. Brown (2015), Expanded Decision-Scaling Framework to Select Robust Long-Term Water-System Plans under Hydroclimatic Uncertainties, *Journal of Water Resources Planning and Management*, *141*(11), doi: 10.1061/(ASCE)WR.1943-5452.0000536.

Steinschneider, S., P. Ray, S. H. Rahat, and J. Kucharski (2019), A weather-regime based stochastic weather generator for climate vulnerability assessments of water systems in the Western United States, *Water Resources Research*, *0*(ja), doi: 10.1029/2018WR024446.

Stephens, G. L., T. L'Ecuyer, R. Forbes, A. Gettlemen, J.-C. Golaz, A. Bodas-Salcedo, K. Suzuki, P. Gabriel, and J. Haynes (2010), Dreary State of Precipitation in Global Models, *Journal of Geophysical Research: Atmospheres*, *115*(D24), D24,211, doi: 10.1029/2010JD014532.

Stohl, A., C. Forster, and H. Sodemann (2008), Remote Sources of Water Vapor Forming Precipitation on the Norwegian West Coast at 60N: A Tale of Hurricanes and an Atmospheric River, *Journal of Geophysical Research: Atmospheres*, *113*(D5), doi: 10.1029/2007JD009006.

Su, Y., J. D. Kern, S. Denaro, J. Hill, P. Reed, Y. Sun, J. Cohen, and G. W. Characklis (2020), An open source model for quantifying risks in bulk electric power systems from spatially and temporally correlated hydrometeorological processes, *Environmental Modelling & Software*, *126*, 104,667, doi: 10.1016/j.envsoft.2020.104667.

Surminski, S., L. M. Bouwer, and J. Linnerooth-Bayer (2016), How Insurance Can Support Climate Resilience, *Nature Climate Change*, *6*(4), 333–334, doi: 10.1038/nclimate2979.

Sutton, R. S., and A. G. Barto (2018), *Reinforcement Learning: An Introduction*, second edition ed., MIT Press.

Sutton, R. S., D. A. McAllester, S. P. Singh, and Y. Mansour (2000), Policy gradient methods for reinforcement learning with function approximation, in *Neural Information Processing Systems 12*, pp. 1057–1063.

Swierczynski, T., A. Brauer, S. Lauterbach, C. Martín-Puertas, P. Dulski, U. von Grafenstein, and C. Rohr (2012), A 1600 Yr Seasonally Resolved Record of Decadal-Scale Flood Variability from the Austrian Pre-Alps, *Geology*, *40*(11), 1047–1050, doi: 10.1130/G33493.1.

Swiss Re Institute (2017), Presliminary Sigma Estimates for 2017: Global Insured Losses of USD 136 Billion Are Third Highest on Sigma Records, *Tech. rep.*, Swiss Re Ltd.

Taleb, N. N. (2007), *The Black Swan: The Impact of the Highly Improbable*, Random House, New York.

Taleb, N. N. (2012), *Antifragile: Things That Gain from Disorder*, Random House, New York.

Taleb, N. N., R. Read, R. Douady, J. Norman, and Y. Bar-Yam (2014), The Precautionary Principle (with Application to the Genetic Modification of Organisms), *arXiv:1410.5787 [q-fin.GN]*.

Talebiyan, H., and L. Dueñas-Osorio (2020), Decentralized decision making for the restoration of interdependent networks, *Journal of Risk and Uncertainty in Engineering Systems*, *6*(2), 04020,012, doi: 10.1061/AJRUA6.0001035.

Tandon, N. F., E. P. Gerber, A. H. Sobel, and L. M. Polvani (2012), Understanding Hadley cell expansion versus contraction: Insights from simplified models and implications for recent observations, *Journal of Climate*, *26*(12), 4304–4321, doi: 10.1175/JCLI-D-12-00598.1.

Tedesco, M., S. McAlpine, and J. R. Porter (2020), Exposure of real estate properties to the 2018 Hurricane Florence flooding, *Natural Hazards and Earth System Sciences*, *20*(3), 907–920, doi: 10.5194/nhess-20-907-2020.

Tellman, B., R. I. McDonald, J. H. Goldstein, A. L. Vogl, M. Flörke, D. Shemie, R. Dudley, R. Dryden, P. Petry, N. Karres, K. Vigerstol, B. Lehner, and F. Veiga (2018), Opportunities for natural infrastructure to improve urban water security in Latin America, *PLOS ONE*, *13*(12), e0209,470, doi: 10.1371/journal.pone.0209470.

Teng, H., and G. Branstator (2016), Causes of Extreme Ridges That Induce California Droughts, *Journal of Climate*, *30*(4), 1477–1492, doi: 10.1175/JCLI-D-16-0524.1.

Thorndahl, S., A. K. Andersen, and A. B. Larsen (2017), Event-based stochastic point rainfall resampling for statistical replication and climate projection of historical rainfall series, *Hydrology and Earth System Sciences*, *21*(9), 4433–4448, doi: 10.5194/hess-21-4433-2017.

Tigchelaar, M., D. S. Battisti, R. L. Naylor, and D. K. Ray (2018), Future warming increases probability of globally synchronized maize production shocks, *Proceedings of the National Academy of Sciences of the United States of America*, *5*, 201718,031, doi: 10.1073/pnas.1718031115.

Timmermann, A., S.-I. An, J.-S. Kug, F.-F. Jin, W. Cai, A. Capotondi, K. Cobb, M. Lengaigne, M. J. McPhaden, M. F. Stuecker, K. Stein, A. T. Wittenberg, K.-S. Yun, T. Bayr, H.-C. Chen, Y. Chikamoto, B. Dewitte, D. Dommenget, P. Grothe, E. Guilyardi, Y.-G. Ham, M. Hayashi, S. Ineson, D. Kang, S. Kim, W. Kim, J.-Y. Lee, T. Li, J.-J. Luo, S. McGregor, Y. Planton, S. Power, H. Rashid, H.-L. Ren, A. Santoso, K. Takahashi, A. Todd, G. Wang, G. Wang, R. Xie, W.-H. Yang, S.-W. Yeh, J. Yoon, E. Zeller, and X. Zhang (2018), El Niño–Southern Oscillation complexity, *Nature*, *559*(7715), 535–545, doi: 10.1038/s41586-018-0252-6.

Tobin, G. A. (1995), The Levee Love-Affair - a Stormy Relationship, *Water Resources Bulletin*, *31*(3), 359–367, doi: 10.1111/j.1752-1688.1995.tb04025.x.

Toomey, M., M. Cantwell, S. Colman, T. Cronin, J. Donnelly, L. Giosan, C. Heil, R. Korty, M. Marot, and D. Willard (2019), The mighty Susquehanna—extreme floods in Eastern North America during the past two millennia, *Geophysical Research Letters*, *46*(6), doi: 10.1029/2018GL080890.

Torrence, C., and G. P. Compo (1998), A Practical Guide to Wavelet Analysis, *Bulletin of the American Meteorological Society*, *79*(1), 61–78, doi: 10.1175/1520-0477(1998)079<0061:APGTWA>2.0.CO;2.

Tortajada, C. (2006), Water Management in Mexico City Metropolitan Area, *International Journal of Water Resources Development*, *22*(2), 353–376, doi: 10.1080/07900620600671367.

Trenberth, K. E. (1999), Atmospheric moisture recycling: Role of advection and local evaporation, *Journal of Climate*, *12*(5), 1368–1381, doi: 10.1175/1520-0442(1999)012<1368:AMRROA>2.0.CO;2.

Trenberth, K. E., and J. T. Fasullo (2012), Climate Extremes and Climate Change: The Russian Heat Wave and Other Climate Extremes of 2010, *Journal of Geophysical Research: Atmospheres*, *117*(D17), doi: 10.1029/2012JD018020.

Trenberth, K. E., A. Dai, R. M. Rasmussen, and D. B. Parsons (2003), The Changing Character of Precipitation, *Bulletin of the American Meteorological Society*, *84*(9), 1205–1217, doi: 10.1175/BAMS-84-9-1205.

Trindade, B. C., P. M. Reed, J. D. Herman, H. B. Zeff, and G. W. Characklis (2017), Reducing regional drought vulnerabilities and multi-city robustness conflicts using many-objective optimization under deep uncertainty, *Advances in Water Resources*, *104*, 195–209, doi: 10.1016/j.advwatres.2017.03.023.

Trindade, B. C., P. M. Reed, and G. W. Characklis (2019), Deeply uncertain pathways: Integrated multi-city regional water supply infrastructure investment and portfolio management, *Advances in Water Resources*, p. 103442, doi: 10.1016/j.advwatres.2019.103442.

Tsoukiàs, A. (2008), From decision theory to decision aiding methodology, *European Journal of Operational Research*, *187*(1), 138–161, doi: 10.1016/j.ejor.2007.02.039.

Tyrlis, E., and B. J. Hoskins (2008), The Morphology of Northern Hemisphere Blocking, *Journal of the Atmospheric Sciences*, *65*(5), 1653–1665, doi: 10.1175/2007JAS2338.1.

USACE (2007), Advanced Measures Report Based on Technical Assistance Investigation, Santa Maria Valley Levees, Santa Barbara County, CA, *Tech. rep.*, United States Army Corps of Engineers Los Angeles District, Los Angeles, CA.

USACE (2014), Dallas Floodway, Dallas TX, *Tech. rep.*, United States Army Corps of Engineers, Fort Worth District, Fort Worth, TX.

USACE (2019), New York – New Jersey Harbor and Tributaries Coastal Storm Risk Management Feasibility Study Interim Report, *Tech. rep.*, United States Army Corps of Engineers New York District, New York, NY.

USEPA (2005), Decentralized wastewater treatment systems: A program strategy, *Tech. Rep. 832-R-05-002*, United States Environmental Protection Agency.

Vallis, G. K. (2006), *Atmospheric and Oceanic Fluid Dynamics: Fundamentals and Large-Scale Circulation*, Cambridge University Press.

van Dantzig, D. (1956), Economic Decision Problems for Flood Prevention, *Econometrica*, *24*(3), 276–287, doi: 10.2307/1911632.

van der Ent, R. J., and H. H. G. Savenije (2013), Oceanic Sources of Continental Precipitation and the Correlation with Sea Surface Temperature, *Water Resources Research*, *49*(7), 3993–4004, doi: 10.1002/wrcr.20296.

van der Walt, S., S. C. Colbert, and G. Varoquaux (2011), The NumPy Array: A Structure for Efficient Numerical Computation, *Computing in Science & Engineering*, *13*(2), 22–30, doi: 10.1109/MCSE.2011.37.

Van der Weele, T. J. (2019), Principles of confounder selection, *European Journal of Epidemiology*, *34*(3), 211–219, doi: 10.1007/s10654-019-00494-6.

van Hasselt, H., A. Guez, and D. Silver (2015), Deep Reinforcement Learning with Double Q-learning, *arXiv:1509.06461 [cs.LG]*.

Velasco, I., and J. M. Fritsch (1987), Mesoscale convective complexes in the Americas, *Journal of Geophysical Research*, *92*(D8), 9591, doi: 10.1029/JD092iD08p09591.

Vera, C., J. Baez, M. Douglas, C. B. Emmanuel, J. Marengo, J. Meitin, M. Nicolini, J. Nogues Paegle, J. Paegle, O. Penalba, P. Salio, A. C. Saulo, M. A. Silva Dias, P. L. S. Dias, and E. Zipser (2006), The South American Low-Level Jet Experiment, *Bulletin of the American Meteorological Society*, *87*(1), 63–78, doi: 10.1175/BAMS-87-1-63.

Vigaud, N., A. W. Robertson, and M. K. Tippett (2017), Multimodel Ensembling of Subseasonal Precipitation Forecasts over North America, *Monthly Weather Review*, *145*(10), 3913–3928, doi: 10.1175/MWR-D-17-0092.1.

Virtanen, P., R. Gommers, T. E. Oliphant, M. Haberland, T. Reddy, D. Cournapeau, E. Burovski, P. Peterson, W. Weckesser, J. Bright, S. J. van der Walt, M. Brett, J. Wilson, K. J. Millman, N. Mayorov, A. R. J. Nelson, E. Jones, R. Kern, E. Larson, C. J. Carey, İ. Polat, Y. Feng, E. W. Moore, J. VanderPlas, D. Laxalde, J. Perktold, R. Cimrman, I. Henriksen, E. A. Quintero, C. R. Harris, A. M. Archibald, A. H. Ribeiro, F. Pedregosa, and P. van Mulbregt (2020), SciPy 1.0: Fundamental algorithms for scientific computing in Python, *Nature Methods*, *17*(3), 261–272, doi: 10.1038/s41592-019-0686-2.

Vitart, F., F. Vitart, C. Ardilouze, A. Bonet, A. Brookshaw, M. Chen, C. Codorean, M. Déqué, M. Déqué, L. Ferranti, L. Ferranti, E. Fucile, E. Fucile, M. Fuentes, M. Fuentes, H. Hendon, J. Hodgson, J. Hodgson, H. S. Kang, H. s Kang, A. Kumar, A. Kumar, H. Lin, H. Lin, G. Liu, G. Liu, X. Liu, X. Liu, P. Malguzzi, P. Malguzzi, I. Mallas, I. Mallas, M. Manoussakis, M. Manoussakis, D. Mastrangelo, D. Mastrangelo, C. MacLachlan, C. MacLachlan, P. McLean, P. McLean, A. Minami, A. Minami, R. Mladek, R. Mladek, T. Nakazawa, T. Nakazawa, S. Najm, S. Najm, Y. Nie, Y. Nie, M. Rixen, M. Rixen, A. W. Robertson, A. W. Robertson, P. Ruti, P. Ruti, C. Sun, C. Sun, Y. Takaya, Y. Takaya, M. Tolstykh, M. Tolstykh, F. Venuti, F. Venuti, D. Waliser, D. Waliser, S. Woolnough, S. Woolnough, T. Wu, T. Wu, D.-J. Won, D. J. Won, H. Xiao, H. Xiao, R. Zaripov, R. Zaripov, L. Zhang, and L. Zhang (2016), The Sub-Seasonal to Seasonal Prediction (S2S) Project Database, *Bulletin of the American Meteorological Society*, *98*(1), 163–173, doi: 10.1175/BAMS-D-16-0017.1.

Von Neumann, J., and O. Morgenstern (1953), *Theory of Games and Economic Behavior*, 3rd edition ed., Princeton University Press, Princeton.

Walker, W., M. Haasnoot, and J. Kwakkel (2013a), Adapt or Perish: A Review of Planning Approaches for Adaptation under Deep Uncertainty, *Sustainability*, *5*(3), 955–979, doi: 10.3390/su5030955.

Walker, W. E., R. J. Lempert, and J. H. Kwakkel (2013b), Deep Uncertainty, in *Encyclopedia of Operations Research and Management Science*, edited by S. I. Gass and M. C. Fu, pp. 395–402, Springer US, Boston, MA, doi: 10.1007/978-1-4419-1153-7_1140.

Wang, S. S. (2002), A universal framework for pricing financial and insurance risks, *ASTIN Bulletin: The Journal of the IAA*, *32*(2), 213–234, doi: 10.2143/AST.32.2.1027.

Wang, Z., T. Schaul, M. Hessel, H. van Hasselt, M. Lanctot, and N. de Freitas (2016), Dueling Network Architectures for Deep Reinforcement Learning, *arXiv:1511.06581 [cs.LG]*.

Ward, P. J., B. Jongman, M. Kummu, M. D. Dettinger, F. C. Sperna Weiland, and H. C. Winsemius (2014), Strong Influence of El Nino Southern Oscillation on Flood Risk around the World, *Proceedings of the National Academy of Sciences of the United States of America*, *111*(44), 15,659–15,664, doi: 10.1073/pnas.1409822111.

Watterson, B. (1990), *The Authoritative Calvin and Hobbes*, Andrews McMeel Publishing.

Weck, O. L. D., D. Roos, and C. L. Magee (2011), *Engineering Systems: Meeting Human Needs in a Complex Technological World*, MIT Press.

Wehner, M. F., R. L. Smith, G. Bala, and P. Duffy (2010), The effect of horizontal resolution on simulation of very extreme US precipitation events in a global atmosphere model, *Climate Dynamics*, *34*(2), 241–247, doi: 10.1007/s00382-009-0656-y.

Weijs, S. V., and B. L. Ruddell (2020), Debates: Does information theory provide a new paradigm for Earth Science? Sharper predictions using Occam's Digital Razor, *Water Resources Research*, *56*(2), e2019WR026,471, doi: 10.1029/2019WR026471.

Weijs, S. V., R. van Nooijen, and N. van de Giesen (2010), Kullback–Leibler Divergence as a Forecast Skill Score with Classic Reliability–Resolution–Uncertainty Decomposition, *Monthly Weather Review*, *138*(9), 3387–3399, doi: 10.1175/2010mwr3229.1.

Weinberg, A. M. (1972), Science and trans-science, *Minerva*, *10*(2), 209–222, doi: 10.1007/BF01682418.

Weitzman, M. L. (2007), A Review of the Stern Review on the Economics of Climate Change, *Journal of Economic Literature*, *45*(3), 703–724, doi: 10.1257/jel.45.3.703.

Wengel, C., D. Dommenget, M. Latif, T. Bayr, and A. Vijayeta (2018), What Controls ENSO-Amplitude Diversity in Climate Models?, *Geophysical Research Letters*, *45*(4), 1989–1996, doi: 10.1002/2017GL076849.

Wheeler, M. C., and H. H. Hendon (2004), An all-season real-time multivariate MJO index: Development of an index for monitoring and prediction, *Journal of Climate*, *132*(8), 1917–1932, doi: 10.1175/1520-0493(2004)132<1917:AARMMI>2.0.CO;2.

Wilby, R. L., C. W. Dawson, and E. M. Barrow (2002), Sdsm — a decision support tool for the assessment of regional climate change impacts, *Environmental Modelling & Software*, *17*(2), 145–157, doi: 10.1016/S1364-8152(01)00060-3.

Wilks, D. S. (2006), Comparison of ensemble-MOS methods in the Lorenz '96 setting, *Meteorological Applications*, *13*(3), 243–256, doi: 10.1017/S1350482706002192.

Wilks, D. S. (2009), Extending logistic regression to provide full-probability-distribution MOS forecasts, *Meteorological Applications*, *16*(3), 361–368, doi: 10.1002/met.134.

Williams, G. (2013), *Washed Away: How the Great Flood of 1913, America's Most Widespread Natural Disaster, Terrorized a Nation and Changed It Forever*, Pegasus Books.

Williams, I. N., and C. M. Patricola (2018), Diversity of ENSO Events Unified by Convective Threshold Sea Surface Temperature: A Nonlinear ENSO Index, *Geophysical Research Letters*, *45*(17), 9236–9244, doi: 10.1029/2018GL079203.

Winsemius, H. C., J. C. J. H. Aerts, L. P. H. van Beek, M. F. P. Bierkens, A. Bouwman, B. Jongman, J. C. J. Kwadijk, W. Ligtvoet, P. L. Lucas, D. P. van Vuuren, and P. J. Ward (2016), Global drivers of future river flood risk, *Nature Climate Change*, *6*(4), 381–385, doi: 10.1038/nclimate2893.

Wise, R. M., I. Fazey, M. Stafford Smith, S. E. Park, H. C. Eakin, E. R. M. Archer Van Garderen, and B. Campbell (2014), Reconceptualising adaptation to climate change as part of pathways of change and response, *Global Environmental Change*, *28*, 325–336, doi: 10.1016/j.gloenvcha.2013.12.002.

Wolfrom, L. (2016), Financial Instruments for Managing Disaster Risks Related to Climate Change, *OECD Journal: Financial Market Trends*, *2015*(1), 25–47, doi: 10.1787/fmt-2015-5jrqdkpxk5d5.

Wong, T. E., and K. Keller (2017), Deep Uncertainty Surrounding Coastal Flood Risk Projections: A Case Study for New Orleans, *Earth's Future*, *5*(10), 1015–1026, doi: 10.1002/2017EF000607.

Wong, T. E., A. M. R. Bakker, and K. Keller (2017), Impacts of Antarctic fast dynamics on sea-level projections and coastal flood defense, *Climatic Change*, *144*(2), 347–364, doi: 10.1007/s10584-017-2039-4.

Wong, T. E., A. Klufas, V. Srikrishnan, and K. Keller (2018), Neglecting model structural uncertainty underestimates upper tails of flood hazard, *Environmental Research Letters*, *13*(7), 074,019, doi: 10.1088/1748-9326/aacb3d.

Woollings, T., C. Czuchnicki, and C. Franzke (2014a), Twentieth century North Atlantic jet variability, *Quarterly Journal of the Royal Meteorological Society*, *140*(680), 783–791, doi: 10.1002/qj.2197.

Woollings, T., C. Franzke, D. L. R. Hodson, B. Dong, E. A. Barnes, C. C. Raible, and J. G. Pinto (2014b), Contrasting Interannual and Multidecadal NAO Variability, *Climate Dynamics*, *45*(1-2), 539–556, doi: 10.1007/s00382-014-2237-y.

Woollings, T., E. A. Barnes, B. Hoskins, Y.-O. Kwon, R. W. Lee, C. Li, E. Madonna, M. McGraw, T. Parker, R. Rodrigues, C. Spensberger, and K. Williams (2018), Daily to Decadal Modulation of Jet Variability, *Journal of Climate*, *31*(4), 1297–1314, doi: 10.1175/JCLI-D-17-0286.1.

World Bank (2015), Financial Protection Against Natural Disasters: An Operational Framework for Disaster Risk Financing and Insurance, *Tech. rep.*, World Bank Group, Washington, DC.

World Bank (2018), Water Scarce Cities : Thriving in a Finite World. World Bank, *Tech. rep.*, World Bank, Washington, DC.

Yan, X., R. Zhang, and T. R. Knutson (2018), Underestimated AMOC Variability and Implications for AMV and Predictability in CMIP Models, *Geophysical Research Letters*, *43*(9-10), 2333, doi: 10.1029/2018GL077378.

Yang, D., D. Kane, Z. Zhang, D. Legates, and B. Goodison (2005), Bias corrections of long-term (1973–2004) daily precipitation data over the northern regions, *Geophysical Research Letters*, *32*(19), doi: 10.1029/2005GL024057.

Yao, Y., A. Vehtari, D. Simpson, and A. Gelman (2018), Using Stacking to Average Bayesian Predictive Distributions, *Bayesian Analysis*, doi: 10.1214/17-BA1091.

Yoon, E. J., J. H. Thorne, C. Park, D. K. Lee, K. S. Kim, H. Yoon, C. Seo, Chul-Hee Lim, H. Kim, and Y.-I. Song (2019), Modeling spatial climate change landuse adaptation with multi-objective genetic algorithms to improve resilience for rice yield and species richness and to mitigate disaster risk, *Environmental Research Letters*, *14*(2), 024,001, doi: 10.1088/1748-9326/aaf0cf.

Zanardo, S., L. Nicotina, A. G. J. Hilberts, and S. P. Jewson (2019), Modulation of Economic Losses From European Floods by the North Atlantic Oscillation, *Geophysical Research Letters*, *46*(5), 2563–2572, doi: 10.1029/2019GL081956.

Zarekarizi, M., V. Srikrishnan, and K. Keller (2020), Neglecting Uncertainties Leads to Suboptimal Decisions About Home-Owners Flood Risk Management, *arXiv:2001.06457 [physics, q-fin, stat]*.

Zebiak, S. E., and M. A. Cane (1987), A Model El Niño-Southern Oscillation, *Monthly Weather Review*, *115*(10), 2262–2278, doi: 10.1175/1520-0493(1987)115<2262:AMENO>2.0.CO;2.

Zeff, H. B., and G. W. Characklis (2013), Managing water utility financial risks through third-party index insurance contracts, *Water Resources Research*, *49*(8), 4939–4951, doi: 10.1002/wrcr.20364.

Zeff, H. B., J. D. Herman, P. M. Reed, and G. W. Characklis (2016), Cooperative drought adaptation: Integrating infrastructure development, conservation, and water transfers into adaptive policy pathways, *Water Resources Research*, *52*(9), 7327–7346, doi: 10.1002/2016WR018771.

Zeff, H. B., G. W. Characklis, and W. Thurman (2020), How do price surcharges impact water utility financial incentives to pursue alternative supplies during drought?, *Journal of Water Resources Planning and Management*, *146*(6), 04020,042, doi: 10.1061/(ASCE)WR.1943-5452.0001228.

Zhang, L., G. Kuczera, A. S. Kiem, and G. Willgoose (2018), Using paleoclimate reconstructions to analyse hydrological epochs associated with Pacific Decadal Variability, *Hydrological and Earth System Science*, pp. 1–38, doi: 10.5194/hess-22-6399-2018.

Živković, T., and K. Rypdal (2013), ENSO dynamics: Low-dimensional-chaotic or stochastic?, *Journal of Geophysical Research: Atmospheres*, *118*(5), 2161–2168, doi: 10.1002/jgrd.50190.

Zscheischler, J., S. Westra, B. J. J. M. van den Hurk, S. I. Seneviratne, P. J. Ward, A. Pitman, A. AghaKouchak, D. N. Bresch, M. Leonard, T. Wahl, and X. Zhang (2018), Future climate risk from compound events, *Nature Climate Change*, *332*, 220, doi: 10.1038/s41558-018-0156-3.